

AFRL-AFOSR-VA-TR-2022-0128

Reducing transient energy growth in shear flows using sensor-based output feedback control

Hemati, Maziar
REGENTS OF THE UNIVERSITY OF MINNESOTA
200 OAK ST SE # 224
MINNEAPOLIS, MN, 55455
USA

04/01/2022
Final Technical Report

DISTRIBUTION A: Distribution approved for public release.

Air Force Research Laboratory
Air Force Office of Scientific Research
Arlington, Virginia 22203
Air Force Materiel Command

REPORT DOCUMENTATION PAGE

PLEASE DO NOT RETURN YOUR FORM TO THE ABOVE ORGANIZATION.

1. REPORT DATE	**2. REPORT TYPE**	**3. DATES COVERED**	
20220401	Final	**START DATE** 20190101	**END DATE** 20221231

4. TITLE AND SUBTITLE
Reducing transient energy growth in shear flows using sensor-based output feedback control

5a. CONTRACT NUMBER	**5b. GRANT NUMBER**	**5c. PROGRAM ELEMENT NUMBER**
	FA9550-19-1-0034	61102F
5d. PROJECT NUMBER	**5e. TASK NUMBER**	**5f. WORK UNIT NUMBER**

6. AUTHOR(S)
Maziar Hemati

7. PERFORMING ORGANIZATION NAME(S) AND ADDRESS(ES)
REGENTS OF THE UNIVERSITY OF MINNESOTA
200 OAK ST SE # 224
MINNEAPOLIS, MN 55455
USA

8. PERFORMING ORGANIZATION REPORT NUMBER

9. SPONSORING/MONITORING AGENCY NAME(S) AND ADDRESS(ES)	**10. SPONSOR/MONITOR'S ACRONYM(S)**	**11. SPONSOR/MONITOR'S REPORT NUMBER(S)**
Air Force Office of Scientific Research 875 N. Randolph St. Room 3112 Arlington, VA 22203	AFRL/AFOSR RTA1	AFRL-AFOSR-VA-TR-2022-0128

12. DISTRIBUTION/AVAILABILITY STATEMENT
A Distribution Unlimited: PB Public Release

13. SUPPLEMENTARY NOTES

14. ABSTRACT
This report documents outcomes of research supported under AFOSR Grant No. FA9550-19-1-0034: “Reducing transient energy growth in shear flows using sensor-based output feedback control” (January 1, 2019–December 31, 2021) monitored by Dr. Gregg Abate. The long-term objective of this work is to use feedback control to suppress sub-critical transition to turbulence, and thus reduce drag in systems of interest to the Air Force and DoD.
The focus of this effort was to develop and use static output feedback control strategies to reduce transient energy growth (TEG) of flow perturbations, thus facilitating transition suppression. Specifically, three objectives related to controller synthesis were investigated:
Objective #1: Robustly reduce transient energy growth (TEG) via static output feedback;
Objective #2: Minimize the worst-case TEG via static output feedback;
Objective #3: Facilitate controller synthesis via low-order control-oriented fluids models.
Technical outcomes for each of these objectives are summarized in the ensuing chapters of this report.

15. SUBJECT TERMS

16. SECURITY CLASSIFICATION OF:			**17. LIMITATION OF ABSTRACT**	**18. NUMBER OF PAGES**
a. REPORT	**b. ABSTRACT**	**c. THIS PAGE**		
U	U	U	UU	143

19a. NAME OF RESPONSIBLE PERSON	**19b. PHONE NUMBER** *(Include area code)*
GREGG ABATE	425-1779

Final Report for
Award No. FA9550-19-1-0034
United States Air Force Office of Scientific Research

Reducing transient energy growth in shear flows using sensor-based output feedback control

Period of Performance:

January 1, 2019 – December 31, 2021

Principal Investigator:

Prof. Maziar S. Hemati
Aerospace Engineering and Mechanics
University of Minnesota

Email: mhemati@umn.edu
Phone: 612-625-6857
Fax: 612-626-1558

Submitted to: Dr. Gregg Abate
AFOSR/RTA1
Unsteady Aerodynamics and Turbulent Flows
Air Force Office of Scientific Research
875 N. Randolph St, Suite 325, Room 3112
Arlington, VA 22203

February 15, 2022

Contents

1 Executive Summary **4**

2 Introduction **5**

3 Channel Flow and Full-Information Control **8**
3.1 Introduction 8
3.2 Numerical Approaches 10
3.2.1 Direct numerical simulation 10
3.2.2 Linearized Navier–Stokes equations and feedback control design 11
3.3 Results and Discussions 13
3.3.1 Transient energy growth of optimal disturbance 13
3.3.2 Suppression of laminar-to-turbulent transition 20
3.4 Conclusions 26

4 Static Output Feedback Control for Reducing Transient Energy Growth **28**
4.1 Introduction 28
4.2 Transient energy growth and controller synthesis 30
4.2.1 Transient energy growth 30
4.2.2 Full-information feedback control synthesis 30
4.2.3 Static output feedback control synthesis 31
4.3 Channel flow model 33
4.3.1 Linearized channel flow system 33
4.3.2 Direct numerical simulation setup 35
4.4 Results 35
4.4.1 Spanwise disturbances 36
4.4.2 Streamwise disturbances 43
4.5 Conclusion 49

5 Control-Oriented Model Reduction **50**
5.1 Introduction 50
5.2 Reduced-order models and controller synthesis 52
5.2.1 Control-oriented reduced-order models 54
5.3 Results 56
5.3.1 Channel Flow System 56

5.3.2 Frequency analysis of control-oriented reduced-order models for the channel flow system . . . 58
5.3.3 Controller performance . . . 59
5.4 Conclusions . . . 66

6 Optimal Sensor Selection **68**
6.1 Introduction . . . 68
6.2 Channel flow model and control synthesis . . . 70
6.2.1 Channel flow . . . 70
6.2.2 Linearized Navier–Stokes equations . . . 71
6.2.3 Transient energy growth and control synthesis . . . 73
6.3 Sensor selection for state feedback performance recovery . . . 74
6.3.1 Sensor selection by column-norm evaluation (CE) . . . 74
6.3.2 Sensor selection by balanced truncation . . . 76
6.4 Results: sensor selection and linear performance analysis . . . 79
6.4.1 Streamwise disturbance $(\alpha, \beta) = (1, 0)$ . . . 80
6.4.2 Oblique disturbance $(\alpha, \beta) = (1, 1)$ . . . 81
6.4.3 Spanwise disturbance $(\alpha, \beta) = (0, 2)$ . . . 83
6.4.4 Controller robustness analysis . . . 86
6.5 Results: nonlinear performance analysis using direct numerical simulations . . . 88
6.5.1 Laminar-to-turbulent transition . . . 90
6.5.2 Transition suppression . . . 90
6.6 Discussion and conclusions . . . 95

7 Nonlinear MTEG Prediction and Control **97**
7.1 Introduction . . . 97
7.2 Waleffe-Kim-Hamilton Model of Transition and Sustained Turbulence . . . 99
7.3 Nonlinear Stability Analysis using Quadratic Constraints . . . 101
7.3.1 Stability: Representing Lossless Nonlinearity with Quadratic Constraints . . . 102
7.3.2 Stability: Representing Local Properties of Nonlinearity using Quadratic Constraints . . . 103
7.3.3 Results: Local stability analysis using quadratic constraints . . . 105
7.4 Estimating Permissible Perturbation Amplitudes . . . 107
7.5 Nonlinear Transient Energy Growth Analysis using Quadratic Constraints . . . 109
7.5.1 Global MTEG Analysis using Quadratic Constraints . . . 110
7.5.2 Local MTEG Analysis using Quadratic Constraints . . . 110
7.5.3 Results: MTEG analysis using quadratic constraints . . . 111
7.6 Lagrange Multiplier Analysis: Drawing Physical Insights Into Nonlinear Flow Interactions . . . 112
7.7 Conclusion . . . 115

8 Personnel **117**

9 Publications **118**

10 Recognitions/Interactions/Transitions **120**

A Stabilizing static output feedback controller **122**

B Computational complexity of the accelerated Anderson-Moore algorithm **124**

C Grid resolution study **125**

D Limitations of Modal truncation for MTEG-minimizing control **127**

E Sector-bounded nonlinearities **129**

F The set bounded by local region R is invariant **130**

Bibliography **131**

1 | Executive Summary

This report documents outcomes of research supported under AFOSR Grant No. FA9550-19-1-0034: "Reducing transient energy growth in shear flows using sensor-based output feedback control" (January 1, 2019–December 31, 2021) monitored by Dr. Gregg Abate. The long-term objective of this work is to use feedback control to suppress sub-critical transition to turbulence, and thus reduce drag in systems of interest to the Air Force and DoD.

The focus of this effort was to develop and use static output feedback control strategies to reduce transient energy growth (TEG) of flow perturbations, thus facilitating transition suppression. Specifically, three objectives related to controller synthesis were investigated:

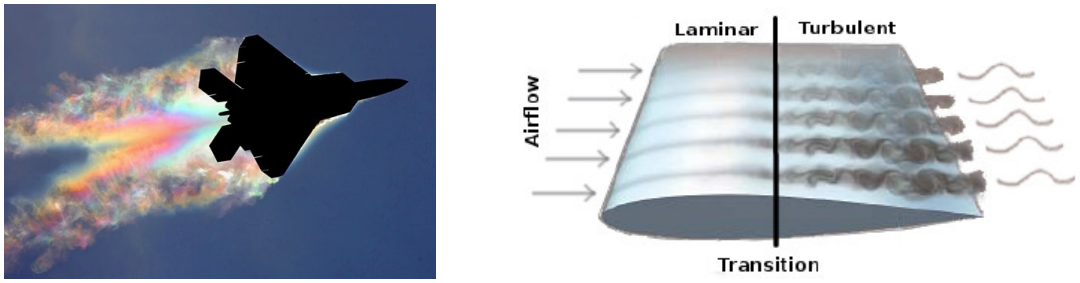
Objective #1: Robustly reduce transient energy growth (TEG) via static output feedback;
Objective #2: Minimize the worst-case TEG via static output feedback;
Objective #3: Facilitate controller synthesis via low-order control-oriented fluids models.

Technical outcomes for each of these objectives are summarized in the ensuing chapters of this report. All objectives were addressed within the context of a channel flow with wall normal blow and suction actuation . A detailed analysis of flow control and transition mechanisms under the assumption of full-information control is reported in Chapter (Chapter 3). Specific contributions toward sensor-based feedback control include static output feedback strategies that robustly reduce the maximum TEG (Chapter 4); control-oriented models that enable the design of otherwise unwieldy feedback controllers that minimize the maximum TEG (Chapter 5); and sensor selection algorithms for enabling sensor-based SOF control to recover full-information control performance (Chapter 6). In addition, the research effort on sensor-based output feedback control for TEG reduction has also contributed to a theoretical framework for accommodating nonlinear flow interactions in the analysis and control of transitional flows, including to estimate upper-bounds on the maximum TEG that can be realized in nonlinear flows (Chapter 7). These techniques were initially developed as part of this effort and are now currently being investigated for analysis and control of transitional and turbulent flows in independent efforts supported by AFOSR, ARO, NSF, and ONR.

Publications supported in whole or in part by AFOSR Grant No. FA9550-19-1-0034 include 12 journal publications (and 2 more in review at the time of writing this report), 5 conference papers, 12 conference presentations, and 2 doctoral dissertations. Personnel supported in whole or in part by this grant include the PI, 1 postdoctoral researcher, 3 PhD students, and 1 undergraduate student.

2 | Introduction

An ability to delay transition from laminar to turbulent flow would enable efficiency and performance enhancements in a variety of internal and external flow configurations of interest to AFOSR and the Air Force. Laminar flows exhibit a lesser degree of skin-friction drag relative to turbulent flows. Thus, reliably maintaining laminar flow over the lifting surfaces of a flight vehicle, for example, would directly result in increased range and endurance, improved fuel economy, lower aircraft weight, weakened sonic boom signatures, and reduced aerodynamic heating.



(a) F-22 Raptor **(b)** Laminar to turbulent transition

Figure 2.1: *Feedback flow control technology that can successfully delay transition to turbulence would offer remarkable performance benefits to a wide range of Air Force platforms.*

Transition to turbulence in many wall-bounded flows can be attributed to the growth of perturbations about a laminar equilibrium state [1]. Even in linearly stable flows at sub-critical Reynolds numbers ($Re < Re_c$), a *linear* non-modal mechanism for transient energy growth (TEG) of small flow perturbations can result in sub-critical transition [2–15]. TEG arises due to the high degree of non-normality of the linearized Navier-Stokes operator: the presence of nearly parallel eigenmodes can cause some disturbances to grow to $O(Re^2)$ in time $O(Re)$ [4, 16]. This amplification of perturbations can cause the flow state to depart from the basin of attraction of the laminar equilibrium and to trigger nonlinearities that give rise to turbulence [17]. In order to assess the possibility of transition due to TEG mechanisms, a non-modal stability analysis is typically performed through the use of a so-called *optimal* or *worst-case disturbance** about the laminar base state [1, 4, 18].

The linear nature of the TEG mechanism for transition has motivated numerous investigations on the use of linear optimal and robust control strategies aimed at delaying transition to turbulence [19–26]. Numerous computational fluid dynamics studies have shown that full-state feedback (i.e., full-

*An optimal or worst-case disturbance is the flow perturbation—among all perturbations with the same energy—that leads to the maximum TEG [1, 4, 18].

information) control can delay transition in a variety of flows [20, 22, 25, 27–32]. The success of these controllers can be attributed to a reduction in the worst-case TEG for the closed-loop system: A reduction in the worst-case TEG guarantees a reduction in TEG for all disturbances, and thus a greater likelihood of successfully delaying transition in practice.

While these prior investigations have demonstrated that full-information control can successfully delay transition in numerical fluids simulations, the performance and reliability of extending these approaches for use with sensor-based output feedback remains a challenge. Indeed, although full-information control is a prevalent design paradigm for feasibility and proof-of-concept studies in the context of computational fluid dynamics simulations, such approaches are out of reach in physical settings. Full-information control assumes direct access to the full state of the flow, which is not directly available outside of computational studies; instead, only sensor measurements—typically confined to solid boundaries—are actually available for feedback in practice (see Figure 2.2).

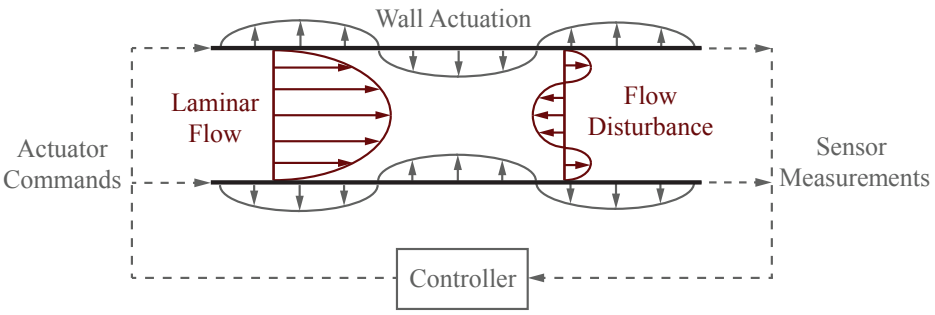


Figure 2.2: *Sensor-based output feedback control of channel flow for transition delay.*

The conventional approach for realizing sensor-based output feedback controllers is to develop an observer (i.e., state estimator) to provide estimates of the full state of the flow, which can then be used in a full-state feedback capacity. This design approach yields an observer-based output feedback law that has its own dynamics, which will depend on the designs of the flow state observer and the flow control law (see Figure 2.3). Observer-based feedback synthesis is among the simplest approaches for output feedback controller design because the *separation principle* of modern control theory guarantees that a stabilizing full-state feedback control law can be designed independently from a stable observer, then combined to yield a stabilizing observer-based output feedback law[†] [33]. For example, linear quadratic Gaussian (LQG) synthesis—which has been widely employed in flow control applications—consists of a full-state feedback linear quadratic regulator (LQR) applied to estimates of the flow state determined by an optimal observer (i.e., the Kalman-Bucy filter) [20, 22, 29, 31, 32].

The flow control engineer commonly argues that designing an accurate flow estimation algorithm would provide an ability to reconstruct the flow state from sensor measurements, which can then be used to achieve comparable performance to full-information control using observer-based feedback strategies. Unfortunately, this claim is false in the context of TEG reduction and transition delay, as recently shown by PI Hemati [34]. The underlying separation structure of LQG and other observer-based designs forges a non-normal closed-loop system, in which adverse "cyber-physical" interactions between the (cyber) control system dynamics and the (physical) fluid dynamics are

[†]Note that the separation principle only guarantees closed-loop stability, *not* closed-loop performance.

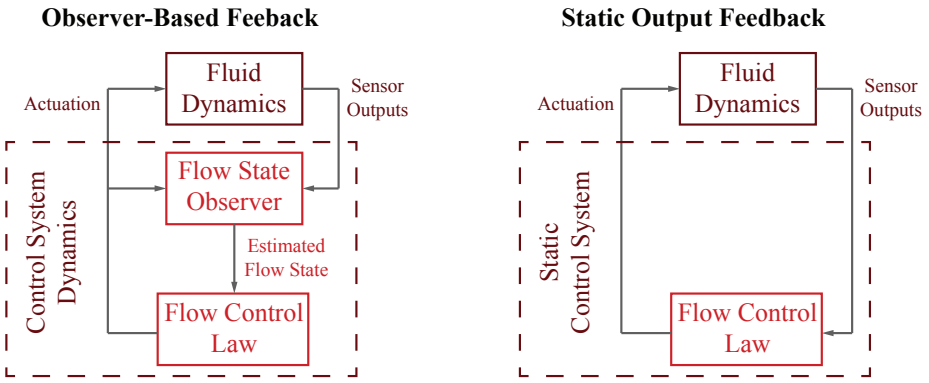


Figure 2.3: *Observer-based feedback structures can lead to adverse "cyber-physical" interactions between the (cyber) control system dynamics and the (physical) fluid dynamics, resulting in large transient energy growth. Static output feedback (SOF) structures remove the control system dynamics, thus providing an alternative control system that removes the possibility of creating these adverse cyber-physical couplings.*

guaranteed to result in large degrees of TEG in response to worst-case disturbances. These cyber-physical interactions can cause the best achievable closed-loop TEG to be even larger than if no control were used at all (see Figure 2.4).

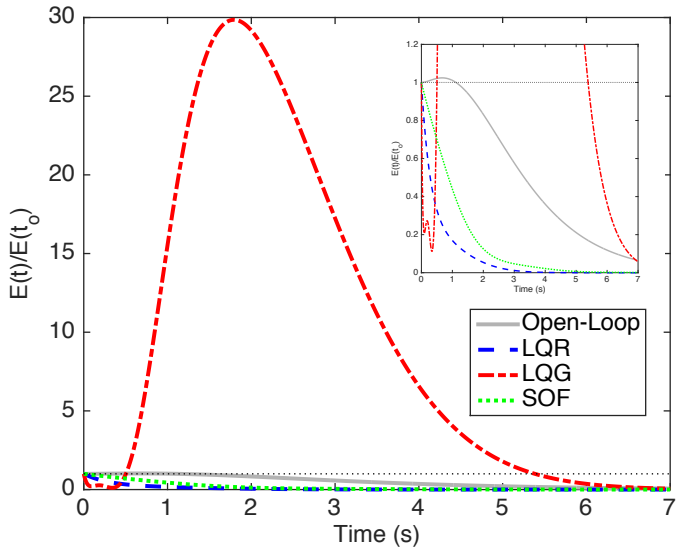


Figure 2.4: *Energy response to optimal disturbances in a 2-dimensional linearly stable non-normal system under full-state feedback (LQR), observer-based feedback (LQG), and stabilizing (non-optimal) static output feedback (SOF) control. Details of this example have been published in [34].*

Recalling that TEG reduction is needed for effective transition control, the possibility of degraded closed-loop TEG performance proves to be problematic. Fortunately, not all forms of output feedback control are subject to these same performance limitations; indeed, certain (semi-proper) output feedback structures can be designed to fully remove the possibility of adverse cyber-physical interactions [34]—as in the case of the static output feedback (SOF) controller shown in Figures 2.3 and 2.4.

Thus, the overarching technical objective of this research effort has been to formulate and leverage alternative sensor-based static output feedback control strategies to reduce TEG and enhance transition delay in wall-bounded shear flows.

3 | Channel Flow and Full-Information Control

Channel flow is used as the benchmark flow configuration for control demonstrations. This chapter outlines the channel flow model and direct numerical simulations to be used in subsequent chapters. We present results from full-information control as a benchmark to compare against in future chapters. The presentation in this chapter is heavily drawn from [35, 36]. For channel flow at subcritical Reynolds numbers ($Re < 5772$), a laminar-to-turbulent transition can emerge due to a large transient amplification in the kinetic energy of small perturbations, resulting in an increase in drag at the walls. The objectives of the present study are three-fold: (1) to study the nonlinear effects on transient energy growth, (2) to design a feedback control strategy to prevent this subcritical transition, and (3) to examine the control mechanisms that enable transition suppression. We investigate transient energy growth of linear optimal disturbance in plane Poiseuille flow at a subcritical Reynolds number of $Re = 3000$ using linear analysis and nonlinear simulation. Consistent with previous studies, we observe that the amplification of the given initial perturbation is reduced when the nonlinear effect is substantial, with larger perturbations being less amplified in general. Moreover, we design linear quadratic optimal controllers to delay transition via wall-normal blowing and suction actuation at the channel walls. We demonstrate that these feedback controllers are capable of reducing transient energy growth in the linear setting. The performance of the same controllers is evaluated for nonlinear flows where a laminar-to-turbulent transition emerges without control. Nonlinear simulations reveal that the controllers can reduce transient energy growth and suppress transition. Further, we identify and characterize the underlying physical mechanisms that enable feedback control to suppress and delay laminar-to-turbulent transition.

3.1 Introduction

Channel flow is ubiquitous in engineering applications, and the laminar-turbulent state of the flow is of great practical consequence. In general, since laminar flows experience smaller wall friction than turbulent flows, laminar-to-turbulent transition suppression has been a primary objective in many flow control studies of channel flow. Extensive studies have been performed to understand the characteristics of channel flows [37–40],among which hydrodynamic stability analysis is widely used to examine behaviors of small perturbations around a laminar equilibrium state of the flow. The linear stability result is often used to determine the critical condition for a laminar-to-turbulent transition to arise [41–44]. For plane Poiseuille flows, linear stability analysis identifies a critical Reynolds number of $Re = 5772$, below which the flow state will remain laminar and infinitesimal perturbations will decay to zero asymptotically [42]. However, a laminar-to-turbulent transition in plane Poiseuille flow has been observed in experiments and simulations at

Reynolds numbers far smaller than the critical one [45–47]. This phenomenon is caused by a short-time transient amplification of small perturbations before their eventual decay. This so-called *transient energy growth* results from the non-normality of the linearized perturbation dynamics [48, 49], which can contribute to the laminar-to-turbulent transition observed in plane Poiseuille flow at subcritical Reynolds numbers.

To delay or suppress a transition in plane Poiseuille flow, modern feedback control theory has been investigated [50–54]. One approach is to reduce transient energy growth by designing feedback control laws based on the linearized perturbation dynamics, as the large energy amplification plays an important role in the transition process. Kim and Bewley have summarized the essential ingredients of linear control theory for fluid mechanics in a review paper [55]. Bewley and Liu applied linear optimal ($\mathcal{H}_2$) and robust ($\mathcal{H}_\infty$) control methods on both subcritical and supercritical channel flows aiming at reducing disturbance response [51]. Moreover, Jovanović and Bamieh have investigated componentwise energy amplification in channel flows via input-output analysis, finding that wall-normal and spanwise forces can affect the flow more significantly than streamwise force [56], which inspires a use of wall-normal or spanwise velocity actuation in flow control studies. Martinelli et al. designed a linear optimal control strategy to suppress the maximum transient energy growth experienced in subcritical channel flow [54]. Although the nonlinearity can be taken into consideration within the control synthesis [57, 58], linear control synthesis is more accessible and has been more commonly employed for flow control.

Among all the possible disturbances, the optimal disturbance leads to the maximum transient energy growth [44], which has the highest chance to induce a laminar-to-turbulent transition of the flow. The optimal disturbance is usually computed based on the linearized operator [59], though nonlinear notions can also be determined [60]. In the present work, we focus on the initial optimal disturbance computed based on the linear model. The optimal disturbance is calculated for the uncontrolled and controlled systems, respectively. Control will alter the perturbation dynamics, and so the optimal disturbance for the controlled flow will differ from that of the uncontrolled flow, in general [61]. This point has been emphasized in recent studies [62–64] aiming to evaluate the overall performance of feedback controllers.

In this chapter, we first perform linear and nonlinear simulations to study transient energy growth and transition in plane Poiseuille flows. We investigate nonlinear effects using direct numerical simulations. In contrast to previous studies, we adopt a relatively large domain to faithfully capture the full transition process. It is found that the nonlinearity serves to suppress the amplification of kinetic energy, and that this effect becomes more pronounced for larger perturbations. For the oblique and streamwise-wave disturbances, streamwise vortices grow based on the development of coherent vortical structures initiated from the optimal disturbances. The breakdown of these streamwise vortices leads to a laminar-to-turbulent transition. For the spanwise-wave disturbance, high shear is induced between merged and large-scale streamwise vortices where secondary instabilities grow and break the coherent structure to trigger a laminar-to-turbulent transition. Although these transition mechanisms are not entirely new, we will focus on how feedback control favorably alters these mechanisms to impede the transition process.

Linear quadratic controllers are designed to reduce the large transient energy growth experienced in the uncontrolled flows. Actuation is implemented in the form of wall blowing/suction within the nonlinear simulation, which has been shown capable of suppressing or delaying transition [54].

Here, we investigate the control mechanism by which actuation favorably conditions the flow to prevent transition. For the oblique and streamwise-wave disturbances, wall actuation modifies the distribution of high shear present in the flow, which prevents the large transient energy growth associated with the development of coherent structures. For the spanwise-wave disturbance, we will show that wall actuation induces small streamwise vortices near the channel wall, which hinders the growth of merged vortices and further reduces the high shear formed between adjacent streamwise vortical structures.

Finally, we note that although numerous studies have considered linear feedback control for transition suppression in channel flow, a detailed investigation into the role of nonlinearities on control performance has not been presented elsewhere. Here, we investigate the role of nonlinearities on controller performance—both in terms of reducing transient energy growth and in suppressing transition—within direct numerical simulations. In an effort to keep our analysis relevant within the context of the established literature, we implement a simple actuator model based on wall-normal blowing and suction along the walls of the channel. Further, by adopting a larger computational domain than previous investigations, our analysis captures a richer set of the relevant nonlinear flow physics underlying the laminar-to-turbulent transition process.

The chapter is organized as follows. Numerical approaches are provided in Section 3.2, including details on the computational setup for direct numerical simulations and methods for feedback control synthesis. In Section 3.3, we discuss uncontrolled flows that exhibit transition for various optimal disturbances. The results for controlled flows are also provided in this section with detailed discussions of the control mechanisms. Finally, conclusions are summarized in Section 5.4.

3.2 Numerical Approaches

3.2.1 Direct numerical simulation

Two- and three-dimensional direct numerical simulations of plane Poiseuille flow are performed using the spectral code *Channelflow* [65, 66] to solve the incompressible Navier–Stokes equations. A second-order Runge–Kutta temporal scheme is used. Streamwise, wall-normal and spanwise directions are indicated by x, y, and z, respectively, and corresponding velocity components are $\boldsymbol{u}$, $\boldsymbol{v}$, and $\boldsymbol{w}$. Time is denoted by t. As shown in Figure 3.1, the flow between two infinite planes has a base velocity profile of $[\bar{\boldsymbol{u}}, \bar{\boldsymbol{v}}, \bar{\boldsymbol{w}}] = [1 - (y/h)^2, 0, 0]$ at Reynolds number of $Re = \bar{u}_c h/\nu = 3000$, where h is the channel half-height, $\bar{u}_c$ denotes the center velocity of the base flow, and ν is the kinematic viscosity of the fluid. The velocity is non-dimensionalized by $\bar{u}_c$. In the simulations, periodic boundary conditions are assumed in the x- and z-directions in which the flow variables (velocity and pressure) are represented by Fourier expansion. In the y-direction, flow variables are represented by Chebyshev polynomials, and no-slip boundary condition is specified at upper and lower walls for the uncontrolled flow. Moreover, a constraint of constant bulk velocity is specified. For the controlled flow, actuation in the form of blowing and suction in the y-direction is introduced on the entire upper and lower walls, which follows the Fourier expansion in the x- and z-directions as well. The actuation is illustrated in Figure 3.1 using an example of a case having streamwise-wavelike actuation. The amplitude of wall actuation is determined by the feedback law described later in Section 3.2.2.

We use a rectangular computational domain of size $8\pi h \times 2h \times 2\pi h$ in x-, y-, and z-directions, respectively. Chebyshev points of $N = 101$ in the y-direction is prescribed to discretize the flow

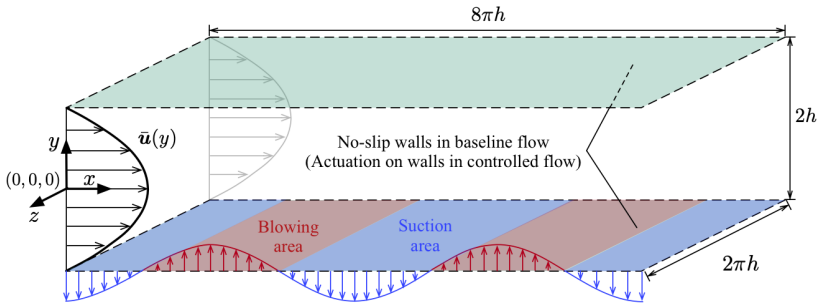


Figure 3.1: *Schematic of plane Poiseuille flow with streamwise-wave disturbance (not to scale), both with and without wall actuation.*

field for all the cases. Uniform grids of 128×64 are used for the x- and z-directions, respectively. Although the cases with either streamwise-constant or spanwise-constant disturbances are two-dimensional flows, the laminar-to-turbulent transition is a three-dimensional flow phenomenon [67] such that a three-dimensional mesh is necessary to resolve the transition process in the simulations. For both uncontrolled and controlled flows, grid resolution studies with doubled grids in each direction have been performed to ensure accuracy of the results. Moreover, we have also studied the influences of computational domain size on the simulations results. In past studies, the domain size is usually set to fit one wavelength of the wavenumber of interest for each direction. However, as the transition includes large-scale deformation of the original perturbation structures, the underlying physics during the transition processes cannot be fully captured with a limited domain size. Hence, we select a relatively large domain to capture a broader extent of flow physics involved in the transition process. This provides a more realistic setting to assess transition control performance. The evolution of the perturbation prior to transition is not affected by the domain size, but the post-transition process is dependent on the domain size. Once a sufficiently large domain size is determined, the simulations are converged and the observations among cases are consistent regardless of increasing domain size.

For the simulations of both uncontrolled and controlled flows, the initial condition of the flow field consists of the base flow $[\bar{\boldsymbol{u}}, \bar{\boldsymbol{v}}, \bar{\boldsymbol{w}}]$ and a small initial perturbation $[\boldsymbol{u}'_0, \boldsymbol{v}'_0, \boldsymbol{w}'_0]$, where subscript $(\cdot)_0$ denotes initial value. The perturbation is the optimal disturbance associated with a wavenumber pair of (α,β), and its kinetic energy density is denoted by E_0. The optimal disturbance can lead to a maximum transient energy growth and it is pre-calculated using the algorithm proposed by Whidborne and Amar [59]. Since the dynamical systems of the uncontrolled and controlled flows are different, the optimal disturbance is calculated for each system independently to guarantee that we examine the largest transient energy growth in each case. Moreover, a random perturbation with kinetic energy density of 1% of E_0 is added to expedite the emergence of a laminar-to-turbulent transition in the flows. The addition of a random perturbation has a negligible influence on the shape of the optimal disturbance, and is a common practice in transition studies [67].

3.2.2 Linearized Navier–Stokes equations and feedback control design

To use modern control theory to design feedback controllers, a state-space representation of the fluid flow problem is required. For plane Poiseuille flow, we decompose the flow state $\tilde{\boldsymbol{q}}$ into a base state $\bar{\boldsymbol{q}}$ and a small perturbation $\boldsymbol{q}'$, where $\boldsymbol{q} = [\boldsymbol{u}, \boldsymbol{v}, \boldsymbol{w}, \boldsymbol{p}]^T$ ($\boldsymbol{p}$ is pressure), and the base state velocity profile is of $[\bar{\boldsymbol{u}}, \bar{\boldsymbol{v}}, \bar{\boldsymbol{w}}] = [1 - (y/h)^2, 0, 0]$. The kinetic energy density of a perturbation is

defined as

$$E = \frac{1}{2V}\int_{vol=V}(\boldsymbol{u}'^2 + \boldsymbol{v}'^2 + \boldsymbol{w}'^2)dvol, \tag{3.1}$$

where V is the volume of the computational domain.

By substituting the expression of $\tilde{\boldsymbol{q}} = \bar{\boldsymbol{q}} + \boldsymbol{q}'$ into the Navier–Stokes equations, and assuming that the perturbation is much smaller than the base state in magnitude ($|\boldsymbol{q}'| \ll |\bar{\boldsymbol{q}}|$), we linearize the equations by retaining linear terms and neglecting higher-order nonlinear terms. Next, the real-valued perturbation is expressed using a Fourier expansion

$$\boldsymbol{q}'(x,y,z,t) = \hat{\boldsymbol{q}}(y,t)e^{i(\alpha x+\beta z)} + \text{complex conjugate}, \tag{3.2}$$

where $\hat{\boldsymbol{q}}(y,t)$ is the amplitude function of the perturbation associated with streamwise wavenumber α and spanwise wavenumber β, such that each disturbance analyzed in the present work is with a prescribed wavenumber pair of (α,β). By substituting Eq. (6.4) into the linearized Navier–Stokes equations, we can reformulate the governing equations into a state-space form

$$\frac{\partial X}{\partial t} = A(\bar{\boldsymbol{q}};\alpha,\beta)X, \tag{3.3}$$

where $X = [\hat{\boldsymbol{v}},\hat{\boldsymbol{\eta}}]^T$, $\hat{\boldsymbol{v}}$ and $\hat{\boldsymbol{\eta}}$ denote wall-normal velocity perturbation and wall-normal vorticity perturbation, respectively, and superscript $(\cdot)^T$ represents transpose. The dynamics matrix A is derived from linearized Navier–Stokes equations, which follows the form proposed by Schmid & Henningson [44]. By choosing a real-valued wavenumber pair (α, β), we can analyze perturbations associated with various structures. In the present work, we examine optimal disturbances for three different wavenumber pairs — (α,β) = (1,0), (0,2) and (1,1). Disturbances associated with these three types of wavenumber pairs—streamwise-wave (Tollmien-Schlichting wave), spanwise-wave, and oblique-wave disturbances—cover the most representative laminar-to-turbulent transitions following different routes [67]. The features of each optimal disturbance will be discussed in Section 3.3.

In the control design, we introduce actuation in the form of blowing and suction on the upper and lower channel walls. We admit the difficulty in implementing such actuation in practice; however, this control configuration has been conventionally adopted in other channel flow studies. In the present study, this choice enables a focused study of nonlinear effects and control mechanisms for successful transition suppression, without introducing complexities of more practical actuator models. To synthesize this actuation into the dynamical system, we add a control input term BU to the uncontrolled system (Eq. (6.6)) to form the system

$$\frac{\partial X_c}{\partial t} = A_c X_c + BU, \tag{3.4}$$

where the control inputs in $U = \frac{\partial}{\partial t}[\hat{v}_{+h},\hat{v}_{-h}]^T$ are the rate of change of wall-normal velocity on the upper and lower walls, and B is the input matrix that maps the influence of control inputs on the system. Due to the no-slip boundary condition ($\hat{v}_{\pm h} = 0$) applied on the walls of the uncontrolled flow, $\hat{v}_{\pm h}$ are excluded while forming the flow state X in Eq. (6.6). As $\hat{v}_{\pm h}$ are nonzero in the controlled flow, we will append these two variables to the flow state X to form a new state $X_c = [X,\hat{v}_{+h},\hat{v}_{-h}]^T$. Analogously, the dynamics matrix A is modified and denoted by A_c to account

for the new state. More information about the system modeling can be found in the work by McKernan et al. [68].

Based on the state-space model in Eq. (3.4), linear-quadratic regulator (LQR) is designed for use in feedback control. The control objective is to minimize the cost function

$$J = \int_0^\infty ({X_c}^T Q X_c + U^T R U) dt \tag{3.5}$$

subject to the linear dynamics (Eq. (3.4)), where Q and R are weight matrices. The term $X_c^T Q X_c$ represents kinetic energy density E. The input weighting matrix R serves to penalize the control effort and is chosen here to be a diagonal matrix with each element equal to 10^{-6}. The weight matrix R is chosen to be small to impose a minimal penalty on the control input. This serves to prioritize the regulation of perturbation energy in the objective function. The feedback control law is given by $U = -KX_c$, where matrix K is the state feedback control gain. This feedback control law requires full knowledge of flow state. Given the dynamics matrix A_c, input matrix B, weight matrices Q and R, the control gain matrix K can be calculated by solving an algebraic Riccati equation [69]. The LQR controller is implemented in the direct numerical simulations, as described earlier. Results are presented in the next section.

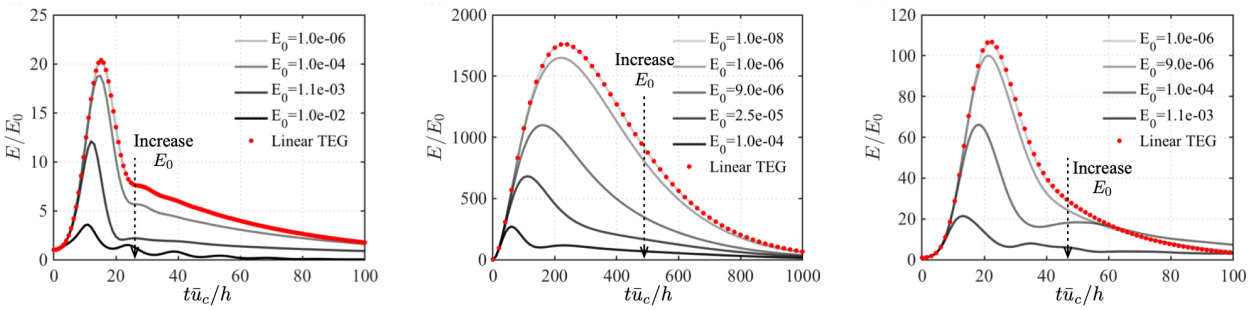
3.3 Results and Discussions

In this section, transient energy growth of optimal disturbances associated with three wavenumber pairs of $(\alpha, \beta) = (1, 0), (0, 2)$ and $(1, 1)$ are investigated using direct numerical simulations for the subcritical plane Poiseuille flow at $Re = 3000$. The required conditions for a laminar-to-turbulent transition to appear in a fully nonlinear flow are examined for each case, and the flow features that are responsible for the transition are examined as well. Moreover, we present LQR feedback controllers that can successfully suppress or delay the transition, then examine the underlying physics related to the control mechanisms.

3.3.1 Transient energy growth of optimal disturbance

We start the discussion from the nonlinear analysis of transient energy growth resulting from a pure optimal disturbance—i.e., without a random perturbation added. Using the optimal disturbance as the initial condition, the Navier–Stokes equations were integrated to obtain the response of kinetic energy density, as shown in Figure 3.2. All of the optimal disturbances considered in the present work experience large transient energy amplifications with orders of magnitude from $O(10^1)$ to $O(10^3)$; the disturbance of streamwise vortices ($(\alpha, \beta) = (0, 2)$ in Figure 3.2(b)) reaches the largest maximum transient energy growth. In the linear simulation—denoted by red dots in each subplot—the normalized energy response E/E_0 does not depend on the magnitude of the initial perturbation.

In the nonlinear simulations, we integrate the Navier–Stokes equations of full state velocity $\tilde{\boldsymbol{q}}$ and report the kinetic energy density of perturbations after subtracting the base flow $\bar{\boldsymbol{q}}$. As shown in Figure 3.2, when the perturbation is small enough such as $E_0 \lessapprox 10^{-6}$ for cases with $(\alpha, \beta) = (1, 0)$ and $(1, 1)$ and $E_0 \lessapprox 10^{-8}$ for case with $(\alpha, \beta) = (0, 2)$, nonlinear effects are negligible and the energy response is identical to that of the linear result. However, when the amplitude of initial disturbance increases, the amplification of kinetic energy density E/E_0 decreases, which indicates that the nonlinearity suppresses energy amplification. In other words, the nonlinearity competes with the linear non-modal growth and inhibits the transient energy amplification for sufficiently large E_0.



(a) $(\alpha, \beta) = (1, 0)$ (b) $(\alpha, \beta) = (0, 2)$ (c) $(\alpha, \beta) = (1, 1)$

Figure 3.2: *Transient energy growth (TEG) of optimal disturbance with a range of initial kinetic energy density E_0 from linear (red dots) and nonlinear (solid lines) simulations for uncontrolled flows.*

Although we have seen transient energy growth in both linear and nonlinear simulations, there is no laminar-to-turbulent transition observed, suggesting that the growth of optimal disturbance alone cannot trigger the transition. As discussed in the study by Reddy et al. [67], the addition of a random perturbation is required to observe transition in simulations. Hence, we added a random perturbation with a contribution of 1% of E_0 to the optimal disturbance to initiate laminar-to-turbulent transition. Before the laminar-to-turbulent transition, the energy response due to this modified disturbance is nearly identical to the energy response due to a purely optimal disturbance. Since the transition process of each wavenumber pair follows different routes, we will discuss all the three paths to transition below respectively.

Oblique disturbance $(\alpha, \beta) = (1, 1)$

Flow fields of a laminar-to-turbulent transition case with $(\alpha, \beta) = (1, 1)$ and $E_0 = 0.5 \times 10^{-4}$ are shown in Figure 3.3, and the iso-surface of Q-criterion [70] is calculated using full flow state $\tilde{\boldsymbol{q}}$. The initial optimal disturbance is in an oblique-wave with large amplitude near the channel walls, as shown in the subplot in Figure 3.3. As the disturbance evolves in time, large-scale oblique structures form with size comparable to the channel half-height. After the transient energy reaches to the maximum value around $t\bar{u}_c/h = 20$ (see Figure 3.4), large amplitude of streamwise vorticity appears in the vicinity of the coherent structures at the channel walls at $t\bar{u}_c/h = 36$. Meanwhile, slight spatial variations of the coherent structures appear along the oblique direction. Later at time $t\bar{u}_c/h = 72$, streamwise vortices are induced from the oblique coherent structures and grow into streamwise streaks, although the overall transient energy density has started to decay, as shown in Figure 3.4. After $t\bar{u}_c/h = 84$, these streamwise streaks break into small-scale structures, and a laminar-to-turbulent transition emerges afterwards.

The time evolution of kinetic energy density E for a range of optimal disturbances is presented in Figure 3.4. For optimal disturbance with $E_0 < 0.5 \times 10^{-4}$ (denoted by grey lines), the initial disturbance is the most amplified, yet the induced streamwise vortices do not grow significantly. The disturbance eventually decays to zero without triggering a laminar-to-turbulent transition. We also note that the nonlinear flow with small disturbance ($E_0 = 1.0 \times 10^{-6}$) is well predicted by the linear analysis as seen by the overlap between nonlinear simulation and linear results in Figure 3.4 (left). By examining the absolute value of the perturbation kinetic energy (Figure 3.4 (right)), the transition cases have relatively high values in E, which suggests that a combined effect of initial optimal disturbance and its corresponding amplification determines whether or not a transition

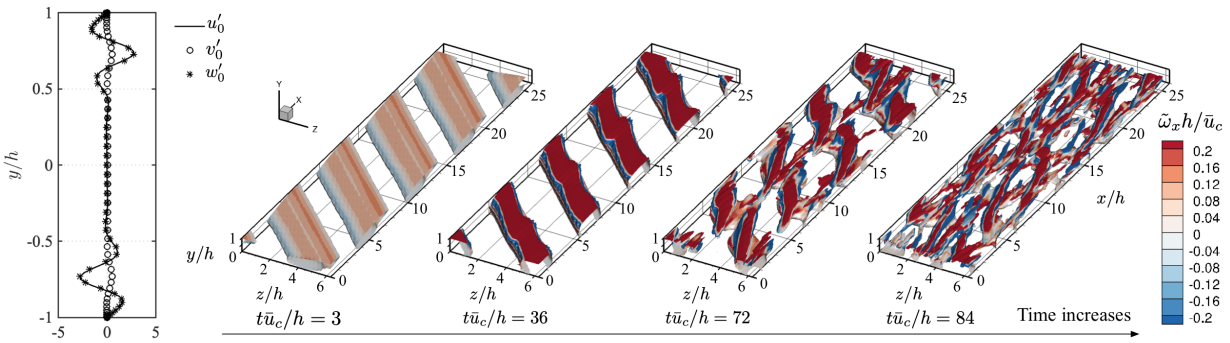


Figure 3.3: *Time evolution of flow field to illustrate the laminar-to-turbulent transition process for the case* $(\alpha, \beta) = (1, 1)$*. The flow is initialized by optimal disturbance with kinetic energy density of* $E_0 = 0.5 \times 10^{-4}$*. Iso-surfaces of* Q*-criterion [70] (*$Q(h/\bar{u}_c)^2 = 0.001$*) colored by streamwise vorticity* $\tilde{\omega}_x h/\bar{u}_c$ *are visualized. Only the upper half domain (*$y \geq 0$*) is displayed for clarity.*

occurs. The larger amplitude disturbance gives a higher chance of triggering transition to turbulent state, which also indicates that a reduction in transient energy growth has potential to suppress or delay the transition observed in the uncontrolled flow. This motivates using control to reduce transient energy growth.

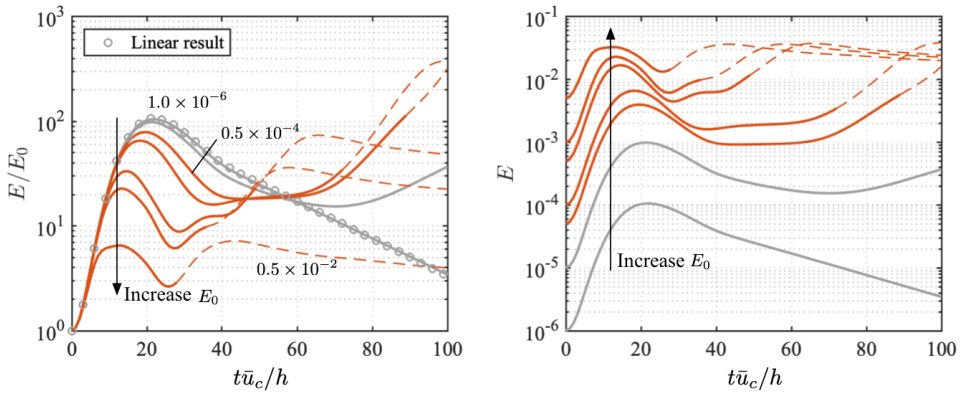


Figure 3.4: *Time evolution of kinetic energy density* E *of case* $(\alpha, \beta) = (1, 1)$ *initialized by different amplitudes of optimal disturbance* E_0*. Red lines represent transition cases, and dashed line indicates that the flow is in turbulent state.*

Friction velocity u^* is defined using wall shear stress τ_w and density of the flow

$$u^* = \sqrt{\frac{\tau_w}{\rho}}, \tag{3.6}$$

where $\tau_w = \mu(\partial u/\partial y)$, μ is dynamic viscosity, and density ρ is set to one for incompressible flow. As a sharp increase in friction velocity u^* indicates an emergence of laminar-to-turbulent transition, a summary of transition cases are shown in Figure 3.5 illustrating the features of friction velocity u^*, in which the flow in turbulent state has been denoted by dashed lines. Based on the feature of friction velocity, the larger the initial disturbance, the earlier laminar-to-turbulent transition appears.

Moreover, a large initial disturbance leads to large shear stress in the wall-normal direction near the channel walls.

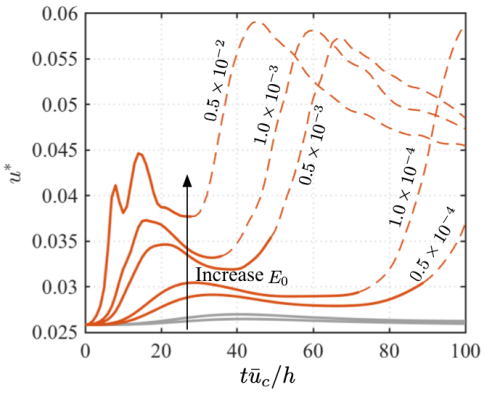


Figure 3.5: *Time evolution of friction velocity u^* of case $(\alpha, \beta) = (1, 1)$ initialized by different amplitudes of optimal disturbance E_0. Red lines represent transition cases, and grey lines denote that the flow remains laminar. Dashed line indicates that the flow is in turbulent state.*

Streamwise-wave disturbance $(\alpha, \beta) = (1, 0)$

The optimal disturbance with wavenumber pair of $(\alpha, \beta) = (1, 0)$ is the well-known Tollmien-Schlichting wave whose structures are uniform in the spanwise direction. The evolution of the optimal disturbance is shown in Figure 3.6 with $E_0 = 1.0 \times 10^{-4}$. The feature of the optimal disturbance is similar to the case with oblique disturbance: a large disturbance is observed in streamwise velocity and resides near the channel walls. As the optimal disturbance grows into large-scale spanwise coherent structures, streamwise vorticity increases near channel walls, especially where the coherent structures reside, as seen in Figure 3.6 at $t\bar{u}_c/h = 60$. When the streamwise vorticity is large enough, a Λ-shaped structure emerges, splits the spanwise coherent structure and connects to the adjacent spanwise coherent structure in front, as seen at $t\bar{u}_c/h = 108$, then the break of these vortices leads to a laminar-to-turbulent transition of the flow.

The transition process in this case is very similar to the oblique disturbance discussed above in Section 3.3.1. The transition is directly caused by a break of streamwise streaks that grow from the amplified optimal disturbance. It suggests that the transient energy growth of the optimal disturbance alone does not trigger the transition; rather, it is the combined effect of the growing optimal disturbance and induced secondary instabilities that leads to a laminar-to-turbulent transition. The friction velocity and evolution of transient energy density of disturbance with $(\alpha, \beta) = (1, 0)$ are shown in Figures 3.7 and 3.8, respectively. The features observed from the case $(\alpha, \beta) = (1, 1)$ also apply on this streamwise-wave disturbance; the flow tends to transition into a turbulent state when the kinetic energy density E of a disturbance becomes large; this is influenced by both the initial amplitude of the disturbance and the corresponding amplification rate.

Spanwise-wave disturbance $(\alpha, \beta) = (0, 2)$

The optimal disturbance associated with wavenumber pair of $(\alpha, \beta) = (0, 2)$ is in the form of streamwise vortices. Shown in Figure 3.9 are the flow fields with initial kinetic energy density of $E_0 = 1.0 \times 10^{-4}$. Relating the flow feature to normalized kinetic energy density of perturbation E/E_0 shown in Figure 3.10 (left), when the optimal disturbance grows initially, two co-rotating

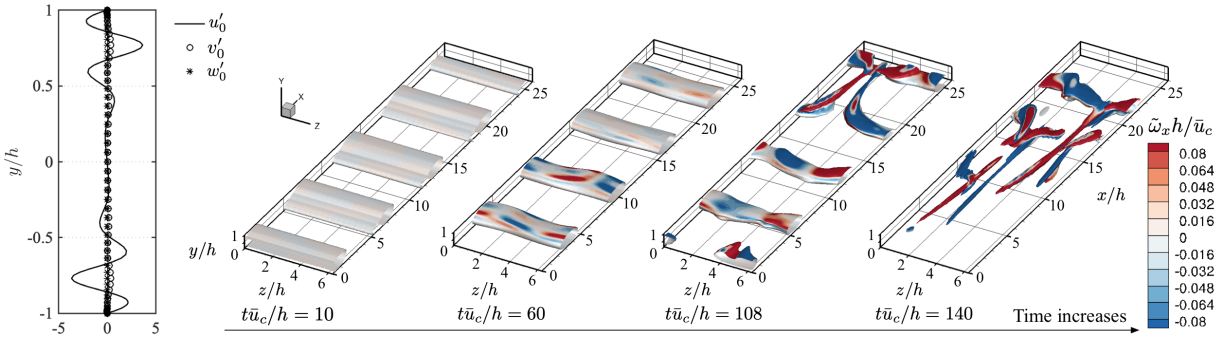


Figure 3.6: *Time evolution of flow field to illustrate the laminar-to-turbulent transition process for the case* $(\alpha, \beta) = (1, 0)$*. The flow is initialized by optimal disturbance with kinetic energy density of* $E_0 = 1.0 \times 10^{-4}$*. Iso-surfaces of* Q*-criterion* ($Q(h/\bar{u}_c)^2 = 0.005$) *colored by streamwise vorticity* $\tilde{\omega}_x h/\bar{u}_c$ *are visualized. Only the upper half domain* ($y \geq 0$) *is displayed for clarity.*

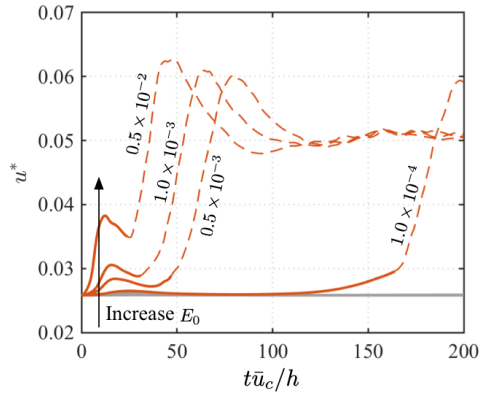


Figure 3.7: *Time evolution of friction velocity* u^* *of case* $(\alpha, \beta) = (1, 0)$ *initialized by different amplitudes of optimal disturbance* E_0*. Red lines represent transition cases, and grey lines denote that the flow remains laminar. Dashed line indicates that the flow is in turbulent state.*

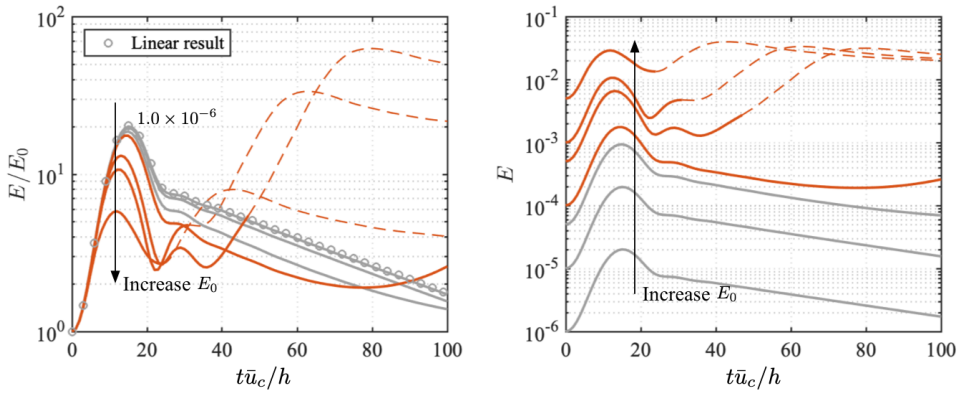


Figure 3.8: *Time evolution of kinetic energy density E of case $(\alpha,\beta) = (1,0)$ initialized by different amplitudes of optimal disturbance E_0. Red lines represent transition cases, and grey lines denote that the flow remains laminar. Dashed line indicates that the flow is in turbulent state.*

vertically aligned vortices merge into a large streamwise vortical structure. The structure remains uniform in the streamwise direction, and the corresponding transient energy reaches the maximum value around $t\bar{u}_c/h = 60$. After the kinetic energy starts to decrease, the flow gradually experiences spatial variation as seen at $t\bar{u}_c/h = 150$. This is associated with axial rotational motion around the streamwise vortical structures with comparable scale to the length of the streamwise domain. Next, the kinetic energy density of the flow increases again after $t\bar{u}_c/h = 150$, and smaller structures appear in the flow (as seen at $t\bar{u}_c/h = 240$). After a short duration of rotational motion in the flow, a laminar-to-turbulent transition occurs around $t\bar{u}_c/h = 300$. Based on the features of transient energy growth and corresponding flow fields, we note that the transition is a slow process covering several stages, which cannot be determined simply based on the features of energy growth time histories. The features of transition cases revealed by friction velocity are similar to the cases of oblique disturbances and streamwise-wave disturbances discussed above, and the friction velocity of case $(\alpha,\beta) = (0,2)$ is shown in Figure 3.11.

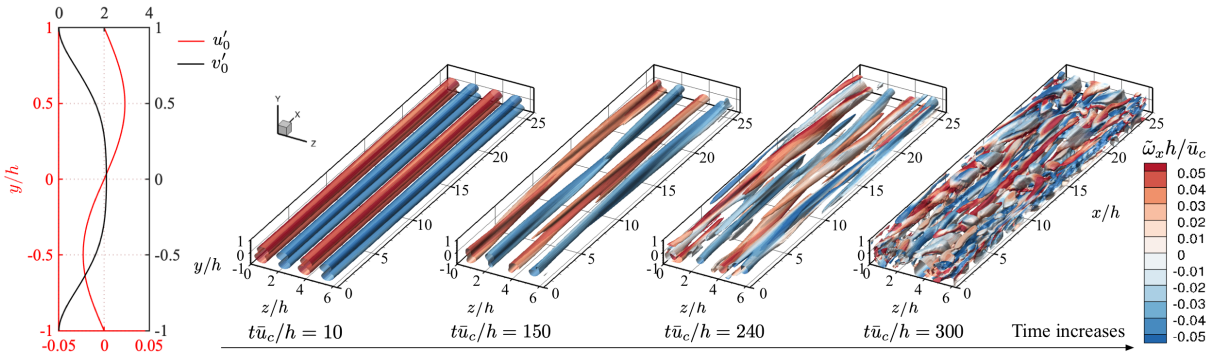


Figure 3.9: *Time evolution of flow field to illustrate the laminar-to-turbulent transition process for the case $(\alpha,\beta) = (0,2)$. The flow is initialized by optimal disturbance with kinetic energy density of $E_0 = 1.0 \times 10^{-4}$. Iso-surfaces of Q-criterion ($Q(h/\bar{u}_c)^2 = 0.0004$) colored by streamwise vorticity $\tilde{\omega}_x h/\bar{u}_c$ are visualized.*

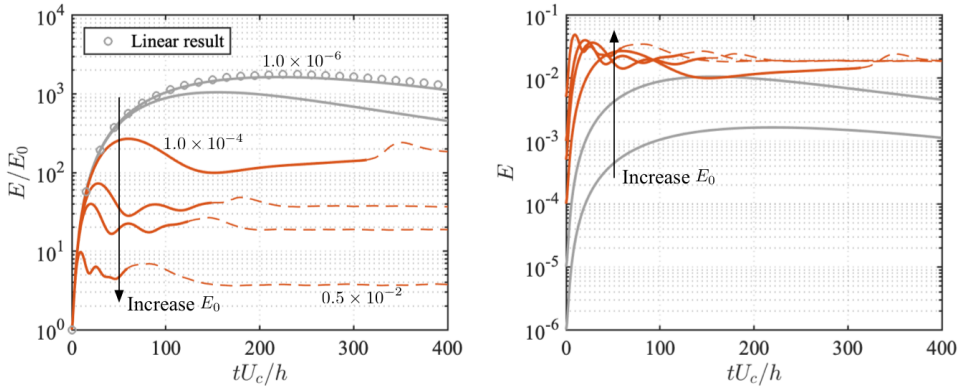


Figure 3.10: *Time evolution of kinetic energy density E of case $(\alpha,\beta) = (0,2)$ initialized by different amplitudes of optimal disturbance E_0. Red lines represent transition cases, and grey lines denote that the flow remains laminar. Dashed line indicates that the flow is in turbulent state.*

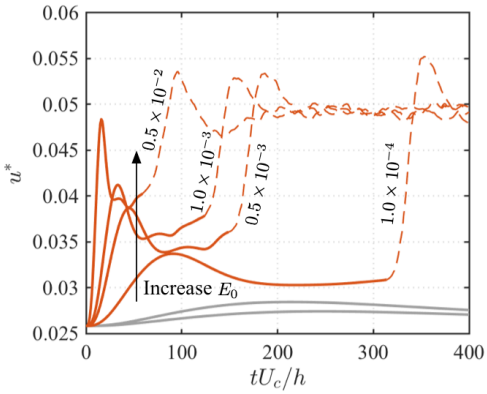


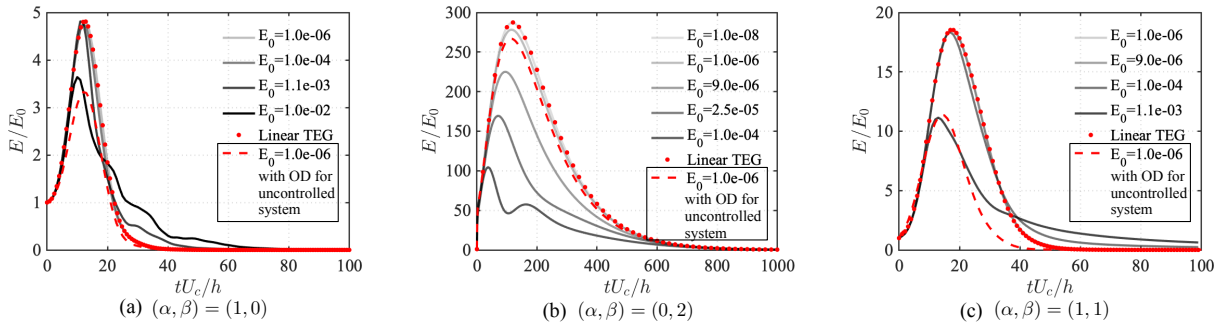
Figure 3.11: *Time evolution of friction velocity u^* of case $(\alpha,\beta) = (0,2)$ initialized by different amplitudes of optimal disturbance E_0. Red lines represent transition cases, and grey lines denote that the flow remains laminar. Dashed line indicates that the flow is in turbulent state.*

3.3.2 Suppression of laminar-to-turbulent transition

We synthesize a full-state feedback LQR controller. The transient energy growth is significantly reduced with the corresponding wall actuation, as shown in Figure 3.12. In the nonlinear simulations, we update the control input U at each time step using the flow state X_c and the gain matrix K calculated from the linear analysis. Accordingly, the boundary condition of wall-normal velocity $v'_{\pm h}$ is modified based on the control input U. To evaluate the overall performance of the controlled flow in terms of reducing large transient energy growth, the optimal disturbance was re-calculated for the closed-loop controlled system to evaluate the maximum transient energy growth.

Reduction in transient energy growth

Transient energy growth in each controlled case is observed to exhibit similar features as in the uncontrolled cases; namely that an increase in initial kinetic energy makes the amplification of perturbation energy decrease as shown in Figure 3.12. Using case $(\alpha,\beta) = (1,0)$ as an example, since the amplification of the optimal disturbance is effectively reduced with the feedback controller, the energy responses with $E_0 \lessapprox 1.1 \times 10^{-3}$ almost overlap the linear result, denoted by red dots. This suggests that, as the growth of the disturbance is suppressed to a small magnitude by introducing control, the importance of the nonlinearity is weakened. Therefore, the results from nonlinear simulations match the result from linear analysis as the small disturbance assumption is satisfied. The kinetic energy density of the controlled flow, initialized from the optimal disturbance calculated for the uncontrolled system, is also shown in figure 3.12. The energy amplification of this disturbance is less than that of the optimal disturbance for the controlled system with the same initial amplitude. Indeed, this trend holds true regardless of the initial perturbation amplitude, though only a single perturbation amplitude is reported in the figure for clarity. This confirms that the optimal disturbance for the closed-loop dynamics should be considered when assessing control performance for transient energy growth reduction.



(a) $(\alpha,\beta) = (1,0)$ (b) $(\alpha,\beta) = (0,2)$ (c) $(\alpha,\beta) = (1,1)$

Figure 3.12: *Transient energy growth (TEG) of optimal disturbance with a range of initial kinetic energy density E_0 from linear (red dots) and nonlinear (solid lines) simulations for controlled flows. Red dashed line: kinetic energy density initialized from the optimal disturbance (OD) associated with the uncontrolled system.*

For each wavenumber pair, a comparison of the maximum of E/E_0 initiated from a range of optimal disturbance amplitudes is shown in Figure 3.13. For small disturbance amplitude, the percent reduction of maximum transient energy remains nearly identical, indicating the nonlinearity of small disturbance is negligible as assumed in the linear analysis. Moreover, each wavenumber scenario reaches the largest reduction of $\approx 80\%$ in $(E/E_0)_{\max}$ for small initial amplitude of dis-

turbance. For the case with $(\alpha,\beta) = (0,2)$, this large amount of reduction in E/E_0 only applies to the cases with $E_0 \lessapprox O(10^{-5})$. As the initial disturbance grows in amplitude, the control performance in terms of suppressing the energy amplification degrades, such that the $(E/E_0)_{\max}$ is nearly unchanged for cases with $E_0 > O(10^{-3})$. Similar findings are also observed in the other two disturbance scenarios, but the reduction in $(E/E_0)_{\max}$ is maintained for $E_0 \lessapprox O(10^{-4})$ and $E_0 \lessapprox O(10^{-3})$ for case $(\alpha,\beta) = (1,1)$ and $(\alpha,\beta) = (1,0)$, respectively.

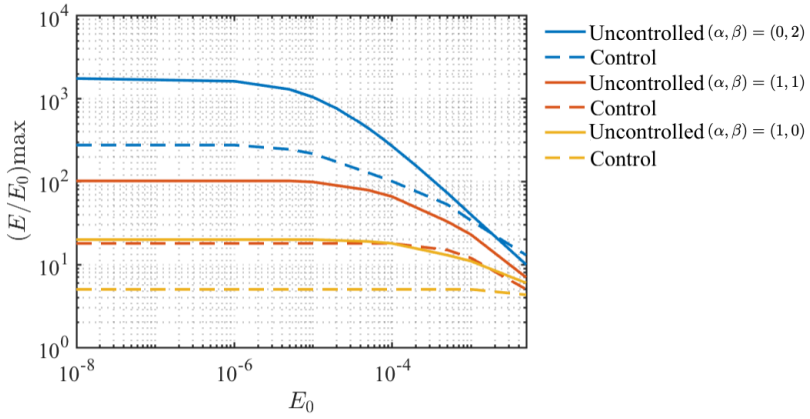


Figure 3.13: *A comparison of maximum amplified transient energy density $(E/E_0)_{max}$ of a range of amplitude of initial optimal disturbance between uncontrolled (solid lines) and controlled (dashed lines) cases.*

Controlled flow with oblique or streamwise-wave disturbances

By reducing the transient energy growth using feedback control, the laminar-to-turbulent transition experienced in the flow with oblique or streamwise-wave disturbances has been successfully suppressed. The threshold becomes higher in terms of triggering the transition process. Here, we examine how the wall actuation modifies the flow characteristics to prevent the transition in the uncontrolled flow. Because the control mechanism is similar in the cases with oblique and streamwise-wave disturbances, i.e., $(\alpha,\beta) = (1,1)$ and $(1,0)$, respectively, we will use the flow with oblique disturbance as an example to illustrate the control mechanism.

As the wall actuation is in the form of Fourier waves in space, here we show the amplitude of the wall-normal velocity at $[x,y,z]/h = [0,-1,0]$ to illustrate the actuation time-history in Figure 3.14. The wall-normal velocity is normalized by the corresponding $\sqrt{E_0}$. For case with $E_0 = 1.0\times10^{-4}$, the transition is successfully suppressed by introducing the wall actuation. The wall-normal velocity is similar to the actuation history of smaller disturbance case ($E_0 = 1.0\times10^{-5}$). Large blowing and suction are applied initially during time $0 < t\bar{u}_c/h < 30$ when large transient energy growth is present in the flow. Once the growth has been suppressed, the wall actuation gradually decays to zero. For the cases with larger perturbations ($E_0 = 1.0\times10^{-3}$ and 1.0×10^{-2}), the linear feedback control strategy fails to suppress the transition, and the flow transitions to a turbulent state. The normalized wall-normal velocity deviates from the successfully controlled cases and oscillates longer in time. In the study of Lee et al. [71], a constant wall blowing and suction in the form of a traveling wave was investigated, in which phase speed and wavenumber of the actuation may not be the same as the disturbance examined. Their work uncovered the phase speed relation between the wall actuation and the flow disturbance needed to stabilize or destabilize the flows via open-loop

control. In contrast, here we investigate a closed-loop control strategy, in which the phase speed and wavenumber of the wall actuation and the disturbance are consistent.

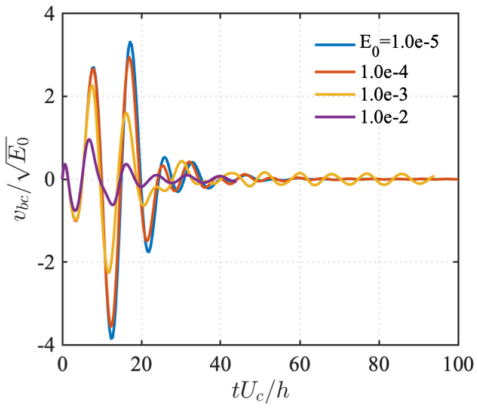


Figure 3.14: *Time history of normalized wall-normal velocity $v_{bc}/\sqrt{E_0}$ at lower wall of case $(\alpha, \beta) = (1, 1)$ when actuation is turned on.*

The transient energy growth present in the uncontrolled flow is caused by a development of large-scale coherent structures, which induce streamwise vortices that further cause a transition to turbulence, as discussed above. A comparison of flow features between uncontrolled and controlled flows during the transition process is shown in Figure 3.15. For a fair comparison, both simulations start from the same optimal disturbance calculated from the uncontrolled flow. In the uncontrolled flow, large magnitude of the initial optimal disturbance is concentrated near the upper and lower walls where coherent structures denoted by Q-criterion gradually grow into large-scale coherent structures. When the vertical size of the structures increases to approximately the half height of the channel ($t\bar{u}_c/h \approx 21$), the kinetic energy of perturbation reaches its maximum value around. During this process, streamwise vortices creep in near the walls following the advection of the coherent structures. After $t\bar{u}_c/h \approx 21$, the coherent structures start to decay, leaving the induced streamwise vortices in the flow; this is especially evident in the vicinity of the channel walls. As these vortices evolve, break, and interact with each other, the flow becomes chaotic and a laminar-to-turbulent transition occurs. Therefore, the key factor leading to the final transition to turbulence is the breakdown of the streamwise vortices. These streamwise vortices are generated by the rapid growth of the large-scale coherent structures.

Compared to the mechanism observed from the uncontrolled flow, the most apparent change in the flow by introducing wall-normal actuation is the growth of the coherent structures. As shown in Figure 3.16, the actuation on the wall modifies the distribution of high shear in the flow, in which local areas of high shear stress are created and constrained in the vicinity of the channel walls. As a consequence, the growth of the coherent structure is confined near the walls. Because the strength of these relatively small coherent structures is not enough to induce high-level of streamwise vorticity, the transition observed from the uncontrolled flow is avoided ultimately (Figure 3.15 (right)).

Controlled flow of spanwise-wave disturbances

Wall-normal velocity histories at $[x, y, z]/h = [0, -1, 0]$ in the controlled flows for spanwise-wave disturbance are shown in Figure 3.17. A sharp increase in wall-normal velocity is induced when the control is turned on, then the velocity quickly decays to a relatively small value and

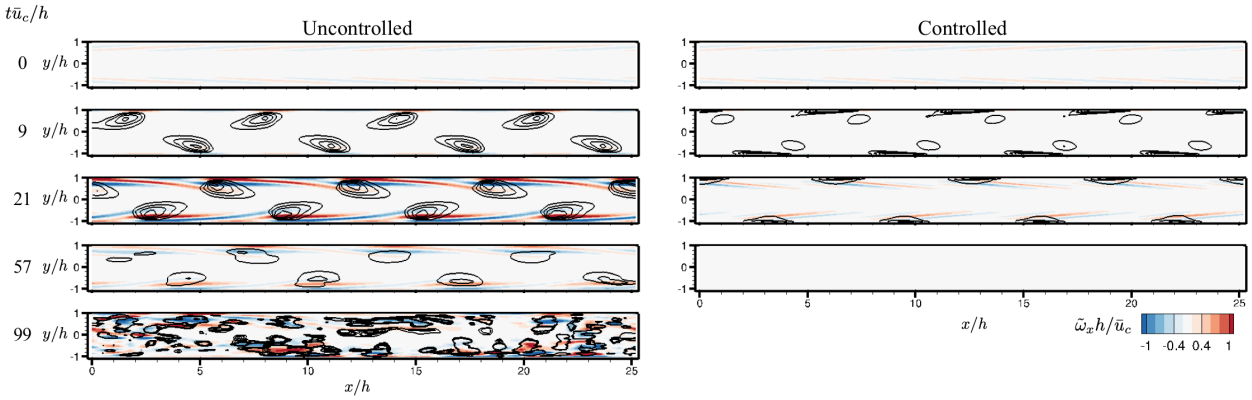


Figure 3.15: *A comparison of instantaneous streamwise vorticity $\tilde{\omega}_x h/\bar{u}_c$ flow fields at slice $z/h = 0$ between uncontrolled and controlled cases with $(\alpha, \beta) = (1, 1)$ and $E_0 = 0.5 \times 10^{-4}$. Black contour lines denote Q-criterion in a range of $0.01 \leq Q(h/\bar{u}_c)^2 \leq 0.05$.*

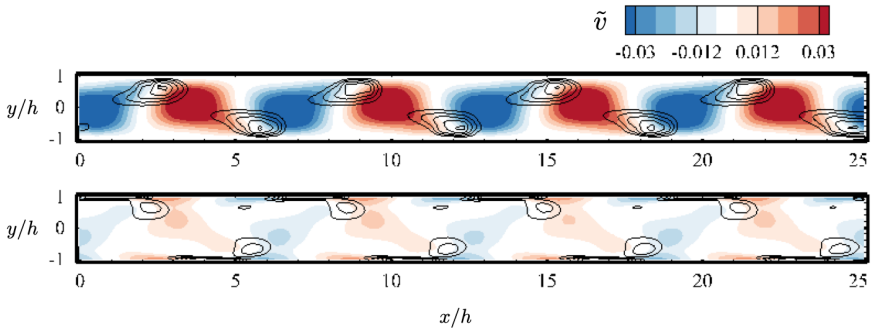


Figure 3.16: *A comparison of instantaneous flow field at slice $z/h = 0$ and $tu_c/h = 12$ between uncontrolled and controlled flow with $(\alpha, \beta) = (1, 1)$ and $E_0 = 0.5 \times 10^{-4}$. Contours are wall-normal velocity $\tilde{v}$, and black contour lines denotes Q-criterion in a range from 0.01 to 0.05 with increment of 0.01.*

gradually decreases later in time. The oscillations in the wall-normal velocity at later times correspond to the fact that the flow has reached a turbulent state.

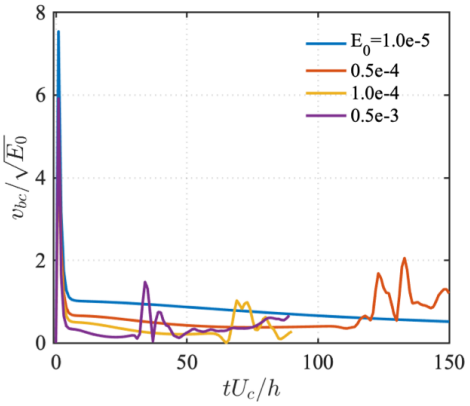


Figure 3.17: *Time history of normalized wall-normal velocity $v_{bc}/\sqrt{E_0}$ at lower wall of case $(\alpha,\beta) = (0,2)$ when actuation is turned on.*

In the transition process associated with a spanwise-wave disturbance $(\alpha,\beta) = (0,2)$, the merging two co-rotating vortices highly distorts the base velocity profile, as seen in Figure 3.18. The generation of high-shear areas introduces secondary instabilities into the flow for the uncontrolled flow. To examine the control mechanism, we compare the shear flow fields at $t\bar{u}_c/h = 50$ in Figure 3.18. In the uncontrolled flow, high magnitude of shear stress $\partial u/\partial z$ is formed between the merged vortices, where we previously observe instabilities in Figure 3.9. In the controlled flow, a strong actuation forms small-scale streamwise vortices near walls, as seen in Figure 3.18 (b). The introduction of these new vortices by control hinders the growth of the merged vortices. Instead, the large streamwise vortical structures are compressed and centralized in the channel. The high shear stress between the vortices is also weakened, as revealed by $\partial\tilde{u}/\partial z$, providing less chances for secondary instabilities to arise.

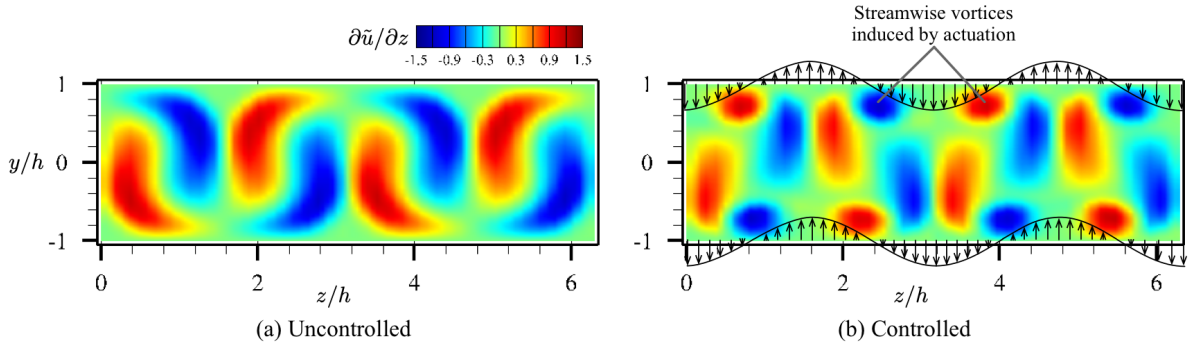


Figure 3.18: *Modification of instantaneous streamwise velocity gradient in spanwise direction $\partial\tilde{u}/\partial z$ at slice $x/h = 0$ and $t\bar{u}_c/h = 50$ in (b) controlled flow compared to (a) uncontrolled flow. Actuation velocity is denoted by black arrows.*

Although the controller has suppressed the growth in large streamwise vortical structures, the actuation actually introduces extra high-shear regions. As shown in Figure 3.19 (a) and (b), the

areas denoted by (i) and (ii) indicate induced high shear stress. Accordingly, as seen in Figure 3.19 (c), new secondary instabilities creep in based on the new high-shear regions of (i) and (ii), which ultimately leads to a transition to turbulence. Hence, the secondary instabilities are introduced by the actuation in the nonlinear simulations, which is not accounted for in the controller design from the linear model.

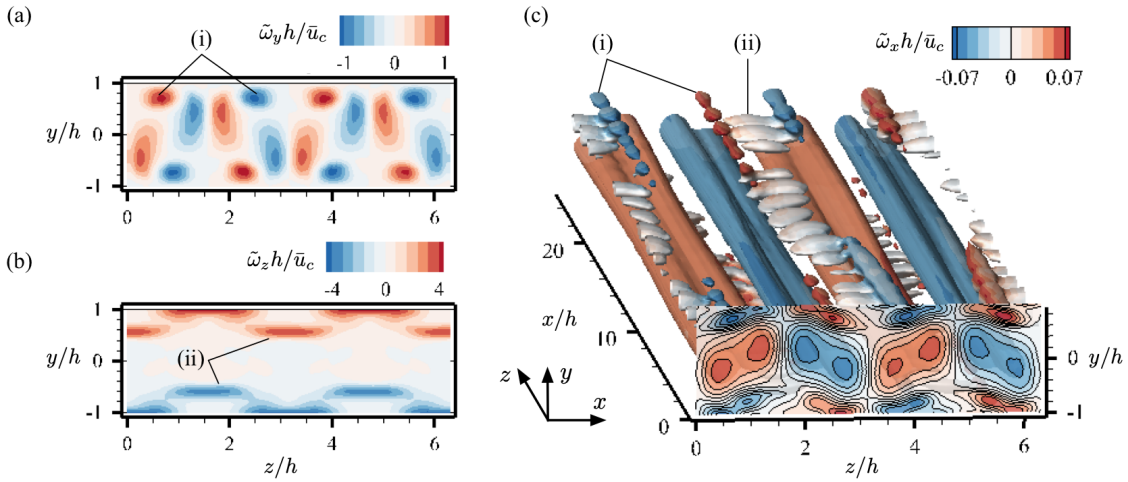


Figure 3.19: *Secondary instabilities induced by the actuation in the flow field at $t\bar{u}_c/h = 66$ of controlled case with $(\alpha,\beta) = (0,2)$ and $E_0 = 1.0 \times 10^{-4}$. (a) Wall-normal vorticity at slice of $x/h = 0$, (b) spanwise vorticity at slice of $x/h = 0$, and (c) iso-surfaces of Q colored by streamwise vorticity.*

Increase in perturbation threshold for laminar-to-turbulent transition

A summary of the cases considered in the present work is provided in Figure 3.20 based on the nonlinear simulation results. For all three wavenumber pairs, the LQR controller successfully suppresses the transient energy growth within linear analysis. In nonlinear simulations, LQR control increases the perturbation threshold E_0 for a laminar-to-turbulent transition by roughly an order of $O(10)$ in amplitude in the cases of streamwise-wave $(\alpha,\beta) = (1,0)$ and oblique $(\alpha,\beta) = (1,1)$ disturbances. For the spanwise-wave disturbance $(\alpha,\beta) = (0,2)$, LQR controller successfully suppresses the transient energy growth of the streamwise coherent structures. However, new instabilities are induced by the strong actuation applied on the walls, which leads to laminar-to-turbulent transition by another route; hence, the perturbation threshold does not change based on the cases considered.

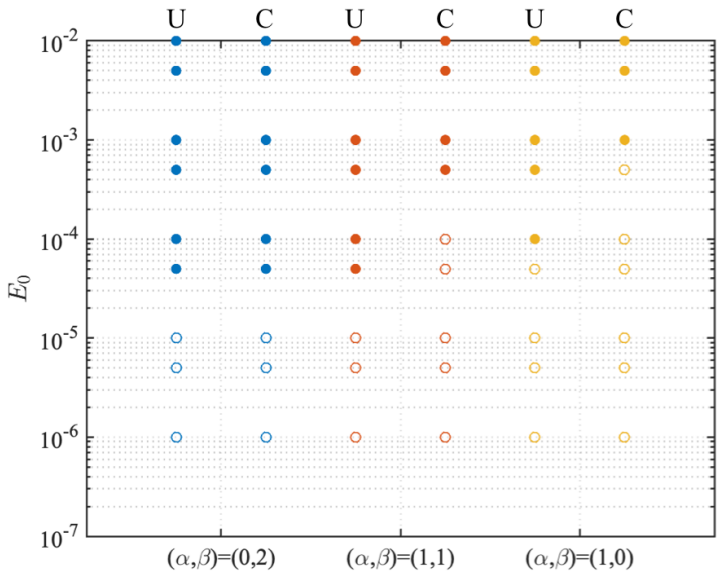


Figure 3.20: *Summary of cases considered in the present work. Solid circle represents that laminar-to-turbulent transition occurs; open circle denotes that the flow remains laminar. U and C denote uncontrolled and controlled cases, respectively.*

3.4 Conclusions

In this chapter, we examined the laminar-to-turbulent transition in plane Poiseuille flow due to transient energy growth of optimal disturbances at a subcritical Reynolds number of $Re = 3000$. A large domain is used in the present work in order to capture the large-scale dynamics that are critical to the laminar-to-turbulent transition process. Nonlinear effects on transient energy growth were investigated by performing direct numerical simulations. We found that with the presence of nonlinearity in the flow, an increase in initial energy density of an optimal disturbance leads to a reduction in amplification rate. Moreover, we uncovered the underlying physics of the transition process for all the disturbances considered. For disturbances associated with $(\alpha, \beta) = (1, 1)$ and (1,0), the transient energy growth corresponds to the development of large coherent structures. The evolution of these large-scale coherent structures induces a growth of streamwise vortices near the channel walls, and the breakdown of these vortices leads to a laminar-to-turbulent transition. For a disturbance associated with $(\alpha, \beta) = (0, 2)$, the base flow is highly distorted due to the growth of streamwise vortices, which results in high-shear-stress regions formed between the streamwise vortical structures. These high-shear areas introduce secondary instabilities that lead to a laminar-to-turbulent transition.

LQR feedback controllers were designed and shown to be capable of reducing transient energy growth via wall-normal blowing and suction actuation at the upper and lower walls. In the controlled flow, the wall actuation modified the shear distribution in the flow, such that coherent structures only formed in the vicinity of the channel walls. For streamwise-wave $(\alpha, \beta) = (1, 0)$ and oblique $(1, 1)$ disturbances, this resulted in a more rapid decay of disturbance energy than for the uncontrolled flow. Laminar-to-turbulent transition was prevented because the hindered growth of coherent structures significantly inhibits the strength of induced streamwise vortices. The control strategy was found to increase the threshold for transition by approximately $O(10)$ in magnitude.

For the case with spanwise-wave disturbance of $(\alpha, \beta) = (0, 2)$, the controller did not effectively increase the threshold for the transition; the actuation was found to induces extra instabilities that led the flow to transition from a laminar to turbulent state.

The results here establish the capabilities of feedback control for suppressing transient energy growth and preventing laminar-to-turbulent transition. The nonlinear effects and underlying physics related to transition process have been investigated by performing direct number simulations. Although LQR control has been shown to suppress transition in past studies, we note that the resulting reduction of transient energy growth is not sufficient to fully suppress transition due to large amplitude perturbations. The nonlinear effects should be considered in control designs in order to improve the control performance for large disturbance. We will consider a framework by which such nonlinear effects can be accommodated for analysis, and subsequently controller design, in Chapter 7. Before we get there, we will first present on static output feedback control strategies for transition suppression (Chapter 4); a framework for model reduction that enables synthesis of controllers that minimize TEG in the linear setting (Chapter 5; and also a framework for sensor selection that enables SOF controllers to recover full-information control performance (Chapter 6).

4 | Static Output Feedback Control for Reducing Transient Energy Growth

As highlighted in the previous chapter, transient energy growth of flow perturbations is an important mechanism for laminar-to-turbulent transition that can be mitigated with feedback control. Linear quadratic optimal control strategies have shown some success in reducing transient energy growth and suppressing transition, but acceptable worst-case performance can be difficult to achieve using sensor-based output feedback control. In this chapter, we investigate static output feedback controllers for reducing transient energy growth of flow perturbations within linear and nonlinear simulations of a sub-critical channel flow. The presentation in this chapter is heavily drawn from [72, 73]. A static output feedback linear quadratic regulator (SOF-LQR) is designed to reduce the worst-case transient energy growth due to flow perturbations. The controller directly uses wall-based measurements to optimally regulate the flow with wall-normal blowing and suction from the upper and lower channel walls. We show that SOF-LQR controllers can reduce the worst-case transient energy growth of flow perturbations. Our results also indicate that SOF-LQR controllers exhibit robustness to Reynolds number variations. Further, direct numerical simulations show that the designed SOF-LQR controllers increase laminar-to-turbulent transition thresholds under streamwise disturbances and delay transition under spanwise disturbances. The results of this study highlight the advantages of SOF-LQR controllers and create opportunities for realizing improved transition control strategies in the future.

4.1 Introduction

An ability to delay transition to turbulence is of great interest, owing to the potential for drag reduction and energy savings in numerous engineering systems. Transient energy growth (TEG) is an important mechanism for sub-critical transition in many shear flows [44, 74]. For linearly stable shear flows, small flow perturbations can be amplified significantly over short time-horizons [75–77]. When this TEG is sufficiently large, the flow state can be driven outside the basin of attraction of the laminar equilibrium, triggering secondary instabilities that transition the flow to turbulence. Worst-case analysis is typical in investigations of such phenomena, since the response leading to the maximum TEG is the one that pushes the flow state furthest from the laminar equilibrium profile. The flow perturbation resulting in the maximum TEG is known as an "optimal perturbation" [78]. As such, if it is possible to reduce the maximum TEG, then it may be possible to delay or suppress transition.

Many studies have investigated the possibility of reducing TEG and suppressing transition by means of feedback control [19, 32, 51, 52, 54, 79, 80]. Full-state feedback control is usually the first choice for feasibility studies in numerical simulations. The full-information linear quadratic

regulator (LQR) has been shown to suppress transition in a channel flow using wall blowing and suction actuation [52, 54, 80, 81]. Worst-case analyses have confirmed that LQR control strategies reduce the maximum TEG due to linear optimal perturbations. It was found that another benefit for the LQR controller is that it exhibits robust TEG reduction under off-design Reynolds numbers and wavenumbers [82]. Despite the successes of full-information LQR control strategies for TEG reduction and transition suppression, full-state feedback control cannot be realized in practice. Typically, measurements of the full state are not directly available for feedback; rather, only measured outputs from a limited set of sensors—typically confined to solid boundaries—can be used for output feedback.

One commonly used approach for output feedback design is observer-based feedback via the separation principle [69]. That is, first, an observer is used to estimate the full state of the flow. Then, this full-state estimate is fed-back to a full-state feedback control law to determine the appropriate actuation. Indeed, the separation principle of modern linear control theory establishes that observer-based feedback will result in a stable closed-loop system if the full-state feedback controller is stabilizing and the observer yields stable estimation error dynamics [69]. Separation-principle-based designs are appealing owing to the great simplicity of the associated design process: a controller and estimator can be designed separately, then combined to guarantee closed-loop stability of the linear dynamics. For example, the widely used linear quadratic Gaussian (LQG) controller possesses an observer-based feedback structure that follows the separation principle. A linear quadratic estimator (LQE) is combined with a full-information LQR controller to solve the associated $\mathcal{H}_2$-optimal control problem. $\mathcal{H}_2$-optimal controllers are designed by solving two independent algebraic Ricatti equations—one for the optimal observer and one for the optimal controller. Numerous studies have investigated $\mathcal{H}_2$-optimal controllers and demonstrated their utility within the context of flow control [32, 83, 84].

While separation-principle-based designs guarantee closed-loop stability for the linear dynamics, such designs can result in degraded closed-loop TEG performance [85]. Indeed, separation-principle-based designs can potentially degrade TEG performance relative to the uncontrolled system, resulting in adverse consequences for transition control based on such designs [84–86]. One way of overcoming these limitations is to couple the controller and observer design problems [83]. Of course, coupling the designs removes the simplicity that is afforded by the separation principle: acceptable designs require an iterative tuning process that can take substantial effort on the part of the designer. In principle, the iterative design process can be circumvented by directly seeking an optimal output feedback controller that minimizes the maximum TEG; however, such approaches can be computationally intractable [87–90]. A potential compromise is introducing additional complexity into the control architecture while maintaining a computationally tractable synthesis problem. For example, it has been shown that tailored design kernels and time-varying feedback gains can be used to achieve substantial TEG reductions [91].

In this chapter, we investigate a simple alternative for TEG reduction within linear and nonlinear simulations of a sub-critical channel flow based on the static output feedback linear quadratic regulator (SOF-LQR). SOF-LQR controllers constitute semi-proper control laws, thus satisfying a necessary condition for overcoming the TEG performance limitations of observer-based feedback [85, 88]. Specifically, we solve the standard LQR problem (Chapter 3, but with an additional constraint that the control law has a static output feedback control structure. The SOF-LQR

controller gain in this study maps the wall-based measurements at the channel walls directly to the control input, which is taken to be the rate of change of wall-normal velocity at upper and lower walls. In order to expedite the computations involved in determining the optimal SOF-LQR gains, we introduce an accelerated gradient method based on the Anderson-Moore algorithm [92]. Controllers are designed using a combination of wall-based shear-stress and pressure sensors. The resulting SOF-LQR controllers reduce the worst-case TEG and exhibit robustness to Reynolds number and wavenumber uncertainties. Furthermore, the nonlinear performance of SOF-LQR control is investigated using nonlinear direct numerical simulations (DNS). The DNS results show that the proposed SOF-LQR control delays transition under spanwise disturbances and increases transition thresholds under streamwise disturbances. As such, SOF-LQR stands as a viable candidate for transition delay and suppression for future studies.

The remainder of the chapter is organized as follows. Full-information LQR and SOF-LQR control strategies for TEG reduction are discussed in Section 4.2. We also introduce an accelerated Anderson-Moore algorithm for designing SOF-LQR controllers in this section. In Section 5.3.1, we present the linearized channel flow model and give the setup for the direct numerical simulation (DNS). The results are sequenced by disturbance type (i.e., spanwise and streamwise) in Section 6.4. Performance and robustness of SOF-LQR control for TEG reduction are investigated using linear simulations. Transition suppression and delay scenarios and mechanisms are investigated using nonlinear simulations. Comparisons are made with the uncontrolled flow and full-information LQR control. Finally, conclusions are presented in Section 6.6.

4.2 Transient energy growth and controller synthesis

4.2.1 Transient energy growth

Consider the state-space representation of the linearized Navier-Stokes equations about a laminar equilibrium solution,

$$\begin{aligned} \dot{X}(t) &= AX(t) + BU(t) \\ Y(t) &= CX(t) \end{aligned} \tag{4.1}$$

where $X \in \mathbb{R}^n$ is the state vector, $U \in \mathbb{R}^m$ is the input vector, $Y \in \mathbb{R}^p$ is the output vector, and $t \in \mathbb{R}$ is time. For an initial flow perturbation $X(t_0) = X_0$, the system response is given in terms of the matrix exponential $X(t) = e^{A(t-t_0)}X_0$, where A represents the system dynamics matrix. The associated perturbation kinetic energy is given as,

$$E(t) = X^{\mathsf{T}}(t)QX(t), \tag{4.2}$$

where $Q = Q^{\mathsf{T}} > 0$. Further, the maximum transient energy growth (TEG) is defined as,

$$G = \max_{t \geq t_0} \max_{E(t_0) \neq 0} \frac{E(t)}{E(t_0)}, \tag{4.3}$$

which results from a so-called *worst-case* or *optimal perturbation* [3]. Certain perturbations will result in non-trivial TEG whenever $G > 1$.

4.2.2 Full-information feedback control synthesis

Feedback controllers have been shown to reduce TEG in various shear flows. In particular, the linear quadratic regulator (LQR) is a well-known design technique that has been proven to be successful at reducing TEG in previous flow control studies [54, 80, 93]. LQR synthesis is based

on solving,

$$\min_{U(t)} J = \int_0^\infty \left[X^\mathsf{T}(t) Q X(t) + U^\mathsf{T}(t) R U(t) \right] dt \tag{4.4}$$

subject to the linear dynamic constraint

$$\dot{X}(t) = AX(t) + BU(t) \tag{4.5}$$

where $R > 0$ penalizes the control input. The resulting LQR controller is a full-state feedback law of the form $U(t) = KX(t)$, where $K \in \mathbb{R}^{m \times n}$ is determined from the solution of an algebraic Riccati equation [69]. LQR controllers are particularly appealing because they can be designed to reduce TEG, while demonstrating robustness to parametric and modeling uncertainties. However, outside of numerical simulations, standard full-state feedback LQR controllers are typically not practically viable for flow control; standard LQR control requires knowledge of the full state of the flow, which is usually not directly available for feedback in practice.

When full-state feedback is not a viable option, an observer (i.e., state estimator) is usually designed to estimate the current state of the flow from available sensor measurements $Y(t)$. The separation principle is often invoked to simplify the design process; however, doing so can degrade the resulting closed-loop TEG performance [52, 64, 85, 86, 91]. This performance degradation arises due to unaccounted adverse interactions that can arise between the fluid dynamics and the control system dynamics [85]. The control system dynamics can be designed to overcome this performance degradation, but proposed strategies introduce complexity in the design procedure and/or in the control law [84, 88]. To address the TEG reduction problem with sensor-based feedback, we introduce an alternative static output feedback control strategy that provides a simple alternative to overcome the performance limitations of the separation principle and associated observer-based designs.

4.2.3 Static output feedback control synthesis

The proposed SOF-LQR control strategy for TEG reduction is based on solving the standard LQR problem, but now with an additional constraint that the resulting feedback law have static output feedback (SOF) control structure,

$$U(t) = FY(t), \tag{4.6}$$

where $F \in \mathbb{R}^{m \times p}$ is the SOF gain matrix. The benefit of the SOF control structure is that the input is determined directly from the measured output, removing the need for state estimation. We note that the SOF control structure is akin to the so-called "opposition control" that has been employed and studied within the context of turbulent drag reduction [94, 95]. Furthermore, the SOF structure constitutes a semi-proper controller, thus satisfying a necessary condition for eliminating TEG [85, 88]. As such, we expect the SOF-LQR controller to improve performance in terms of the worst-case TEG relative to strictly proper control structures, such as LQG controllers and other observer-based feedback controllers designed via the separation principle.

The closed-loop dynamics under SOF-LQR control are of the form,

$$\dot{X}(t) = (A + BFC)X(t). \tag{4.7}$$

Thus, the standard LQR objective function in (6.12) can be rewritten to conform to the SOF structure in (4.6). However, doing so introduces a complication: the problem formulation and its

solution will depend on the specific initial condition $X(0)$, which is unknown a priori. As such, it is common to replace the performance index in (6.12) by its expected value (see, e.g., [96]):

$$J = \mathbb{E}\left(\int_0^\infty X^\mathsf{T}(t)[Q + (FC)^\mathsf{T} R(FC)]X(t)dt\right). \tag{4.8}$$

Now, the solution of this SOF-LQR problem can be calculated iteratively using Anderson-Moore methods [92]. To do so, define the set of all stabilizing SOF controllers $D_s = \{F \in \mathbb{R}^{m\times p} | Re\{\lambda(A + BFC)\} < 0\}$, where $\lambda(\cdot)$ denotes the set of all eigenvalues of $(\cdot)$. Then, re-write the SOF-LQR design problem as [96, 97],

$$\min_F \quad J(F) = \text{trace}[S(F)X_E] \quad \text{subject to} \quad F \in D_s, \tag{4.9}$$

where $X_E = \mathbb{E}\{X(0)X(0)^\mathsf{T}\}$ and $S(F)$ is a solution to the algebraic Ricatti equation,

$$S(F)[A + BFC] + [A + BFC]^\mathsf{T} S(F) + C^\mathsf{T} F^\mathsf{T} RFC + Q = 0. \tag{4.10}$$

Note that $X_E := \mathbb{E}\{X(0)X(0)^\mathsf{T}\}$ is a symmetric matrix representing the autocorrelation of the initial state. Here, we assume that all initial conditions are equally likely, and so take the initial state to be uniformly distributed over the unit ball, i.e., $X_E = I$.

Next, the gradient of the cost function J with respect to the SOF control gain F can be expressed as

$$\frac{\partial J}{\partial F} = 2[B^\mathsf{T} S(F)H(F)C^\mathsf{T} + RFCH(F)C^\mathsf{T}], \tag{4.11}$$

where $H(F)$ is the solution to the Lyapunov equation

$$H(F)[A + BFC]^\mathsf{T} + [A + BFC]H(F) + X_E = 0. \tag{4.12}$$

Then, the optimal SOF gain $F^* \in D_s$ will be a minimizer of (4.9) and so must satisfy a zero gradient condition, which reduces to

$$[B^\mathsf{T} S(F^*)H(F^*)C^\mathsf{T} + RF^*CH(F^*)C^\mathsf{T}] = 0. \tag{4.13}$$

After some further manipulation, we find that a necessary condition for optimality is

$$F = -R^{-1}[B^\mathsf{T} S(F)H(F)C^\mathsf{T}][CH(F)C^\mathsf{T}]^{-1}, \tag{4.14}$$

yielding a search direction to use in the Anderson-Moore method,

$$[T_i = -F_{i-1} - R^{-1}[B^\mathsf{T} S(F_{i-1})H(F_{i-1})C^\mathsf{T}][CH(F_{i-1})C^\mathsf{T}]^{-1}.] \tag{4.15}$$

Although the expressions above are sufficient for implementing the Anderson-Moore method, such methods tend to require a significantly large number of iterations. For high-dimensional fluid flows, each iteration can require a significant computational demand on the order of $O(n^3)$, and so it is desirable to reduce the total number of iterations through an accelerated technique. The step-size ξ along the gradient direction must be chosen with care in order to balance precision with the total number of iterations. An inappropriate choice of ξ will lead to slow convergence. In order to overcome this challenge, we formulate an accelerated Anderson-Moore algorithm that incorporates Armijo-type adaptations. Instead of using a fixed step-size ξ, we instead use an Armijo-rule [98] to adaptively update the step-size to achieve a better balance between precision and iteration count. The method we propose and use in this study is summarized as Algorithm 1.

Algorithm 1: ***Anderson-Moore algorithm with Armijo-type adaptation***

step 0: Set i = 0; initialize $F_i = F_0$ to be any $F_0 \in D_s$. Set $0 < \xi < 1$, $0 < \sigma < 1/2$, and $\delta > 0$.

step 1: Solve (4.10) for $S(F_i)$.

step 2: Solve (4.12) for $H(F_i)$.

step 3: Use (4.15) to find the smallest integer $\gamma_1 \geq 1$ such that $F_i + \xi^{\gamma_1} T_i \in D_s$.

step 4: Find the smallest integer $\gamma_M \geq \gamma_1$ such that

$$J(F_i + \xi^{\gamma_M} T_i) \leq J(F_i) + \sigma \xi^{\gamma_M} \text{trace}(\frac{\partial J}{\partial F}^{\mathsf{T}} T_i).$$

step 5: Find integer $\ell \in \{\gamma_1, \ldots, \gamma_M\}$ such that

$$J(F_i + \xi^{\ell} T_i) = \min J(F_i + \xi^{j} T_i), \text{ where } j \in \{\gamma_1, \cdots, \gamma_M\}$$

step 6: Set $F_{i+1} = F_i + \xi^{\ell} T_i$, $i = i + 1$

step 7: Check $\|\frac{\partial J}{\partial F}\|_2 \leq \delta$. If true, stop. Otherwise, go to **step 1**.

Note that all Anderson-Moore methods require initialization with a stabilizing SOF gain $F_0 \in D_s$ [99]. For an asymptotically stable system, setting $F_0 = 0$ is a valid choice. In the present study, actuator dynamics are modeled via an integral term, and so the resulting linear system model will not be asymptotically stable. Thus, we first determine a stabilizing static output feedback gain F_0 using the iterative linear matrix inequality (ILMI) method proposed in [100], then proceed to compute the optimal SOF-LQR controller using the accelerated Anderson-Moore algorithm in Algorithm 1. Additional details on the ILMI method used for initialization in this study are presented in Appendix A. We note that use of the ILMI method was not necessary, but was chosen out of convenience in this study. Alternatives to the ILMI method (e.g., pole placement) would have been equally valid for determining the initial stabilizing gain. The computational complexity of Algorithm 1 is detailed in Appendix B.

4.3 Channel flow model

The proposed SOF-LQR controller will be evaluated using both linear analysis and nonlinear direct numerical simulations in Section 6.4. In this section, we present the linearized channel flow model used for controller design and provide details of the direct numerical simulations.

4.3.1 Linearized channel flow system

Consider the pressure-driven flow between two infinite parallel walls separated by a distance $2h$, shown in Figure 6.1. Here, x, y, and z represent the streamwise, wall-normal, and spanwise directions, respectively. The laminar equilibrium solution of this plane Poiseuille flow is a parabolic profile in the form of $\boldsymbol{U}_b(y) = \bar{u}_c(1 - y^2/h^2)$, where $\bar{u}_c$ is the centerline velocity of the base flow, $\bar{u}_c = 1, h = 1$. The incompressible Navier-Stokes and continuity equations for small perturbations are linearized about this laminar profile. Transforming into velocity-vorticity form and Fourier transforming in the streamwise and spanwise directions, yields the Orr-Sommerfeld and Squire

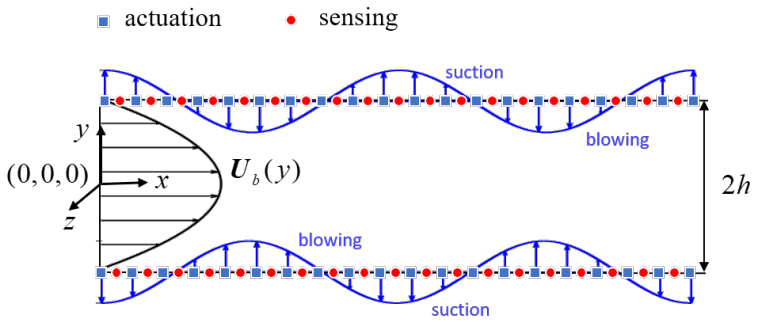


Figure 4.1: *Illustration of wall-based sensing and actuation in channel flow.*

equations for the linear perturbation dynamics [44]:

$$\begin{aligned}(\mathcal{D}^2 - k^2)\dot{\tilde{\boldsymbol{v}}} &= \left[-i\alpha \boldsymbol{U}_b(\mathcal{D}^2 - k^2) + i\alpha \boldsymbol{U}_b'' + \frac{1}{Re}(\mathcal{D}^2 - k^2)^2\right]\tilde{\boldsymbol{v}} \\ \dot{\tilde{\boldsymbol{\eta}}} &= \left[-i\alpha \boldsymbol{U}_b + \frac{1}{Re}(\mathcal{D}^2 - k^2)\right]\tilde{\boldsymbol{\eta}} - i\beta \boldsymbol{U}_b'\tilde{\boldsymbol{v}},\end{aligned} \tag{4.16}$$

where v is the wall-normal velocity, η is the wall-normal vorticity, $\tilde{(\cdot)}$ denotes the Fourier amplitude of the associated variable, $\mathcal{D}$ represents differentiation with respect to y, and $k^2 = \alpha^2 + \beta^2$, where α and β are wavenumbers of the streamwise and spanwise Fourier modes, respectively. $Re = \frac{\bar{u}_c h}{\nu}$ denotes the Reynolds number based on the channel half-height. No-slip boundary conditions are imposed at the solid walls for uncontrolled flow, i.e., $\tilde{\boldsymbol{v}} = \mathcal{D}\tilde{\boldsymbol{v}} = \tilde{\boldsymbol{\eta}} = 0$. Next, $\tilde{\boldsymbol{v}}$ and $\tilde{\boldsymbol{\eta}}$ can be approximated by a finite Chebyshev series expansion along the wall-normal direction with $N + 1$ discrete collocation points. For this uncontrolled channel flow, the state variable is $X_u = (a_{v0}, \ldots, a_{vN}, a_{\eta 0}, \ldots, a_{\eta N})^{\mathsf{T}}$, where a_i are the Chebyshev polynomial coefficients.

For flow control, actuation is achieved using wall-normal velocity at the upper and lower walls via wall-transpiration boundary conditions denoted as $\tilde{\boldsymbol{v}}|_{+h}$ and $\tilde{\boldsymbol{v}}|_{-h}$. The control input is taken to be the rate of wall-normal blowing and suction at each wall. Thus, the input vector in (4.1) is $U = \frac{\partial}{\partial t}[\hat{v}|_{+h}, \hat{v}|_{-h}]^T$. Upon discarding redundant terms, the associated system state vector consists of the Chebyshev polynomial coefficients and the actuator states:

$$X = (a_{v0}, \ldots, a_{vN-4}, a_{\eta 0}, \ldots, a_{\eta N-2}, \tilde{\boldsymbol{v}}|_{+h}, \tilde{\boldsymbol{v}}|_{-h})^{\mathsf{T}}. \tag{4.17}$$

We consider several wall-based sensors in this study, each of which can be represented in Fourier space. Shear-stress measurements are given by

$$\begin{aligned}\tilde{\tau}_x|_{y=\pm h} &= \frac{1}{Re}\left(\frac{\partial \tilde{u}}{\partial y}\right), \\ \tilde{\tau}_z|_{y=\pm h} &= \frac{1}{Re}\left(\frac{\partial \tilde{w}}{\partial y}\right),\end{aligned} \tag{4.18}$$

where $\tilde{u}$ and $\tilde{w}$ correspond to Fourier coefficients of streamwise and spanwise velocity components, respectively. Also, we consider the pressure measurements $\tilde{p}$ at the upper and lower channel walls. The Fourier coefficient for pressure can be expressed in terms of the wall-normal velocity and

Table 4.1: *Wall-based sensor configurations*

Configuration	Sensors
s	$\tilde{\tau}_x, \tilde{\tau}_z$
sp	$\tilde{\tau}_x, \tilde{\tau}_z, \tilde{p}$

vorticity using the x- and z-momentum equations.

$$\tilde{p}|_{y=\pm h} = \frac{1}{\alpha^2+\beta^2}\frac{1}{Re}\left(\frac{\partial^3 \tilde{\boldsymbol{v}}}{\partial y^3} + \frac{\alpha-\beta}{\alpha+\beta}\frac{\partial^2 \tilde{\boldsymbol{\eta}}}{\partial y^2}\right) + \frac{i}{\alpha+\beta}\tilde{\boldsymbol{v}}\frac{\partial \boldsymbol{U}_b}{\partial y}. \tag{4.19}$$

Further details about the model formulation can be found in [101].

For sensor-based output feedback control, we investigate two different sensor combinations among the quantities reported in equations (4.18)-(4.19). Specific configurations are listed in Table 4.1, and will be referenced accordingly in the remainder of this chapter.

4.3.2 Direct numerical simulation setup

Three-dimensional direct numerical simulations (DNS) of plane Poiseuille flow are performed to analyze the nonlinear performance of the designed controllers. A detailed overview was provided in Chapter 3, but we further summarize details needed for the current chapter. The incompressible Navier-Stokes equations are solved using a modified version of the spectral code *Channelflow* [65, 80]. The flow response to optimal disturbances for a given controller is simulated. A second-order semi-implicit Crank-Nicolson Runge–Kutta temporal scheme is used. Spanwise $(0, \beta)$ and streamwise $(\alpha, 0)$ disturbance scenarios are considered. The kinetic energy density of the initial optimal perturbation is denoted by E_0. For each wavenumber pair, several amplitudes of E_0 are considered to demonstrate the role of the nonlinearity in the laminar-to-turbulent transition. A random disturbance with perturbation kinetic energy density of 1% of E_0 is superposed with the optimal disturbance profile to ensure that a laminar-to-turbulent transition can be initiated [67]. A three-dimensional computational domain is used in order to resolve the complete transition process. We use a rectangular computational domain of size $8\pi h \times 2h \times 2\pi h$ in x-, y- and z-directions, respectively. To discretize the flow field, $N = 101$ Chebyshev points are specified in the y-direction, and 128×64 points are uniformly spaced along x- and z-directions, respectively. For both baseline and controlled flows, grid resolution studies with doubled grids in each direction have been performed to ensure the accuracy of results (see Appendix C).

4.4 Results

The utility of SOF-LQR control for TEG reduction will first be evaluated using linear simulations. DNS will then be performed to evaluate the nonlinear performance of SOF-LQR control for transition suppression and delay. We design SOF-LQR controllers for a sub-critical Reynolds number $Re = 3000$, then evaluate the worst-case performance associated with spanwise $(\alpha, \beta) = (0, 2)$ and streamwise $(\alpha, \beta) = (1, 0)$ linear optimal perturbations. As shown in section 6.2.2, the dynamical systems of the uncontrolled and controlled flows are different; thus, the optimal disturbances are calculated independently for each system to ensure a fair comparison based on the largest TEG under each setting. In the nonlinear DNS, as described in section 4.3.2, we adopt the same optimal disturbances scaled with different amplitudes and add a small random perturbation to trigger the laminar-to-turbulent transition. We investigate two different sensor combinations for feedback control. These are listed in Table 4.1.

4.4.1 Spanwise disturbances

Linear analysis

For spanwise disturbances, we investigate SOF-LQR control using sensor configuration "s" in Table 4.1, which consists solely of shear-stress measurements $\tilde{\tau}_x$ and $\tilde{\tau}_z$. We note that the addition of pressure measurements (resulting in sensor configuration "sp" in Table 4.1) was found to have a negligible influence on the controlled flow performance. Thus, for brevity, we only report on control using sensor configuration "s" for both linear and nonlinear simulations of spanwise disturbances. The linear worst-case response for SOF-LQR-s control with $(\alpha,\beta) = (0,2)$ and $Re = 3000$ is reported in Figure 4.2 (red dotted line). The SOF-LQR-s controller reduces the maximum TEG (G) by approximately 50% relative to the uncontrolled flow (black solid line). The worst-case response for the full-information LQR controlled system (blue dashed line) yields a larger TEG reduction, achieving approximately 80% reduction relative to the uncontrolled flow. This result is not surprising since the SOF-LQR-s design operates based on considerably less information than the full-information case. As we will see momentarily, this reliance on limited information actually improves the robustness of the flow control strategy to parameter and modeling uncertainties. We will discuss physical mechanisms surrounding the TEG reduction within the context of nonlinear simulations after we report results on flow control robustness.

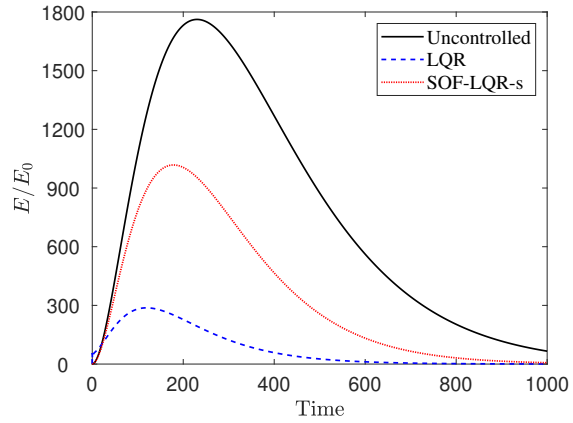
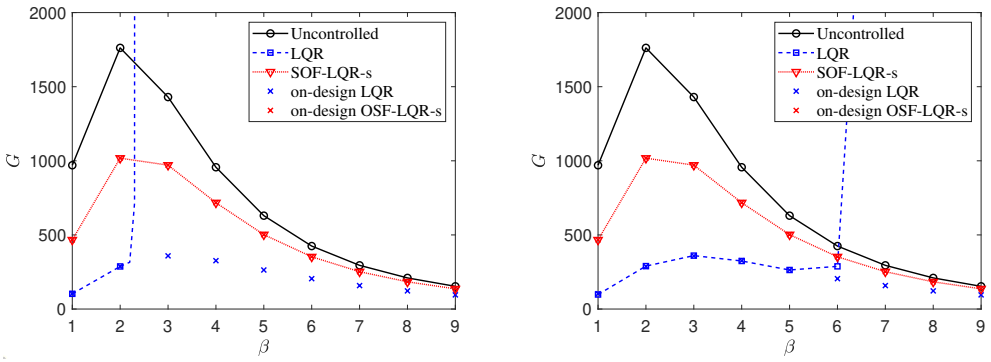


Figure 4.2: *Linear worst-case response to spanwise optimal perturbations with* $(\alpha,\beta) = (0,2)$ *and* $Re = 3000$.

Thus far, we have considered control performance at a fixed Reynolds number of $Re = 3000$ and a fixed spanwise disturbance $(\alpha,\beta) = (0,2)$. In practice, the fluid flow could experience a mix of disturbances, and the underlying parameters may not be precisely known. As such, we conduct additional linear simulations to better characterize and understand the robustness of SOF-LQR-s performance to other spanwise disturbances and Reynolds numbers. In these studies, we will design the controller under the assumption of $Re = 3000$ and $(\alpha,\beta) = (0,2)$, but then analyze the response to "off-design" disturbances and Reynolds numbers. We again consider the flow response to an optimal perturbation that results in maximum TEG (G) for the associated closed-loop system.

We first consider the controller robustness to perturbation-wavenumber variations. In figure 4.3a, the LQR and SOF-LQR-s controllers are designed for wavenumber pair $(\alpha,\beta) = (0,2)$ at $Re = 3000$, and the controller is applied at off-design wavenumber conditions of $\alpha = 0$ and $\beta = [1,9]$ at $Re = 3000$. In conducting this study, we observe a remarkable finding: the full-



(a) Controllers designed for $(\alpha, \beta) = (0, 2)$

(b) Controllers designed for $(\alpha, \beta) = (0, 5)$

Figure 4.3: *Robustness of LQR and SOF-LQR controllers to off-design spanwise perturbations at* $Re = 3000$.

information LQR controller results in an unstable closed-loop response for $\beta \geq 2.5$, whereas the SOF-LQR-s maintains comparable performance to the on-design responses as marked by the black crosses. It seems that under spanwise disturbances, the same richness of information that results in superior on-design TEG performance is deleterious to robust performance. In full-information control, modeling uncertainties contaminate the control through many more channels than is possible for the static output feedback case. The fact that the SOF-LQR-s controller leverages only limited information about shear-stress at the walls can limit TEG performance but also lends itself to robustness against modeling uncertainties. We extend this analysis further by considering a controller designed at the on-design condition of $(\alpha, \beta) = (0, 5)$, then applying it over the same set of off-design wavenumbers (see figure 4.3b). Interestingly, the full-information LQR controller exhibits robust performance when applied to off-design conditions with spanwise wavenumber less than the on-design value (i.e., $\beta \leq 5$). However, when applied to mitigate spanwise disturbances at off-design wavenumbers larger than the on-design wavenumber (i.e., $\beta > 5$), even the closed-loop stability of the same full-information LQR controllers is lost.

Next, we consider controller performance at off-design Reynolds numbers, keeping the disturbance wavenumber pair at the "on-design" condition. Specifically, the SOF-LQR-s and full-information LQR controllers are designed for $Re = 3000$ with $(\alpha, \beta) = (0, 2)$ for spanwise disturbance. Then the controllers are applied at "off-design" Reynolds numbers in the sub-critical range of $Re = [500, 5500]$ (see Figure 4.4). The lower limit is based on the observations of turbulence onset at $Re = 500$ [102]; the upper limit is chosen to be slightly less than the critical Reynolds number for linear instability, $Re_c = 5772$ [103]. The results in Figure 4.4 indicate that both controllers are able to reduce the maximum TEG at off-design Reynolds numbers. The relative reduction is comparably smaller at lower Re—owing to the low degree of TEG in the uncontrolled flow—and becomes more pronounced at larger Re. These results demonstrate robust control performance to Reynolds number variations in the context of spanwise disturbances.

Nonlinear direct numerical simulation

Nonlinear direct numerical simulations (DNS) are performed under the optimal disturbance associated with Reynolds number $Re = 3000$ and wavenumber pair $(\alpha, \beta) = (0, 2)$. We start the

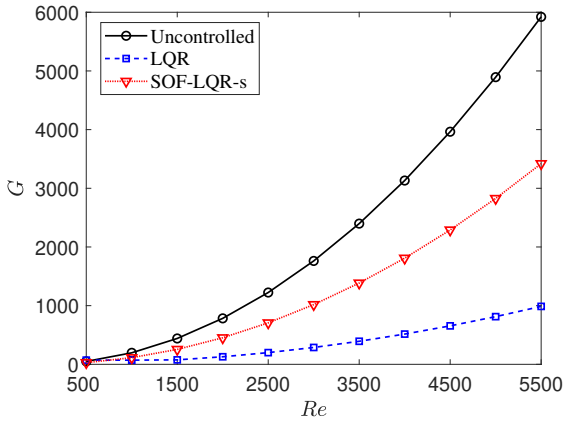


Figure 4.4: *Robustness of LQR and SOF-LQR-s controllers to off-design Reynolds numbers. Both controllers are designed for* $Re = 3000$ *and* $(\alpha, \beta) = (0, 2)$*, but robustly reduce TEG from spanwise optimal perturbations over a range of off-design Reynolds numbers.*

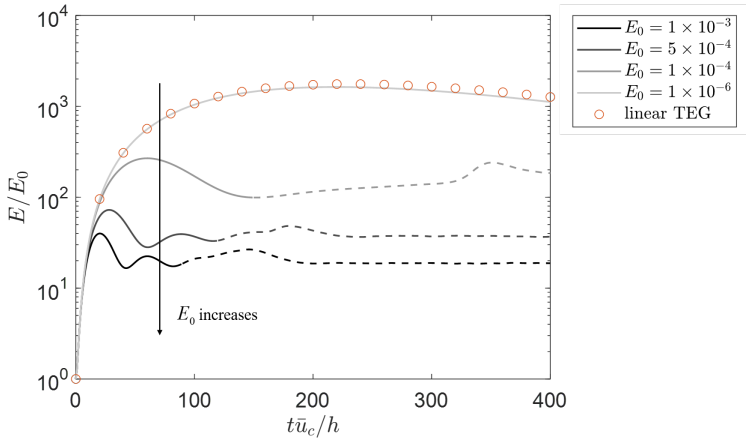


Figure 4.5: *[Transient energy growth of optimal disturbance* $(\alpha, \beta) = (0, 2)$ *in uncontrolled flow with various amplitudes of* E_0*. Dashed lines represent turbulence regime.]*

nonlinear simulation by initializing the flow field with the base flow and the optimal disturbance resulting from the linear analysis. The amplitude of the perturbation's kinetic energy density E_0 is implemented over the range from 1×10^{-6} to 1×10^{-3}. The smallest amplitude of the kinetic energy density of disturbance $E_0 = 1 \times 10^{-6}$ considered overlaps the linear result, as shown in figure 4.5. To trigger laminar-to-turbulent transition, a random perturbation of 1% of E_0 is added to the optimal disturbance. The nonlinear effects are illustrated by reporting the normalized perturbation energy E/E_0. For the spanwise disturbance, as shown in figure 4.5, the uncontrolled flow undergoes a laminar-to-turbulent transition for kinetic energy density at and above the threshold of $E_0 = 1 \times 10^{-4}$.

In figure 4.6, we illustrate the sub-critical transition from laminar to turbulent state for the uncontrolled and controlled cases with $E_0 = 1 \times 10^{-4}$. The energy response of the uncontrolled case (black solid line) and the SOF-LQR-s controlled case (red dotted line) exhibit a similar trend. Transient energy growth reaches a peak value around $t\bar{u}_c/h = 60$, then decays until E/E_0 reaches

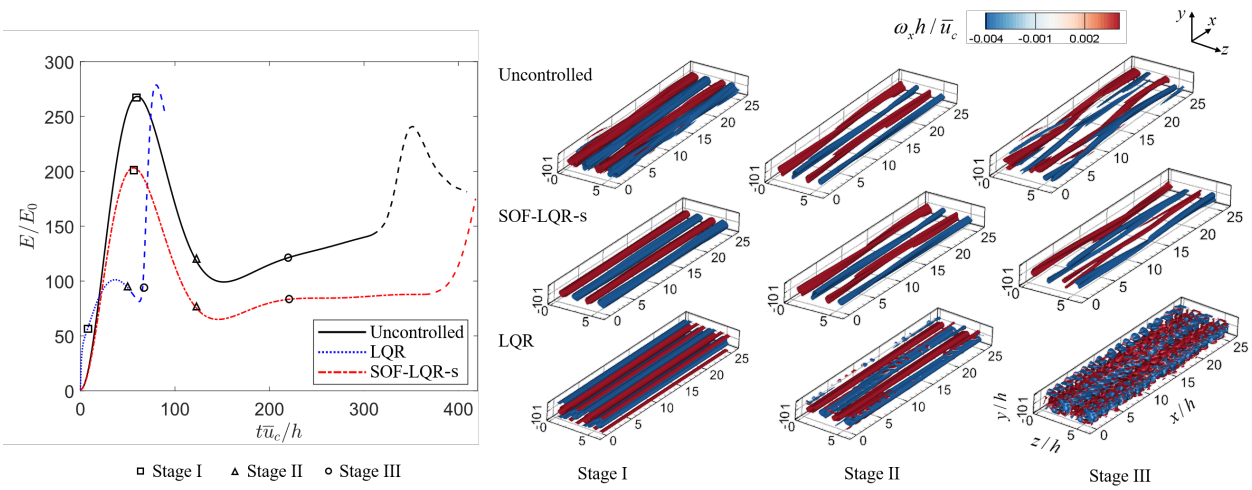


Figure 4.6: *[Transient energy growth of uncontrolled and controlled flows due to linear optimal perturbations of $E_0 = 1 \times 10^{-4}$. Inserts correspond to iso-surfaces of Q-criterion [70] ($Q(h/\bar{u}_c)^2 = 4 \times 10^{-4}$) colored by streamwise vorticity $\omega_x h/\bar{u}_c$.Dashed lines represent turbulence regime.]*

approximately 40% (uncontrolled) and 30% (SOF-LQR-s) of its maximum value. During this process ($0 \leq t\bar{u}_c/h \lessapprox 130$), the SOF-LQR-s continuously shows a lower magnitude of E/E_0 compared to the uncontrolled flow. Additionally, the SOF-LQR-s controller delays the secondary increase in E/E_0 from $t\bar{u}_c/h \approx 300$ in the uncontrolled case to $t\bar{u}_c/h \approx 400$. This secondary increase in perturbation energy in both cases corresponds to a laminar-to-turbulent transition. Thus, it is evident that the SOF-LQR-s controller delays transition relative to the uncontrolled flow. In contrast, the LQR controlled flow (blue dashed line) reaches a comparably lower maximum TEG value earlier in time, but the system is quickly destabilized, and the flow transitions to turbulence. From the energy responses alone, we can expect for the SOF-LQR-s to delay the laminar-to-turbulent transition, and for the LQR control to promote instability and expedite transition relative to the uncontrolled flow.

To better understand the laminar-to-turbulent transition mechanism, we examine the features of the flow field and divide the entire transition process for each case into several characteristic stages as shown in figure 4.6 (right). Representative stages in the flow evolution are marked as stage I, II and III. For each stage, the flow snapshot is taken at the same time step for the uncontrolled and the SOF-LQR-s cases. For the LQR case, due to a much earlier transition, the flow field slices are reported for the same stages, but at different time steps. In all three cases, the initial flow perturbation exhibits streamwise coherent structures. For both the uncontrolled and SOF-LQR-s cases, the flow field remains uniform in the streamwise direction in stage I, and then gradually undergoes spatial distortion after the peak in the kinetic energy density, entering into stage II. Shortly after, rotations start to appear around the streamwise vortical structures with comparable scale to the streamwise domain length. Meanwhile, the kinetic energy density of the flow increases again, initiating stage III, in which the large structures break down and smaller structures can be observed in the flow. After a short duration, the flow transitions into a turbulent state with a rapid increase in E/E_0. With a similar transition mechanism as the uncontrolled case, the SOF-LQR-s controlled case displays all the three stages of laminar-to-turbulent transition, but their emergence

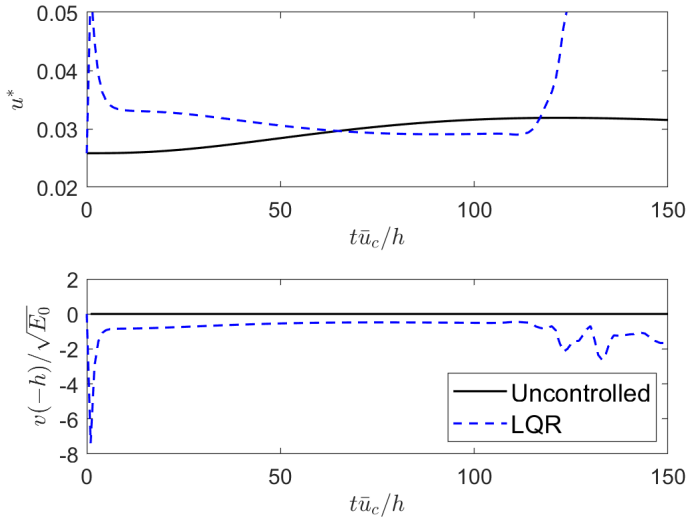


Figure 4.7: *DNS of the uncontrolled flow and the full-information LQR controlled flow with* $(\alpha, \beta) = (0, 2)$*,* $Re = 3000$*, and* $E_0 = 5 \times 10^{-5}$*. (Top) Friction velocity and (Bottom) normalized wall-normal velocity* $v(-h)/\sqrt{E_0}$ *at the lower channel wall with* $x = 0$*,* $z = 0$*.*

is delayed relative to the uncontrolled case. When the break-down of large structures is observed in the uncontrolled flow, the streamwise vortical structures remain in the SOF-LQR-s as shown at stage III. Hence, the SOF-LQR-s controlled flow results in a delay of the transition. The LQR case encounters flow transition with different stages compared to the uncontrolled and the SOF-LQR-s cases. In stage I, the streamwise vortical structures are generated by both the optimal disturbance and the actuation. A short duration after stage I, secondary instabilities grow in proximity to the walls. The instabilities continuously grow, forming small structures as shown in stage II and later. As time progresses, the small structures become irregular and drive the flow to transition to turbulence, as shown in stage III. A second increase in E/E_0 is also observed around $t\bar{u}_c/h = 70$.

To examine the transition phenomenon further, we note that a sudden increase in friction velocity u^* has been used as evidence for transition in channel flow, since turbulent boundary layers tend to have larger shear-stress at the walls than laminar ones. The friction velocity is defined as,

$$u^* = \sqrt{\frac{\tau_w}{\rho}}, \tag{4.20}$$

where τ_w is the wall shear-stress, and ρ is the density of the fluid. The transition events in the uncontrolled and controlled flows are illustrated by a sharp increase of the friction velocity u^* as shown in figures 4.7 and 4.8. Interestingly, although the LQR controller reduces TEG to a great extent, it causes a decrease in the transition threshold. As shown in figure 4.7, the uncontrolled flow stays in the laminar regime with $E_0 = 5 \times 10^{-5}$ when the LQR controlled flow has already transitioned to turbulence. The LQR controller gives rise to an initial peak of the friction velocity and a sudden drop in the normalized lower wall velocity. This is due to the relatively high control input introduced by the LQR controller, which also relates to the earlier onset of transition in this case, as will be discussed in detail momentarily. In contrast, with less reduction in the TEG, the SOF-LQR-s controller delays the laminar-to-turbulent transition compared to the uncontrolled flow, as shown in figure 4.8. The delay is more significant under lower kinetic energy density

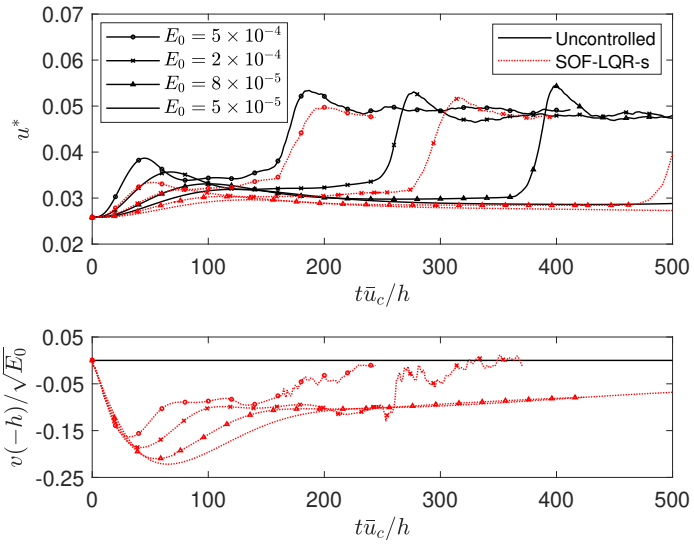


Figure 4.8: *DNS of the uncontrolled flow and the SOF-LQR-s controlled flow with* $(\alpha, \beta) = (0, 2)$*,* $Re = 3000$*, and various perturbation amplitudes* E_0*. (Top) Friction velocity and (Bottom) normalized wall-normal velocity* $v(-h)/\sqrt{E_0}$ *at the lower channel wall* $x = 0$*,* $z = 0$*.*

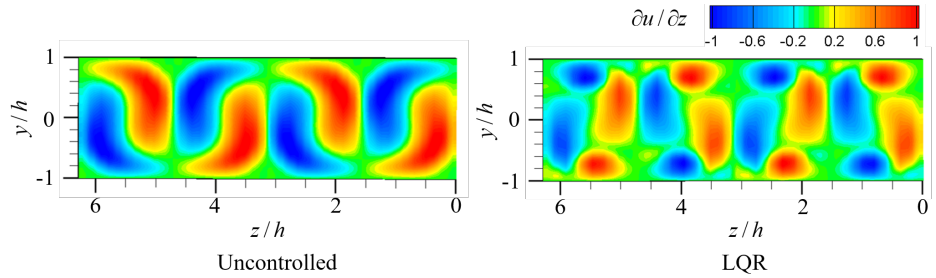
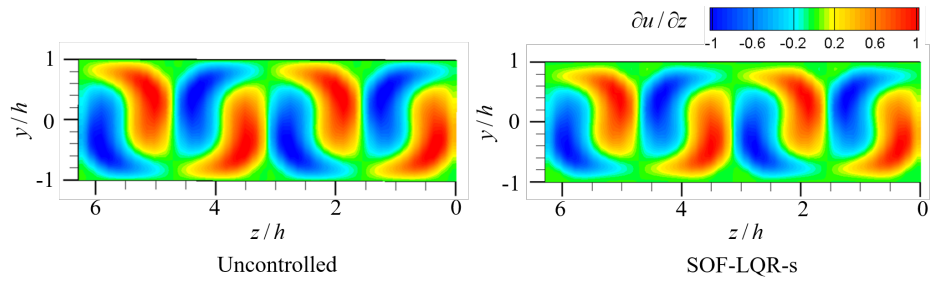


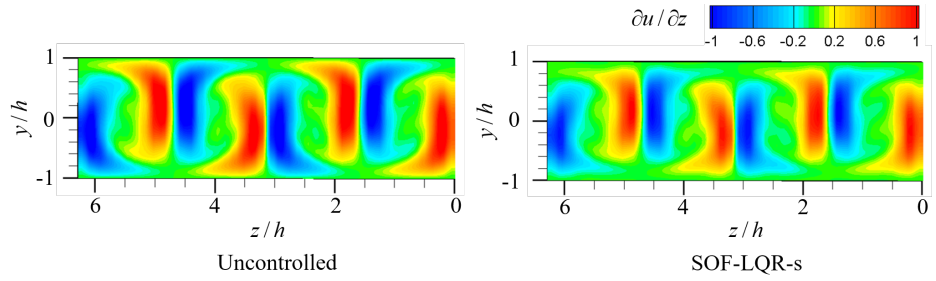
Figure 4.9: *Comparison between uncontrolled flow (left) and LQR controlled flow (right) with* $(\alpha, \beta) = (0,2)$*,* $Re = 3000$*. Modification of instantaneous streamwise velocity gradient in spanwise direction* $\partial u/\partial z$ *at* $t\bar{u}_c/h = 49$*,* x/h*=0.m*

amplitudes. Moreover, although transition still arises in the controlled flow, the friction velocity is significantly reduced compared to the uncontrolled flow, which ultimately yields a drag reduction in the controlled flow. The control input generated by the SOF-LQR-s has a similar trend as the normalized lower wall velocity history. Compared to the LQR case, the SOF-LQR-s control input is much smaller and avoids rapid changes, which benefits the delaying of transition.

From the observations above, it appears that the onset of transition cannot be reliably determined from an examination of the TEG alone. Consider that the LQR reduces TEG to less than a quarter of the TEG for the uncontrolled flow. Yet, the LQR controller drives the flow to transition even earlier than the baseline uncontrolled case. This phenomenon has been closely examined in our previous study [80]. As shown in figure 4.9, the actuation introduced by the LQR controller forms small-scale streamwise vortices near the walls and suppresses transient energy growth by weakening the growth of the large streamwise vortical structures in the uncontrolled flow. However, the generation of extra high-shear regions introduces secondary instabilities and drives the flow to transition. Comparably, the SOF-LQR-s reduces TEG to about half of the baseline case. The



(a) Slice at $t\bar{u}_c/h = 49$, $x/h = 0$



(b) Slice at $t\bar{u}_c/h = 120$, $x/h = 0$

Figure 4.10: *Comparison between uncontrolled flow (left) and SOF-LQR-s controlled flow (right) with* $(\alpha,\beta) = (0,2)$, $Re = 3000$. *Modification of instantaneous streamwise velocity gradient in spanwise direction* $\partial u/\partial z$ *at* $t\bar{u}_c/h = 49$, $x/h = 0$ *(a) and* $t\bar{u}_c/h = 120$, $x/h = 0$ *(b).*

reduction is less than what is achieved by the LQR control; however, this is sufficient to successfully delay the transition. By considering slices of the flow field (see figure 4.10), it becomes apparent that the SOF-LQR-s does not change the shape of the coherent structures, but does shrink their size and reduce the shear-stress amplitude. Notably, it decreases the magnitude of the shear-stress in the vicinity of the walls. This is more clearly observed in the later stages (e.g., $t\bar{u}_c/h = 120$ in figure 4.10b). Also, while limiting the size of coherent structure, the control input is not so large as generate additional small-scale vortices near the walls, in contrast to the LQR control case. Thus, we observe both TEG reduction and transition delay in the SOF-LQR-s controlled flow.

Note that for controller design in this study, we have opted to design the LQR and SOF-LQR-s without penalization on the control inputs. That is, the weighting matrix R in (6.12) and (4.8) is chosen to be small ($R = 1\times10^{-6}I$) in order to achieve the best regulation possible without regard for the control effort. However, considering that the enhanced transition mechanism in LQR control is due to the heavy-handed actuation, we can modify the design objective to penalize the control input for achieving improved nonlinear transition performance. Indeed, it is possible to design the LQR controller to regulate the flow while preventing the appearance of additional large-shear areas near the walls, which are otherwise introduced by the control input. This would be done by sacrificing the large TEG reduction for a more moderate reduction. As such, the results above do not suggest that the full-state feedback LQR will always fail for transition control. Rather, we include these results to emphasize that the "right" objective for transition control must strike a balance between reducing TEG and avoiding secondary instabilities caused by the control input.

4.4.2 Streamwise disturbances

Linear analysis

For streamwise disturbances $(\alpha,\beta) = (1,0)$, we investigate SOF-LQR control using sensor configuration "sp" (i.e. $\tilde{\tau}_x, \tilde{\tau}_z, \tilde{p}$) as outlined in Table 4.1. Although not reported here, SOF-LQR-s controllers—using only $\tilde{\tau}_x$ and $\tilde{\tau}_z$ sensors for feedback—were found to increase the maximum TEG arising from streamwise optimal disturbances. The inclusion of pressure information along with the shear-stress sensors (i.e., configuration "sp") was found to be important for TEG suppression. In the linear simulations of the worst-case response for $(\alpha,\beta) = (1,0)$ and $Re = 3000$ (see Figure 4.11), the full-information LQR controller (dashed blue line) reduces the maximum TEG (G) by 76% relative to the uncontrolled flow (black solid line). The SOF-LQR-sp controller also reduces the maximum TEG relative to the uncontrolled flow by 41%.

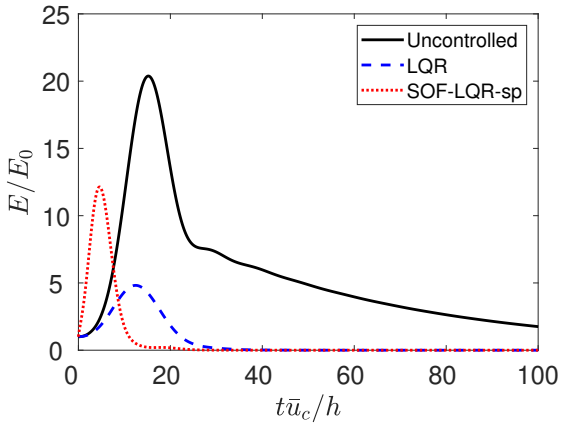
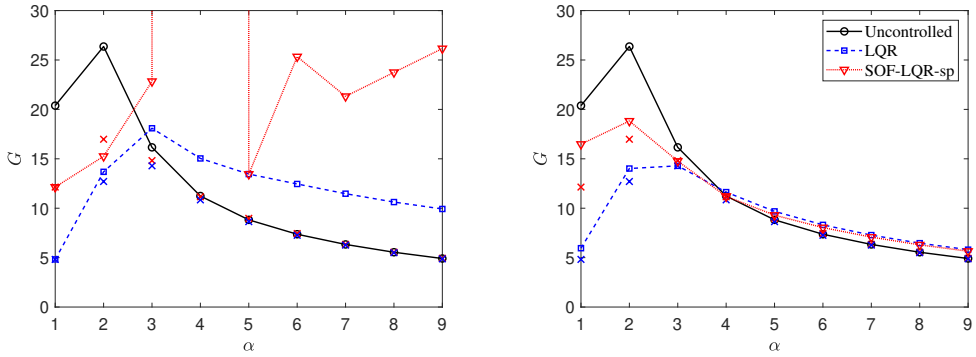


Figure 4.11: *Linear worst-case response to streamwise optimal perturbations with* $(\alpha,\beta) = (1,0)$ *and* $Re = 3000$.

Next, we consider the robust performance of SOF-LQR controllers at off-design conditions. As with the case of robust control of spanwise disturbances, we will see that the choice of on-design conditions can have a remarkable impact on robust control performance. We begin by considering controllers designed for the on-design condition of $(\alpha,\beta) = (1,0)$ and $Re = 3000$, then apply these controllers to streamwise optimal disturbances at off-design conditions with $\alpha = [1,9]$, $\beta = 0$, and $Re = 3000$ (see Figure 4.12a). The SOF-LQR-sp controller designed at on-design condition guarantees closed-loop stability for off-design perturbations, except when subjected to optimal streamwise perturbations with $\alpha = 4$. Nonetheless, the robust performance characteristics of SOF-LQR-sp with regards to TEG at other off-design streamwise wavenumbers tends to be larger than that of the uncontrolled flow. This is also true for the full-information LQR controller when subjected to off-design streamwise disturbances, but to a lesser degree than SOF-LQR controller.

Based on the analysis above, it seems that SOF-LQR strategies lack robustness to off-design conditions; however, this is not necessarily the case. Consider controllers designed at the on-design condition of $(\alpha,\beta) = (3,0)$ and $Re = 3000$ (see Figure 4.12b). In this case, all of the TEG control strategies exhibit robust performance when subjected to off-design streamwise optimal disturbances. When subjected to off-design streamwise disturbances with $\alpha > 3$, the full-information LQR and SOF-LQR-sp controllers result in a (moderately) larger TEG than the uncontrolled flow. Further,



(a) Controllers designed for $(\alpha,\beta) = (1,0)$

(b) Controllers designed for $(\alpha,\beta) = (3,0)$

Figure 4.12: *Robustness of LQR and SOF-LQR controllers to off-design streamwise perturbations at* $Re = 3000$.

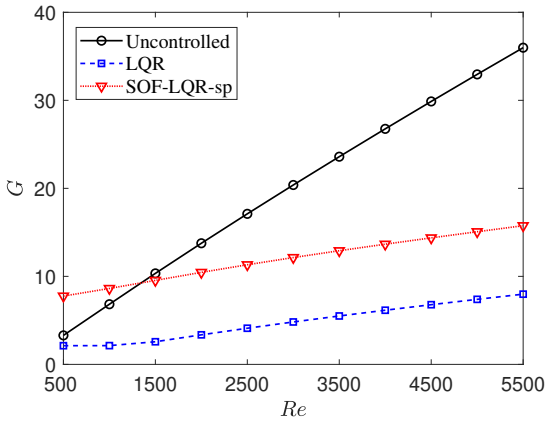


Figure 4.13: *Robustness of LQR and SOF-LQR controllers to off-design Reynolds numbers. Both controllers are designed for* $Re = 3000$*, but robustly reduce TEG from streamwise optimal perturbations over a range of off-design Reynolds numbers.*

when subjected to off-design streamwise disturbances with $\alpha < 3$, the full-information LQR and SOF-LQR-sp controllers have moderately larger TEG than what would be achieved by designing the respective controllers for these specific disturbances (marked as crosses). For mitigation of TEG due to streamwise disturbances, we observe a similar phenomenon as in the spanwise disturbance mitigation scenario: Controllers designed for higher streamwise wavenumber disturbances exhibit better robustness properties. These controllers yield linear stable closed-loop dynamics at off-design streamwise wavenumbers lower than the on-design one, and to a larger range of off-design streamwise wavenumbers above the on-design one (i.e., robust stability). However, off-design TEG performance tends to be degraded when subjected to higher wavenumber disturbances (i.e., robust performance), but this can be avoided with the choice of on-design condition. This analysis suggests that on-design conditions for controller synthesis are important to robust TEG control, both for full-information and sensor-based output feedback strategies.

We additionally assess streamwise controller robustness to Reynolds number variations. To

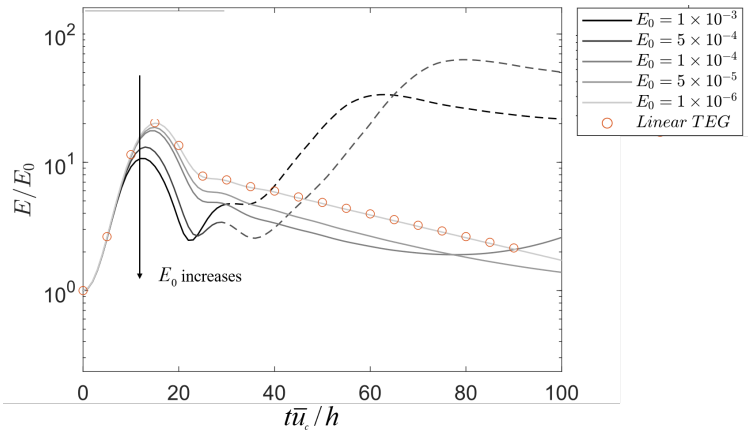


Figure 4.14: *[$(\alpha,\beta) = (1,0)$ transient energy growth of optimal disturbance in uncontrolled flow with various amplitudes of E_0. Dashed lines represent turbulence regime.]*

do so, we again consider $(\alpha,\beta) = (1,0)$ and $Re = 3000$ as the on-design condition, then apply the resulting controllers at "off-design" sub-critical Reynolds number conditions in the range, $Re = [500, 5500]$ (see Figure 4.13). For off-design $Re \geq 1500$, the full-information LQR controller and SOF-LQR controller reduce TEG relative to the uncontrolled flow. At lower off-design Re, the SOF-LQR controller gives rise to moderately higher TEG than without control at $Re < 1500$.

Nonlinear direct numerical simulation

Direct numerical simulations are performed under the linear optimal streamwise disturbance with $(\alpha,\beta) = (1,0)$ and $Re = 3000$. Results in figure 4.14 show that when the kinetic energy density amplitude is $E_0 = 1 \times 10^{-6}$, the nonlinear flow response overlaps with the linear result (see red circles). The uncontrolled flow transitions to turbulence at an amplitude threshold of $E_0 = 1 \times 10^{-4}$, as shown in figure 4.14. In figure 4.15, we report the results for the uncontrolled flow and the controlled flow in response to linear optimal disturbances with $E_0 = 1 \times 10^{-4}$. The flow fields at different time stages illustrate the transition mechanism in the uncontrolled flow and the transition suppression mechanisms in the controlled flows. In figure 4.15, representative stages are marked on the energy plot on the left with the corresponding flow fields illustrated on the right. Stages I and II correspond to the time that E/E_0 reaches its peak and when E/E_0 decays after this peak, respectively. The uncontrolled and LQR flow snapshots for stages I and II correspond to the same convective times. The SOF-LQR-sp stages arise at different times due to an earlier appearance of the E/E_0 peak. Stage III corresponds to transition to turbulence (uncontrolled), or to the return to the laminar regime (controlled).

As shown in figure 4.15 on the left, the uncontrolled flow reaches a maximum transient energy growth of $E/E_0 \approx 17$ at $t\bar{u}_c/h \approx 15$. For the controlled cases, the full-information LQR controlled flow reaches maximum transient energy growth around a similar time, but with a reduced amplitude of $E/E_0 \approx 5$. The representative flow fields show that the initial optimal streamwise disturbance grows into large-scale spanwise coherent structures. In the uncontrolled flow, streamwise vorticity increases near the channel walls, leading to the formation of Λ-shaped structures (dash-square highlighted in stage III) and a transition to turbulence shortly after. In the full-information LQR controlled flow, the spanwise coherent structures remain separate from stage I to II. Although high-shear regions can be observed in stage II, these large structures quickly decay and break-down into smaller isolated structures in stage III. These small structures eventually decay completely,

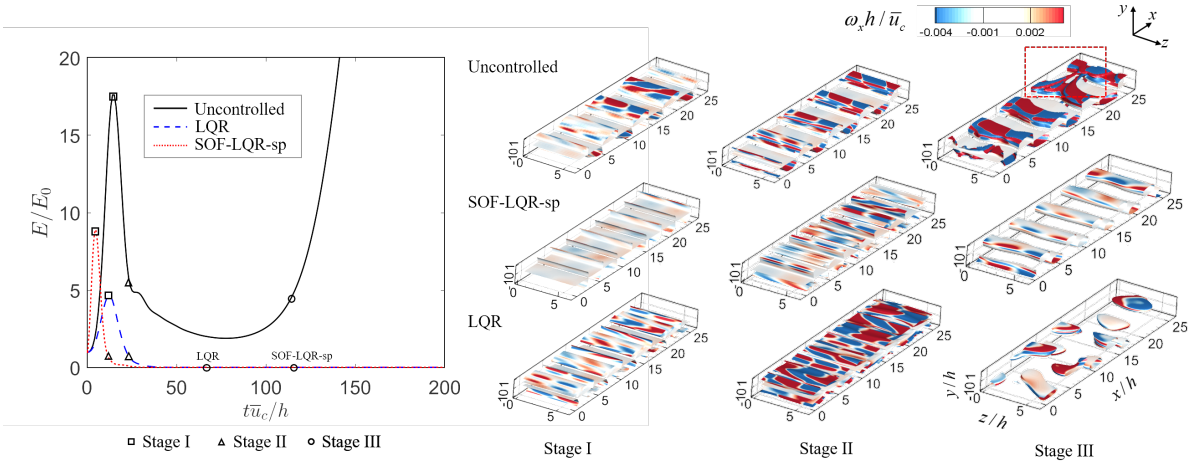
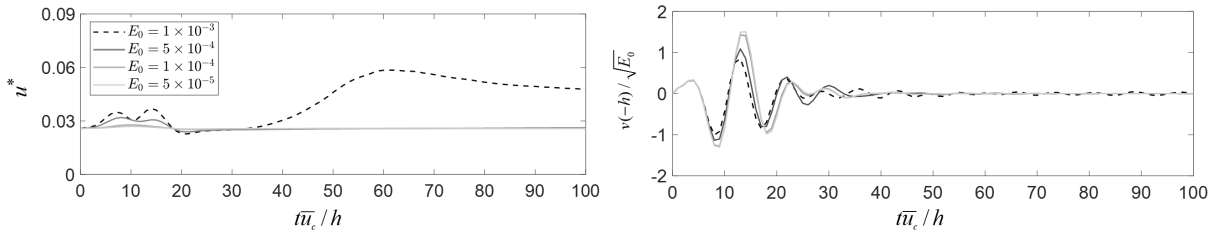


Figure 4.15: *Transient energy growth energy and friction velocity on walls of uncontrolled flow ($E_0 = 1{\times}10^{-4}$). Inserts are corresponding iso-surface of Q-criterion [70] ($Q(h/\bar{u}_c)^2 = 1{\times}10^{-4}$) colored by streamwise vorticity $\omega_x h/\bar{u}_c$.*

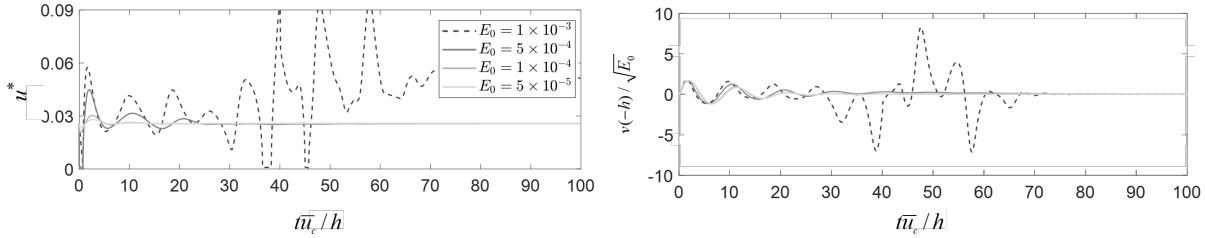
and the flow remains laminar. In the SOF-LQR-sp controlled flow, the maximum transient energy growth occurs at an earlier time than under full-information LQR control. For SOF-LQR-sp, the maximum transient energy growth reaches $E/E_0 \approx 9$ at $t\bar{u}_c/h \approx 5$. The transition suppression scenarios are demonstrated by flow fields. The spanwise coherent structures that evolve out of the optimal streamwise disturbance persist until a later stage than for the full-information LQR controlled case. From stage I to stage III, the spanwise coherent structures decay while remaining intact, not breaking apart as in the case of full-information LQR control. The streamwise vorticity magnitude also tends to be smaller compared to either the uncontrolled flow or the full-information LQR controlled flow. The large spanwise coherent structures in SOF-LQR-sp persist for a longer time compared to the full-information LQR case, but do ultimately fully decay. However, the SOF-LQR control is able to prevent the formation of Λ-structures that would cause the spanwise coherent structures to merge, and thus successfully suppresses transition to turbulence.

The time-histories of friction velocity and normalized wall-normal velocity at the lower wall for the uncontrolled and controlled flows are shown in figure 4.16. By analyzing different perturbation amplitude levels, we see that the full-information LQR controller increases the transition threshold from $E_0 = 1 \times 10^{-4}$ of the uncontrolled flow to $E_0 = 1 \times 10^{-3}$, as shown in figure 4.16 and as reported in our previous work [80]. The SOF-LQR-sp controller also increases the transition threshold to $E_0 = 1 \times 10^{-3}$. Although all controllers increase the transition threshold, we again point out that TEG reduction is not a reliable predictor of transition control performance. However, based on TEG reduction performance alone, one would expect the full-information LQR controller to exhibit a better transition control performance. Yet, this is not the case that we observe in nonlinear simulations with the given controller designs.

All the controllers modify the uncontrolled flow features through wall normal actuation. The actuated wall-normal velocity histories are shown in figure 4.16 (on the right). The controllers generate large actuation to suppress TEG over a relatively short transient time-horizon of $0 < t\bar{u}_c/h < 30$. For the small amplitude disturbances, when the controller is able to reduce the TEG as well as suppress transition, the actuation gradually settles to zero. When facing the large



(a) LQR

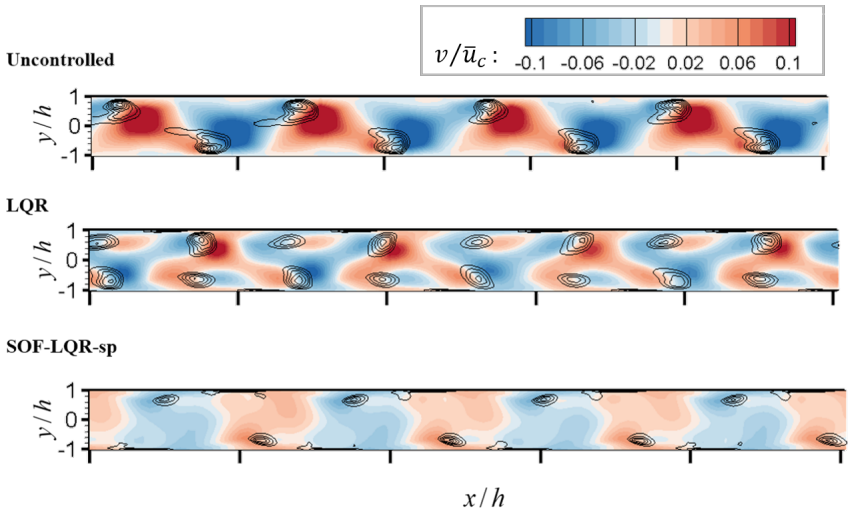


(b) SOF-LQR-sp

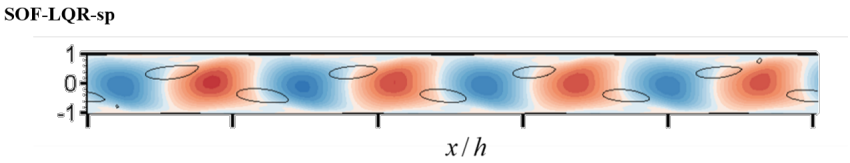
Figure 4.16: *DNS of the uncontrolled flow and the controlled flow with* $(\alpha, \beta) = (1, 0)$*,* $Re = 3000$*, and various perturbation amplitudes* E_0*. (Left) Friction velocity and (Right) normalized wall-normal velocity* $v(-h)/\sqrt{E_0}$ *at the lower channel wall.*

amplitude disturbances, the actuation fails to prevent the flow from transitioning to turbulence, and so the actuation will oscillate for a longer time associated with the disturbance phase speed and wavenumber [80]. In figure 4.17, we present x-y slices of the uncontrolled and the controlled flow fields along with coherent structures visualized using the Q-criterion. The first group of slices is extracted at convective time $t\bar{u}_c/h = 10$, as shown in figure 4.17a. At this time, both the uncontrolled flow and LQR controlled flow reach a maximum E/E_0. Since the SOF-LQR controller reaches the E/E_0 peak at an earlier time, we additionally take a slice from the SOF-LQR-sp controller at $t\bar{u}_c/h = 3$, as shown in figure 4.17b. Compared to the uncontrolled flow, the controller decreases the wall-normal velocity and limit the size of the coherent structures when the normalized perturbation kinetic energy density reaches its peak value. This reduction also decreases the likelihood for break-down of streamwise vortical structures caused by the large spanwise coherent structures discussed in the context of figure 4.15. As a result, the controllers are able to successfully delay or prevent laminar-to-turbulent transition.

As noted earlier, even though the full-information LQR controller yields superior performance for TEG reduction, comparable transition threshold is actually provided by the SOF-LQR-sp controller. A comparison of the flow field slices reveals that SOF-LQR-sp controller reduce velocity fluctuations and growth of large coherent structures to a greater extent than the full-information LQR controller. From this analysis, we see that the reduction of the linear TEG is useful in guiding controller design, but is not the only metric that should be used when considering laminar-to-turbulent transition control.



(a) Slices at convective time $t\bar{u}_c/h = 10$ for uncontrolled and controlled flow



(b) Slice at convective time $t\bar{u}_c/h = 3$ for SOF-LQR controller

Figure 4.17: *Flow fields of* $(\alpha, \beta) = (1, 0)$ *with* $E_0 = 1 \times 10^{-3}$ *for uncontrolled and controlled flow. Contours are wall-normal velocity, and black contour lines denotes* Q*-criterion in a range of* $[0.05,\ 1]$.

4.5 Conclusion

In this chapter, we investigated SOF-LQR controllers for reducing transient energy growth (TEG) of flow perturbations in a channel flow with wall-based sensing and actuation. Control was achieved using wall-normal blowing and suction actuation. Two wall-based sensor combinations were investigated, including shear-stress and pressure. SOF-LQR controllers were designed using an Anderson-Moore algorithm. These computations were accelerated by leveraging Armijo-type adaptations to reduce the iteration count and expedite calculations.

SOF-LQR controllers were found to reduce the worst-case TEG relative to the uncontrolled flow in linear simulations. Spanwise perturbations are associated with the largest levels of TEG for the linearized channel flow, and TEG reduction can be achieved using shear-stress measurements alone. The designed SOF-LQR controllers were found to reduce TEG under streamwise perturbations with shear-stress and pressure measurements. All SOF-LQR controllers investigated here exhibited robustness to Reynolds number uncertainties. Robustness to wavenumber uncertainties was also evaluated. We found that designing SOF-LQR controllers at a proper on-design condition enabled robust performance to these modeling uncertainties at off-design conditions based on linear worst-case analysis.

In nonlinear direct numerical simulations, SOF-LQR controllers were also found to suppress and delay transition to turbulence, increasing transition thresholds relative to the uncontrolled flow. For spanwise disturbances, SOF-LQR control was found to delay transition relative to the uncontrolled flow. In the case of streamwise disturbances, SOF-LQR control suppressed transition and increased the transition threshold for the uncontrolled flow by up to two orders of magnitude. The results show that SOF-LQR controllers provide a simple and reliable alternative to other sensor-based output feedback control strategies for TEG reduction and transition control. The encouraging results presented here motivate further investigation of static output feedback control in more complex flows in the future. In Chapter 6, we will show that a judicious choice of sensors enables SOF controllers to recover full-information control performance. In fact, an appropriate set of sensors can be determined using one of two sensor selection algorithms developed during this research effort. These are presented in Chapter 6

5 | Control-Oriented Model Reduction

A linear nonmodal mechanism for transient amplification of perturbation energy is known to trigger subcritical transition to turbulence in many shear flows. In prior chapters, we consider reducing TEG using relatively simple linear quadratic control strategies. In the present chapter, we consider the problem of *minimizing* the maximum transient energy growth. Feedback control strategies for minimizing this transient energy growth can be formulated as convex optimization problems based on linear matrix inequalities. Unfortunately, solving the requisite linear matrix inequality problem can be computationally prohibitive within the context of high-dimensional fluid flows. This chapter investigates the utility of control-oriented reduced-order models to facilitate the design of feedback flow control strategies that minimize the maximum transient energy growth. An output projection onto proper orthogonal decomposition modes is used to faithfully capture the system energy. Subsequently, a balanced truncation is performed to reduce the state dimension, while preserving the system's input-output properties. The model reduction and control approaches are studied within the context of a linearized channel flow with blowing and suction actuation at the walls. Controller synthesis for this linearized channel flow system becomes tractable through the use of the proposed control-oriented reduced-order models. Further, the resulting controllers are found to reduce the maximum transient energy growth compared with more conventional linear quadratic optimal control strategies Despite the optimality of the resulting control laws, performance is found to be fragile to uncertainties. This make the linear quadratic control approaches more appealing from a practical standpoint, especially given the great care that must be put into constructing reduced-order models and designing optimal (MTEG minimizing) controllers. Materials in this chapter are heavily drawn from [104].

5.1 Introduction

The transition of flows from a laminar to turbulent regime has been extensively studied, and remains a topic of continuing interest. It is well known that turbulent flows exhibit specific detrimental effects on systems, e.g., an increase in skin friction drag in wall-bounded shear flows [44]. It has been observed that transition to turbulence in many shear flows occurs at a Reynolds number (Re) much below the critical Re predicted by linear (modal) stability analysis of a steady laminar base flow [105, 106]. This sub-critical transition is associated with non-modal amplification mechanisms that cause small disturbances to grow before undergoing an eventual modal decay, based on the linear analysis [74, 75]. This transient energy growth (TEG) of disturbances can trigger non-linear instabilities and lead to bypass transition by driving the flow state beyond the region of attraction of the laminar equilibrium profile [75, 107].

Numerous investigations have considered the possibility of reducing TEG and delaying transition by employing feedback control techniques. Excellent reviews of past works can be found

in [32, 55, 108]. Linear quadratic optimal control has been a common approach for such applications. The full-information linear quadratic regulator (LQR) has been investigated in various capacities, and has been shown to increase transition thresholds within the channel flow system [51, 54, 109]. Observer-based output-feedback controllers have also been invoked with some success [51, 52, 110]. In [110], the authors successfully design a linear quadratic Gaussian (LQG) controller on a reduced-order Poiseuille flow system—combining the optimal LQR law with optimal state estimates from a Kalman filter. The study in [51] investigates LQG/$\mathcal{H}_2$ and $\mathcal{H}_\infty$ controllers, with particular emphasis on the use of appropriate transfer function norms to minimize the energy of flow perturbations in a channel flow system. The study in [52] further investigates LQG control of the channel flow system, giving careful attention to the design of the Kalman filter for optimal state estimation for use in observer-based feedback control. More recently, it has been shown that observer-based feedback strategies may exacerbate TEG in the controlled system, due to an adverse coupling between the fluid dynamics and the control system dynamics [85]. As a potential alternative, static output feedback formulations of the LQR problem have shown some promise in overcoming the limitations of LQG strategies under certain flow conditions within the channel flow system [111, 112]. Interestingly, although all of these investigations have shown the promise of feedback control for reducing TEG and delaying transition, it stands that linear quadratic optimal control techniques and related synthesis approaches do not necessarily minimize—nor even reduce—TEG. Indeed, in the case of LQR, the objective function to be minimized is the balance of integrated perturbation energy and input energy—not explicitly the TEG itself. Thus, the most commonly employed controller synthesis approaches aim to achieve an objective that does not necessarily address the TEG problem directly.

Given the central role of TEG and non-modal instabilities in the transition process, it seems that a more appropriate objective function for transition control would be to minimize the maximum transient energy growth (MTEG), as proposed in [88]. This objective has direct connections with notions of *worst-case* or *optimal perturbations*, which correspond to disturbances that result in the maximum TEG [78]. The objective also has connections with optimal forcing functions determined from input-output analysis [56], though these types of "persistent disturbances" will not be considered in the present work. The minimum-MTEG optimal control problem—which can be specified for either full-state or output feedback [88]—can be posed as a linear matrix inequality (LMI). The LMI constitutes a convex optimization problem that can be solved using standard methods, such as interior-point methods [113]. However, the specific LMI problem that arises for MTEG minimization is computationally intractable for high-order systems, such as fluid flows; the memory requirements associated with existing solution methods scale as system order to the sixth power [114].

Despite the computational challenge, control laws that minimize the MTEG can be desirable over linear quadratic optimal control techniques. MTEG-minimizing controllers have been found to outperform LQR controllers in reducing TEG within a channel flow configuration [114]. To achieve this, a modal truncation was performed to obtain a reduced-order model (ROM) that would make controller synthesis tractable for the linearized channel flow system [114]. In spite of the noteworthy performance reported in their study, it is well-established that modal truncation methods tend to yield ROMs that are poorly suited for controller synthesis [57, 115]. (A demonstration of this point is given in Appendix D.) Thus, it may be possible to synthesize MTEG-minimizing controllers with even better performance than those reported in [114] by exploiting an appropriately tailored

control-oriented model reduction strategy.

Various ROM approaches have been studied in the literature (see [116, 117]) for excellent reviews of such techniques within the context of fluid dynamics). However, developing ROMs that facilitate the design of MTEG-minimizing controllers requires a tailored approach. Control-oriented ROMs within this context must address a dual need: (i) approximate the perturbation energy to concisely and adequately describe the energy-based control objective; and (ii) reduce dimensionality to faithfully represent the input-output dynamics, as needed for computationally tractable controller synthesis. Identifying states that contribute substantially to both the perturbation energy and a system's input-output properties (e.g., controllability and observability) is a non-trivial task [118]. A projection onto proper orthogonal decomposition (POD) modes is known to be optimal for capturing the energy of a given signal; however, projection-based model reduction based on POD modes often fails to capture a system's input-output dynamics, making such models poor candidates for controller synthesis [93, 117]. In contrast, balanced truncation can be performed to obtain ROMs that retain a system's input-output properties [119, 120]. The balanced truncation procedure can be shown to be equivalent to a Petrov-Galerkin ROM based on a projection onto a subspace spanned by a reduced set of balanced modes. For high-dimensional fluid flow systems, the balanced POD (BPOD) and related methods provide efficient tools for computing these balanced modes [118, 120, 121]. Alternative control-oriented model reduction techniques can also be devised to retain a system's input-output properties, e.g., using ideas from robust control [57, 120].

The contribution of the present study is to investigate the utility of control-oriented model reduction for designing MTEG-minimizing controllers. The study focuses on full-information control of a linearized channel flow system, but the lessons learned can be generalized to other flows and control architectures as well. The ROMs in this work use POD and balanced truncation in conjunction. First, we perform an output-projection of the full-state onto a set of dominant POD modes. Subsequently, a balanced truncation is performed to reduce the state-dimension, while retaining the most controllable and observable modes that contribute to the input-output dynamics. As we will see, this dual approach results in control-oriented ROMs that can yield effective MTEG-minimizing controllers. The resulting models are able to represent the perturbation energy in terms of a small number of POD modes, thus providing a convenient approximation of the objective function. Further, state-dimension is reduced to a computationally tractable level, while retaining the most controllable and observable states that are critical for effective controller design.

The organization of this chapter is as follows: Section 5.2 summarizes preliminaries on TEG and the relevant controller synthesis strategies, including the synthesis of LQR controllers and the LMI-based synthesis of MTEG-minimizing controllers. The control-oriented model reduction approach is then introduced in Section 5.2.1. Section 5.3 presents all of the results, which are based on the linearized channel flow system described in Section 5.3.1. ROMs are analyzed in an open-loop context in Section 5.3.2. Controller performance of ROM-based controller designs is evaluated in Section 5.3.3, which also includes a comparative analysis of the flow response to LQR and MTEG-minimizing control laws. Finally, Section 5.4 summarizes the findings and contributions of this study.

5.2 Reduced-order models and controller synthesis

Consider the linearized dynamics of flow perturbations $\mathbf{x}(t)$ about a steady laminar base-flow,

$$\dot{\mathbf{x}}(t) = A\mathbf{x}(t) + B\mathbf{u}(t) \tag{5.1}$$

where $\mathbf{x}$ is a vector of n state variables, $\mathbf{u}$ is a vector of p control inputs, and t is time. Specific details on arriving at such a representation for a channel flow setup will be described in Section 5.3.1. The free-response of the system to an initial perturbation $\mathbf{x}(t_o) = \mathbf{x}_o$ at time t_o is given in terms of the matrix exponential $\mathbf{x}(t) = \mathrm{e}^{A(t-t_o)}\mathbf{x}_o$. The perturbation energy for this system is defined as $E(t) := \mathbf{x}^{\mathsf{T}}(t)Q\mathbf{x}(t)$, where $Q = Q^{\mathsf{T}} > 0$. In this study, we are primarily interested in the maximum transient energy growth (MTEG),

$$\Theta_{\max} = \max_{t \geq t_0} \max_{E(t_0) \neq 0} \frac{E(t)}{E(t_0)}, \tag{5.2}$$

which corresponds to the peak energy over all disturbances and all time. The flow perturbation $\mathbf{x}_o^{\mathrm{opt}}$ that results in this MTEG is called the *worst-case disturbance* or the *optimal perturbation* [78].

Owing to the role of transient energy growth in sub-critical transition, our aim here will be to reduce the MTEG using full-information feedback control laws of the form $\mathbf{u}(t) = -K\mathbf{x}(t)$, where K is a gain matrix determined by an appropriate synthesis strategy. In this study, two controller synthesis approaches will be considered: (i) linear quadratic regulation (LQR), and (ii) MTEG minimization via LMI-based synthesis. LQR is an optimal control technique that has been commonly employed in a variety of flow control applications, including transition control. LQR controllers are designed to minimize the integrated balance between perturbation energy and control effort; i.e.,

$$\min_{\mathbf{u}(t)} J = \int_0^\infty (\mathbf{x}^T Q\mathbf{x} + \mathbf{u}^T R\mathbf{u})dt \tag{5.3}$$

subject to the linear dynamic constraint in (5.1) and $R > 0$. The feedback control law that minimizes this cost function is given by $\mathbf{u} = -K\mathbf{x}$, where the control gain $K = R^{-1}B^T P$ and $P = P^{\mathsf{T}} > 0$ is determined from the algebraic Riccati equation,

$$A^T P + PA - PBR^{-1}B^T P + Q = 0. \tag{5.4}$$

LQR is a widely used optimal control strategy owing to properties like guaranteed stability margins and robustness to parameter variations. However, it must be noted that the LQR formulation does not necessarily guarantee reductions in MTEG, let alone its minimization. In principle, a controller that minimizes the balance of integrated energies in (5.3) could still yield large energy peaks.

A state feedback control gain for minimizing the MTEG in a closed-loop system can be found from the solution of a linear matrix inequality (LMI), as shown in [88]. The solution approach leverages the relationship between MTEG and a system's condition number. From this, a control law can be devised to minimize the condition number of the closed-loop system in order to minimize the associated $\Theta_{\max}$. In what follows, it is assumed that an appropriate transformation has been made so that $Q = I$. A feedback control law that minimizes the upper bound Θ_u of the MTEG can be determined from the solution to the LMI generalized eigenvalue problem [88]:

$$\begin{aligned} &\min \gamma \\ \text{subject to} \quad &I \leq P \leq \gamma I \\ &P = P^T > 0 \\ &AP + PA^T + BY + Y^T B^T < 0. \end{aligned} \tag{5.5}$$

This LMI problem can be solved using standard convex optimization methods, such as those available in the cvx software package for Matlab [122]. Here, γ upper bounds Θ_u. Thus, minimizing γ also minimizes Θ_u, which consequently minimizes the upper bound on $\Theta_{\max}$. The resulting full-state feedback control law is given by $\mathbf{u} = -YP^{-1}\mathbf{x}$, where Y and P are determined from (5.5).

Standard solution techniques for the LMI problem in (5.5) are presented in [113]. However, available algorithms are computationally demanding, with memory requirements scaling as $O(n^6)$ [114], making controller synthesis intractable for the high-dimensional systems of interest in flow control. The aim of the present study is to investigate the role of reduced-order models (ROMs) for facilitating controller synthesis by making the solution of this LMI problem tractable. Further, constructing reliable control-oriented ROMs requires consideration of the specific control objective. Since the LQR and MTEG-minimizing controllers to be studied here are based on energy-based control objectives, it stands that approximating the energy $E(t)$ will be an important consideration for reduced-order modeling. Section 5.2.1 presents a method for obtaining control-oriented ROMs for LQR and MTEG-minimizing controller synthesis. Finally, we note that the same types of computational challenges will arise in the nonlinear analysis problems that we will present in Chapter 7. We anticipate the control-oriented ROMs presented here will also be useful in that setting.

5.2.1 Control-oriented reduced-order models

Procedures for generating ROMs often rely upon truncating state variables from the system description, with the details of the truncation procedure varying with the given application. A ROM intended to facilitate controller synthesis should faithfully capture a system's input-output dynamics, motivating the use of techniques such as balanced truncation [119]. On the other hand, within the context of the energy-based control objectives considered in the present study, it will also be important for the ROM to faithfully reproduce the system energy $E(t)$. POD modes have been shown to optimally capture the energy of a given signal [116]. Here, we will combine these two approaches in order to realize ROMs that can facilitate the synthesis of controllers with energy-based control objectives. Similar approaches have been described in the literature [117, 123], but have not been leveraged for LMI-based synthesis of MTEG-minimizing controllers. In Appendix D, we demonstrate the need for tailored ROMs that favor control design.

The basic idea underlying the ROMs proposed here is to first append an output equation to (5.1) to keep track of the state response in terms of $r < n$ POD modes,

$$\begin{aligned} \dot{\mathbf{x}} &= A\mathbf{x} + B\mathbf{u} \\ \mathbf{z} &= \Phi_r^T \mathbf{x}. \end{aligned} \tag{5.6}$$

Here, $\mathbf{z} \in \mathbb{R}^r$ is a vector of POD coefficients and $\Phi_r \in \mathbb{R}^{n\times r}$ is a matrix whose columns are the r dominant POD modes, defined with respect to an appropriate inner-product, such that $E(t) \approx \tilde{E}(t) = \mathbf{z}^T(t)\mathbf{z}(t)$. Thus, rather than requiring full-state information to compute energy, only the r-dimensional output of POD coefficients is needed to approximate the energy response. This approach is sometimes described as an output projection onto POD modes, since the output could also be viewed as a projection of the full-state output onto the dominant POD modes [118]. It should be noted that output projection in (5.6) does not change the state dimension n of the model.

To find the POD modes, we use the snapshot POD approach [116]. Through heuristics, we found that POD modes obtained from snapshots of the system's impulse response matrix provided an adequate basis for the projection. Therefore, to compute the POD modes (Φ_r), we obtain

the impulse response $G_i(t)$ from the i^{th} input to the full-state output for each of the p inputs. In generating this data, we first transform the state $\mathbf{x}$ into a coordinate system in which $Q = I$. These impulse response data are then collected and arranged within a single snapshot matrix $H := \begin{bmatrix} G_1(t) & G_2(t) & \cdots & G_p(t) \end{bmatrix}$. The POD modes are then computed by taking the singular value decomposition (SVD) of $H = U\Sigma V^{\mathsf{T}}$. The dominant POD modes are then determined as the leading $r \leq n$ left singular vectors—i.e., $\Phi_r = [\mathbf{u}_1, \mathbf{u}_2, \ldots, \mathbf{u}_r]$, where $\mathbf{u}_i$ are columns $i = 1, \ldots, r$ of U. We note that the POD modes could also be computed analytically, though the data-driven method of snapshots is most commonly used in practice [116]. Thus, important parameters for generating the impulse response data will be the length of the simulation (t_f) and sampling interval (δ_t). We address the specifics of these parameters for ROM construction in Section 5.3.2.

Up to this point, we have shown that the system energy can be approximated using just r POD modes, with the associated POD coefficients tracked as the system output $\mathbf{z}$. However, in order to make the LMI problem for MTEG-minimizing controller synthesis computationally tractable, we still need to reduce the state dimension of the system. In the study here, we will perform a balanced truncation of (5.6) and retain only the dominant s balanced modes. Such a truncation will ensure that the input-output dynamics are preserved, making the resulting s-dimensional ROM suitable for controller synthesis [120]. In order to perform a balanced truncation, we first apply a balancing transformation $\mathbf{x} = T\bar{\mathbf{x}}$. In the *balanced coordinates* $\bar{\mathbf{x}}$, the controllability Gramian $\bar{W}_c$ and the observability Gramian $\bar{W}_o$ are equal and diagonal. To determine the balanced realization, one must first compute the controllability Gramian W_c and observability Gramian W_o from the Lyapunov equations, $AW_c + W_cA^T - BB^T = 0$ and $W_oA + A^TW_o + C^TC = 0$, respectively. Once the Gramians are computed, the balancing transformation $\mathbf{x} = T\bar{\mathbf{x}}$ can be found in three steps [124]: (i) compute the lower triangular Cholesky factorizations of $W_o = L_oL_o^T$ and $W_c = L_cL_c^T$; (ii) compute the SVD of the products of Cholesky factors $L_o^TL_c = \bar{U}S\bar{V}^T$; and (iii) form the balancing transformation $T = L_r\bar{V}S^{\frac{1}{2}}$ and $T^{-1} = S^{\frac{1}{2}}\bar{U}^TL_o^T$.

In balanced coordinates, each mode's relative contribution to the input-output dynamics of the system is clear. We have $\bar{W}_c = \bar{W}_o = \text{diag}(\bar{\sigma}_1, \ldots, \bar{\sigma}_n)$, where $\bar{\sigma}_1 \geq \bar{\sigma}_2 \geq \cdots \geq \bar{\sigma}_n > 0$ are the system's Hankel Singular Values (HSVs). Since the HSVs relay information about relative contributions to the input-output dynamics, truncating balanced modes with "small" HSVs provides a convenient strategy for reducing state-dimension while preserving the input-output dynamics [120]. Upon performing the balanced truncation, the dominant s balanced modes of the system are retained, and the $n - s$ modes corresponding to the lowest HSVs are truncated. The resulting state-space realization is given by,

$$\dot{\bar{\mathbf{x}}}_s = \bar{A}_s\bar{\mathbf{x}}_s + \bar{B}_s\mathbf{u} \tag{5.7}$$

$$\bar{\mathbf{z}}_s = \bar{C}_s\bar{\mathbf{x}}_s \tag{5.8}$$

where $\bar{\mathbf{x}}_s \in R^s$ is the reduced state vector and the system matrices are defined as $\bar{A}_s := T_s^{-1}AT_s$, $\bar{B}_s := T_s^{-1}B$, $\bar{C}_s := \Phi_r^TT_s$. Here, $T_s \in \mathbb{R}^{n\times s}$ denotes a matrix whose s columns are the leading s columns of T, and $T_s^{-1} \in \mathbb{R}^{s\times n}$ denotes a matrix whose s rows are the leading s rows of T^{-1}. Finally, the perturbation energy $E(t)$ can now be approximated from this control-oriented ROM as,

$$\bar{E} = \bar{\mathbf{x}}_s^T\bar{Q}\bar{\mathbf{x}}_s, \tag{5.9}$$

where $\bar{Q} = T_s^T\Phi_r\Phi_r^TT_s \in R^{s\times s}$. In this study, we take $s = r$, and so will solely report r as the dimension of the reduced-order model.

In order to assess feedback control performance with respect to the MTEG that can be experienced in closed-loop, additional care must be taken when computing the optimal disturbances in this study. Since MTEG analysis is to be performed on the full order system, feedback controllers designed using the ROMs described here are first "lifted" to a control gain with compatible dimensions as the full order model. In this way, the optimal disturbance for the full order closed-loop system can be computed directly. Of course, to actually implement the resulting feedback controllers in practice, one would simply use the reduced-order gain matrix to take advantage of the reduced computational complexity at run-time.

The procedure outlined here will enable a means of obtaining control-oriented reduced-order models that can be used to synthesize feedback controllers, especially those aimed at achieving certain energy-based objectives—as with MTEG-minimization. We emphasize that the control-oriented model reduction procedure described here and other similar approaches have been explored in a number of previous studies [53, 118, 119, 121, 123]. The contribution of the present study is to investigate the applicability of such model reduction techniques for the purposes of minimizing the MTEG using the LMI-based synthesis procedure proposed in [54, 88].

5.3 Results

Next, the control-oriented reduced-order modeling approach introduced in the previous section is investigated within the context of controlling TEG in a linearized channel flow. The channel flow system is presented in Section 5.3.1. In Section 5.3.2, the frequency-responses of various ROMs are analyzed to assess open-loop modeling performance. Finally, ROM-based controller performance is investigated in Section 5.3.3, by comparing the MTEG resulting in the closed-loop system response. The associated flow responses are also studied and discussed.

5.3.1 Channel Flow System

Consider the flow between two infinitely long parallel plates separated by a distance of $2h$ (see Figure 5.1). We are interested in the linear evolution of perturbations about a steady laminar base flow $U(y) = U_{cl}\big(1 - \frac{y^2}{h^2}\big)$. Thus, we linearize the Navier-Stokes equations about this base flow, and non-dimensionalize based on the centerline velocity U_{cl} and the channel half-height h. Taking the divergence of the continuity equation and using the y-momentum equation to eliminate the pressure term, we obtain an equivalent representation for the evolution equations, now in terms of the wall-normal velocity (v) and the wall-normal vorticity (η). A Fourier transform is applied in the streamwise and spanwise directions to obtain the well-known Orr-Sommerfeld and Squire equations [44],

$$\begin{aligned} \Delta\dot{\tilde{v}} &= \left[i\alpha U\Delta + i\alpha U'' + \frac{\Delta\Delta}{Re} \right]\tilde{v}, \\ \dot{\tilde{\eta}} &= \left[-i\beta U' \right]\tilde{v} + \left[-i\alpha U + \frac{\Delta}{Re} \right]\tilde{\eta}, \end{aligned} \tag{5.10}$$

where $\Delta = \frac{\delta}{\delta y^2} - \kappa^2$. Here, $\kappa^2 = \alpha^2 + \beta^2$, and (α, β) denotes the pair of streamwise and spanwise wavenumbers, respectively. The no-slip boundary conditions in velocity-vorticity form are $\tilde{v}(y = \pm 1) = \frac{\partial \tilde{v}}{\partial y}\,|_{(y=\pm 1)} = \tilde{\eta} = 0$. The wall-normal direction is discretized using Chebychev polynomials of the first kind [125], allowing $\tilde{v}$ and $\tilde{\eta}$ to be approximated at N discrete collocation points. At each point, the approximation uses Chebychev basis functions Γ_i and the respective unknown coefficients

a_i. The resulting equations of motion can be expressed in the form $\dot{\mathbf{x}} = \mathcal{A}\mathbf{x}$, where $\mathbf{x}$ is a vector of Chebychev coefficients; i.e., $\mathbf{x} = (a_{v_0}, \ldots, a_{v_N}, a_{\eta_0}, \ldots, a_{\eta_N})^T$.

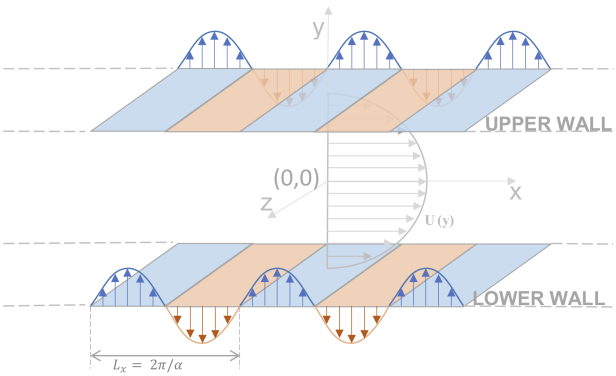


Figure 5.1: *Channel flow setup.*

One of the stages to bypass transition within the channel flow setting is the transient energy growth (TEG) of flow perturbations about the base-flow due to non-modal effects [44]. In accordance with previous studies, we use the kinetic energy density as a measure of this TEG,

$$E(t) = \frac{1}{V}\int_V \rho \frac{u^2 + v^2 + w^2}{2} dV\,, \tag{5.11}$$

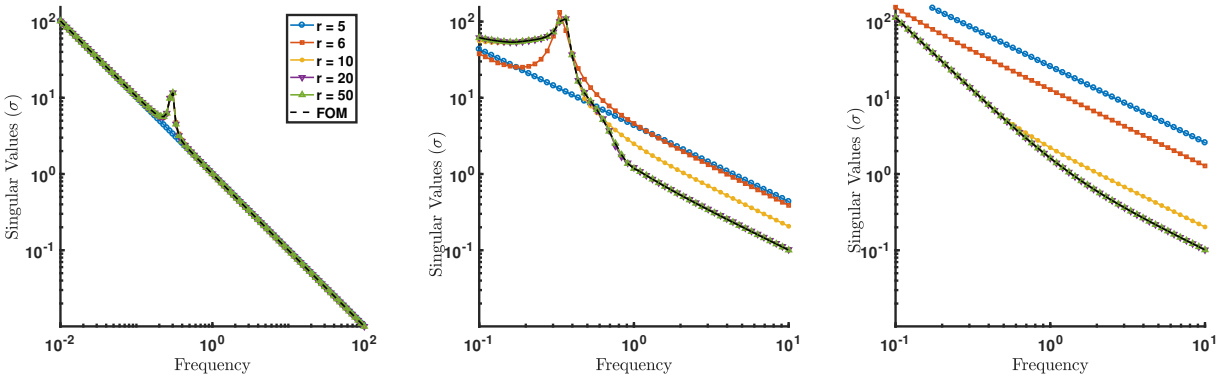
where ρ is the fluid density and V is the volume of a unit streamwise length of channel. In relation to earlier discussions, the kinetic energy density can be re-expressed as $E(t) := \mathbf{x}^T Q \mathbf{x}$, where $Q = Q^T > 0$ [126].

In order to implement flow control, we introduce wall-normal blowing and suction actuation at the upper- and lower-walls—consistent with prior investigations on controlling channel flow [54, 108, 110]. Following the modeling procedure in [127], this can be modeled via the wall-transpiration boundary conditions $\tilde{v}(y = 1) = q_u$, $\tilde{v}(y = -1) = q_l$, $\frac{\partial \tilde{v}}{\partial y}\,|_{y=\pm 1} = 0$. Here, q_u and q_l are wall-normal velocities at the upper- and lower-wall, respectively. The final system formulation uses $\dot{q}_u$ and $\dot{q}_l$ as the control inputs, while reclassifying q_u and q_l as system states. This introduces two integrators—associated with the controls—within the system model. Finally, the actuated channel flow system can be expressed in state-space form, as in (5.1), with the state vector defined as $\mathbf{x} = (a_{v_0}, \ldots, a_{v_N}, a_{\eta_0}, \ldots, a_{\eta_N}, q_u, q_l)^T$ and the input vector defined as $\mathbf{u} = (\dot{q}_u, \dot{q}_l)^T$. It must be noted that the resulting system here is complex-valued, owing to the introduction of Fourier transformations in the streamwise and spanwise directions. As such, a final step is needed to transform the system into an equivalent real-valued state-space realization. Further modeling details can be found in [127].

In the remainder, we consider this linearized channel flow model at a sub-critical Reynolds number of $Re = 3000$ (unless otherwise stated) for three different wavenumber pairs (α, β): $(1, 0)$, $(1, 1)$, and $(0, 2)$. In all cases, the number of collocation points N is chosen so that the resulting state dimension is $n = 199$. The optimal spanwise disturbance to the uncontrolled system with $(\alpha, \beta) = (0, 2)$ yields the largest MTEG among all other streamwise, spanwise, and oblique wavenumber configurations. Hence, this spanwise disturbance is an important case to study for controller performance evaluation; The other two wavenumber pairs considered here have also been widely studied in the literature [52, 54].

5.3.2 Frequency analysis of control-oriented reduced-order models for the channel flow system

Here, we examine how the control-oriented ROMs introduced in Section 5.2.1 approximate the dynamics of the full-order model (FOM) for the linearized channel flow system, for which $n = 199$. Specifically, we examine whether the ROMs developed here capture the input-output behavior of the FOM accurately. In multi-input multi-output (MIMO) systems, the singular values σ of the system's transfer function over various frequencies provide a means of characterizing the input-output behavior of the system. The singular values provide information on the variation in the system's principal gains in any of the p input direction. Here, we investigate these characteristics as a function of ROM order r from the input $\dot{q}_u$ to the flow-state (see Figure 5.2). In this work, the scaled frequency is given by $f^* = ftU_{cl}/h$. The frequency response data reveal that increasing the order r of the ROM decreases the approximation error with respect to the FOM response. Indeed, the trend is more clear from Table 5.1, which summarizes the root mean square error (RMSE) between the ROM and FOM frequency responses. The acceptable accuracy of a ROM in approximating a FOM response is mostly application specific. For the case here, the RMSE metric suggests that ROMs of $r \geq 20$ perform moderately well. Further, even using the higher-order $r = 50$ models—which reflect excellent agreement with the FOM frequency-response—will make LMI-based controller synthesis tractable. The transfer function from input channel $\dot{q}_l$ to the flow-state exhibits similar convergence in the frequency-response.



(a) $\alpha = 1,\ \beta = 0$ **(b)** $\alpha = 1,\ \beta = 1$ **(c)** $\alpha = 0,\ \beta = 2$

Figure 5.2: *Frequency response from $\dot{q}_u$ to the flow-state at $Re = 3000$.*

	$r = 5$	$r = 6$	$r = 10$	$r = 20$	$r = 50$
$\alpha = 1, \beta = 0$	1.079	0.049	0.0033	1.340×10^{-4}	5.726×10^{-6}
$\alpha = 1, \beta = 1$	18.765	14.135	2.990	0.0891	9.603×10^{-5}
$\alpha = 0, \beta = 2$	119.19	61.0560	13.332	1.705	0.0193

Table 5.1: *RMSE between the frequency-response of the FOM ($n = 199$) and the ROM of order r at $Re = 3000$.*

Finally, it should be noted that, for the ROMs presented here, the data-sampling parameters t_f and δ_t in the snapshot POD stage of the ROM-procedure were tuned to ensure convergence of the

ROM response to the FOM response. In the $Re = 3000$ setting, for streamwise waves and oblique waves $\delta_t = 0.01$ and $t_f = 30$ and 50 respectively. While for spanwise waves we use $\delta_t = 1$ and $t_f = 500$ to obtain adequate models. All times reported in this work are non-dimensionalized, and correspond to non-dimensional convective time units $\frac{tU_{cl}}{h}$.

5.3.3 Controller performance

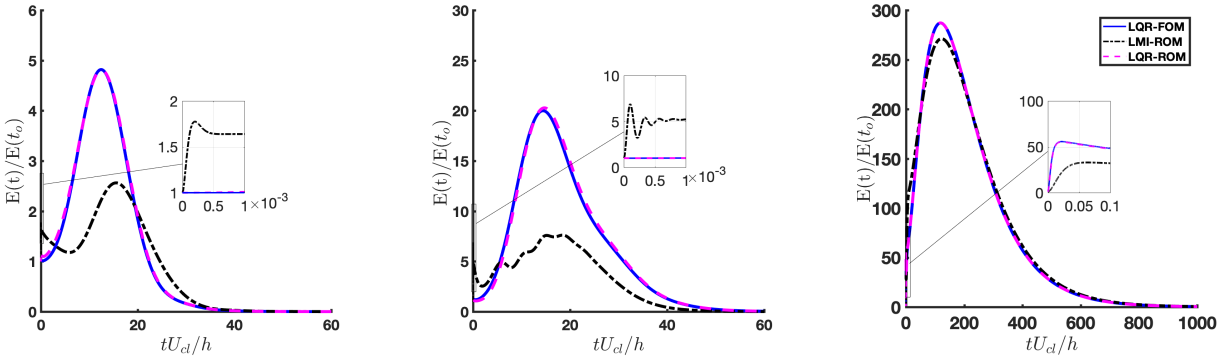
The synthesis of MTEG-minimizing controllers via the solution of the LMI-problem in (5.5) is enabled by the control-oriented ROMs reported in Section 5.3.2 above. The resulting controllers will be referred to as *LMI-ROM controllers* here. For benchmarking, we compare MTEG performance with two sets of LQR controllers—one designed based on the FOM ("LQR-FOM") and one designed based on the same ROM that was used for the LMI-based synthesis ("LQR-ROM"). Additionally, since the MTEG-minimizing controller in the LMI-ROM was designed without constraining the control input, we relax the penalty on the input effort within the LQR cost function in (5.3) by setting $R = 10^{-6}I$, where I denotes the identity matrix. This is done in an effort to make a fair comparison between the LMI-ROM, LQR-ROM, and LQR-FOM controllers. Note, this differs from the approach taken in [114], in which a constrained version of the controller was implemented. All controllers are applied to the full-order channel flow model described in Section 5.3.1 above, then compared based on the MTEG $\Theta_{\max}$ for each respective closed-loop system. In general, the optimal perturbation will differ between each closed-loop system, and will also differ from that of the uncontrolled system. Here we use the optimal perturbation of the respective closed-loop system to perform MTEG analysis. In this study, each optimal perturbation is calculated using the algorithm presented in [128].

As shown in Figure 5.3, the LMI-ROM controller reduces the MTEG in the system relative to each of the LQR-based controllers for each of the wavenumber pairs considered. For $(\alpha, \beta) = (1, 0)$, the LMI-ROM controller reduces $\Theta_{\max}$ by a factor of ≈ 1.88 in comparison with the LQR controllers (see Figure 5.3a). Similarly, the LMI-ROM reduces MTEG by a factor of ≈ 2.6 relative to the LQR controllers for $(\alpha, \beta) = (1, 1)$ (see Figure 5.3b). Finally, for $(\alpha, \beta) = (0, 2)$, the difference in MTEG reduction between the LMI-ROM controller and the LQR controllers is only marginally greater (See Figure 5.3c). This result is consistent with the findings in [114], for which wall-normal blowing/suction was found to be less effective for TEG control than spanwise blowing/suction at the walls. For all controllers and all wavenumber pairs considered here, MTEG was reduced relative to the uncontrolled flow. These results are summarized in Table 5.2.

	r	$\Theta_{\max}$			
		Uncontrolled	LMI-ROM	LQR-FOM	LQR-ROM
$\alpha = 1, \beta = 0$	40	20.31	2.56	4.81	4.81
$\alpha = 1, \beta = 1$	58	107.00	7.58	20	20.28
$\alpha = 0, \beta = 2$	40	1762	271.2	287.1	287.1

Table 5.2: *MTEG Θ_{max} for the uncontrolled and controlled channel flow system at $Re = 3000$.*

Although the LMI-ROM controller outperforms both of the LQR controllers in reducing the MTEG ($\Theta_{\max}$) in the results above, these results depend on the order r of the ROM used for controller synthesis. To investigate this influence, we vary r in the ROM design, then study controller performance on the FOM for streamwise and oblique waves—$(1, 0)$ and $(1, 1)$, respectively—still with $Re = 3000$. We only report values of r for which the open-loop ROMs successfully converge



(a) $\alpha = 1, \beta = 0$ with $r = 40$.

(b) $\alpha = 1, \beta = 1$ with $r = 58$

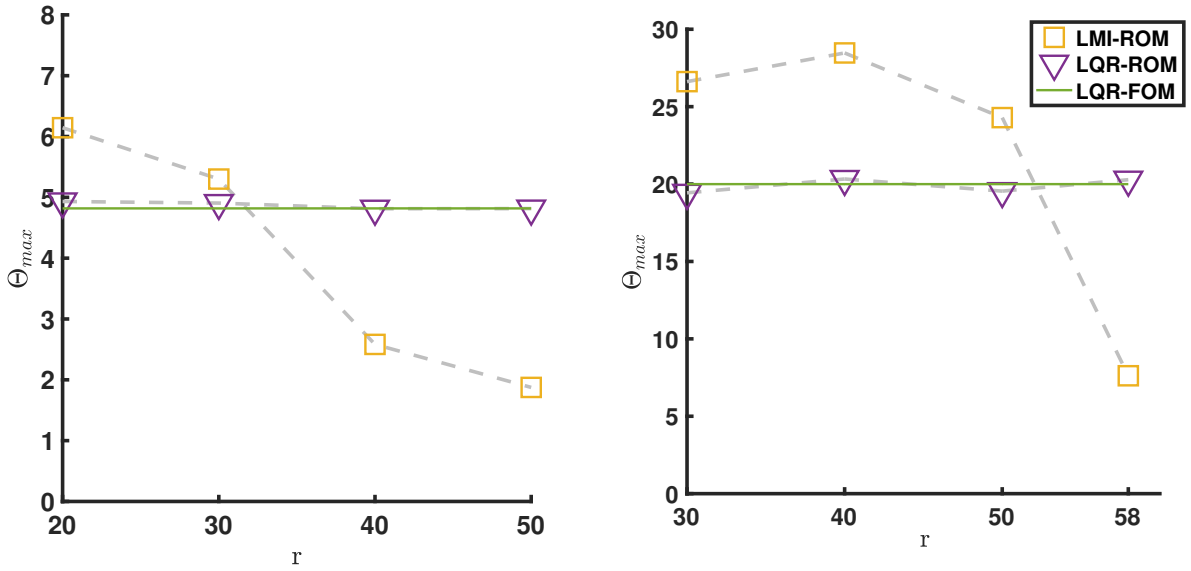
(c) $\alpha = 0, \beta = 2$ with $r = 40$

Figure 5.3: *Worst-case closed-loop TEG responses at* $Re = 3000$.

to the FOM dynamics, and so do not consider r smaller than these values here. Figure 5.4 shows that $\Theta_{\max}$ decreases with increasing ROM order r using the LMI-ROM controller. The same is true for the LQR-ROM controller, but the convergence is more rapid. MTEG for the LQR-ROM converges to that of the LQR-FOM for $r = 20$ for streamwise and spanwise waves, and for $r = 25$ for oblique waves. We found that for streamwise and oblique wavenumber pairs considered, there exists a ROM order r such that the LMI-ROM controller will outperform both of the LQR controllers for MTEG reduction. We note that although the LMI-ROM yields a reduction in MTEG relative to both LQR-based controllers in the spanwise wave case, this case was also found to be relatively insensitive to the ROM order. Again, this finding is consistent with the results reported in [114], which found that spanwise blowing/suction actuation was required to achieve meaningful reductions in MTEG. Since the current investigation is focused on control-oriented ROM, we continue to focus on wall-normal blowing/suction actuation. Lastly, note that the fact that the LMI-ROM requires a larger r than the LQR-ROM for MTEG performance to converge is to be expected; TEG is a phenomenon intimately related to $\dot{E}(t)$, whose approximation requires higher-precision estimates of $E(t)$.

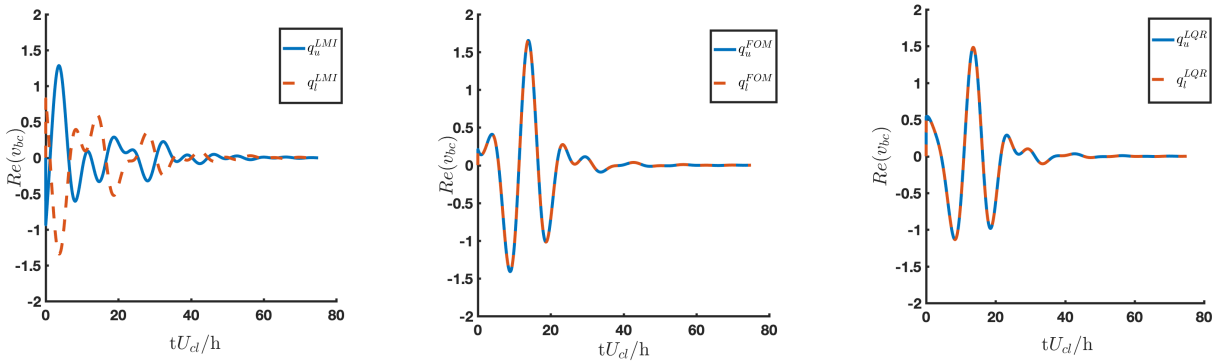
It is clear that the LMI-ROM controller in the above cases outperforms both of the LQR controllers. In order to investigate this further, we proceed to analyze the details of the wall-normal actuation and its influence on the flow perturbations. Figure 5.5 shows the actuated wall-normal velocity at the upper- and lower-walls—q_u and q_l, respectively—for each controller. The case of $(\alpha, \beta) = (1, 0)$, shown in Figure 5.5a, reveals that LMI-ROM controller results in blowing and suction at the upper- and lower-walls that are equal in magnitude, but opposite in direction. In contrast, each of the LQR-ROM and the LQR-FOM controllers produces almost identical (both in magnitude and direction) blowing and suction at the upper- and lower-walls. Interestingly, the LQR-ROM controls differ from the LQR-FOM controls for a short period at the beginning of the response, which is an expected artifact of the modal truncation. The 5% settling time on the actuation for the LMI-ROM controllers is ≈ 43 convective time units; the LQR controllers settle in ≈ 34 convective time units, indicating a shorter duration of control.

In the oblique wave case of $(\alpha, \beta) = (1, 1)$, shown in Figure 5.6a, the LMI-ROM controller results in a maximum wall-normal blowing/suction velocity that is ≈ 1.6 times lower than either



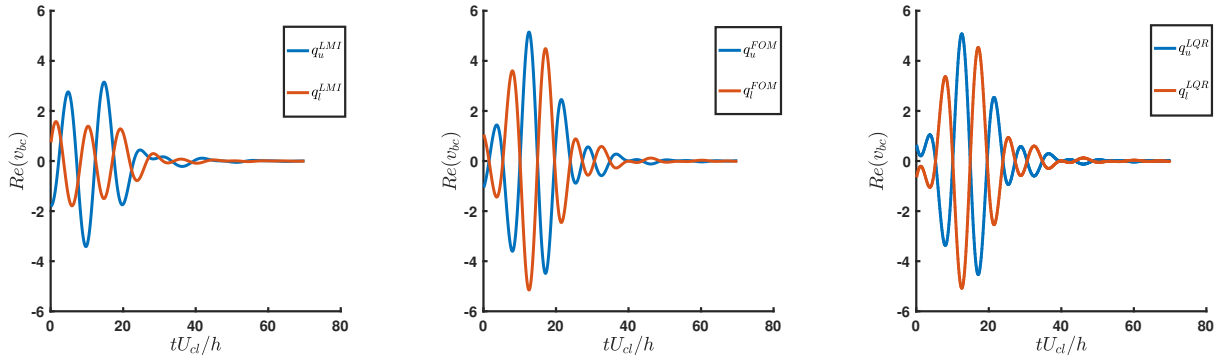
(a) $\alpha = 1, \beta = 0$. **(b)** $\alpha = 1, \beta = 1$

Figure 5.4: *Closed-loop MTEG* Θ_{max} *as a function of ROM order* r *at* $Re = 3000$.



(a) LMI-ROM control **(b)** LQR-FOM control **(c)** LQR-ROM control

Figure 5.5: *Actuated wall-normal velocity for* $r = 40$, $(\alpha, \beta) = (1, 0)$, *and* $Re = 3000$.



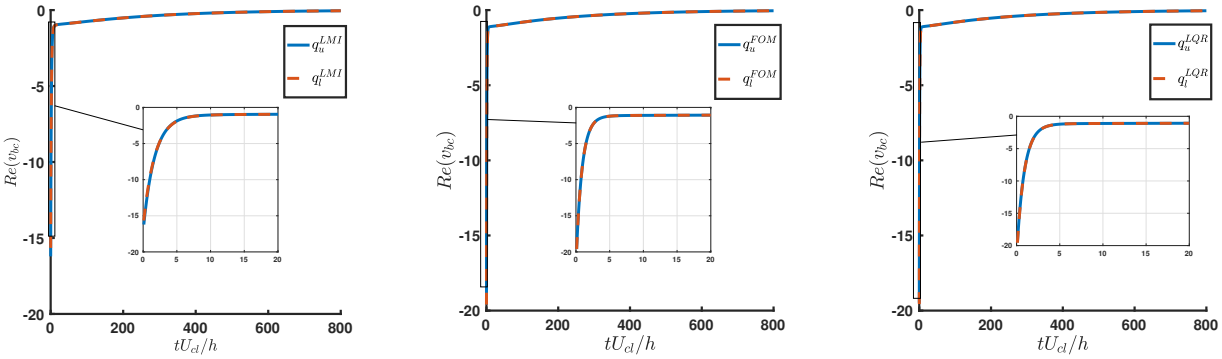
(a) LMI-ROM control

(b) LQR-FOM control

(c) LQR-ROM control

Figure 5.6: *Actuated wall-normal velocity for* $r = 58$, $(\alpha, \beta) = (1, 1)$, *and* $Re = 3000$.

of the LQR controllers. From Figure 5.6a we find that the q_u produces a control input of larger magnitude compared to q_l, i.e., the actuator on the upper-wall is inducing a larger velocity compared to the actuator on the lower-wall. In Figures 5.6b and 5.6c the upper-wall and lower-wall actuators produce a velocity of similar magnitude, but opposite directions relative to each other. In the oblique wave case, the 5% settling time of the actuation signal for the LMI-ROM controller is ≈ 41 convective time units, while the LQR-FOM and LQR-ROM each have a settling time of ≈ 37 convective time units. In the spanwise waves setting, shown in Figure 5.7, the LMI-ROM controller actuates the system similarly to both of the LQR controllers, but with a lower initial magnitude. For all controllers, wall-normal transpiration at the upper-wall is identical to that at the lower-wall (see Figure 5.7).



(a) LMI-ROM control

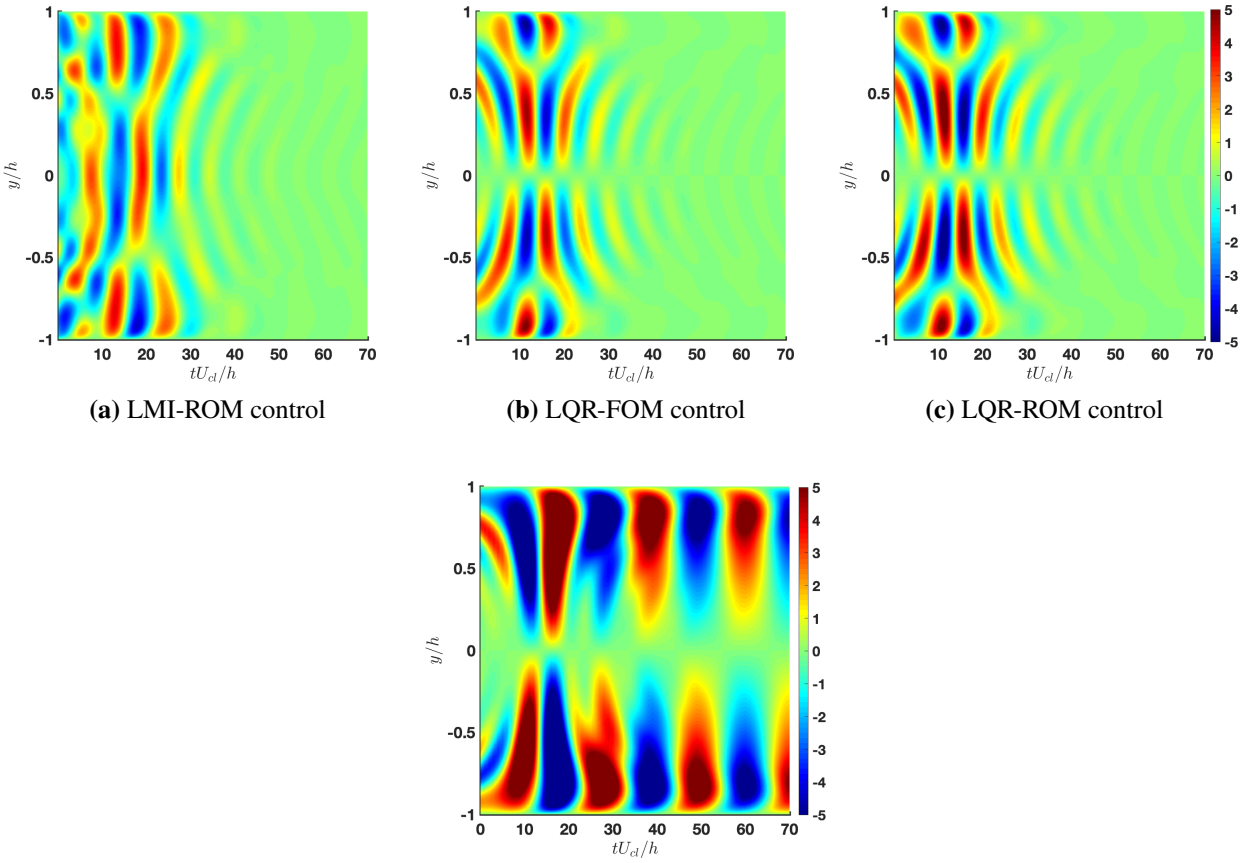
(b) LQR-FOM control

(c) LQR-ROM control

Figure 5.7: *Actuated wall-normal velocity for* $r = 40$, $(\alpha, \beta) = (0, 2)$, *and* $Re = 3000$.

Next, we examine the evolution of perturbations in streamwise velocity (u) to analyze the effect of the different controllers on the flow response. Figures 5.8 – 5.10 show the evolution of normalized u perturbations. In these figures, the initial optimal perturbation has been normalized such that $E(0) = 1$. Figure 5.8 shows the response for the case of streamwise waves. Note that the

LMI-ROM controller has a streamwise perturbation profile different from that of the LQR-ROM and the LQR-FOM. The u perturbations die out faster with the LMI-ROM controller than with either of the LQR controllers. The LQR-FOM and the LQR-ROM result in a similar evolution of u perturbation, as is to be expected from the similarity in TEG profiles we noted earlier in Figure 5.3a. In the case of oblique waves (see Figure 5.9), the LQR-ROM and LQR-FOM again yield a similar response in u-perturbations. In contrast to these responses, the LMI-ROM controller results in a reduced magnitude of u at the lower walls of the channel. Again, the LMI-ROM results in a faster decay of u perturbations than the LQR-ROM and LQR-FOM controllers. Finally, in the case of spanwise waves (see Figure 5.10), all the three controllers yield similar responses in u.

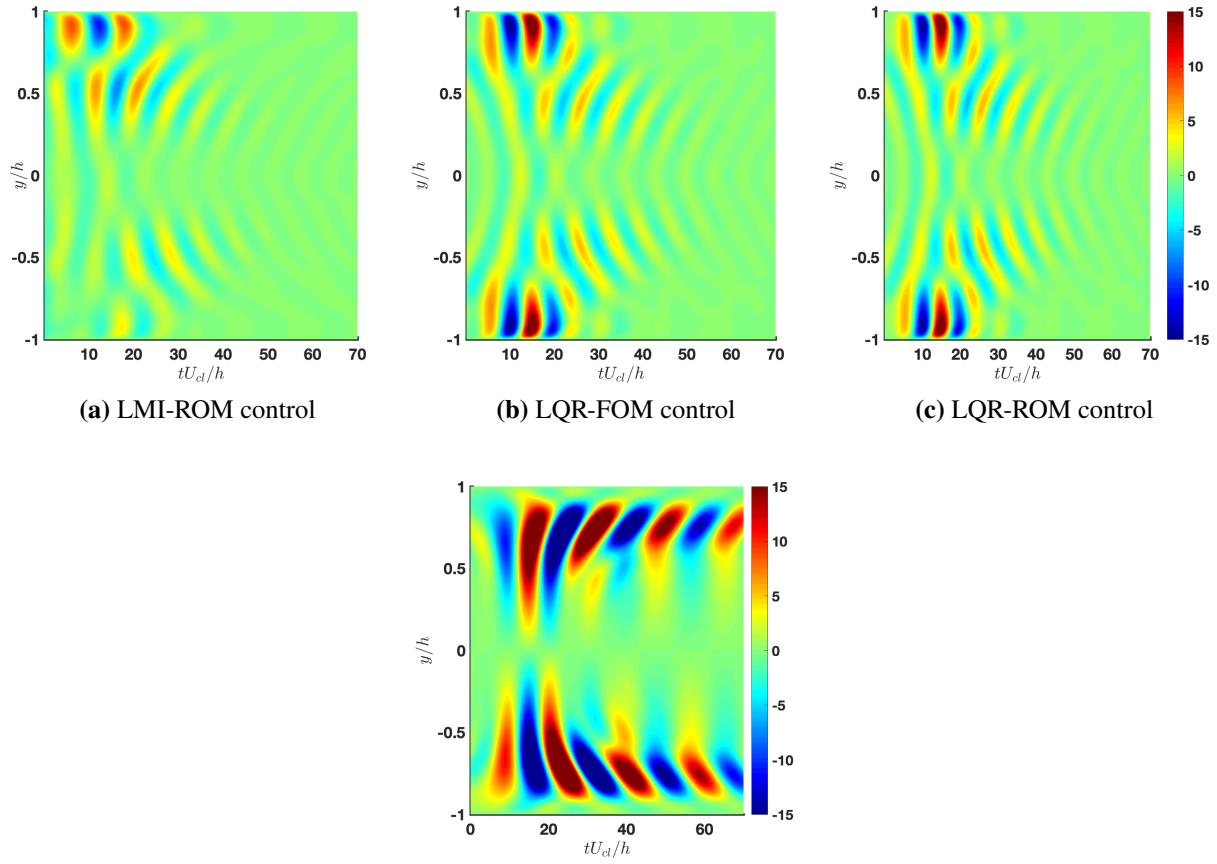


(a) LMI-ROM control **(b)** LQR-FOM control **(c)** LQR-ROM control

(d) Uncontrolled

Figure 5.8: *Evolution of streamwise velocity perturbations (u) for* $r = 40$, $(\alpha, \beta) = (1, 0)$, *and* $Re = 3000$.

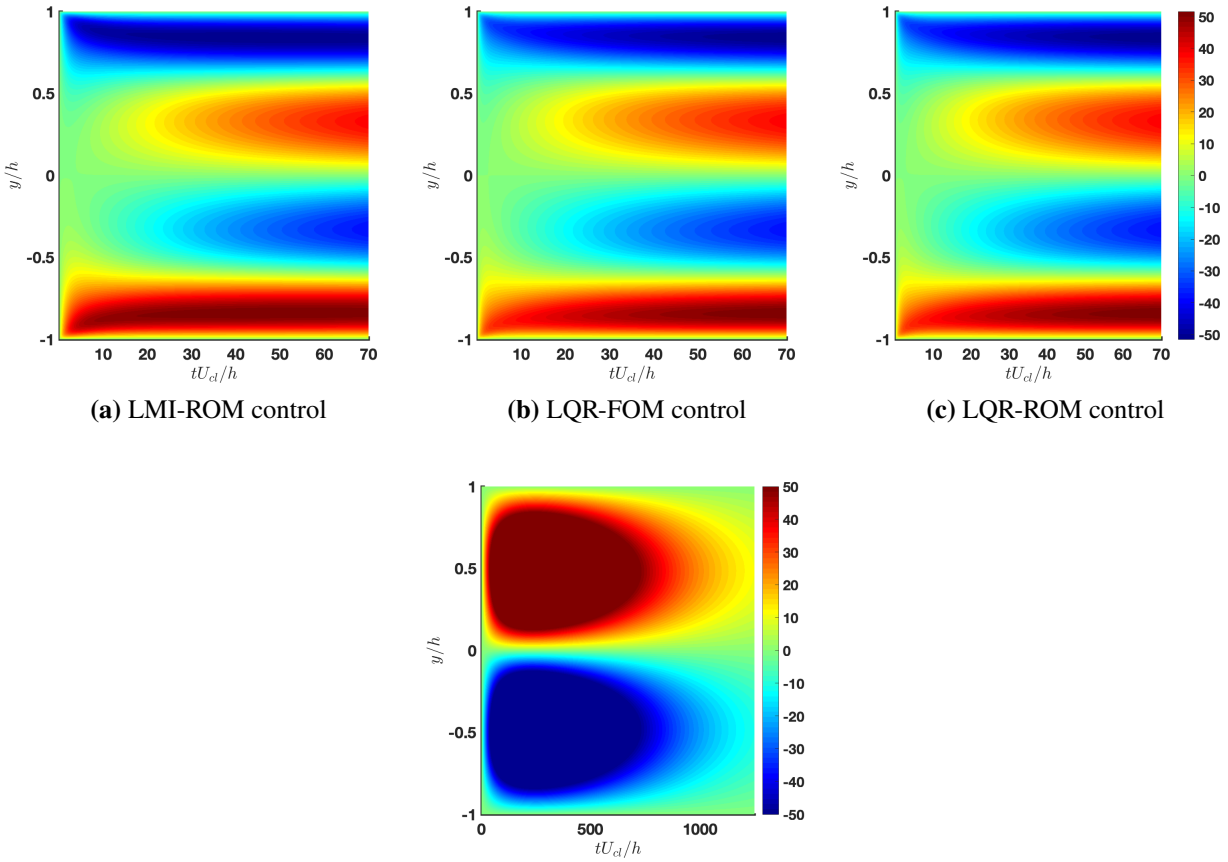
Finally, we repeat our study for other Re values to ensure that the ROMs and controllers can be used in other settings as well. ROMs are developed and tuned to converge for $Re = 1000$, 5000, and $10,000$. Then, we follow the same procedure for control synthesis as in the $Re = 3000$ cases described earlier. Note that for the case of $Re = 10,000$, the flow is linearly unstable; thus, the balanced truncation procedure for the model reduction is only performed on the stable subspace of the linearized dynamics. Figures 5.11 and 5.12 report performance results for the cases of $(\alpha, \beta) = (1, 0)$ and $(1, 1)$, respectively. The results clearly show that the LMI-ROM controllers



(a) LMI-ROM control **(b)** LQR-FOM control **(c)** LQR-ROM control

(d) Uncontrolled

Figure 5.9: *Evolution of streamwise velocity perturbations (u) for* $r = 58$, $(\alpha, \beta) = (1, 1)$, *and* $Re = 3000$.

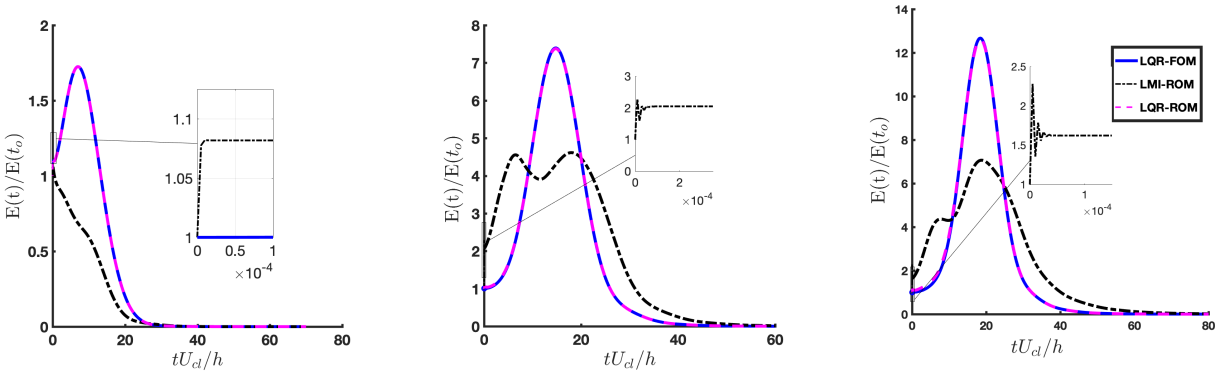


(a) LMI-ROM control **(b)** LQR-FOM control **(c)** LQR-ROM control

(d) Uncontrolled

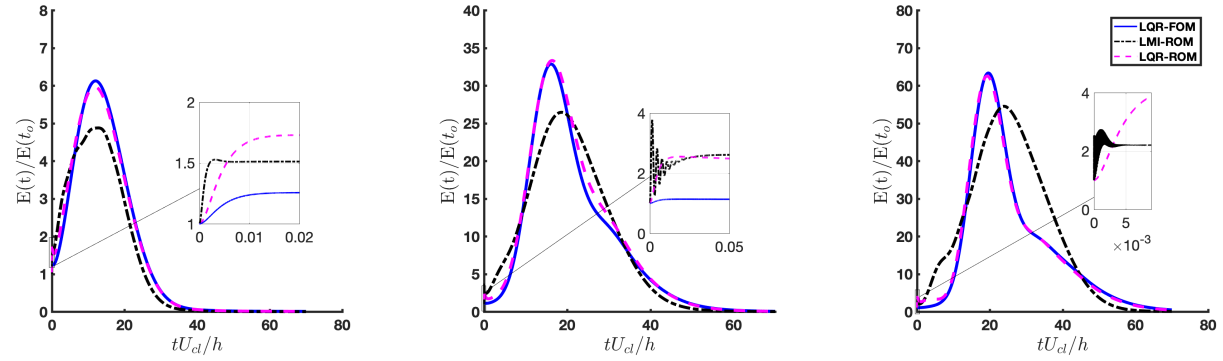
Figure 5.10: *Evolution of streamwise velocity perturbations (u) for* $r = 40$, $(\alpha, \beta) = (0, 2)$, *and* $Re = 3000$.

reduce TEG to a greater extent than the LQR controllers. However, with the increase in Re, the closed-loop response to the LMI-ROM control exhibits oscillations on a transient time scale, on the order of of approximately 10^{-2} to 10^{-4} convective time units. The transient oscillations appear to be a property of the closed-loop system, which has a set of eigenvalues with large imaginary parts—on the order of 10^4—that lead to lightly damped oscillations. Further investigation is necessary to determine the underlying cause of these transient oscillations and the observed spectral properties of the closed-loop system.



(a) $Re = 1000$ ($r = 40$) **(b)** $Re = 5000$ ($r = 50$) **(c)** $Re = 10,000$ ($r = 58$)

Figure 5.11: *Worst-case closed-loop TEG responses for* $(\alpha, \beta) = (1, 0)$.



(a) $Re = 1000$ ($r = 40$) **(b)** $Re = 5000$ ($r = 58$) **(c)** $Re = 10,000$ ($r = 58$)

Figure 5.12: *Worst-case closed-loop TEG responses for* $(\alpha, \beta) = (1, 1)$.

5.4 Conclusions

In this chapter, we have investigated the use of control-oriented ROMs for designing feedback controllers that minimize the MTEG of flow perturbations within a linearized channel flow. The ROMs were formed using an output projection onto POD modes, followed by a balanced truncation procedure to reduce the state dimension. POD modes were chosen in order to best approximate the perturbation energy, as needed for representing the objective function for control. Note that this output projection does not alter the state dimension of the system. As such, a balanced truncation

was performed to reduce the state dimension, retaining only state variables that were essential to preserving the system's input-output dynamics. ROMs of the linearized channel flow system enabled the synthesis of MTEG-minimizing controllers through the solution of an LMI problem that would otherwise have been computationally prohibitive. Specifically, the dimension of the full-order model ($n = 199$) was reduced to yield ROMs with order $r = 40 - 60$, depending on the specific configuration. This constitutes a significant reduction in the computational demand for the subsequent LMI-based controller synthesis, since the computational requirements for LMI-based controller synthesis scale as $O(n^6)$. Further, the MTEG-minimizing controllers designed using the proposed ROMs were found to outperform LQR controllers in suppressing TEG, even when these LQR controllers were designed based on the full-order system model. Although not explicitly reported here, the present investigation revealed that ROM-based MTEG-minimizing controllers can be sensitive to Re variations, leading to linearly unstable closed-loop systems when applied in "off-design" settings. As such, future investigations will need to focus on addressing these fragilities. It is expected that both the model reduction and controller synthesis approaches will need to be re-formulated to robustly minimize MTEG.

6 | Optimal Sensor Selection

The choice and placement of sensors and actuators is an essential factor determining the performance that can be realized using feedback control. This determination is especially important, but difficult, in the context of controlling transitional flows. The highly non-normal nature of the linearized Navier-Stokes equations makes the flow sensitive to small perturbations, with potentially drastic performance consequences on closed-loop flow control. Full-information controllers, such as the linear quadratic regulator (LQR), have demonstrated some success in reducing transient energy growth and suppressing transition; however, sensor-based output feedback controllers with comparable performance have been difficult to realize. In this chapter, we propose two methods for sensor selection that enable sensor-based output feedback controllers to recover full-information control performance: one based on a sparse controller synthesis approach, and one based on a balanced truncation procedure for model reduction. Both approaches are investigated within linear and nonlinear simulations of a sub-critical channel flow with blowing and suction actuation at the walls. We find that sensor configurations identified by both approaches allow sensor-based static output feedback LQR controllers to recover full-information LQR control performance, both in reducing transient energy growth and suppressing transition. Further, our results indicate that both the sensor selection methods and the resulting controllers exhibit robustness to Reynolds number variations. The presentation in this chapter is heavily drawn from [72, 129].

6.1 Introduction

Preventing or delaying transition to turbulence via flow control is a topic of great technological interest. At a sufficiently high Reynolds number, a flow will transition from a low-skin-friction laminar regime to a high-skin-friction turbulent regime. For many wall-bounded shear flows, a sub-critical transition can arise due to non-modal instabilities [44, 74]. The high degree of non-normality of the linearized Navier-Stokes equations can cause flow perturbations to exhibit large peaks in kinetic energy, even when the flow is linearly stable. This so-called *transient energy growth (TEG)* of flow perturbations serves as a driving mechanism for sub-critical transition. TEG causes large deviations of the flow state from the laminar equilibrium, pushing it outside the basin of attraction and triggering secondary instabilities that ultimately transition the flow to turbulence [75–77, 130–132]. An ability to reduce TEG—e.g., using flow control—could provide a means of suppressing transition to turbulence.

In studying TEG, it is important to note that not all flow perturbations will trigger transient growth, and so it is important to consider "optimal" or "worst-case" perturbations that give rise to the maximum TEG for a fixed perturbation amplitude [78]. Considerations of worst-case performance are especially important when investigating and comparing the performance of different flow control strategies that aim to reduce TEG and suppress transition to turbulence. The optimal disturbance for

the uncontrolled flow will not necessarily be the same as the optimal disturbance for the controlled flow. These optimal disturbances will vary further depending on the specific control design, and may even involve perturbations in the control system dynamics due to various sources of uncertainty [85]. Comparing worst-case performance ensures that comparisons of control performance remain fair.

Feedback control has been proposed as a way to reduce TEG and suppress transition in a number of flow configurations. Within numerical simulations, the linear quadratic regulator (LQR) has shown some success in reducing TEG and delaying transition in shear-flows using wall blowing and suction actuation [52, 54, 80, 81]. LQR controllers are designed to minimize a balance between flow perturbation energy and control effort. LQR control is an attractive choice because of its simplicity, but also because these controllers robustly reduce TEG in the face of parameter uncertainties (e.g., Reynolds number variations) [82]. Unfortunately, LQR controllers require full-state information that can be difficult to access outside of numerical simulations. For incompressible flows, full-state information corresponds to measurements of the entire velocity and/or vorticity field. Instead, sensor-based output feedback controllers are required to act based on partial information. In principle, one can adopt an observer-based feedback approach, wherein measurements from a limited set of sensors are used to first estimate the full state of the flow, and to then apply a full-state feedback control law to these estimates. Unfortunately, such approaches can exhibit degraded TEG performance if not properly designed [85, 86]. Although sophisticated estimation strategies can be devised to overcome some of these performance issues [83, 91], these strategies have not been shown to recover full-information control performance.

Static output feedback controllers have been proposed as a convenient design alternative to observer-based feedback control [85, 86]. Static output feedback LQR (SOF-LQR) control, in particular, can be designed using the same objective function as the full-information LQR controller, but with a constraint that the controller act as a direct feed-through from the measured sensor-outputs to commanded inputs [64, 96, 99, 100]. This feed-through structure ensures that SOF-LQR controllers satisfy a necessary condition for TEG elimination [85, 88]. As noted in earlier chapters, in our previous studies [64, 73, 86] we have found that SOF-LQR using wall-based shear-stress sensing is able to reduce TEG, but as with LQG controllers, these control laws are unable to recover the same worst-case performance as the full-information LQR counterpart. This is not entirely surprising, as the achievable performance of a control law is intimately tied to the specific choice of actuators and sensors implemented for control. Thus, the specific choice and arrangement of sensors is an important consideration in the design of sensor-based output feedback control strategies.

A number of studies have considered the problems of sensor selection for flow reconstruction [133–138] and actuator selection for flow control [139–142]. Sensor selection for flow reconstruction has been of particular interest because it can benefit the design of flow estimation and diagnostic strategies. However, in the context of TEG and transition control, even a "perfect" flow estimator can result in degraded control performance when the estimator design is decoupled from the design of the control law [85]. Here, we are interested in selecting a set of sensors that enables sensor-based output feedback control to achieve comparable performance as a full-state feedback controller. In particular, we aim to do this in the context of TEG reduction and transition control, without resorting to flow reconstruction and observer-based feedback designs.

In this chapter, we propose two approaches for sensor selection that enable performance recovery of sensor-based output feedback controllers. Both approaches are formulated as down-selection

problems from a library of candidate sensors. In this proof-of-concept investigation, we consider a library of candidate velocity sensors distributed throughout the interior of a channel flow. One approach leverages the fact that full-information LQR and SOF-LQR controllers can be made equivalent when the library of candidate sensors is sufficiently rich. Thus, the controller gain for the associated SOF-LQR controller can be evaluated to determine the relative contribution of each candidate sensor to the control performance. In doing so, sensors with little contribution to control actions can be identified and discarded to yield a sparse set of sensors without sacrificing flow control performance. The second approach is based on ideas from linear model reduction using balanced truncation. Balanced truncation yields a low-dimensional model that maintains the input-output dynamics of the system. The low-order representation of the state-space for these reduced-order models also exposes redundant signals from sensors in the candidate library. These redundant sensors can be identified and removed using a pivoted QR decomposition to yield a sparse set of sensors for SOF-LQR controller synthesis. We find that both of these approaches identify sensor configurations that allow SOF-LQR to recover full-state LQR TEG performance within linear simulations of a channel flow with wall-normal blowing and suction actuation. Each approach identifies a different configuration of velocity sensors distributed along the interior of the channel. We further evaluate the control performance using direct numerical simulations (DNS) of a nonlinear channel flow. DNS are performed with various optimal disturbance amplitudes to examine the nonlinear effects and the control mechanism that delays or suppresses the laminar-to-turbulent transition.

The chapter is organized as follows: In section 6.2, we present the linearized channel flow model and an overview of relevant controller synthesis approaches. In section 6.3, we formulate two approaches for sensor selection that can be used for flow control performance recovery. Section 6.4 presents sensor configurations and linear performance analysis results for a sub-critical channel flow. This is followed by nonlinear performance results from direct numerical simulations of a sub-critical channel flow in section 6.5. Finally, we draw conclusions in section 6.6.

6.2 Channel flow model and control synthesis

6.2.1 Channel flow

We consider plane Poiseuille flow at sub-critical Reynolds number of $Re = \bar{\boldsymbol{u}}_{\boldsymbol{c}} h/\nu = 3000$ defined by the centerline velocity of the base flow $\bar{\boldsymbol{u}}_{\boldsymbol{c}}$, half height of the channel h, and kinematic viscosity ν. As shown in figure 6.1, the velocity profile of the base flow is $[\bar{\boldsymbol{u}}, \bar{\boldsymbol{v}}, \bar{\boldsymbol{w}}] = [1-(y/h)^2, 0, 0]$ with coordinate origin at the center line between walls, where $\bar{\boldsymbol{u}}, \bar{\boldsymbol{v}}, \bar{\boldsymbol{w}}$ represent velocity components in streamwise x, wall-normal y, and spanwise z directions, respectively. The parabolic profile of the velocity is the laminar equilibrium solution of the flow. In this study, length-scale variables are non-dimensionalized by the channel half-height h, and velocities are non-dimensionalized by the centerline velocity of base flow $\bar{\boldsymbol{u}}_{\boldsymbol{c}}$. Time is denoted by t.

The flow at this condition is linearly stable, since there are no unstable modes from the linear stability analysis. However, a large transient energy growth of small perturbations is observed at this flow condition, and a laminar-to-turbulent transition emerges as a result of certain flow perturbations. Hence, our objective is to design feedback control strategies to suppress the transient energy growth and further prevent the emergence of laminar-to-turbulent transition.

The flow control configuration is illustrated in figure 6.1. We introduce actuation in the form of blowing and suction in the wall-normal direction on the upper and lower channel walls. The

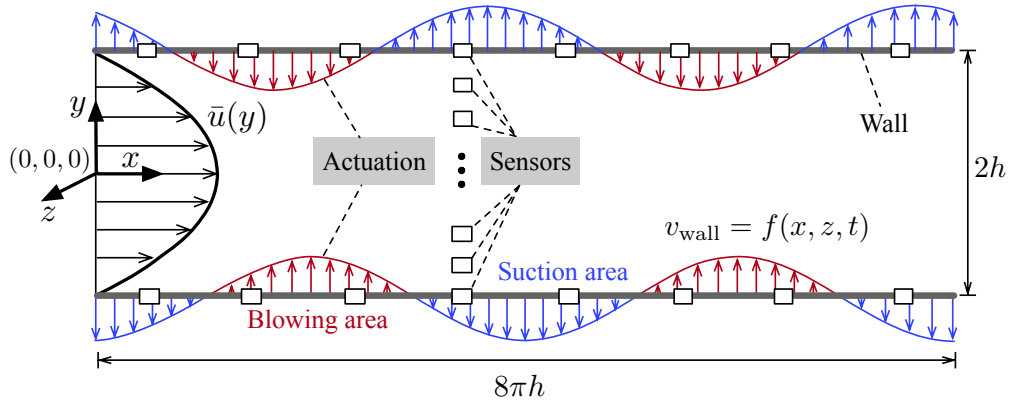


Figure 6.1: *Schematic of plane Poiseuille flow and implementation of sensing and actuation used for flow control (not to scale).*

velocity profile of the actuation is spatially periodic in the streamwise and spanwise directions, in accordance with the channel flow model discussed below. In this study, we consider velocity sensors along the channel interior, but the methods we introduce are valid equally with wall-based sensing as well.

6.2.2 Linearized Navier–Stokes equations

We decompose the flow state $\boldsymbol{q}$ into base state $\bar{\boldsymbol{q}}$ and small perturbation $\boldsymbol{q}'$ ($\boldsymbol{q} = \bar{\boldsymbol{q}} + \boldsymbol{q}'$), where $\boldsymbol{q} = [\boldsymbol{u}, \boldsymbol{v}, \boldsymbol{w}, \boldsymbol{p}]^\mathsf{T}$ ($\boldsymbol{p}$ is pressure), and $(\cdot)^\mathsf{T}$ represents transpose. The kinetic energy density of a perturbation is defined as,

$$E = \frac{1}{2V}\int_V (\boldsymbol{u}'^2 + \boldsymbol{v}'^2 + \boldsymbol{w}'^2) dV, \tag{6.1}$$

where V is the volume of the computational domain.

By substituting the expression of $\boldsymbol{q}=\bar{\boldsymbol{q}}+\boldsymbol{q}'$ into the Navier–Stokes equations, and assuming that the perturbation is much smaller than the base state in magnitude ($|\ \boldsymbol{q}'\ | \ll |\ \bar{\boldsymbol{q}}\ |$), we linearize the equations by retaining linear terms and neglecting higher-order nonlinear terms as follows,

$$\begin{aligned}
\frac{\partial \boldsymbol{u}'}{\partial x} + \frac{\partial \boldsymbol{v}'}{\partial y} + \frac{\partial \boldsymbol{w}'}{\partial z} &= 0 \\
\frac{\partial \boldsymbol{u}'}{\partial t} + \bar{\boldsymbol{u}}\frac{\partial \boldsymbol{u}'}{\partial x} + \boldsymbol{v}'\frac{\partial \bar{\boldsymbol{u}}}{\partial y} &= \frac{\partial \boldsymbol{p}'}{\partial x} + \frac{1}{Re}\nabla^2 \boldsymbol{u}' \\
\frac{\partial \boldsymbol{v}'}{\partial t} + \bar{\boldsymbol{u}}\frac{\partial \boldsymbol{v}'}{\partial x} &= \frac{\partial \boldsymbol{p}'}{\partial y} + \frac{1}{Re}\nabla^2 \boldsymbol{v}' \\
\frac{\partial \boldsymbol{w}'}{\partial t} + \bar{\boldsymbol{u}}\frac{\partial \boldsymbol{w}'}{\partial x} &= \frac{\partial \boldsymbol{p}'}{\partial z} + \frac{1}{Re}\nabla^2 \boldsymbol{w}'.
\end{aligned} \tag{6.2}$$

The linearzied Navier–Stokes equations are further manipulated to be expressed in terms of wall-normal velocity $\boldsymbol{v}'$ and wall-normal vorticity $\boldsymbol{\eta}'$ as described in [44] as,

$$\begin{aligned}
\frac{\partial(\nabla^2 \boldsymbol{v}')}{\partial t} + \bar{\boldsymbol{u}}\frac{\partial(\nabla^2 \boldsymbol{v}')}{\partial x} - \frac{\partial^2 \bar{\boldsymbol{u}}}{\partial y^2}\frac{\partial \boldsymbol{v}'}{\partial x} - \frac{1}{Re}\nabla^2(\nabla^2 \boldsymbol{v}') &= 0 \\
\frac{\partial \boldsymbol{\eta}'}{\partial t} + \frac{\partial \bar{\boldsymbol{u}}}{\partial y}\frac{\partial \boldsymbol{v}'}{\partial z} + \bar{\boldsymbol{u}}\frac{\partial \boldsymbol{\eta}'}{\partial x} - \frac{1}{Re}\nabla^2 \boldsymbol{\eta}' &= 0.
\end{aligned} \tag{6.3}$$

Next, the real-valued three-dimensional perturbation of wall-normal velocity and wall-normal vorticity are expressed using Fourier expansions in the homogeneous x- and z-directions,

$$\begin{aligned} \boldsymbol{v'}(x,y,z,t) &= \hat{\boldsymbol{v}}(y,t)e^{i(\alpha x+\beta z)} + \text{complex conjugate}, \\ \boldsymbol{\eta'}(x,y,z,t) &= \hat{\boldsymbol{\eta}}(y,t)e^{i(\alpha x+\beta z)} + \text{complex conjugate}, \end{aligned} \tag{6.4}$$

where $\hat{\boldsymbol{v}}(y,t)$ and $\hat{\boldsymbol{\eta}}(y,t)$ are amplitude functions of the perturbation associated with streamwise wavenumber α and spanwise wavenumber β. By plugging (6.4) into the linearized Navier–Stokes equations (6.2), we obtain the Orr-Sommerfeld and Squire equations as follows,

$$\begin{bmatrix} \dot{\hat{\boldsymbol{v}}} \\ \dot{\hat{\boldsymbol{\eta}}} \end{bmatrix} = \begin{bmatrix} -i\alpha\bar{\boldsymbol{u}} + \frac{i\alpha\bar{\boldsymbol{u}}_{yy}}{(\mathcal{D}^2-k^2)} + \frac{1}{Re}(\mathcal{D}^2-k^2) & 0 \\ -i\beta\bar{\boldsymbol{u}}_y & -i\alpha\bar{\boldsymbol{u}} + \frac{1}{Re}(\mathcal{D}^2-k^2) \end{bmatrix} \begin{bmatrix} \hat{\boldsymbol{v}} \\ \hat{\boldsymbol{\eta}} \end{bmatrix}, \tag{6.5}$$

where $\mathcal{D}$ represents differentiation with respect to the wall-normal direction y, $\bar{\boldsymbol{u}}_y$ and $\bar{\boldsymbol{u}}_{yy}$ denote the first and second derivatives of $\bar{\boldsymbol{u}}$ with respect to y, and $k^2 := \alpha^2 + \beta^2$. The governing equations (6.5) are in a state-space form

$$\frac{\partial X_u(y)}{\partial t} = A_u(\bar{\boldsymbol{q}};\alpha,\beta)X_u(y), \tag{6.6}$$

where $X_u = [\hat{\boldsymbol{v}},\hat{\boldsymbol{\eta}}]^\mathsf{T}$ is the state, and subscript $(\cdot)_u$ indicates uncontrolled system.

In the y-direction, flow variables are represented by Chebyshev polynomials with $N = 101$ discrete collocation points, and a no-slip boundary condition is prescribed at the upper and lower walls for the uncontrolled baseline flow: i.e., $\hat{\boldsymbol{v}}(\pm h) = \hat{\boldsymbol{v}}_y(\pm h) = \hat{\boldsymbol{\eta}}(\pm h) = 0$.

In the control design, we introduce actuation in the form of wall-normal blowing and suction at the upper and lower channel walls (see figure 6.1). This actuation modifies the uncontrolled dynamic system (6.6) to form a controlled dynamical system

$$\frac{\partial X}{\partial t} = AX + BU, \tag{6.7}$$

where A is the system matrix, X is the state, U is the input, and B is the input matrix that maps the influence of control inputs to the state evolution. Here the control input is selected to be $U = \frac{\partial}{\partial t}[\hat{\boldsymbol{v}}\mid_{+h}, \hat{\boldsymbol{v}}\mid_{-h}]^T$, representing the rate of change of wall-normal velocity on the upper and lower walls. Since the control input U represents the change of Fourier coefficients of wall-normal velocity $\hat{\boldsymbol{v}}$, in figure 6.1 it is shown in the form of a sinusoidal wave. The no-flow-through boundary conditions ($\hat{\boldsymbol{v}}\mid_{\pm h}= 0$) are excluded from X_u in (6.6). In the controlled case, $\hat{\boldsymbol{v}}\mid_{\pm h}$ are nonzero, so we append these two state variables to the flow state X_u to form a new state $X = [X_u, \hat{\boldsymbol{v}}\mid_{+h}, \hat{\boldsymbol{v}}\mid_{-h}]^\mathsf{T}$. Analogously, the dynamics matrix A_u is modified and denoted by A to account for the new state.

In all that follows, we transform all quantities to their equivalent real-valued representations so that $A \in \mathbb{R}^{n\times n}$, $X \in \mathbb{R}^n$, $B \in \mathbb{R}^{n\times m}$, and $U \in \mathbb{R}^m$. Further, all measured sensor outputs $Y \in \mathbb{R}^p$ to be considered in this study will be represented by the output equation

$$Y(t) = CX(t). \tag{6.8}$$

Further details about the model formulation can be found in [126].

6.2.3 Transient energy growth and control synthesis

In this study, we aim to use feedback control to reduce the transient energy growth (TEG). We consider TEG due to some initial flow perturbation $X(t_0) = X_0$.

The associated system response is given by $X(t) = e^{A(t-t_0)}X_0$, and the associated perturbation kinetic energy is given as,

$$E(t) = X^{\mathsf{T}}(t)QX(t), \tag{6.9}$$

where $Q = Q^{\mathsf{T}} > 0$. Further, the maximum TEG is defined as,

$$G = \max_{t \geq t_0} \max_{E(t_0) \neq 0} \frac{E(t)}{E(t_0)}, \tag{6.10}$$

which results from a so-called *worst-case* or *optimal perturbation* [3]. The system can exhibit TEG whenever $G > 1$. In this study, we always evaluate the maximum TEG for a given system. The worst-case perturbations are calculated using the algorithm proposed in [128], which performs a bisection over an iteratively refined time interval to determine the optimal perturbation to arbitrary accuracy. We emphasize that, in general, perturbation for the uncontrolled flow will be different from the one for the controlled flow, and so these perturbations must be determined independently.

To use feedback control to achieve TEG reduction, the control input vector U at a given instant is determined from available system information. For a full-state feedback control, the state X is assumed to be known and available for feedback, i.e., full-information control:

$$U(t) = KX(t), \tag{6.11}$$

where the design variable $K \in \mathbb{R}^{m \times n}$ is called the state feedback gain matrix.

LQR synthesis is based on solving,

$$\min_{U(t)} J = \int_0^\infty X^{\mathsf{T}}(t)QX(t) + U^{\mathsf{T}}(t)RU(t)dt \tag{6.12}$$

subject to the linear dynamic constraint given in (6.7), where $R > 0$. The resulting full-state feedback LQR controller gain matrix K is determined from the solution of an algebraic Riccati equation [69]. Although LQR controllers will not necessarily minimize TEG, they have been shown to reduce TEG in shear flows and to exhibit robustness to parametric uncertainties [54, 80, 81].

Outside of numerical simulations, it can be challenging to obtain the full velocity and/or vorticity field information in an efficient manner. This makes it difficult to obtain full-state information as required for performing full-state feedback controller. In order to achieve feedback control with the measured information from sensors, in this study, we propose to use a static output feedback (SOF) control structure. For SOF control, the control input is determined directly from the measured output Y in an analogous manner to full-state feedback, with

$$U(t) = FY(t), \tag{6.13}$$

where the design variable $F \in \mathbb{R}^{m \times p}$ is called the SOF feedback gain matrix. The SOF form of LQR control was proposed for TEG control in [64, 86].The SOF-LQR solves the same minimization

problem as shown in (6.12), but with an SOF constraint on the feedback law. This is equivalently written as,

$$J = \int_0^\infty X^\top(t)[Q + (FC)^\top R(FC)]X(t)dt. \tag{6.14}$$

The SOF-LQR can be solved using iterative Anderson-Moore methods [96, 97]. In this study, we use the Anderson-Moore algorithm with Armijo-type adaptation proposed in [86]. The details are given in Chapter 4.

6.3 Sensor selection for state feedback performance recovery

In this section, we propose two methods for selecting a sparse set of sensors to enable sensor-based SOF controllers to recover full-information control performance. We restrict the discussion to sensor selection and linear quadratic performance, but the approach is applicable more generally and can be used for actuator selection and other performance measures just as well.

The basic idea begins by recognizing that SOF-LQR control can be made equivalent to full-information LQR control if an available set of $p \geq n$ sensors is *sufficiently rich*. Here, the term *sufficiently rich* amounts to requiring the output matrix to have full column rank (i.e., $C = C_n \in \mathbb{R}^{p\times n}$ with $\text{rank}(C_n) = n$). Since the closed-loop dynamics for SOF-LQR control are given by

$$\dot{X}(t) = (A + BF_nC_n)X(t), \tag{6.15}$$

it follows that the SOF-LQR gain F_n can be designed from the full-state feedback LQR gain K to recover full-state feedback LQR performance exactly: simply find a gain F_n that satisfies $F_nC_n = K$. From this insight, it follows that if we form a sufficiently rich library of candidate sensors, then the sensor selection problem can be recast as a problem of sensor down-selection. That is, given a sufficiently rich library of sensors, we aim to determine which sensors can be removed from the library such that the closed-loop performance of the controlled system (6.15) will be minimally impacted. Doing so will result in a sparse set of $r < n$ sensors with associated output matrix $C_r \in \mathbb{R}^{r\times n}$. The general problem of optimal sensor selection for state feedback performance recovery is non-convex and combinatorially hard to solve. Here, we propose two heuristic methods for overcoming this challenge to achieve performance recovery via sensor down-selection from a sufficient rich library of candidate sensors: one based on controller gain evaluation (see section 6.3.1), and another based on a balanced truncation procedure (see section 6.3.2). These methods are motivated by sparse control synthesis [143, 144] and greedy Gramian-based optimization methods [135, 142], respectively. Both methods will make it possible for SOF-LQR controllers to recover full-state LQR performance, as will be demonstrated in sections 6.4 and 6.5. In this work, we focus on velocity sensors for simplicity. However, other (heterogeneous) sensor libraries can be used just the same. We also emphasize that any sensor type/location constraints should be considered in the construction of the library—i.e., only permissible sensors should be included in the library.

6.3.1 Sensor selection by column-norm evaluation (CE)

The first approach we propose is motivated by sparse controller synthesis techniques [143, 144], by which a convex optimization problem is posed to solve for a controller gain that achieves the performance objective while balancing either row- or column-sparsity in the resulting controller gain. Due to the computational complexity of generic off-the-shelf solvers, these sparse synthesis methods tend to require specialized and dedicated solvers for high-dimensional system such as

fluid flows. As such, rather than working with this optimization problem directly, here propose a heuristic approach that is comparatively simpler to implement.

The basic approach we propose stems from the fact that a controller gain matrix contains important information regarding the relative contribution of individual sensors and actuators to the controlled closed-loop dynamics in (6.15). If we design a controller gain F_n based on a sufficiently rich library of candidate sensors, then each column in F_n corresponds to a specific sensor in the candidate library, represented as a row of C_n. Thus, by evaluating the relative norm of each column in F_n, we can determine the relative contribution of a particular sensor to the control action and the closed-loop dynamics in (6.15). Here, we assess the relative importance of sensors by evaluating the relative L_2-norm of each column in the gain matrix F_n. Let $F_n(:,i)$ indicate the i^{th} column of F_n, then the L_2-norm is calculated as

$$\|F_n(:,i)\|_2 = \sqrt{\sum_{j=1}^{n} F_n(j,i)^2}, \tag{6.16}$$

where $F_n(j,i)$ is the j^{th} element of the i^{th} column of F_n. Consider, for example, that a column in F_n of all zeros and the associated row in C_n could be removed completely without altering the closed-loop system response in (6.15). In general, columns of F_n with large norm contribute more to the closed-loop response than the columns of F_n with small norm. Thus, the rows in C_n associated with the dominant columns in F_n indicate sensors that are "more important" for the controlled system dynamics. Therefore, we identify the subset of r columns with the largest relative norm, denoted by their indices $j_1, \cdots, j_r$. Then, a new output matrix C_r containing a reduced set of r sensors can be constructed from the rows $j_1, \cdots, j_r$ of C_n. In principle, a gain matrix F_r for this reduced set of sensors can be determined directly from the columns $j_1, \cdots, j_r$ of F_n, but it is actually beneficial to compute an optimal gain F by re-designing the SOF gain for the system (A, B, C_r). In the present work, we consider linear quadratic control objectives, so the re-design is performed based on SOF-LQR synthesis via an iterative Anderson-Moore algorithm (see Chapter 4).

The method proposed here for sensor selection by column-norm evaluation (CE) is summarized in Algorithm 2. Note that it can be useful to scale the outputs of the candidate sensor library so that each row of C_n has unit norm. This results from the fact that the scaling of the sensor output is inversely associated with the scale of the associated column norm in F_n. Performing this scaling to unit norm output tends to be important when a heterogeneous set of sensors is used to construct the candidate library (e.g., velocity, pressure, and shear-stress); otherwise, the importance of a particular type of sensor can be artificially inflated or deflated by the nature of observable quantity itself.

Lastly, note that a similar procedure to Algorithm 2 can be formulated for actuator selection by considering the relative norm of rows in F_n, each corresponding to an actuator represented as a column of the input matrix B in (6.15). Step 0 in this "actuator selection by row-norm evaluation" would then be to match full-information control performance $B_n F_n = K$ using a sufficiently rich library of candidate actuators B_n. The remaining steps in Algorithm 2 would then follow analogously, replacing "sensors" with "actuators", all "C" matrices with "B" matrices, and also interchanging all references to "rows" with "columns" and "columns" with "rows". We note again that these ideas are closely related to sparse controller synthesis techniques based on convex

optimization, which can be used to explicitly promote sparsity and design controller gains with many columns or rows of all zeros [143, 144].

Algorithm 2: ***Sensor selection by column-norm evaluation (CE)***

step 0: Form a sufficiently rich library of candidate sensors C_n, and design an SOF controller F_n that achieves the same performance as the desired full-information controller by solving $F_n C_n = K$.

step 1: Evaluate the L_2-norm of each column in F_n, then save the indices $\{j_1, \cdots, j_r\}$ of the r columns with the largest relative L_2-norm.

step 2: Construct a reduced measurement matrix C_r whose r rows consist of rows $j_1, \cdots, j_r$ of C_n.

step 3: Re-design an SOF controller based on (A, B, C_r).

6.3.2 Sensor selection by balanced truncation

Another sensor selection procedure can be devised using the notion of balanced truncation [119, 120, 124]. Balanced truncation is a model reduction method for linear systems that works by truncating states with a lesser contribution to a system's input-output dynamics. To do so, the state-space is first transformed into balanced coordinates $\bar{X}_b = TX$, so that the controllability Gramian W_c and the observability Gramian W_o are equal and diagonal. That is, in balanced coordinates we have $\bar{W}_c = \bar{W}_o = \text{diag}(\sigma_1, \cdots, \sigma_n)$, where $\sigma_1 \geq \sigma_2 \geq \cdots \geq \sigma_n$ are the system's Hankel Singular Values (HSVs). Larger HSVs indicate directions of state-space with greater contribution to the input-output dynamics, whereas smaller HSVs indicate directions of state-space with lesser contribution to the input-output dynamics. As such, truncation in balanced coordinates of the $n - r$ states with the smallest HSVs will allow a reduction to an r-dimensional state-space, while preserving information that is most important for capturing the input-output dynamics. This idea can be extended for sensor selection from a sufficiently rich library of candidate sensors C_n, since a reduction to an r-dimensional state-space will necessarily lead to an output matrix with redundant rows. Upon eliminating these redundant rows in C_n—e.g., by means of a pivoted QR decomposition—we will be left with r linearly independent rows (sensors) that are relevant for feedback control. The basic approach here boils down to a greedy selection procedure for Gramian-based optimization and $\mathcal{H}_2/\mathcal{H}_\infty$ performance objectives [135, 142].

The balancing transformation can be determined by first computing the system Gramians from the associated Lyapunov equations,

$$\begin{aligned} AW_c + W_c A^T + BB^T &= 0 \\ W_o A + A^T W_o + C_n^T C_n &= 0. \end{aligned} \tag{6.17}$$

Then, using the lower triangular Cholesky factorizations L_o and L_c of W_o and W_c, respectively, and the singular value decomposition of their product $L_o^T L_c = \Phi \Sigma \Psi^T$, the balancing transformation can be computed as

$$\begin{aligned} T &= L_c \Psi \Sigma^{\frac{1}{2}} \\ T^{-1} &= \Sigma^{\frac{1}{2}} \Phi^T L_o^T. \end{aligned} \tag{6.18}$$

By retaining the r states with the largest HSVs and truncating the rest, the reduced-order system

resulting from balanced truncation can be expressed as

$$\begin{aligned} \dot{X}_b(t) &= A_b X_b(t) + B_b U(t) \\ Y_b(t) &= C_b X_b(t), \end{aligned} \tag{6.19}$$

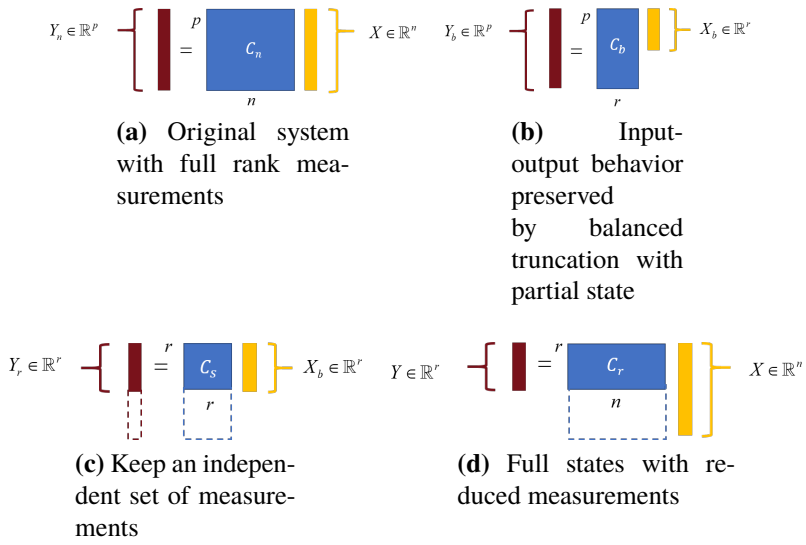
where $A_b \in \mathbb{R}^{r\times r}$, $B_b \in \mathbb{R}^{r\times m}$, $C_b \in \mathbb{R}^{p\times r}$, the reduced-order state $X_b \in \mathbb{R}^r$, input vector $U \in \mathbb{R}^m$, and output vector $Y_b \in \mathbb{R}^p$. Since $r < n$, the output matrix C_b will necessarily have redundant rows. Thus, only r linearly independent rows (sensors) are needed to achieve the same feedback control performance as the reduced-order system with the full sensor library. To see this, consider that the static output feedback control determines the control action directly from the measured output as $U = F_n Y_n$. This can be approximately achieved based on the reduced-order model attained via balanced truncation as $U = F_n Y_n \approx F_n Y_b$ (see figure 6.2). Now, since $Y_b = C_b X_b$ and C_b has redundant rows, it is possible to exactly reproduce this control signal from a reduced set of r outputs $Y_r = C_s X_b$ with $C_s \in \mathbb{R}^{r\times r}$ as $U = F_n Y_b = F_r Y_r$. This final output signal can be represented in the original basis for the full n-dimensional state-space, which determines the specific sensors that are needed to recover full-information feedback control performance using output feedback control.

In order to down-select to a set of r linearly independent rows from the output matrix C_b, we make use of the column-pivoted QR decomposition as

$$C_b^{\mathsf{T}}\mathbf{E} = \mathbf{QR}, \tag{6.20}$$

where $\mathbf{Q} \in \mathbb{R}^{r\times r}$ is an orthogonal matrix and $\mathbf{R} \in \mathbb{R}^{r\times p}$ is an upper triangular matrix with diagonal elements r_{ii}, with $\mid r_{11} \mid \geq \mid r_{22} \mid \geq \cdots \geq \mid r_{nn} \mid$. The independent rows $j_1, \cdots, j_r$ of C_b can be identified by entries in the column permutation matrix $\mathbf{E} \in \mathbb{R}^{p\times p}$. Thus, only these rows of C_b are retained in order to down-select the number of sensors and obtain the associated output matrix C_s shown graphically in figure 6.2c. Similarly, these same indices can be used to construct the output matrix C_r in the original n-dimensional basis for the state-space: simply construct C_r from rows $j_1, \cdots, j_r$ of C_n. All that remains at this point is to re-design an SOF controller based on the system (A, B, C_r) that uses this reduced set of sensors. A summary of this balanced truncation (BT) sensor selection approach is summarized as Algorithm 3 below. Note that, as with the CE sensor selection approach, this BT approach can be formulated analogously for actuator selection as well, again by solving the dual problem. That is, step 0 in this "actuator selection by balanced truncation" would then be modified to form a sufficiently rich library of candidate actuators B_n, then replacing all "C" matrices with "B" matrices and interchanging all references to "rows" with "columns" and "columns" with "rows". The only subtle difference in the actuator selection algorithm would arise in step 3, where the column-pivoted QR factorization of B_b would be used (or the row-pivoted QR factorization of B_b^{T}. Similar ideas for using balanced model reduction methods for sensor and actuator selection have been investigated in [135].

The choice of r in the carrying out the above steps to is important for ensuring that the final sensor configuration is able to achieve the desired control performance. One way to make this determination is to evaluate the difference between the input-output dynamics of the r-dimensional reduced-order balanced truncation model relative to the n-dimensional full-order model. We can evaluate this error by first defining an error system Σ_e that maps any input U to the associated error



(a) Original system with full rank measurements

(b) Input-output behavior preserved by balanced truncation with partial state

(c) Keep an independent set of measurements

(d) Full states with reduced measurements

Figure 6.2: *Illustration of measurement selection by balanced truncation.*

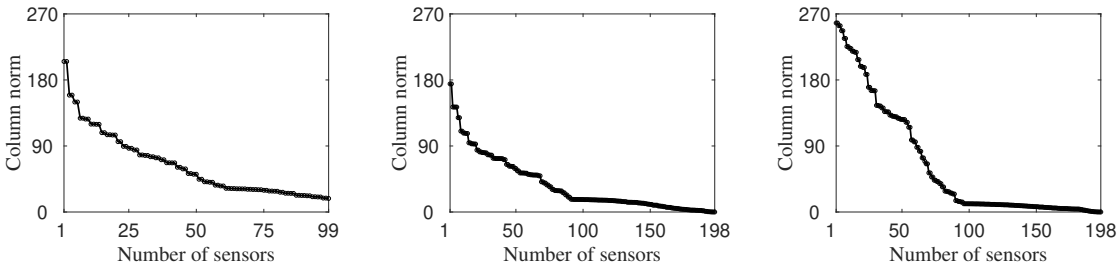
at the output $e = Y_n - Y_b$:

$$\begin{aligned} \begin{bmatrix} \dot{X}(t) \\ \dot{X}_b(t) \end{bmatrix} &= \begin{bmatrix} A & 0 \\ 0 & A_b \end{bmatrix} \begin{bmatrix} X(t) \\ X_b(t) \end{bmatrix} + \begin{bmatrix} B \\ B_b \end{bmatrix} U(t) \\ e(t) \quad &= \begin{bmatrix} C_n & -C_b \end{bmatrix} \begin{bmatrix} X(t) \\ X_b(t) \end{bmatrix}. \end{aligned} \tag{6.21}$$

Then, an appropriate r can be determined by evaluating an associated system norm of Σ_e and ensuring it falls below some threshold err. A small system norm When the error system holds small system norms, the ROM captures the original system's input-output dynamics well. In this study, we can consider both the $\mathcal{H}_2$- and $\mathcal{H}_\infty$-norms of Σ_e. The $\mathcal{H}_2$-norm of Σ_e is denoted as $\|\Sigma_e\|_{\mathcal{H}_2}$ and corresponds to the root-mean-square of the impulse response of Σ_e. The $\mathcal{H}_\infty$-norm of Σ_e is denoted by $\|\Sigma_e\|_{\mathcal{H}_\infty}$ and corresponds to the peak value of the largest singular value of Σ_e.

Algorithm 3: ***Sensor selection by balanced truncation (BT)***

step 0: Form a sufficiently rich library of candidate sensors C_n.
step 1: Transform the system (A, B, C_n) to balanced coordinates using the balancing transformation in (6.18).
step 2: Perform a balanced truncation to the r-dimensional system representation in (6.19), with associated output matrix C_b.
step 3: Perform a column-pivoted QR factorization of C_b^T as in (6.20) to identify a set of r linearly independent rows $\{j_1, \cdots, j_r\}$ from C_b.
step 4: Construct a new output matrix C_r from rows $\{j_1, \cdots, j_r\}$ of the original candidate library of sensors C_n. This C_r represents the sparse sensor configuration.
step 5: Design an SOF controller based on the system (A, B, C_r).



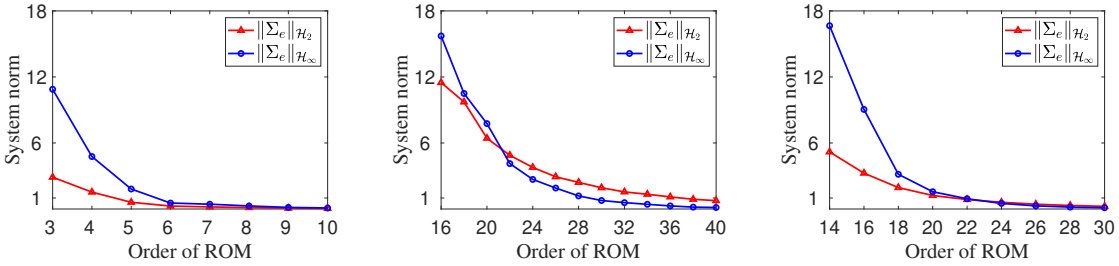
(a) $(\alpha, \beta) = (1, 0)$ **(b)** $(\alpha, \beta) = (1, 1)$ **(c)** $(\alpha, \beta) = (0, 2)$

Figure 6.3: *In the gain column norm evaluation approach, evaluate the column norm of the gain matrix F_n. The L2-norms of each column are sorted in descend order.*

6.4 Results: sensor selection and linear performance analysis

In the previous section, we proposed two approaches for sensor selection—one based on column-norm evaluation (CE) and one based on balanced truncation (BT)—that can enable a sensor-based SOF controller to recover full-information control performance. Here, we apply each method for sensor-based output feedback control of the linearized channel flow with $Re = 3000$ described in section 6.2.1. The SOF-LQR controllers here will be designed to recover the full-information LQR control TEG performance subject to worst-case streamwise $(\alpha, \beta) = (1, 0)$, oblique $(\alpha, \beta) = (1, 1)$, and spanwise $(\alpha, \beta) = (0, 2)$ disturbances. Sensors will be determined from a sufficiently rich library of velocity sensors, distributed at Chebyshev collocation points along the wall-normal direction throughout the interior of the channel, but excluding points nearest to the walls (see figure 6.1). Since the flow is spatially invariant, the sensor library is constructed based on Fourier coefficients. For streamwise disturbances, only wall-normal velocity information is relevant and so a sufficiently rich sensor library in this case is built-up using $\hat{\boldsymbol{v}}$ sensors only. For oblique and spanwise disturbances, we use $\hat{\boldsymbol{u}}$ and $\hat{\boldsymbol{v}}$ to build up our sensor library, so that $\text{rank}(C_n) = n$. We emphasize that these choices in the construction of the sensor library are not unique, and are selected here mainly for simplicity.

In carrying out the CE approach (Algorithm 2), we begin by evaluating the L_2-norm for each column of the controller gain F_n, then rank these from largest to smallest (see figure 6.3). For each of the three wavenumber combinations reported in figure 6.3, there are a few columns with a relatively large L_2-norm compared to the others. Recall that a larger norm indicates that a sensor has a more dominant contribution to the control action, and so this indicates that the corresponding sensors should be retained, while sensors associated with smaller norms can be truncated. We do this in sequence, truncating all but the largest norm sensors, then re-designing the SOF-LQR controller. We compare the worst-case TEG for the new SOF-LQR controller with that of the full-information LQR. If the worst-case performance is not satisfactorily matched between the two, then we proceed to introduce the next set of dominant sensors according to the rankings in figure 6.3, and repeat this process until the resulting SOF-LQR controller recovers full-information LQR controller performance. Each graph of column norm versus number of sensors r_{CE} in figure 6.3 exhibits at least one "elbow point", and so we expect that we will be able to recover full-information LQR performance using a sparse sensor configuration with SOF-LQR control. Indeed, this will be the case. These results will be presented and discussed in more detail after we discuss the preliminary aspects of the BT procedure for sensor selection.



(a) $(\alpha,\beta) = (1,0)$ **(b)** $(\alpha,\beta) = (1,1)$ **(c)** $(\alpha,\beta) = (0,2)$

Figure 6.4: *In the balanced truncation approach, the error system norms are shown as a function of ROM order.*

In conducting the BT approach for sensor selection, it is useful to evaluate system norms for the error dynamics associated with reduced-order balanced-truncation models as a function of model order r_{BT}. In the present study, the actuator dynamics are non-trivial—they are modeled with integral effect—and so the balancing transformation and associated model reduction procedure are specifically conducted only with respect to the input-output response of the fluid dynamic states $[\hat{\boldsymbol{v}}, \hat{\boldsymbol{\eta}}]^T$. Both the $\mathcal{H}_2$- and $\mathcal{H}_\infty$-norm of the error system are reported in figure 6.4, for each of the three disturbances considered. As expected, both system norms decrease with increasing model order. In fact, it is possible to find r_{BT} such that both system norms are less than a tolerance value err, where err is small. This indicates that the BT procedure will be able to identify a sparse sensor configuration for each disturbance by which SOF-LQR control will be able to recover full-information LQR control performance.

In the ensuing sections, we will analyze the sensor selection results from the CE and BT procedures more closely. We will do this for three types of disturbances: streamwise $(\alpha,\beta) = (1,0)$, oblique $(\alpha,\beta) = (1,1)$, and spanwise $(\alpha,\beta) = (0,2)$. In each case, the worst-case (TEG maximizing) disturbance associated with the specific control law will be considered.

6.4.1 Streamwise disturbance $(\alpha,\beta) = (1,0)$

The sensor configurations and the associated worst-case SOF-LQR control performance for streamwise disturbance with $(\alpha,\beta) = (1,0)$ are presented in figure 6.5. The maximum TEG of the full-information LQR controller (blue dotted line), the maximum TEG (G) for the SOF-LQR controlled flow are reported as a function of the number of sensors in figure 6.5a, with CE configurations denoted as red crosses and BT configurations as green dots. From this analysis, we see that SOF-LQR control recovers full-information LQR TEG performance when $r_{BT} \geq 6$ sensors are used based on the BT approach. Using the CE approach, SOF-LQR TEG performance recovers to within 5% of the full-information LQR TEG when $r_{CE} \geq 14$ sensors are used. In this case, the sufficiently rich library of candidate sensors C_n was constructed using only $\hat{\boldsymbol{v}}$ sensors. As such, the observed differences between the sensor configurations from BT and CE is purely due to the locations of these sensors. The specific sensor configurations obtained by the CE and BT sensor selection methods are illustrated in figure 6.5b and figure 6.5c respectively. By both approaches, the near-wall sensors are identified as important for the control starting with as few as $r_{CE} = r_{BT} = 3$ sensors. Except for the case with $r_{CE} = 9$, all the sensors selected by the CE approach are located either close-to-wall or clustered symmetrically about the channel centerline in the range $|y/h| = [0.77, 0.84]$. In contrast, the BT approach tends to yield asymmetrical arrangements in the

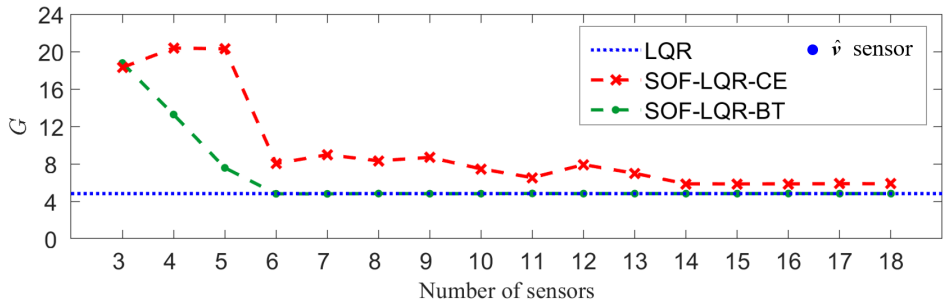
channel and distributes sensors more uniformly between the channel walls. That said, BT does tend to place a higher concentration of sensors in a similar range as that of the CE from $|y/h| = [0.79, 1)$. As we will see, near-wall $\hat{\boldsymbol{v}}$ information also tends to be important for performance recovery due to oblique and spanwise disturbances as well.

We further investigate control performance for streamwise disturbances using the CE sensor configuration for $r_{CE} = 14$ and the BT sensor configuration for $r_{BT} = 6$. The sensor locations along with the optimal disturbance profiles for the SOF-LQR controllers leading from the CE and BT sensor arrangements are shown in figure 6.6. As can be seen here, the SOF-LQR controllers designed for sensor configurations from the CE and BT approaches yield similar optimal disturbance profiles as the full-information LQR controller. The sensors selected by the CE approach capture the near-wall spatial features of the $\hat{\boldsymbol{v}}$ disturbance profile. The BT approach yields sensors arrangements that tend to capture spatial features throughout the channel. Interestingly, the largest qualitative differences in the SOF-LQR optimal disturbance profiles arise in $\hat{\boldsymbol{u}}$, even though the sensor configurations are restricted to only $\hat{\boldsymbol{v}}$ sensors. These differences—compared to the full-information case—are most visually prominent near the centerline for the BT configuration and near the walls for the CE configuration.

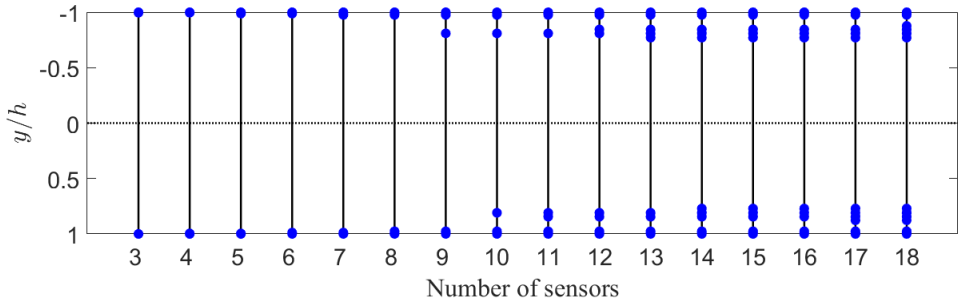
6.4.2 Oblique disturbance $(\alpha, \beta) = (1, 1)$

Sensor configurations and the associated worst-case SOF-LQR control performance for oblique disturbances with $(\alpha, \beta) = (1, 1)$ are reported in figure 6.7. Figure 6.7a illustrates the maximum TEG (G) performance as a function of the number of sensors associated with the sensor configurations determined by CE (red cross) and BT (green dots) methods relative to the full-information LQR control performance (blue dotted line). The CE and BT approaches both recover full-information LQR performance when at least $r_{CE} = 14$ and $r_{BT} = 13$ total sensors are used, respectively. In figure 6.7b and figure 6.7c, the specific sensor configurations obtained by the CE and BT sensor selection methods are reported. Note that both approaches were applied to the same candidate library of streamwise ($\hat{\boldsymbol{u}}$) and wall-normal ($\hat{\boldsymbol{v}}$) sensors. The BT method identifies both streamwise and wall-normal velocity sensors as important; whereas, the CE approach identifies that only wall-normal velocity sensors are important. In both approaches, the near-wall wall-normal velocity sensors are immediately identified as important for control, starting with $r_{CE} = r_{BT} = 2$ sensors. As the number of sensors is increased, the CE approach identifies wall-normal velocity sensors in the range $|y/h| = [0.48, 0.63]$ as important. In contrast, the BT approach does not select any $\hat{\boldsymbol{v}}$ sensors far from the walls until at least $r_{BT} \geq 11$ sensors are to be used. Instead, the BT approach tends to place $\hat{\boldsymbol{u}}$ sensors at or near the centerline of the channel. When $r_{BT} = 7$ or greater, SOF-LQR control based on the BT sensor arrangement yields TEG performance comparable to the full-information LQR controller. This appears to be due to the placement of $\hat{\boldsymbol{u}}$ sensors in the range $|y/h| = [0.5, 1)$. The CE approach requires more sensors for this performance recovery. For SOF-LQR controllers based on the CE approach, TEG performance is comparable to the full-information LQR control when $r_{CE} \geq 13$. As in the BT case, the CE approach finds that information in the approximate range $|y/h| = [0.5, 1)$ is important for recovering this performance, except now it is $\hat{\boldsymbol{v}}$ information that is deemed important.

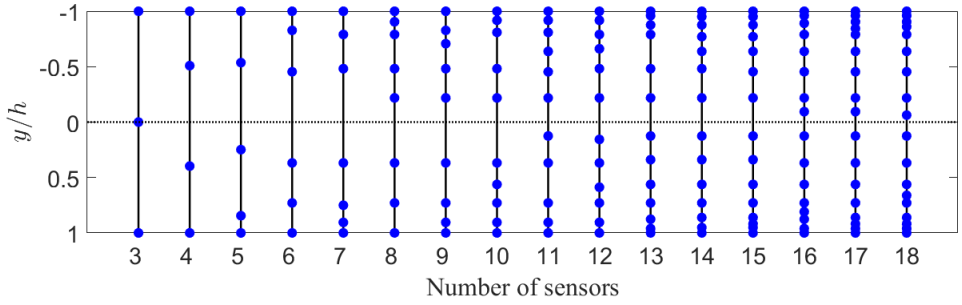
We will investigate control performance for oblique disturbances in the remainder using the CE sensor configuration for $r_{CE} = 14$ and the BT sensor configuration for $r_{CE} = 13$. The optimal disturbance profile leading to the maximum TEG for controllers based on these CE and BT sensor arrangements are reported in figure 6.8. Similar to the streamwise disturbance case, the SOF-LQR



(a) Maximum TEG (G) versus number of sensors.



(b) Sensor locations from CE approach.



(c) Sensor locations from BT approach.

Figure 6.5: *Controller performance and sensor configurations for worst-case streamwise disturbances with* $(\alpha, \beta) = (1, 0)$.

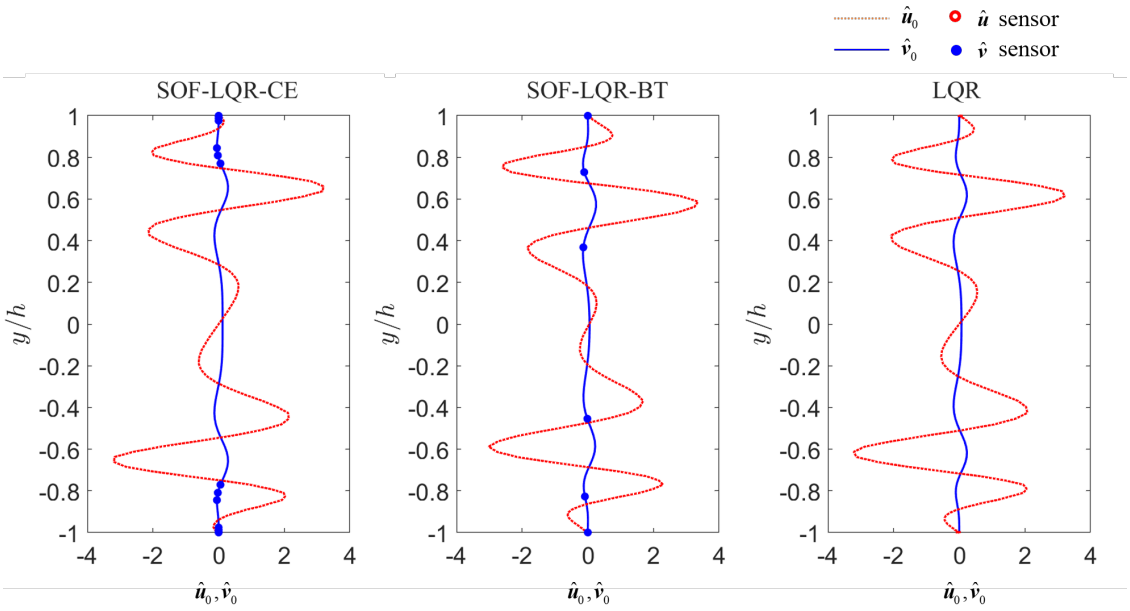
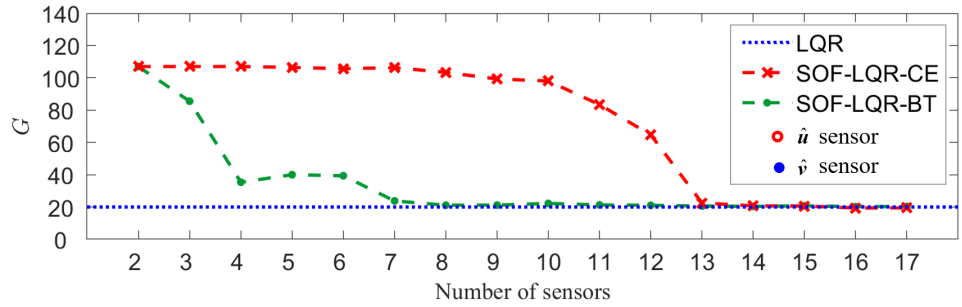


Figure 6.6: *The final selected sensor locations along with the optimal disturbance profile for wavenumber pair* $(\alpha, \beta) = (1, 0)$. *Sensor number* $r_{CE} = 14$, $r_{BT} = 6$.

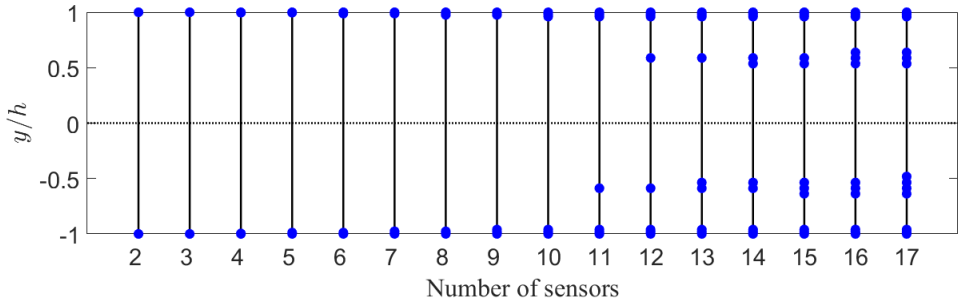
optimal disturbance profiles from both the CE and BT sensor configurations are qualitatively similar to the full-information LQR optimal disturbance profiles. In both the CE and BT approaches, the placement of $\hat{\boldsymbol{v}}$ sensors indicates that near-wall wall-normal velocity information is important. In the CE case, the $\hat{\boldsymbol{v}}$ sensors capture the dominant spatial features of the $\hat{\boldsymbol{v}}$ disturbance profile. The distribution of $\hat{\boldsymbol{v}}$ sensors along the interior of the channel suggests that spatial derivatives $\hat{\boldsymbol{v}}$ are important. In contrast, the BT approach introduces only a single $\hat{\boldsymbol{v}}$ sensor away from the walls, which captures information near the spatial peak in the optimal wall-normal velocity disturbance profile. The BT approach emphasizes sensors that capture the prominent spatial features of the $\hat{\boldsymbol{u}}$ optimal disturbance profile.

6.4.3 Spanwise disturbance $(\alpha, \beta) = (0, 2)$

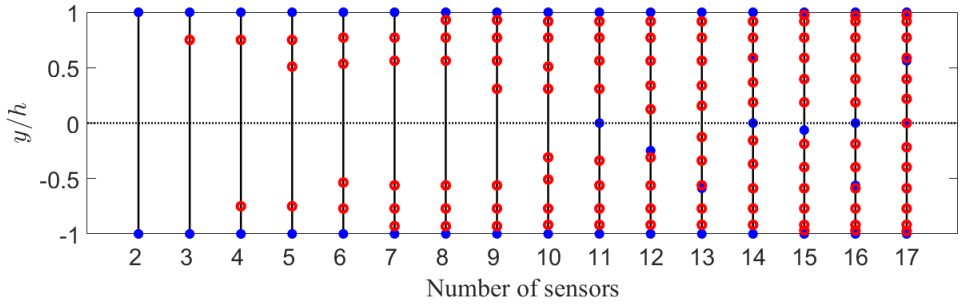
Sensor configurations and the associated worst-case SOF-LQR control performance for spanwise disturbances with $(\alpha, \beta) = (0, 2)$ are reported in figure 6.9. The maximum TEG (G) for the controlled flow is reported as a function of the number of sensors for sensor configurations determined by CE (red crosses) and BT (green dots) methods in figure 6.9a. These are compared with the maximum TEG (G) for the full-information LQR controller (blue dotted line). From this analysis, it is evident that the BT approach yields a controller that recovers—at least approximately—the full-information control performance when $r_{BT} \geq 10$. In contrast, the CE approach requires $r_{CE} \approx 32$ sensors to get within 1% of the full-information TEG performance. Investigating the specific sensor configurations obtained by the CE and BT sensor selection methods—see figures 6.9b and 6.9c, respectively—provides some guidance on why this way be the case. The BT method identifies both streamwise and wall-normal velocity sensors as important; whereas, the CE approach identifies that only wall-normal velocity sensors are important. Even more significant, the BT approach immediately ($r_{BT} = 2$) identifies that near-wall sensors are important for control. In contrast, CE does not identify this same near-wall information as important until $r_{CE} \geq 32$. Up until $r_{CE} = 32$, all of the sensors from the CE approach are clustered symmetrically about the channel center



(a) Maximum TEG (G) versus number of sensors.



(b) Sensor locations from CE approach.



(c) Sensor locations from BT approach.

Figure 6.7: *Controller performance and sensor configurations for worst-case oblique disturbances with* $(\alpha, \beta) = (1, 1)$.

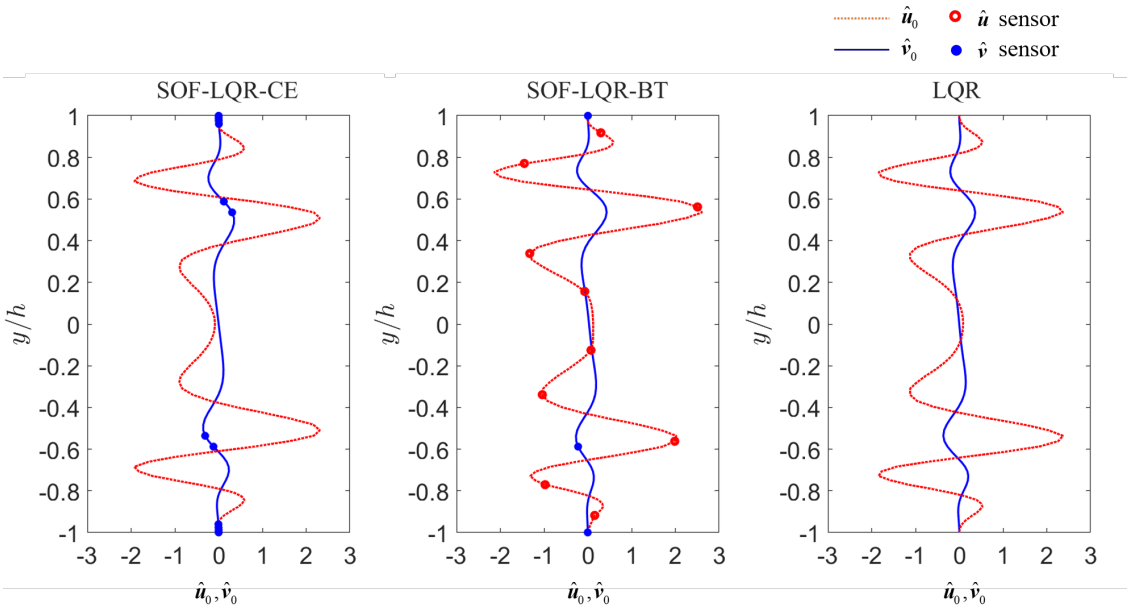


Figure 6.8: *The final selected sensor locations along with the optimal disturbance profile for wavenumber pair* $(\alpha, \beta) = (1, 1)$. *Sensor number* $r_{CE} = 14$, $r_{BT} = 13$.

line in the range $| \ y/h \ | = [0.187, 0.588]$. The BT approach does not always yield asymmetric sensor arrangement, but the sensors are more evenly distributed throughout the interior of the channel. Given the TEG performance achieved with these sensor configurations, it is evident that wall-normal information in the vicinity of the walls and at the channel center line are important for TEG reduction for spanwise disturbances. Wall-normal velocity information at the center line is important, as the introduction of such a sensor allows the BT approach to recover full-information control performance with $r_{BT} = 10$ sensors. In some of the BT arrangements, the center line $\hat{\boldsymbol{v}}$ sensor is replaced by or augmented with a $\hat{\boldsymbol{u}}$ sensor. In these cases, a pair of $\hat{\boldsymbol{v}}$ sensors tend to appear asymmetrically about the center line.

We note that the resulting asymmetric placement of sensors about the centerline in the BT approach is related to the numerical setup in the column-pivoted QR factorization. Specifically, in step 3 of Algorithm 3, the set of linearly independent rows in C_b—i.e., choice of sensors—is not unique, and the QR factorization yields one instantiation of a linearly independent set. Additionally, in this study, the candidate sensor library was constructed using velocity sensors located at Chebyshev points, which are especially dense in the vicinity of the channel walls. Thus, even though asymmetries arise in the resulting placement of sensors near the walls, this asymmetry tends to be within y/h=0.01 from an exactly symmetric placement. In cases where symmetry is required, we expect that this issue can be resolved by imposing constraints within the column-pivoted QR factorization and/or by ensuring that the candidate library includes sensors with adequate differences in type and location.

We will investigate control performance for spanwise disturbances in the remainder using the CE sensor configuration for $r_{CE} = 32$ and the BT sensor configuration for $r_{BT} = 16$. Note that the choice of $r_{BT} = 16$ is motivated by the fact that the direct numerical simulations in section 6.5 run to completion more quickly for this case than for $r_{BT} = 10$. The optimal disturbance profile leading to the maximum TEG for controllers based on these CE and BT sensor arrangements are

(α, β)	Balanced Truncation	Gain Column Norm Evaluation
(1,0)	0 u-sensors 6 v-sensors	0 u-sensors 14 v-sensors
(1,1)	10 u-sensors 3 v-sensors	0 u-sensors 14 v-sensors
(0,2)	11 u-sensors 5 v-sensors	0 u-sensors 32 v-sensors

Table 6.1: *Sensor configurations used for detailed performance evaluation.*

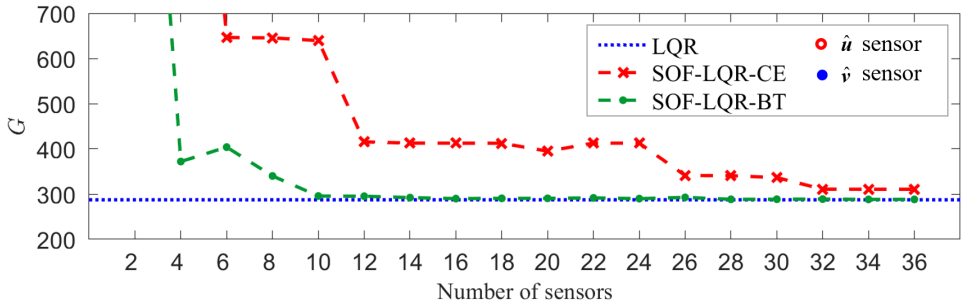
reported in figure 6.10. Interestingly, the optimal disturbance profiles for the SOF-LQR controllers are strikingly similar to one another and to the optimal disturbance profile for the full-information LQR controller—even more so than in the previous cases considered for streamwise and oblique disturbances. In some sense, this is to be expected based on previously reported findings regarding the $(\alpha, \beta) = (0, 2)$ disturbance case. This wave-number pair exhibits the highest TEG among all wave-number pairs, and is the least affected by control [54, 80, 82]. In both the CE and BT approaches, we see that the $\hat{\boldsymbol{v}}$ sensors capture the dominant spatial features of the $\hat{\boldsymbol{v}}$ disturbance profile. However, only the BT sensor placements are able to capture the spatial profile associated with the $\hat{\boldsymbol{u}}$ component of the optimal disturbance. Although the $\hat{\boldsymbol{u}}$ component is smaller in magnitude compared with the $\hat{\boldsymbol{v}}$ component, this has an important consequence for TEG control performance.

6.4.4 Controller robustness analysis

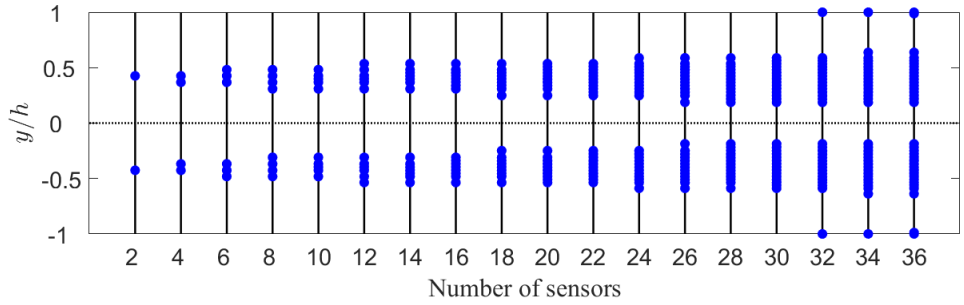
Up to this point, all of the control performance analysis has been conducted for nominal conditions at $Re = 3000$. In this section, we will investigate the robustness of the TEG reduction when the controllers designed for $Re = 3000$ are applied at "off-design" sub-crital Re values. The specific sensor arrangements we will investigate here correspond to the cases with a corresponding detailed analysis in the sections above. These are summarized in table 6.1.

To investigate robust TEG performance, we again consider closed-loop system responses for optimal perturbations that result in the maximum TEG (G) for a given closed-loop system with control applied at the off-design Re. Results for SOF-LQR controllers designed at $Re = 3000$ then applied at $Re = [500, 5500]$ are reported in figure 6.11. The performance of both controllers at off-design Reynolds numbers is strikingly similar to the corresponding performance at on-design conditions at Reynolds numbers higher than 1000. These results demonstrate that SOF-LQR controllers can be designed based on BT and CE sensor arrangements *robustly* recover full-information LQR control performance; however, this robustness is not unconditional.

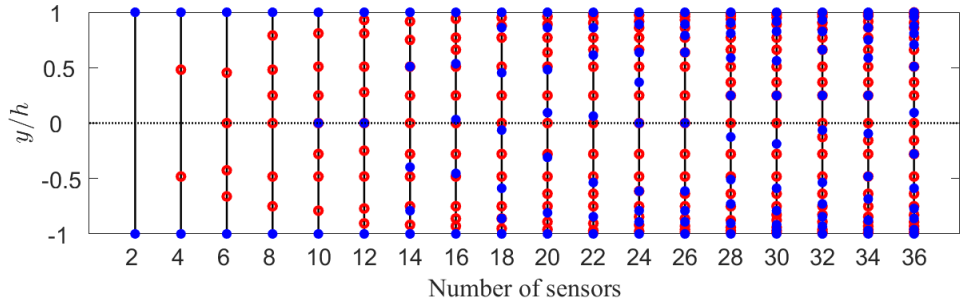
For streamwise wave disturbances at $Re \leq 500$, the SOF-LQR controllers designed for $Re = 3000$—using either CE or BT sensor arrangements—fail to reduce TEG relative to the uncontrolled flow. For spanwise wave disturbances at $Re \leq 1000$, the SOF-LQR designed for $Re = 3000$ based on the BT sensor arrangement lacks the same robust performance recovery characteristics as the CE sensor arrangement. In fact, the BT arrangement fails to reduce TEG relative to the uncontrolled



(a) Maximum TEG (G) versus number of sensors.



(b) Sensor locations from CE approach.



(c) Sensor locations from BT approach.

Figure 6.9: *Controller performance and sensor configurations for worst-case spanwise disturbances with* $(\alpha, \beta) = (0, 2)$.

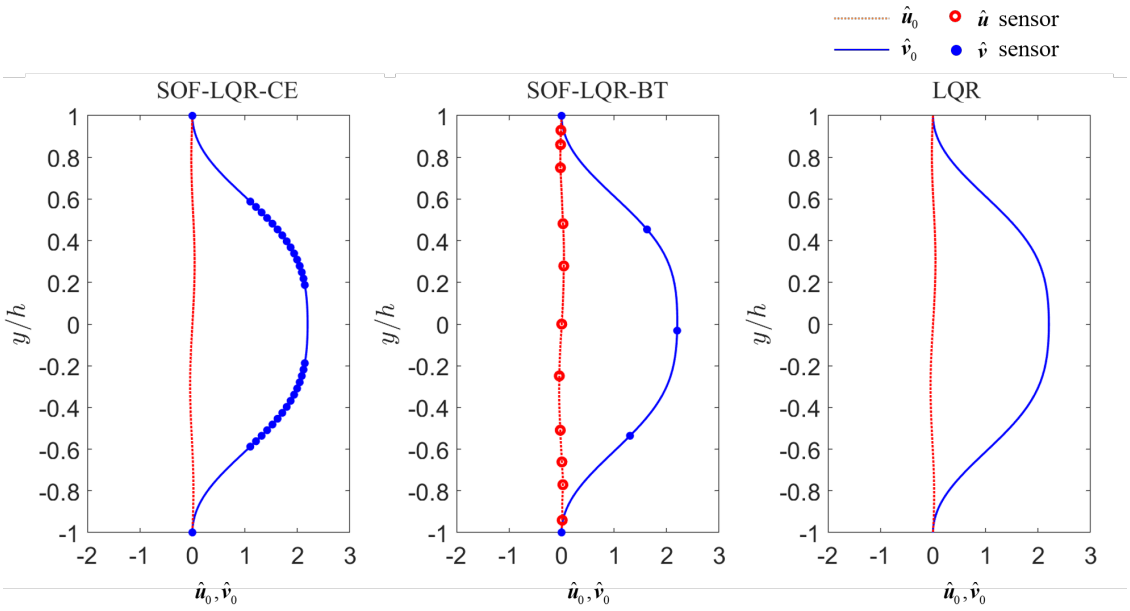
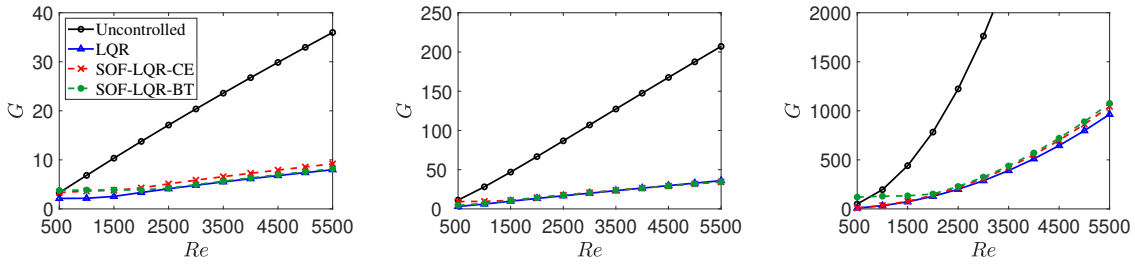


Figure 6.10: *The final selected sensor locations along with the optimal disturbance profile for wavenumber pair* $(\alpha, \beta) = (0, 2)$. *Sensor number* $r_{CE} = 32$, $r_{BT} = 16$.



(a) $(\alpha, \beta) = (1, 0)$
$r_{CE} = 14$, $r_{BT} = 6$

(b) $(\alpha, \beta) = (1, 1)$
$r_{CE} = 14$, $r_{BT} = 13$

(c) $(\alpha, \beta) = (0, 2)$
$r_{CE} = 32$, $r_{BT} = 16$

Figure 6.11: *Robustness analysis*

flow at $Re \leq 500$. However, designs based on the CE sensor arrangement maintain the TEG reduction even at these lower Reynolds numbers. As the TEG under smaller Reynolds number is relatively low, it is not surprising that the TEG reduction ability also decreases. Though there are fewer chances that the transition will happen compared to higher Reynolds numbers, this suggests that we need to design the SOF-LQR controllers separately for TEG reduction at low Reynolds numbers. Indeed, SOF-LQR controllers designed using either BT and CE sensor arrangements at "on-design" conditions would recover the full-information LQR performance and reduce TEG relative to the uncontrolled flow.

6.5 Results: nonlinear performance analysis using direct numerical simulations

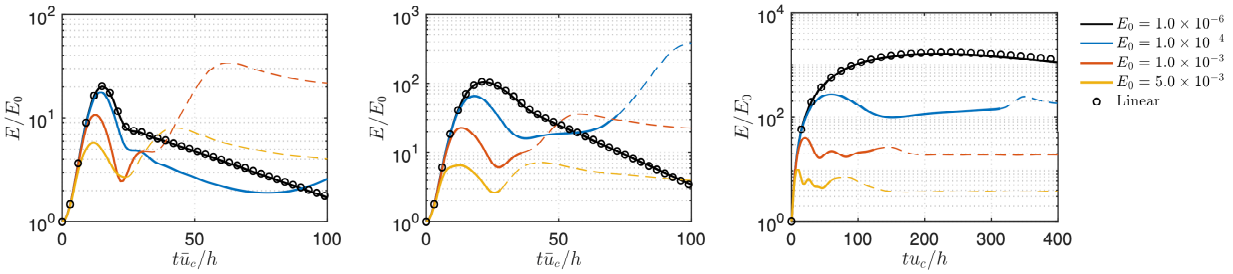
Sensor selection for controller performance recovery was investigated using linear analysis in the previous section. Here, we are interested in determining the reliability of the resulting sensor-based output feedback control laws for transient energy growth reduction and transition control in the

nonlinear setting. To this end, three-dimensional direct numerical simulations of plane Poiseuille flow at $Re = 3000$ are performed using a modified version of the spectral code *Channelflow* [65, 66] to solve the incompressible Navier–Stokes equations. A second-order semi-implicit Crank-Nicolson Runge–Kutta temporal scheme is used. In past studies, the domain size is usually set to fit one wavelength of the wavenumber of interest for each direction. However, as the transition includes large-scale deformation of the original perturbation structures, the underlying physics during the transition processes cannot be fully captured with a limited domain size. Hence, we use a rectangular computational domain of size $8\pi h \times 2h \times 2\pi h$ in x-, y- and z-directions, respectively, which is relatively large in space to capture a broader extent of flow physics involved in the transition process. This provides a more realistic setting to assess transition control performance. To discretize the flow field, $N = 101$ Chebyshev points are specified in the y-direction, and 128×64 points are uniformly spaced along x- and z- directions, respectively. Periodic boundary conditions are assumed in the x- and z-directions in which the flow variables (velocity and pressure) are represented by Fourier expansion. No-slip boundary condition is specified at upper and lower walls for the uncontrolled flow. In the controlled flow, wall-normal velocity $\boldsymbol{v}(\pm h)$ is determined via feedback control law, while streamwise and spanwise velocities are zeros at the walls. Moreover, a constraint of constant bulk velocity is specified. Grid resolution studies have been performed to ensure accuracy of results, as discussed in Appendix C.

Actuation in the form of blowing and suction in y-direction is implemented on the entire upper and lower walls via temporally changing amplitude of wall-normal velocity $\boldsymbol{v}(\pm h)$. Because the control strategy is designed based on the linear dynamical system discussed above, both actuation and measurement are associated with the same wavenumber pair (α, β) as the optimal perturbation, but implemented within the nonlinear simulations; this allows flow control mechanisms to be isolated and investigated. In practice, a bank of linear controllers over all wave number combinations would be most effective. However, we note that the need for such a bank of controllers would have practical ramifications on the sensor configuration as well, since the set of sensors required for control at different wavenumber pairs within the bank would not necessary overlap. Nonetheless, it may be possible to achieve the desired performance with a small number of controllers in this bank: LQR and SOF-LQR controllers designed at certain wavenumbers exhibit robust TEG reduction at "off-design" wave numbers, as reported in [73]. This suggests that a single sensor configuration designed for each of the three disturbance types (streamwise, spanwise, and oblique disturbances) may be sufficient to achieve transition control; however, we do not investigate this possibility further in this study. In all cases, the value of wall-normal velocity on walls is determined by the feedback control law described above in section 6.3.

In the linear analysis of section 6.4, characteristics of the optimal disturbance were examined solely using the linear dynamics. In the direct numerical simulations, baseline and controlled flows have an initial condition consisting of the base flow $[\bar{\boldsymbol{u}}, \bar{\boldsymbol{v}}, \bar{\boldsymbol{w}}] = [1 - (y/h)^2, 0, 0]$ and optimal disturbance $[\boldsymbol{u}'_0, \boldsymbol{v}'_0, \boldsymbol{w}'_0]$ with a small amplitude. The kinetic energy density of the initial optimal disturbance is denoted by E_0. Moreover, a random perturbation is also introduced with kinetic energy density of 1% of E_0 into the flow to expedite an emergence of a laminar-to-turbulent transition in the flows, but has negligible influence on the feature of the optimal disturbance [67].

Simulations of 200 convective time units of the streamwise and oblique disturbance responses require approximately 200 CPU hours, regardless of whether or not the flow transitions to turbu-



(a) $(\alpha, \beta) = (1, 0)$ **(b)** $(\alpha, \beta) = (1, 1)$ **(c)** $(\alpha, \beta) = (0, 2)$

Figure 6.12: *Transient energy growth of optimal disturbance with amplitude E_0. Dashed lines indicate that flow is turbulent state.*

lence. The spanwise disturbance case is comparatively more computationally intensive, requiring approximately 1000 CPU hours to fully resolve the evolution of the flow from transient energy growth through a possible transition to turbulence. This difference is primarily driven by the fact that the transient energy growth mechanism in the spanwise disturbance response evolves on a longer time-scale than the associated responses to streamwise or oblique disturbances.

6.5.1 Laminar-to-turbulent transition

Direct numerical simulations are performed with various optimal disturbance amplitudes for each wavenumber pair. As shown in figure 6.12, the transient energy growth density for the smallest disturbance amplitude considered overlaps the linear result. Moreover, we find that the amplification of initial disturbance is suppressed as the amplitude of disturbance increases and nonlinear effects become prominent. Although smaller transient energy growth is observed in the cases with larger initial disturbances, the laminar-to-turbulent transition still emerges as indicated by dashed lines in figure 6.12. Indeed, large values of the absolute transient energy E, rather than the amplification E/E_0, is more likely to lead to transition. This also indicates that for the same initial disturbance, an ability to reduce the transient amplification can serve to suppress the laminar-to-turbulent transition.

6.5.2 Transition suppression

In the controlled flow, the sensor selection strategy evaluated in the direct numerical simulations are listed in table 6.1. These strategies require the least number of sensors in output feedback control to recover the full-state LQR control performance in terms of reducing transient energy growth. For the streamwise disturbance with $(\alpha, \beta) = (1, 0)$, the threshold of minimal seed that leads to a laminar-to-turbulent transition increases from $E_0 = 1.0 \times 10^{-4}$ to $E_0 = 1.0 \times 10^{-3}$. For the oblique disturbance, the threshold increases from $E_0 = 5.0 \times 10^{-5}$ to $E_0 = 5.0 \times 10^{-4}$. However, for the spanwise disturbance, the controllers do not suppress transition, and actually lead to an earlier emergence of transition. This occurs for the full-information controller as well [80]. Although TEG performance is recovered, this case shows that TEG reduction is not the only objective to be considered when it comes to transition control.

Oblique and streamwise disturbances

Because the transition and control mechanisms in oblique $(\alpha, \beta) = (1, 1)$ and streamwise $(\alpha, \beta) = (1, 0)$ disturbances are similar, we will mainly use oblique case as an example to discuss how the controller modifies the flow and ultimately suppresses laminar-to-turbulent transition.

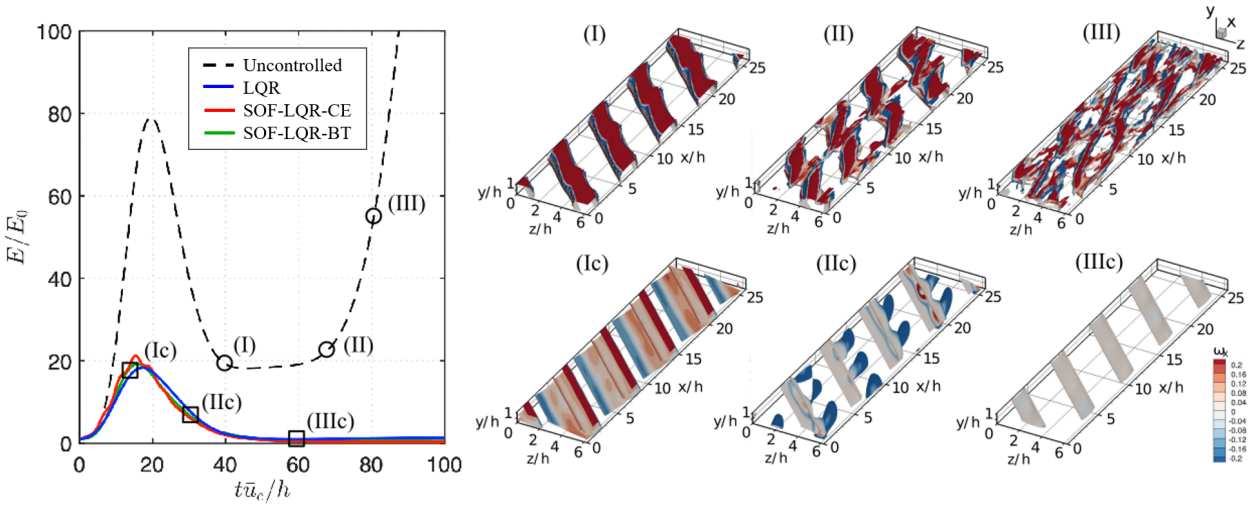


Figure 6.13: *In the oblique case, transient energy growth energy of uncontrolled flow and controlled flows ($E_0 = 5\times10^{-5}$) with controllers designed from LQR, balanced truncation, and gain column norm evaluation methods. Inserts are corresponding iso-surface of Q-criterion [70] colored by streamwise vorticity ω_x.*

In the case of oblique disturbance with optimal disturbance amplitude of $E_0 = 5 \times 10^{-5}$, the transient energy growth density reaches maximum amplification of $E/E_0 \approx 80$ at $t\bar{\boldsymbol{u}}_c/h = 20$ as shown in figure 6.13. Representative flowfields at different stages are displayed to illustrate the transition mechanism. Before stage (I), oblique coherent structures develop from small to large scale as transient energy grows. At stage (I), although the transient increase of perturbation kinetic energy has decreased to a relatively lower value, a large value of streamwise vorticity is observed along the oblique coherent structures near the wall. At stage (II), streamwise vortical structures start to grow stemming from the oblique coherent structures. As these structures develop, they interact with each other and break down into small scale structures. From this, a laminar-to-turbulent transition emerges at stage (III). In all the three controlled flows, the maximum transient energy growth densities are reduced to $E/E_0 \approx 20$ around $t\bar{\boldsymbol{u}}_c/h = 18$, and their trajectories are similar. The control mechanism is similar among the SOF-LQR controllers based on BT and CE sensor configurations and the full-information LQR controller. Here we use snapshots of flow fields with the SOF-LQR controller designed using the sensor configuration from the BT method as an example in figure 6.13. At stage (Ic) in the controlled flow, the coherent structures remain almost uniform in the oblique direction, with smaller values of streamwise voriticty generated near the walls. As transient energy decreases at stage (IIc), the only oblique structures observed in figure 6.13 are induced from the wall actuation. As time further elapses, the streamwise vortical structures decay and actuation amplitude also decreases, ultimately suppressing the transition observed in the uncontrolled flow.

Friction velocity has been used as a quantity to identify the laminar-to-turbulent transition in the flow, which is defined as

$$u^* = \sqrt{\frac{\tau_w}{\rho}}, \tag{6.22}$$

where $\tau_w = \mu(\partial u/\partial y)$, μ is dynamic viscosity, and the density ρ is set to one for the incompressible flow. The friction velocity at the lower wall is calculated using mean flow quantity. The time-history

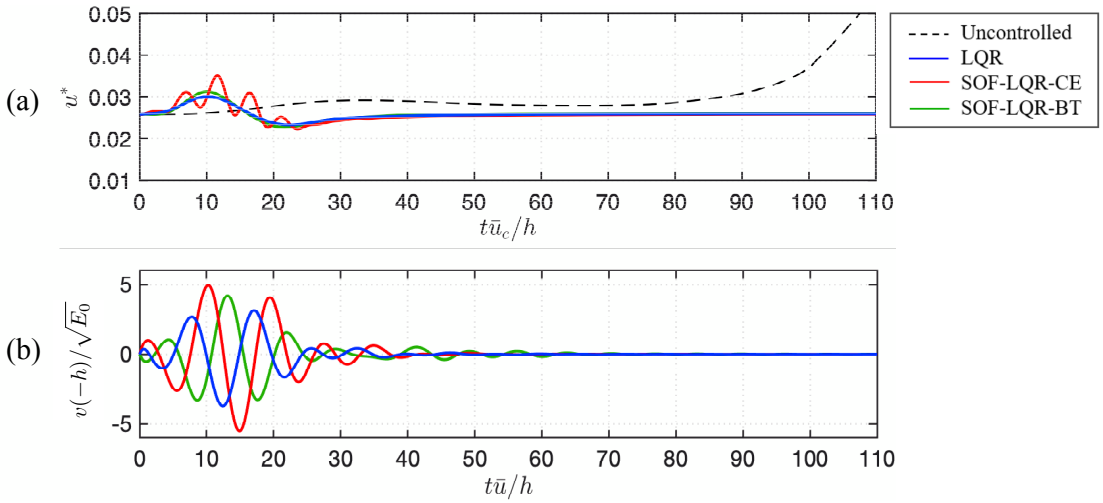


Figure 6.14: *(a) Friction velocity and (b) Fourier coefficient of wall-normal velocity boundary condition $v(-h)$ at lower wall of flow ($E_0 = 5 \times 10^{-5}$) with $(\alpha, \beta) = (1, 1)$.*

of the friction velocity for uncontrolled and controlled flows are shown in figure 6.14. A sudden increase in friction velocity in the uncontrolled flow (see figure 6.14 (a)) indicates an emergence of the transition. In the controlled flows, the actuation is turned on to introduce blowing and suction during the transient energy growth period (see figure 6.14). Correspondingly, we also observed that the friction velocity varies as the actuation is active. As the kinetic energy grows, the friction velocity increases. When the kinetic energy decreases, the friction velocity reduces to a lower value and then stays at a constant value. Particularly, the friction velocity with the controller designed using the CE sensor configuration has a high-frequency oscillation during the transient process, but the general trend is similar to the other two controlled cases.

Slices of uncontrolled and controlled flowfields are displayed in figure 6.15 to show modifications of the flow features due to wall actuation. The slices are extracted at convective time of $t\bar{\boldsymbol{u}}_c/h = 18$, when the kinetic energy density reaches its maximum value. In the uncontrolled flow, large wall-normal velocity fluctuations reside in the center between the upper and lower walls. The size of the coherent structures highlighted by Q-criterion is about half height of the channel as the transient energy grows. From the flowfields shown in figure 6.13 and our previous study [80], the existence of these large coherent structures induces a large value of streamise vorticity and generates streamwise vortical structures. Once these vortical structures break down, a transition to turbulence emerges. In all the three controlled flows, we observed that the wall-normal velocity actuation modifies the pattern of velocity flowfields and changes the distribution of high-shear regions. This change of flow hinders the formation of large coherent structure, which in turn prevents laminar-to-turbulent transition from arising in the flow.

Spanwise disturbance

In the cases with spanwise $(\alpha, \beta) = (0, 2)$ optimal disturbance considered in the present work, none of the controllers increase the threshold of laminar-to-turbulent transition. In fact, the controllers actually worsen the transition scenario. As shown in figure 6.16 (a) of case with $E_0 = 5\times10^{-5}$, there is no laminar-to-turbulent transition in the uncontrolled flow, but the controllers trigger the transition. While the controller is active, actuation amount in the form of blowing and suction gradually decreases as shown in figure 6.16 (b). As being closely examined in our previous

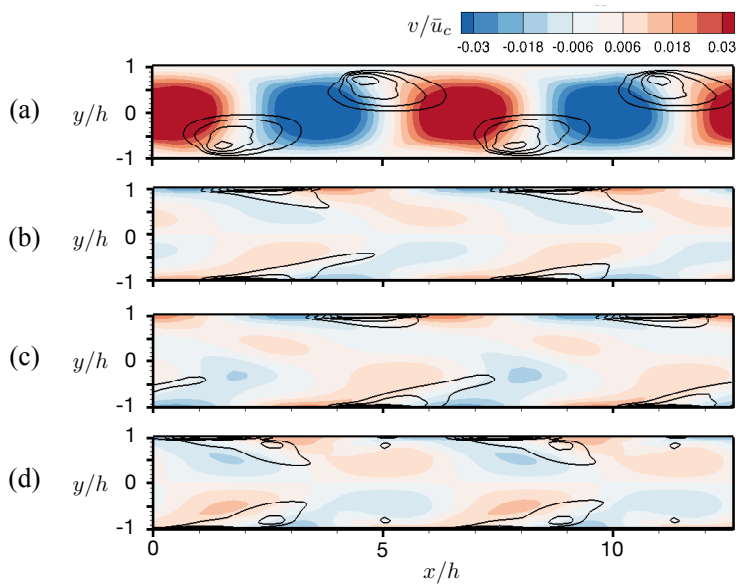


Figure 6.15: *Contours of wall-normal velocity and Q-criterion over a range of [0.01, 0.05] at slice of $z/h = 0$ of flow ($E_0 = 5 \times 10^{-5}$) with $(\alpha, \beta) = (1, 1)$ at $t\bar{u}_c/h = 18$ (a) Uncontrolled flow, and controlled flow with controller designed by (b) LQR, (c) balanced truncation, and (d) gain column norm evaluation methods.*

study [80], the control input introduces streamwise vortices near walls, which hinder the merging process of vortex pairs in the center of the channel, resulting in a reduction of transient energy growth. However, the control input creates high-shear regions near the wall where secondary instabilities creep in and cause a laminar-to-turbulent transition. This phenomenon suggests that decreasing transient energy growth from linear analysis is not sufficient to suppress (or even delay) the transition.

Interestingly, using the same objective function, but limiting the information available for static output feedback control to wall shear stress measurements only, actually enables transition suppression in this case, and transition delay for large amplitude disturbances [73] as shown in figure 6.17 (a). During the time period considered in the present study, the SOF-LQR controller does not worsen the transition and leads to a lower friction velocity compared to uncontrolled flow. As seen in figure 6.17 (b), the normalized actuation velocity is smaller than the one shown in figure 6.16. Correspondingly, the reduction of transient energy growth with SOF-LQR control with only shear stress measurements is roughly 40% of the reduction achieved by full-information LQR with respect to maximum transient energy growth (see figure 6.17 (c)). This SOF-LQR with shear-stress sensors at the walls is able to modify the flow sufficiently to delay transition and does so with a gentle actuation such that the control does not trigger other instabilities in the nonlinear flow that cause a transition.

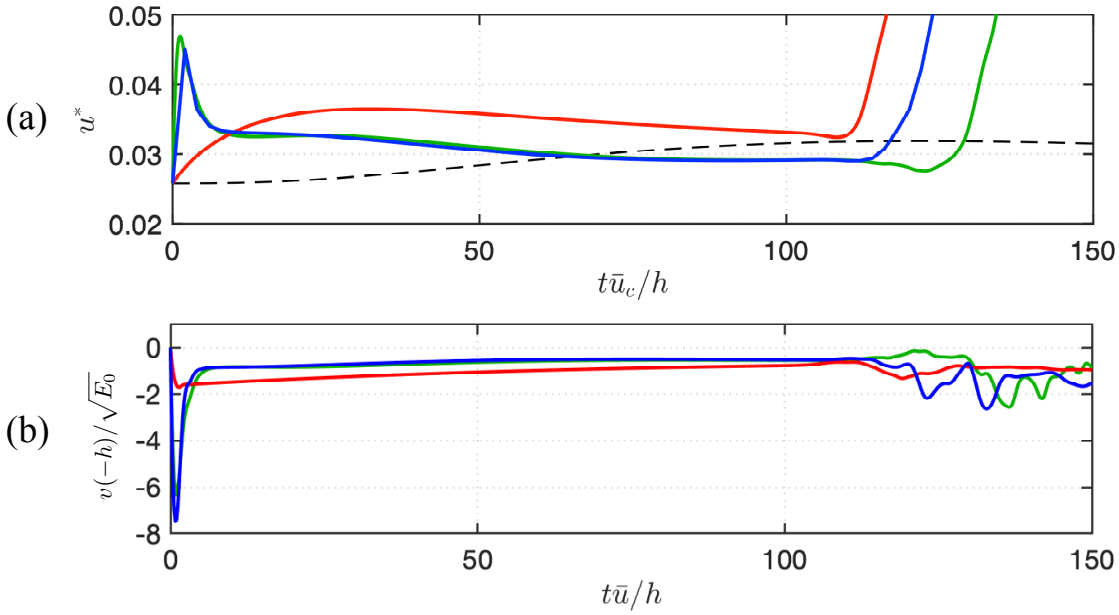


Figure 6.16: *(a) Friction velocity and (b) Fourier coefficient of wall-normal velocity boundary condition $v(-h)$ at lower wall of flow ($E_0 = 5 \times 10^{-5}$) with $(\alpha, \beta) = (0, 2)$.*

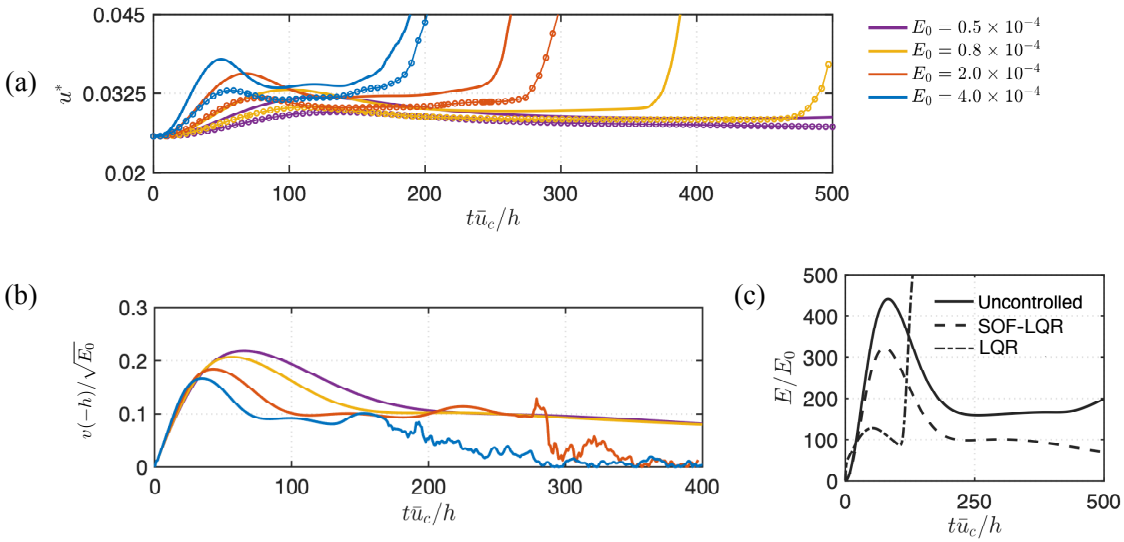


Figure 6.17: *With only shear-stress sensors at the walls, (a) friction velocity of uncontrolled and controlled cases. Solid line with circles represents controlled case.*
(b) Fourier coefficient of wall-normal velocity boundary condition $v(-h)$ in controlled flows. (c) Transient energy growth of uncontrolled and controlled flow with disturbance amplitude of $E_0 = 5 \times 10^{-5}$.

6.6 Discussion and conclusions

In this chapter, we proposed and investigated two approaches for sensor selection to enable sensor-based output feedback controllers to recover full-information performance. Both approaches leveraged the fact that, with a sufficiently rich set of sensors, a static output feedback (SOF) controller can always be designed to recover full-information control performance exactly. Thus, we showed that the problem of sensor selection for performance recovery could be recast as a problem of sensor down-selection from a sufficiently rich library of candidate sensors. One approach for sensor selection was based on a column-norm evaluation (CE) of the SOF controller gain matrix used to achieve full-information performance; the other approach was based on a balanced truncation (BT) procedure for model order reduction of linear dynamic systems.

Both sensor-selection methods were demonstrated on the problem of transient energy growth (TEG) reduction and transition suppression in a channel flow at the sub-critical Reynolds number of $Re = 3000$ using linear quadratic optimal control strategies. All sensor-based output feedback controllers in this study were designed based on SOF-LQR synthesis and compared with full-information LQR controllers designed based on the same quadratic control objective. Based on linear performance analyses, both the CE and BT sensor selection approaches identified sensor configurations that enabled SOF-LQR control to recover full-information LQR control performance for optimal streamwise, oblique, and spanwise disturbances. In all cases where performance recovery was achieved, the optimal disturbance profiles for the SOF-LQR controlled flows were qualitatively similar to those for the full-information LQR controlled flows. These similarities were most striking in the case of spanwise disturbances, but all corroborate the fact that the dynamic responses of all of these controlled systems are approximately the same. Sensors selected by the BT and CE approaches tended to be placed in the vicinity of prominent spatial features associated with these optimal disturbance profiles. Further, we found that SOF-LQR controllers designed based on these sensor configurations also exhibited robustness to variations in the Reynolds number. Controllers designed for $Re = 3000$ continued to achieve comparable worst-case TEG performance to the full-information LQR controller when applied over a range of "off-design" sub-critical Reynolds numbers.

In general, the BT approach required fewer sensors to recover full-information control performance compared to the CE approach. Wall-normal velocity information near the channel walls was consistently determined to be important for control performance by both methods over all disturbances considered. However, the arrangement and type of other sensors between the CE and BT approaches differed otherwise. Our results for the oblique and spanwise disturbance designs suggest that TEG control benefits from streamwise velocity information—more so than wall-normal velocity information—along the channel interior. For these cases, both streamwise and wall-normal velocity sensors were available in the candidate sensor library. Yet, the CE approach consistently removed streamwise velocity sensors in favor of wall-normal velocity sensors, which may contribute to the need for more sensors for performance recovery relative to the BT approach. The BT approach consistently yielded a heterogeneous set of sensors, with wall-normal velocity sensors near the walls and streamwise velocity sensors along the channel interior.

In addition to the linear analysis, we conducted direct numerical simulations (DNS) to evaluate control performance in the nonlinear setting. SOF-LQR controllers designed based on both sensor selection approaches continued to recover full-information controller performance in DNS. For streamwise and oblique disturbances, the SOF-LQR controllers successfully increased the distur-

bance energy threshold for transition by an order of magnitude. We found that control hindered the formation of large coherent structures, in part because actuation from the wall served to modify the shear distribution in the flow. With a reduced size of coherent structures, the amount of induced streamwise vortical streaks decreased and ultimately suppressed the transition that was observed in the uncontrolled flow. We also note that TEG reduction observed in linear analysis was not sufficient for preventing transition in the nonlinear simulations. The linear analysis missed the secondary instabilities that were excited by actuation in the case of spanwise disturbances. These nonlinear interactions promoted an earlier transition, even though the TEG was reduced. Controller designs that explicitly account for these nonlinear interactions should be investigated in future studies.

Finally, we note that the sensor selection methods presented here are more generally applicable to other performance objectives, sensor-types, and flow configurations. In addition, the sensor selection methods proposed here can provide insights into the most important sensors for closed-loop performance. This creates opportunities to guide the choice of sensors in the numerous applications where a complete recovery of full-information control performance is not required.

In addition, both the CE and BT approaches introduced for sensor selection in this study can be trivially extended to the problem of actuator selection, simply by considering the dual problem and a sufficiently rich library of candidate actuators. We hope that the promising results demonstrated in this chapter will lead to further adoption and refinement of these strategies into the future.

7 | Nonlinear MTEG Prediction and Control

The dynamics of transitional flows are governed by an interplay between the non-normal linear dynamics and quadratic nonlinearity in the incompressible Navier-Stokes equations. In this work, we propose a framework for nonlinear stability analysis that exploits the fact that nonlinear flow interactions are constrained by the physics encoded in the nonlinearity. In particular, we show that nonlinear stability analysis problems can be posed as convex feasibility and optimization problems based on Lyapunov matrix inequalities, and a set of quadratic constraints that represent the nonlinear flow physics. The proposed framework can be used to conduct global stability, local stability, and transient energy growth analysis. The approach is demonstrated on the low-dimensional Waleffe-Kim-Hamilton model of transition and sustained turbulence. Our analysis correctly determines the critical Reynolds number for global instability. For local stability analysis, we show that the framework can estimate the size of the region of attraction as well as the amplitude of the largest permissible perturbation such that all trajectories converge back to the equilibrium point. Additionally, we show that the framework can predict bounds on the maximum transient energy growth. Finally, we show that careful analysis of the multipliers used to enforce the quadratic constraints can be used to extract dominant nonlinear flow interactions that drive the dynamics and associated instabilities. Materials in this chapter are drawn heavily from [145–148].

7.1 Introduction

Many complex flow phenomena arise from the interplay between the non-normal linear dynamics and quadratic nonlinearity in the incompressible Navier-Stokes equations (NSE). In wall-bounded shear flows, the high-degree of non-normality of the linearized NSE results in a transient energy growth (TEG) of small flow perturbations [44, 74, 75], even when the dynamics are linearly asymptotically stable. As a result, the linear analysis tends to over predict the critical Reynolds number (Re_c) for instability in many shear flows [44, 74, 106]. The fact that the flow transitions at Reynolds numbers (Re) below the predicted linear stability limit is partly attributed to the non-modal growth that pushes the flow state away from the equilibrium base flow [44, 74, 75, 106]. Indeed, TEG is a necessary condition for transition [149, 150]. Nevertheless, non-modal TEG alone is not sufficient to cause transition: it is the interaction of non-modal TEG with the nonlinearity that triggers secondary instabilities and drives the state outside the region of attraction. Without the nonlinear terms, the notion of a finite region of attraction would not make sense. Interestingly, although the nonlinearity is lossless and energy-conserving [149, 151], it can interact with the linear dynamics in such a way as to increase the maximum transient energy growth (MTEG) that can be realized [152]. These transition scenarios cannot be fully analyzed without accounting for the nonlinear terms in the NSE.

Analysis methods have been proposed to account for the interplay between the linear and

nonlinear terms in transitional and turbulent flows. One such approach is the resolvent analysis framework [56, 153, 154], which leverages the fact that the NSE can be expressed as a feedback interconnection between a linear operator and a nonlinear operator—a so-called *Lur'e decomposition* [155]. Resolvent analysis goes a step further to consider the nonlinearity as an implicit forcing input on the linear dynamics [116, 153]. This perspective greatly simplifies the resulting analysis problem, as only the linear system—described by the input-output properties of the linear resolvent operator—needs to be analyzed. Within the context of turbulent flows, resolvent analysis provides information on how fluctuations in a time-averaged flow are attenuated or amplified from nonlinear effects. Resolvent analysis has been successfully employed in the study of various flows [156, 157], including pipe flows [158], open cavity flows [159], and flows over riblets [160].

Related methods have been proposed to account for the nonlinearity in NSE more directly. The passivity framework has been shown to be effective in flow control based on the nonlinear NSE [161–163]. In these studies, the passivity property [155] of the nonlinear terms in the incompressible NSE are leveraged to design a linear controller that can stabilize the system. Further advances have been made in input-output methods to study performance, worst-case amplification, stability, and transition for NSE using dissipation inequalities [164]. Dissipation inequalities derived from NSE can be posed as linear matrix inequality (LMI) problems, which are then solved using convex optimization methods to analyze various wall-bounded shear flows. These techniques generalize the classical energy-based analysis approaches [44, 165] and also have close ties with nonlinear Lyapunov stability analysis approaches developed for NSE based on sum-of-squares (SOS) optimization [166].

In this chapter, we propose an alternate framework for nonlinear stability analysis that uses quadratic constraints to account for nonlinear flow interactions with minimal complexity. The approach is predicated on the fact that nonlinear flow interactions are constrained by the physics encoded within the nonlinear terms in the incompressible NSE—e.g., the nonlinearity is quadratic, energy conserving, and lossless. Mathematically, these physics can be expressed as quadratic constraints between the inputs and outputs of the nonlinearity. In turn, these quadratic constraints serve as reduced-complexity models for the nonlinear terms, and can be incorporated within a Lyapunov-based analysis to perform reliable stability and input-output analysis in the nonlinear setting. The general framework introduced here is applicable to any system that has (non-normal) linear dynamics acting in feedback with a lossless nonlinearity—the incompressible NSE being a special case.

To establish a proof-of-concept, we formulate and demonstrate the proposed analysis framework on the nonlinear Waleffe-Kim-Hamilton (WKH) model of transition and sustained turbulence [149]. As with the NSE, the WKH model admits a Lur'e decomposition with non-normal linear dynamics and a quadratic lossless nonlinearity, making it relevant for formulating and demonstrating the proposed quadratic constraints framework for nonlinear stability analysis of fluid flows.

The chapter proceeds as follows. In Section 7.2, we introduce the WKH model in Lur'e form. We then introduce the quadratic constraints framework and associated stability analysis problem in Section 7.3. In Section 7.3.1, we account for the energy conserving nonlinearity in global stability analysis via the addition of a quadratic lossless constraint. In Section 7.3.2, we show that additional quadratic constraints can be introduced to conduct local stability analysis, which is needed when $Re > Re_c$ and the equilibrium point is no longer globally asymptotically stable. In

Section 7.4, we formulate the problem for obtaining the size of the largest permissible perturbation such that the state trajectories remain in the region of attraction. In Section 7.5, we formulate an analysis problem to determine bounds on the MTEG that can be realized by the system dynamics. In Section 7.6, we show that we can obtain insights into dominating nonlinear flow interactions that underlie the dynamics by analyzing the multipliers used to enforce the constraints within the analysis framework. Finally, we provide concluding remarks of our study in Section 7.7.

The section-wise specific contributions of this chapter are as follows:

1. Section 7.3.1: We find that the lossless constraint alone enables prediction of the Re_c for global instability, consistent with the Re_c found by other means in [150].
2. Section 7.3.2 and 7.3.3: The "local" quadratic constraints represent the influence of the nonlinearity when the flow is restricted to a local neighborhood about the equilibrium point. We also show that the local region corresponds to the region of attraction and study how the region of attraction changes with Re.
3. Section 7.4: We show that the proposed framework can be used to predict the size of largest permissible perturbation such that system stability is ensured (i.e., a "transition threshold"). We find that the size of the permissible perturbations decreases with increasing Re.
4. Section 7.5: The proposed framework can be used to estimate bounds for MTEG in the nonlinear system. We verify the results from the proposed framework with nonlinear simulations, which indicate that the bounds can be conservative.
5. Section 7.6: We demonstrate that—without any a priori knowledge—the proposed analysis approach is able to extract the same dominant nonlinear flow interactions whose physical importance is argued in [149, 150].

7.2 Waleffe-Kim-Hamilton Model of Transition and Sustained Turbulence

The Waleffe-Kim-Hamilton (WKH) model is a low-order mechanistic model for transition and sustained turbulence in shear flows. The model is based on observations from direct numerical simulations (DNS) of a plane Couette flow [167], and was introduced to highlight the importance of nonlinear interactions with the non-normal linear dynamics in the NSE. The WKH model was studied in greater detail by Waleffe in [150] and is given by,

$$\begin{bmatrix} \dot{u} \\ \dot{v} \\ \dot{w} \\ \dot{m} \end{bmatrix} = \frac{1}{Re}\begin{bmatrix} 0 \\ 0 \\ 0 \\ \sigma \end{bmatrix} - \frac{1}{Re}\begin{bmatrix} \lambda u \\ \mu v \\ \nu w \\ \sigma m \end{bmatrix} + \begin{bmatrix} 0 & 0 & -\gamma w & v \\ 0 & 0 & \delta w & 0 \\ \gamma w & -\delta w & 0 & 0 \\ -v & 0 & 0 & 0 \end{bmatrix}\begin{bmatrix} u \\ v \\ w \\ m \end{bmatrix}. \tag{7.1}$$

Here, Re denotes the Reynolds number; u represents the amplitude of the spanwise modulation of streamwise velocity; v represents the amplitude of the streamwise rolls; w represents the amplitude of the inflectional streak instability; and m represents the amplitude of the mean shear [150]. The constants λ, μ, ν, σ are positive parameters corresponding to viscous decay rates. The constants γ and δ represent nonlinear interaction coefficients and should have the same sign [150].

The WKH system in Eq. (7.1) captures the processes underlying sustained turbulence [150]: the rolls (v) create streaks (u) which eventually break down to maintain the rolls. In the WKH model, the mean shear m is not frozen in time and changes due to nonlinear interactions captured by the

$-vu$ term. A few important aspects of this model are that the instability w grows from the streaks u via the γwu interaction term. It can also be observed that the same instability feeds streamwise rolls by nonlinear quadratic interactions δw^2. The nonlinear couplings between w and v are important in sustaining turbulence [150]. As we will show in Section 7.6, the importance of these same interactions in driving instabilities can be identified from our proposed analysis framework.

The WKH model admits a laminar equilibrium point at $(u, v, w, m)_e = (0, 0, 0, 1)$. For the proposed stability analysis, we perform a change of coordinates to translate the equilibrium point of Eq. (7.1) to the origin. The equilibrium point in these new coordinates is $\mathbf{x}_e = (0, 0, 0, 0)$ and the state is $\mathbf{x} = (u, v, w, \bar{m})$, where $\bar{m} = m - 1$. The system in this translated coordinate system is,

$$\underbrace{\begin{bmatrix} \dot{u} \\ \dot{v} \\ \dot{w} \\ \dot{\bar{m}} \end{bmatrix}}_{\dot{\mathbf{x}}} = \underbrace{\begin{bmatrix} -\frac{\lambda}{Re} & 1 & & \\ & -\frac{\mu}{Re} & & \\ & & -\frac{\nu}{Re} & \\ & & & -\frac{\sigma}{Re} \end{bmatrix} \begin{bmatrix} u \\ v \\ w \\ \bar{m} \end{bmatrix}}_{A\mathbf{x}} + \underbrace{\begin{bmatrix} 0 & 0 & -\gamma w & v \\ 0 & 0 & \delta w & 0 \\ \gamma w & -\delta w & 0 & 0 \\ -v & 0 & 0 & 0 \end{bmatrix} \begin{bmatrix} u \\ v \\ w \\ \bar{m} \end{bmatrix}}_{N(\mathbf{x})=Q(\mathbf{x})\mathbf{x}}, \tag{7.2}$$

which makes the non-normality of the linear dynamics explicit [168].

The WKH system in Eq. (7.2) can be represented as

$$\dot{\mathbf{x}} = A\mathbf{x} + N(\mathbf{x}), \tag{7.3}$$

where the linear operator A is non-normal and asymptotically stable, and $N(\mathbf{x})$ is a quadratic nonlinearity given by $N(\mathbf{x}) = Q(\mathbf{x})\mathbf{x}$. Note that the nonlinear term is skew-symmetric: i.e., $Q(\mathbf{x}) = -Q(\mathbf{x})^T \in \mathbb{R}^{4\times 4}$. The linear and nonlinear terms can be partitioned into Lur'e form [155], with the two systems acting in feedback with each other (see FIG. 7.1):

$$\dot{\mathbf{x}} = L(\mathbf{x}, \mathbf{z}) := A\mathbf{x} + \mathbf{z} \tag{7.4a}$$

$$\mathbf{z} = N(\mathbf{x}) \tag{7.4b}$$

where $\mathbf{z} \in \mathbb{R}^4$. This Lur'e decomposition of the WKH system is denoted as an upper linear fractional transformation $F_u(L, N)$. The advantage of writing this system in a Lur'e form is that Eq. (7.4a) alone is a linear dynamical system with an input $\mathbf{z}$. Although $\mathbf{z}$ is a nonlinear forcing given by Eq. (7.4b), we can instead account for it using input-output properties of $\mathbf{z} = N(\mathbf{x})$. In this way, we are able to perform a nonlinear analysis of WKH model through analysis of linear dynamics in Eq. (7.4a) subject to constraints between $\mathbf{x}$ and $\mathbf{z}$ determined by Eq. (7.4b).

In all that follows, we study the proposed framework on the WKH system with two separate sets of parameters (see TABLE 7.1). Both sets of parameters have been investigated in prior studies: the Waleffe (W) parameters in [150], and the Baggett and Trefethen (B&T) parameters in [169]. The W and B&T parameters each yield different behaviors in the system dynamics, and the parameters chosen in this study result in notable differences in stability regions, permissible perturbation size, and transient energy growth [150, 169]. In the remainder of this work, the only parameter that is varied for stability and transient energy growth analysis is Re. Other choices of parameters are possible, and changing of the nonlinear interaction coefficients will lead to different types of bifurcations and correspondingly different stability regimes.

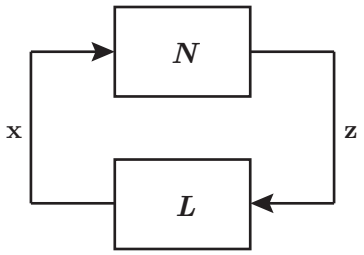


Figure 7.1: *Lur'e representation of the WKH system $F_u(L, N)$.*

Parameter set	Parameter Value					
	λ	μ	ν	σ	δ	γ
W [150]	10	10	15	10	1	0.1
B&T [169]	1	1	1	1	1	1

Table 7.1: *The two parameter sets and the value of the corresponding coefficients used in this work.*

7.3 Nonlinear Stability Analysis using Quadratic Constraints

Lyapunov stability methods [155] can be used to analyze the stability of a system given by Eq. (7.4). Here, the stability is analyzed around the equilibrium point $\mathbf{x}_e = \mathbf{0}$. To analyze stability using Lyapunov stability methods, we define a quadratic scalar energy function $V : \mathbb{R}^n \rightarrow \mathbb{R}$. The energy function $V(\mathbf{x}) = \mathbf{x}^T P\mathbf{x}$ is a candidate Lyapunov function [155]. From the Lyapunov stability theorem, the equilibrium point $\mathbf{x}_e = \mathbf{0}$ is globally asymptotically stable when $dV(\mathbf{x})/dt < 0 \; \forall \; \mathbf{x} \neq \mathbf{0}$, $t > 0$ and $P \succ 0$ *. In other words, the system is globally asymptotically stable around the equilibrium point $\mathbf{x}_e = \mathbf{0}$ if the energy continuously decreases in time. The time derivative of the Lyapunov function for the nonlinear system in Eq. (7.4), along trajectories of the system is given by:

$$\begin{aligned} \frac{d}{dt}V(\mathbf{x}) &= 2\mathbf{x}^T P(A\mathbf{x} + \mathbf{z}) \\ &= 2\mathbf{x}^T P(A\mathbf{x} + N(\mathbf{x})). \end{aligned} \tag{7.5}$$

Including the effects of N($\mathbf{x}$) to analyze stability is crucial to understanding the global asymptotic stability of the nonlinear system. However, accounting for the nonlinear term N($\mathbf{x}$) complicates the stability analysis and a quadratic Lyapunov function will not necessarily be a good choice as a candidate Lyapunov function. Here, we leverage the fact that the inputs and outputs of the nonlinearity N satisfy a set of quadratic constraints, thereby enabling stability analysis of the whole feedback interconnection $F_u(L, N)$ without the full complexity involved in an explicit treatment of the nonlinearity.

To do so, we first show that stability analysis benefits from consideration of the nonlinear term as energy conserving and lossless, neither producing nor dissipating energy. The lossless property can be represented as a quadratic constraint to represent the nonlinear term within the Lyapunov analysis. The lossless constraint captures global behavior of the nonlinearity. Further, we analyze

*The condition "$\forall t > 0$" is implied for all Lyapunov-based arguments, even without explicit statement. Also, the relational operators $\prec 0, \succ 0$ ($\preceq 0, \succeq 0$) denote positive and negative (semi-) definite matrices, respectively.

local behavior of the nonlinearity around a neighborhood by representing its local properties as "local" constraints. We also show that local nonlinear properties play a role in destabilizing the system, whereas a linear stability analysis predicts the WKH system to be globally asymptotically stable for all *Re*. Both global and local stability analysis and the results are discussed in the following sections.

7.3.1 Stability: Representing Lossless Nonlinearity with Quadratic Constraints

The nonlinear term in Eq. (7.2) is skew-symmetric, therefore

$$\mathbf{x}^T N(\mathbf{x}) = \mathbf{x}^T Q(\mathbf{x})\mathbf{x} = 0, \ \forall \ \mathbf{x}. \tag{7.6}$$

The physical interpretation of this property is that the nonlinearity is energy conserving, serving only to redistribute energy between modes. This "lossless" property of the nonlinear term is also observed in many wall-bounded shear flows [151]. The stability analysis reduces to the following question: Does the constraint in Eq. (7.6) imply $\dot{V}(\mathbf{x}) < 0$ in Eq. (7.5) for all $\mathbf{x} \neq \mathbf{0}$? The answer is yes, if there exists a $P > 0$ and a Lagrange multiplier ξ_{p_0} (positive or negative) such that

$$2\mathbf{x}^T P(A\mathbf{x} + N(\mathbf{x})) + 2\xi_{po}\mathbf{x}^T N(\mathbf{x}) < 0, \tag{7.7}$$

which essentially says that the energy function $V(\mathbf{x})$ decreases for any $\mathbf{x}$ and $N(\mathbf{x})$ satisfying the lossless constraint in Eq. (7.6).

Consider now that the lossless property in Eq. (7.6) can be expressed equivalently as a quadratic constraint between the inputs $\mathbf{x}$ and outputs $\mathbf{z} = N(\mathbf{x})$ of the nonlinearity:

$$\begin{pmatrix}\mathbf{x}\\ \mathbf{z}\end{pmatrix}^T \underbrace{\begin{pmatrix}\mathbf{0} & \mathbf{I}\\ \mathbf{I} & \mathbf{0}\end{pmatrix}}_{:=M_0} \begin{pmatrix}\mathbf{x}\\ \mathbf{z}\end{pmatrix} = 0, \ \forall \ \mathbf{x} \text{ and } \mathbf{z} \in \mathbb{R}^4, \tag{7.8}$$

where $\mathbf{0}, \mathbf{I} \in \mathbb{R}^{4\times4}$ denote the zero and identity matrices, respectively. Thus, Eq. (7.7) can be recast as,

$$\begin{bmatrix}\mathbf{x}\\ \mathbf{z}\end{bmatrix}^T \left\{ \begin{bmatrix} A^T P + PA & P\\ P & \mathbf{0}\end{bmatrix} + \xi_{p_0} M_0 \right\} \begin{bmatrix}\mathbf{x}\\ \mathbf{z}\end{bmatrix} < 0. \tag{7.9}$$

The lossless constraint $\mathbf{z}^T\mathbf{x} = 0$ is captured by the block matrix $M_0 \in \mathbb{R}^{8\times8}$ defined in Eq. (7.8). The term in braces in Eq. (7.9) must be strictly negative definite for the strict inequality to be satisfied. However, for a matrix to be strictly negative definite, it is necessary for all principle sub-matrices to also be strictly negative definite [170, 171]. The bracketed term has $\mathbf{0}$ as a principle sub-matrix and hence the strict inequality in Eq. (7.9) cannot be satisfied. As such, we introduce a positive perturbation on Eq. (7.7) to relax the requirement for a strict inequality as,

$$2\mathbf{x}^T P(A\mathbf{x} + N(\mathbf{x})) + 2\xi_{po}\mathbf{x}^T N(\mathbf{x}) + 2\epsilon\mathbf{x}^T P\mathbf{x} \leq 0, \tag{7.10}$$

where $\epsilon > 0$. This new condition is equivalent to $\dot{V}(\mathbf{x}) \leq -\epsilon V(\mathbf{x})$ for all $\mathbf{x} \neq \mathbf{0}$, which guarantees exponential stability with a minimum convergence rate of ϵ when satisfied.

The stability condition in Eq. (7.10) can be recast in terms of the quadratic lossless constraint in Eq. (7.8) to yield,

$$\begin{bmatrix}\mathbf{x}\\ \mathbf{z}\end{bmatrix}^T \left\{ \begin{bmatrix} A^TP + PA & P \\ P & \mathbf{0}\end{bmatrix} + \xi_{p_0} M_0 + \begin{bmatrix}\epsilon P & \mathbf{0}\\ \mathbf{0} & \mathbf{0}\end{bmatrix} \right\} \begin{bmatrix}\mathbf{x}\\ \mathbf{z}\end{bmatrix} \leq 0. \tag{7.11}$$

Unlike the stability condition in Eq. (7.9), it is possible for this new stability condition in Eq. (7.11) to be satisfied because the inequality is non-strict. For Eq. (7.11) to hold, the matrix in braces has to be negative semi-definite. However, from the generalized Schur's complement [172] we know that the bracketed term will be negative semi-definite if and only if both $A^TP + PA + \epsilon P \preceq 0$ and $P + \xi_{p0}\mathbf{I} = 0$ for some $\xi_{p0} < 0$. Note that the condition $A^TP + PA + \epsilon P \preceq 0$ is the condition for verifying exponential stability of the linear system and by itself does not account for the nonlinearity; the addition of the quadratic constraints accounts for the lossless nonlinearity in this stability condition. In the limit $\epsilon \to 0$, this condition is equivalent to $A + A^T \prec 0$, which is a necessary and sufficient condition for unity maximum transient energy growth due to linear non-modal dynamics [88]. Thus, our analysis is consistent with the fact that unity linear MTEG is necessary for global stability in the nonlinear system.

In light of the stability condition in (7.11), it follows that stability of the linear element L and a lossless nonlinearity can be formulated as an LMI feasibility problem in the variables $P \succ 0$ and ξ_{p0}. In particular, the system $F_u(L, N)$ is globally asymptotically stable if there exists $P \succ 0$ and ξ_{p_0} such that the following LMI holds for a given $\epsilon > 0$:

$$\begin{bmatrix} A^TP + PA & P \\ P & \mathbf{0}\end{bmatrix} + \xi_{p_0} M_0 + \begin{bmatrix}\epsilon P & \mathbf{0}\\ \mathbf{0} & \mathbf{0}\end{bmatrix} \leq 0. \tag{7.12}$$

The feasibility of the LMI in Eq. (7.12) is only sufficient to establish the global asymptotic stability of the WKH system, as it only relies on the lossless property and does not depend on any other specific details of the nonlinearity. The condition in Eq. (7.12) is an LMI feasibility problem that can be solved using standard numerical tools. Unless otherwise specified, in the remainder of this work, we use CVX [122, 173], which is a package for specifying convex optimizations, combined with the commercially available solver MOSEK [174].

To analyze the global stability of the WKH system, we solve the LMI in Eq. (7.12) with $\epsilon = 10^{-6}$ for variables P and ξ_{p_0} at different values of Re. On performing the global stability analysis using the lossless constraint, we find that the WKH model for the W parameter values (see TABLE 7.1) is globally asymptotically stable for $Re \leq 20$. This finding is consistent with $Re_c = 20$ for global asymptotic stability reported by Waleffe [150]. Similarly we find that the WKH system with B&T parameters (see TABLE 7.1) is globally asymptotically stable for $Re \leq 2$.

Note that the linear WKH system is globally asymptotically stable for all Re, and so the nonlinear term is destabilizing. In the nonlinear WKH system, considering only the lossless constraint, we show that global stability cannot be established for $Re > 20$ for the W parameters and $Re > 2$ for the B&T parameters. To investigate this further, we propose a set of local constraints on the nonlinearity that enable a local stability analysis, as described in the next section.

7.3.2 Stability: Representing Local Properties of Nonlinearity using Quadratic Constraints

The WKH system with the lossless constraint is globally asymptotically stable for $Re \leq 20$ for the W parameters and for $Re \leq 2$ for the B&T parameters. To analyze the system for larger Re, we propose a "local" stability analysis as follows: Select a local neighborhood $\|\mathbf{x}\|^2 \leq R^2$ around the equilibrium point $\mathbf{x}_e = \mathbf{0}$. Local analysis restricts the state $\mathbf{x}$ to lie in a local region R, which result in "local" constraints for $N(\mathbf{x})$ within this local region. The analysis condition, given below, attempts to use these local quadratic constraints to show that: (i) the system state remains within the local region and (ii) it converges asymptotically back to $\mathbf{x}_e = \mathbf{0}$. These quadratic constraints are tighter (more powerful) for smaller values of R and become looser (less powerful) as R becomes larger. Thus, these local analysis results provide a range of results between global asymptotic stability (roughly as $R \to \infty$) and stability of the linearized system (roughly as $R \to 0$). We will show later in this section that R can be used to estimate the region of attraction (ROA) for the equilibrium point.

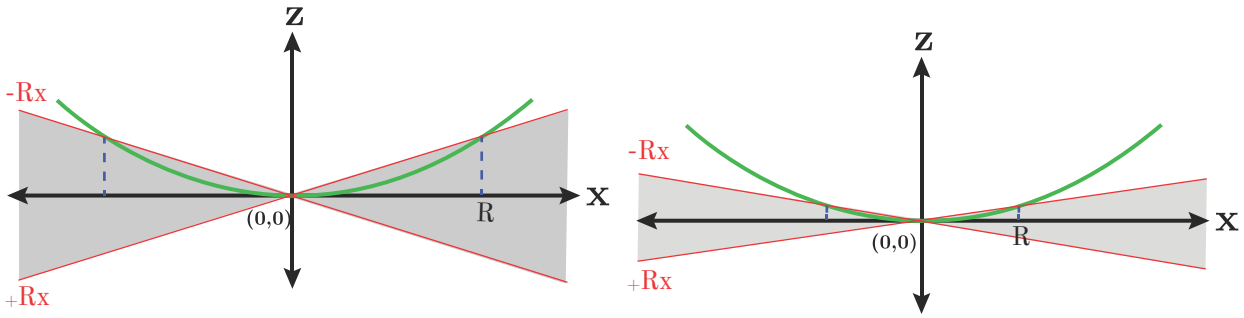
Recall that the nonlinearity in the WKH model is quadratic and can be expressed as $\mathbf{z} = \mathbf{x}^T Q(\mathbf{x})\mathbf{x}$ (see Eq. (7.2)). To illustrate the approach, first consider the scalar example $z = x^2$ (green curve in FIG. 7.2). Within a given region $|\mathbf{x}| < R$, the output satisfies $z^2 = x^4 < R^2 x^2$. Which further implies that $|z| < R|x|$, where R is the slope of the line. The quadratic function is restricted by the bound R, but this bound would graphically correspond to drawing a line of slope $+R$ and $-R$ (red lines in FIG. 7.2). The slope R can have a large value or a small value, as illustrated in FIGs. 7.2a and 7.2b, respectively. If x remains in the interval $[-R, +R]$, then the nonlinear function lies between these two linear lines with slope $\pm R$ (gray shaded region in FIGs. 7.2a and 7.2b). The dashed blue line in both these figures represents the maximum possible value of the pair (x, z), such that $|x| \leq R$ for a given slope. It can be seen that as the slope R is made larger (FIG. 7.2a), then the pair (x, z) also gets bigger, thereby moving the blue dashed line further away from the origin. Similarly, as slope of R is made smaller (FIG. 7.2b), the pair (x, z) gets smaller, thereby moving the dashed line towards the origin, which corresponds to a reduction in maximum value of z. Finally, note that as the slope R tends to zero, the sector shrinks to zero. Thus, $R \to 0$ corresponds to a nonlinear term with zero output—equivalent to a linear analysis. Conversely, as $R \to \infty$, then this sector becomes arbitrarily large and provides essentially no information—corresponding to a global analysis.

The sector formed by lines of slope $\pm R$ facilitates bounding the pair (x, z) to perform analysis in a localized setting, where the value of R also determines the amount of nonlinear behavior captured by the local constraint. A brief introduction to scalar sector bounded nonlinearities is presented in Appendix E. The remainder of this section generalizes this basic concept to the multivariable quadratic terms that appear in the WKH model.

From Eq. (7.2), each individual nonlinear term can be expressed as a quadratic function:

$$\mathbf{z} = \begin{bmatrix} z_1 \\ z_2 \\ z_3 \\ z_4 \end{bmatrix} = \begin{bmatrix} \mathbf{x}^T Q_1 \mathbf{x} \\ \mathbf{x}^T Q_2 \mathbf{x} \\ \mathbf{x}^T Q_3 \mathbf{x} \\ \mathbf{x}^T Q_4 \mathbf{x} \end{bmatrix}. \tag{7.13}$$

Here each $Q_i \in \mathbb{R}^{4\times 4}$ is a symmetric matrix. Hence each Q_i has real eigenvalues, and the spectral radius $\rho(Q_i)$ denotes the largest (magnitude) of these eigenvalues [171]. Moreover, quadratic terms with symmetric matrices are upper bounded as follows [171]:



(a) Large slope R forms larger sectors

(b) Small slope R forms smaller sectors

Figure 7.2: *Illustration of a scalar quadratic function $x = z^2$ that lies inside the sector formed by lines of slope $-R$ and R (red). The blue dashed lines mark the maximum value of the pair (x, z) for a given slope such that $|x| \leq R$.*

$$|z_i| = |\mathbf{x}^T Q_i \mathbf{x}| \leq \rho(Q_i)\mathbf{x}^T\mathbf{x}, \text{ for } i = 1 \text{ to } 4. \tag{7.14}$$

Next, assume the state $\mathbf{x}$ remains within a ball of radius R, i.e. $\mathbf{x}^T\mathbf{x} \leq R^2$. We can then square Eq. (7.14) to obtain the following constraint:

$$z_i^2 \leq \underbrace{\rho(Q_i)^2 R^2}_{\alpha_i(R)^2} \mathbf{x}^T\mathbf{x}, \text{ for } i = 1 \text{ to } 4. \tag{7.15}$$

This is a constraint involving squares of $\mathbf{x}$ and z_i. It can be written in a more useful quadratic constraint form. Let $E_i \in \mathbb{R}^{4\times 4}$ denote the matrix with the diagonal (i, i) entry equal to one and all other entries equal to zero. The constraint in Eq. (7.15) is equivalent to:

$$\begin{bmatrix}\mathbf{x}\\ \mathbf{z}\end{bmatrix}^T \underbrace{\begin{bmatrix}\alpha_i(R)^2\mathbf{I} & \mathbf{0}\\ \mathbf{0} & -E_i\end{bmatrix}}_{M_i(R)} \begin{bmatrix}\mathbf{x}\\ \mathbf{z}\end{bmatrix} \geq 0, \text{ for } i = 1 \text{ to } 4. \tag{7.16}$$

The above multivariable quadratic constraint in Eq. (7.16) is similar to the sector constraint in the scalar case, shown in Eq. (E.1) of Appendix E. The above constraint provides a bound on the nonlinear term z_i that holds over the local region $\mathbf{x}^T\mathbf{x} \leq R^2$. A local bound can be obtained for each of the four quadratic nonlinearities in Eq. (7.16). It should be noted that the lower right block in each $M_i(R)$ matrix is non-zero, and so we can use the strict inequality $\dot{V}(\mathbf{x}) + \xi_{p0}M_0 + \sum_{i=0}^{4} \xi_{pi}M_i < 0$. We will make use of these local constraints to study local stability of the WKH system in section 7.3.3, and show that they can be used for transient energy growth analysis as well in Section 7.5.2.

7.3.3 Results: Local stability analysis using quadratic constraints

The lossless property in Eq. (7.8) captures the global behavior of the quadratic nonlinearity. Given that the WKH system is not globally stable for $Re > 20$, it is still beneficial to understand its local stability properties. The linearization around $\mathbf{x}_e = \mathbf{0}$ is stable for all $Re > 0$ because A is Hurwitz. A more quantitative local stability analysis can be performed around $\mathbf{x}_e = \mathbf{0}$ using the local constraints derived in Eq. (7.16). Specifically, our goal is to estimate the region of attraction

(ROA), which corresponds to the set of initial conditions whose trajectories converge back to $\mathbf{x}_e = 0$. We will consider the local constraints on the nonlinearity that hold over the sphere $\|\mathbf{x}\| \leq R$. The local stability analysis for the nonlinear system can be performed by solving the following LMI feasibility problem:

$$\begin{aligned} & P \succeq I \\ & \xi_{p_i} \geq 0 \qquad (\text{for } i = 1 \text{ to } 4) \\ & \begin{bmatrix} A^T P + PA & P \\ P & \mathbf{0} \end{bmatrix} + \xi_{p_0} M_0 + \sum_{i=1}^{4} \xi_{p_i} M_i(R) \prec 0. \end{aligned} \tag{7.17}$$

Note that the local quadratic constraints depend on the radius R as explicitly denoted by $M_i(R)$. If Eq. (7.17) has a feasible solution, then $V(\mathbf{x}) = \mathbf{x}^T P \mathbf{x}$ is a Lyapunov function. Moreover, the level set $S_R := \{\mathbf{x} : V(\mathbf{x}) < R^2\}$ is an inner approximation to the region of attraction (ROA). These facts are formally proved in Appendix F. For a given Re and R, we solve the feasibility problem in Eq. (7.17). If the problem is feasible for a region of size R, we know that the problem is also feasible for a region whose size is smaller than R as well. This enables us to use bisection to obtain the lower bound on R. However, solving the feasibility problem via bisection for numerous R can be computationally cumbersome. Hence, we re-pose the problem for finding the largest lower bound on R as a quasi-convex generalized eigenvalue problem (GEVP) [175].

To find the estimate of the largest inner approximation for the ROA, we first decompose each local constraint matrix $M_i(R)$ as

$$M_i(R) = R^2 \underbrace{\begin{bmatrix} \rho(Q_i)^2 & \mathbf{0} \\ \mathbf{0} & \mathbf{0} \end{bmatrix}}_{\tilde{M}_i} + \underbrace{\begin{bmatrix} \mathbf{0} & \mathbf{0} \\ \mathbf{0} & -E_i \end{bmatrix}}_{\hat{M}_i}. \tag{7.18}$$

Now an estimate for the ROA can be obtained by using a change of variables $t = -R^2$ and solving the GEVP,

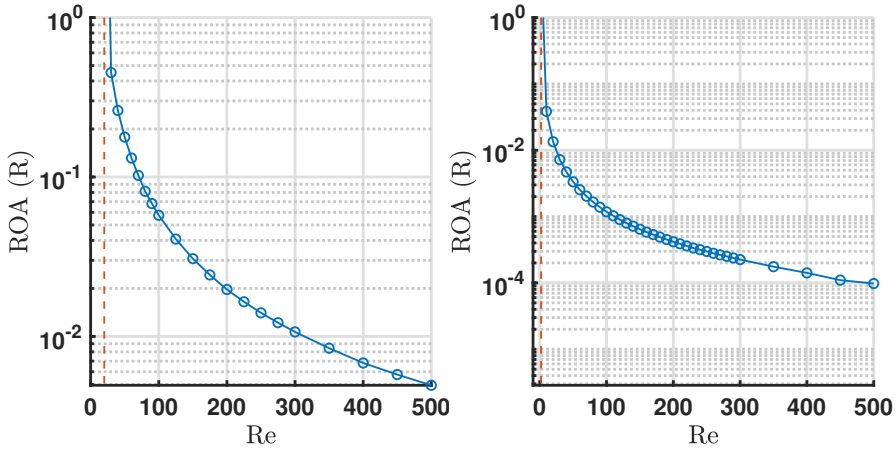
$$\begin{aligned} \text{minimize} \quad & t \\ \text{subject to } & P \succeq \mathrm{I} \\ & \xi_{p_i} \geq 0 \qquad (\text{for } i = 1 \text{ to } 4) \\ & \begin{bmatrix} A^T P + PA & P \\ P & \mathbf{0} \end{bmatrix} + \xi_{p_0} M_0 + \sum_{i=1}^{4} \xi_{p_i} \hat{M}_i \prec t \sum_{i=1}^{4} \xi_{p_i} \tilde{M}_i, \end{aligned} \tag{7.19}$$

where ξ_{p_i} ($i = 1$ to 4) are Lagrange multipliers for the local constraints. These Lagrange multipliers also provide information on the relative contribution of each constraint in the local region, as will be discussed in Section 7.6. In this work, the GEVPs are solved using LMI-Lab [176].

The analysis condition in Eq. (7.19) can be used to estimate the largest lower bound of R as a function of Re. The resulting relationship between Re and R is shown in FIG. 7.3. Note that R decreases monotonically as Re tends to ∞. This implies that the local stability region shrinks as Re

increases. On the other hand, R tends to ∞ as Re decreases to 20 as shown in FIG. 7.3a for the W parameter case. In the W parameter case, the local stability region increases in size as $Re \to 20$. This is consistent with the previous global stability result, where $Re \leq 20$ was found to be global stable using only the lossless constraint.

Similarly, we also analyze the local stability for the B&T parameters in FIG. 7.3b. Here, the system is globally stable for $Re \leq 2$, demarcated by the dashed red line in FIG. 7.3b. The same relation between R and Re is observed with the B&T parameter as with W parameters; that is, the size of R is decreases with increasing Re.



(a) W parameter **(b)** B&T parameter

Figure 7.3: *As the Re is increased, the local stability region R decreases. The red dashed line shows the Re for global stability limit. In both (a) and (b) as we approach the global stability limit, the size of $R \to \infty$. As $Re \to \infty$, the size of region $R \to 0$, which corresponds to the linear analysis of infinitesimal perturbations.*

7.4 Estimating Permissible Perturbation Amplitudes

We have shown that the GEVP in Eq. (7.19) can be solved to obtain the largest lower bound on R. Now we aim to identify the largest perturbation size R_0, such that trajectories originating in a sphere of radius R_0 will converge back to the equilibrium. The sphere of radius R_0 is obtained by finding the largest inner approximation of the ROA—this sphere is a sub-level set of the ellipsoid $V(\mathbf{x}) \leq R^2$. The size and shape of the ellipsoid depends on the energy weight matrix P found in Eq. (7.19). We will show that the GEVP can be used to estimate the largest perturbation amplitude R_0 that drives the trajectory to the edge of stability.

Consider initial conditions inside a sphere of radius R_0 around the equilibrium point such that $||\mathbf{x}_0||^2 \leq R_0^2$. Let $q := \lambda_{max}(P)/\lambda_{min}(P)$ be the condition number of P with λ_{max} and λ_{min} being the largest and smallest eigenvalues of P, respectively. The condition number q of matrix P provides information on the skewness of the bounding ellipsoid. To bound the skewness of the elliptical set, we can simply bound P as $I \preceq P \preceq qI$. We now seek to determine the largest sphere of initial conditions $\|\mathbf{x}_0\|^2 \leq R_0^2$ such that trajectories remain inside the ROA. From the inequality $I \preceq P \preceq qI$ and $\dot{V}(\mathbf{x}) < 0$, it follows that $\|\mathbf{x}\|^2 \leq \mathbf{x}^T P \mathbf{x} \leq \mathbf{x}_0^T P \mathbf{x}_0 \leq q\|\mathbf{x}_0\|^2$, which implies that $\|\mathbf{x}\|^2 \leq q\|\mathbf{x}_0\|^2$. Therefore, we have $\|\mathbf{x}\|^2 \leq qR_0^2 = R^2$, and we can find the largest allowable sphere

of radius R_0. To do so, we can now use the decomposition of $M_i = R^2\tilde{M}_i + \hat{M}_i$ (see Eq. (7.18)) and the relation $R^2 = qR_0^2$, then solve the following GEVP

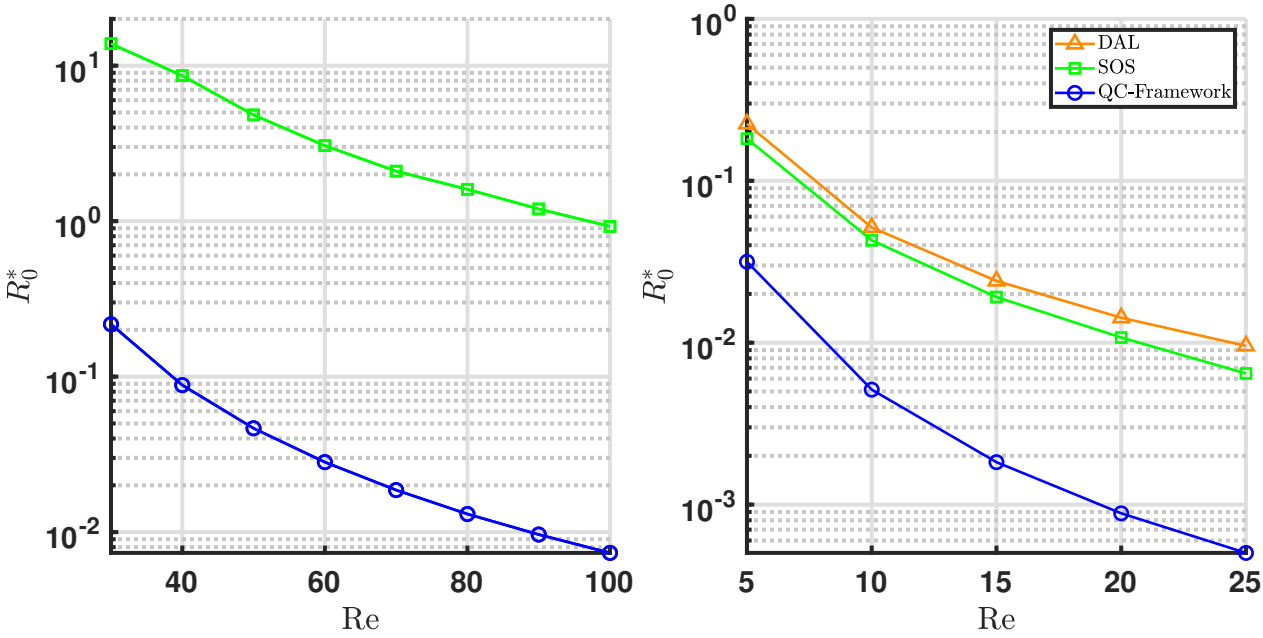
$$\begin{aligned}
&\text{minimize} \quad t_0 \\
&\quad \text{subject to } I \preceq P \preceq qI \\
&\qquad \xi_{p_i} \geq 0 \qquad \text{(for i=1 to 4)} \\
&\qquad \begin{bmatrix} A^TP + PA & P \\ P & \mathbf{0} \end{bmatrix} + \xi_{p_0} M_0 + \sum_{i=1}^{4} \xi_{p_i} \hat{M}_i \prec t_0 q \sum_{i=1}^{4} \xi_{p_i} \tilde{M}_i,
\end{aligned} \tag{7.20}$$

where $t_0 = -R_0^2$. To solve for the largest permissible perturbation amplitude, we solve Eq. (7.20) over a grid of q values, then pick the solution corresponding to the largest R_0.

We verify our findings by comparing the R_0 obtained from the proposed quadratic constraints (QC) framework with the nonlinear optimal perturbations obtained using nonlinear direct-adjoint looping (DAL), as detailed in [152, 177]. In the DAL method, a so-called "minimal seed" is obtained using the calculus of variations and a gradient method to find the nonlinear optimal perturbation on a sphere of radius R_0. If divergent trajectories are found for perturbations of size R_0, we update the upper and lower bounds on R_0 via bisection. Once the upper and lower bounds converge to some tolerance $\epsilon > 0$ (here $\epsilon = 10^{-8}$) and no divergent trajectories are found, we terminate the bisection procedure. Since DAL uses the exact nonlinear equations of motion, it provides accurate estimates for the minimal seed of the nonlinear system and the permissible amplitude. In addition to the DAL method, we also compare with results from the sum-of-squares (SOS) framework using quadratic energy functions [166]. Both the SOS and QC framework use Lyapunov-based methods to compute the largest sphere of radius R_0, which is an inner approximation of the ROA, and hence these methods are conservative in their estimates of the permissible perturbation amplitude.

In FIG. 7.4, we report the largest radius of initial conditions R_0^* versus Re using the three methods mentioned above. For the B&T parameters we show results of the DAL ($\triangle$), SOS framework ($\square$), and QC framework ($\bigcirc$) in FIG. 7.4b. However, for the W parameters we compare the results of the SOS framework and QC framework only in FIG. 7.4a, this is because for the W parameters no divergent trajectories were found using DAL. Even though there are no divergent trajectories the SOS framework and QC framework provide conservative estimates for R_0, as expected.

For the B&T parameters, the largest allowable perturbation size for $Re = 100$ is found to be $R_0^* \approx 1.5 \times 10^{-5}$ using the QC framework; this is a conservative estimate relative to $R_0^* = 10^{-4}$ in [169]. As seen in both figures in FIG. 7.4, we observe that the R_0^* predicted by the QC framework is conservative. Since the QC framework does not use detailed information of the nonlinear terms—it only uses a few constraints that characterize the input-output behavior of the nonlinear terms—this behavior is expected. In exchange for this conservatism, the QC framework is less computationally expensive compared to the SOS and DAL methods, which are more computationally expensive and may not be suitable for large systems. We finally note that recent works by Liu and Gayme [178]—which appeared during the review of this manuscript—have aimed to reduce conservatism of these estimates within the QC framework.



(a) W parameters **(b)** B&T parameters

Figure 7.4: *The maximum allowable perturbation size R_0 as a function of Re for W and B&T parameters compared against the SOS framework and DAL method.*

7.5 Nonlinear Transient Energy Growth Analysis using Quadratic Constraints

In this section, we aim to determine the least upper bound on the maximum transient energy growth (MTEG) in the nonlinear system using the QC framework. We first review how the MTEG bounds can be obtained for a linear system by solving a GEVP. We then extend this GEVP to determine the MTEG in the nonlinear system using the QC framework.

For a globally asymptotically stable linear system $\dot{\mathbf{x}} = A\mathbf{x}$, the state trajectories $\mathbf{x}(t) \to \mathbf{0}$ for any initial condition. If the matrix A is non-normal, then the system energy $E := \mathbf{x}^T\mathbf{x}$ will grow on transient time scales before decaying back to zero. The definition of energy E here is without loss of generality, since any energy of the form $E = \tilde{\mathbf{x}}^T W \tilde{\mathbf{x}}$ is recovered with $\mathbf{x} = W^{1/2}\tilde{\mathbf{x}}$. In what follows, the associated MTEG, given by Θ, is defined as:

$$\Theta := \max_{t\geq 0} \max_{\|\mathbf{x}(0)\|=1} \|\mathbf{x}(t)\|^2 \ . \tag{7.21}$$

We can obtain an upper bound q on the MTEG (Θ) using Lyapunov theory. Specifically, assume $V(\mathbf{x}) = \mathbf{x}^T P\mathbf{x}$ is a Lyapunov function for a given system with $I \preceq P \preceq qI$. If the initial condition $\mathbf{x}_0$ lies in the ellipsoid $\{\mathbf{x} : \mathbf{x}^T P\mathbf{x} \leq 1\}$, then $\mathbf{x}(t)$ remains in this level set for all $t \geq 0$ [88, 179]. Thus $\mathbf{x}(t)^T P\mathbf{x}(t) \leq \mathbf{x}(0)^T P\mathbf{x}(0)$. Combining this with $I \preceq P \preceq qI$ yields $E(t) \leq \mathbf{x}(t)^T P\mathbf{x}(t) \leq \mathbf{x}(0)^T P\mathbf{x}(0) \leq qE(0)$. Therefore, $\Theta \leq q$ [180].

The least upper bound q^* is defined as $q^* := \lambda_{max}(P)\lambda_{max}(P^{-1})$ such that $P = P^T \succ 0$ and P satisfies $A^T P + PA \prec 0$. The problem of estimating q^* can be formulated as that of minimizing the condition number of P and is obtained by solving the following GEVP [88, 113]:

$$
\begin{aligned}
q^* := \text{minimize} \quad & q \\
\text{subject to } & \mathrm{I} \preceq P \preceq q\mathrm{I}\,, \\
& A^T P + PA \prec 0.
\end{aligned}
\tag{7.22}
$$

Here, the bounds $I \preceq P \preceq qI$ ensure that $\lambda_{max}(P)/\lambda_{min}(P) \leq q$. This optimization with LMI constraints and a linear cost involving variables (P, q) is known as a semidefinite program (SDP). The LMI constraints imply that $V(\mathbf{x}) := \mathbf{x}^T P\mathbf{x}$ is a Lyapunov function for the system such that $V(\mathbf{x}(t)) \leq V(\mathbf{x}(0))$ for all $t \geq 0$. The bounds on P further imply that $\|\mathbf{x}(t)\|^2 \leq q^*\|\mathbf{x}(0)\|^2$. These LMI constraints are conservative in general, and hence q^* is a (possibly non-tight) upper bound on the MTEG. Next, we will extend these ideas for MTEG analysis of nonlinear systems using QCs.

7.5.1 Global MTEG Analysis using Quadratic Constraints

An optimization problem similar to Eq. (7.22) can be formulated to study the MTEG in the nonlinear WKH system. The lossless property for the nonlinear term in Eq. (7.8) can again be used as a global constraint. Taking a similar approach as in Section 7.3.1, we perturb the Lyapunov inequality to ensure a feasible solution can exist when only the lossless constraint is used. This yields the following optimization for a given $\epsilon > 0$:

$$
\begin{aligned}
q^* := \text{minimize} \quad & q \\
\text{subject to } & \mathrm{I} \preceq P \preceq q\mathrm{I}\,, \\
& \begin{bmatrix} A^T P + PA & P \\ P & \mathbf{0} \end{bmatrix} + \xi_{p_0} M_0 + \begin{bmatrix} \epsilon P & \mathbf{0} \\ \mathbf{0} & \mathbf{0} \end{bmatrix} \preceq 0
\end{aligned}
\tag{7.23}
$$

Equation (7.23) is now a SDP in the variables (P, q, ξ_{p_0}). As before, the LMI constraints imply that the Lyapunov function evaluated at the initial time upper bounds the Lyapunov function for all $t \geq 0$. The bounds on P imply that $E(t) \leq q^* E(0)$ and are obtained by means of a Lyapunov function that describes a trajectory bounding ellipsoid, known as an invariant set. As with the linear MTEG analysis in Eq. (7.22), the quadratic constraint analysis problem in Eq. (7.23) is expected to yield a conservative upper bound on MTEG.

7.5.2 Local MTEG Analysis using Quadratic Constraints

The ability to obtain MTEG bounds is of interest even beyond the globally stable regime considered in Section 7.5.1. Hence, we use the local properties of the nonlinearity derived in Section 7.3.3 to study the "local" MTEG performance in the nonlinear system.

A formulation similar to Eq. (7.23) can be used to study the effect of nonlinearity on MTEG in the nonlinear system. To perform the local MTEG analysis, additional local constraints are added to the optimization problem listed in Eq. (7.23). The local constraints that capture input-output properties of the nonlinear term are captured by matrices M_i (for $i = 1$ to 4) defined in Eq. (7.18). The addition of these constraints facilitates the study of local MTEG on the nonlinear system. The local MTEG for the nonlinear system is computed via the following convex optimization:

$$
\begin{aligned}
&\text{minimize} \quad q \\
&\text{subject to } \mathrm{I} \preceq P \preceq q\mathrm{I}\,, \\
&\qquad \xi_{p_i} \geq 0 \qquad (\text{for } i = 1 \text{ to } 4)\,, \\
&\qquad \begin{bmatrix} A^T P + PA & P \\ P & \mathbf{0} \end{bmatrix} + \xi_{p_0} M_0 + \sum_{i=1}^{4} \xi_{p_i} M_i \prec 0.
\end{aligned} \tag{7.24}
$$

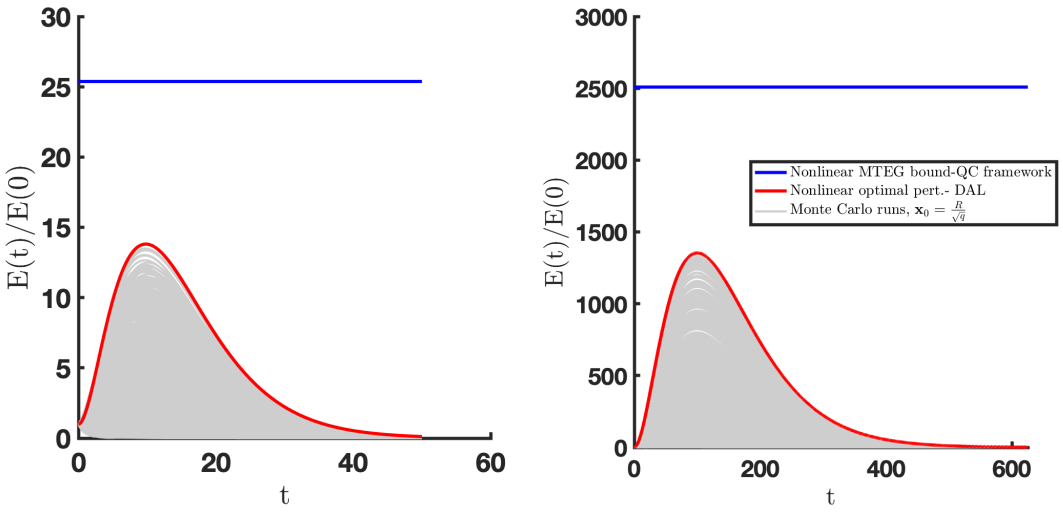
We will identify MTEG bounds for the system about a local equilibrium point $\mathbf{x}_e = \mathbf{0}$ by solving this optimization for P, q, ξ_{p_0}, and ξ_{p_i} (for $i = 1$ to 4). The proof in Appendix F also applies for Eq. (7.24), therefore ensuring the states always remain inside the invariant set for all time $t \geq 0$.

7.5.3 Results: MTEG analysis using quadratic constraints

Global MTEG analysis

By solving the SDP in Eq. (7.23) with $\epsilon = 10^{-6}$, we find that the MTEG bound is unity for all $Re < 20$ using the W parameters. It is interesting to note that the linear part of the WKH system exhibits unity MTEG for $Re < 20$ as well. Yet, the same MTEG bound from Eq. (7.23) is stronger because it applies to the nonlinear system $F_u(L, N)$ with a lossless nonlinearity. Similarly, from global MTEG analysis of the WKH system with B&T parameters, we find that the system is globally stable for $Re \leq 2$ and the system holds unity MTEG for $Re < 2$.

Local MTEG analysis



(a) W parameter, $Re = 100$ **(b)** B&T parameter, $Re = 100$

Figure 7.5: *5000 Monte Carlo simulations from various initial conditions such that* $\|\mathbf{x}_0\|^2 \leq \frac{R}{\sqrt{q}}$, *with* $R = 10^{-2}$ *and* $R = 10^{-4}$ *for W parameter and B&T parameters respectively. The solid blue line shows the MTEG upper bound for nonlinear system predicted by the quadratic constraint framework proposed here. The solid gray curves show the Monte Carlo simulations for various initial conditions and the red curve shows the worst case MTEG of the nonlinear system.*

For a given Re and local region R, we solve Eq. (7.24) for the MTEG bounds for both the W and B&T parameters. In FIG. 7.5, we compare MTEG bounds from the QC framework with Monte

Carlo simulations and the MTEG obtained from the DAL method [152, 177]. From FIGs. 7.5a and 7.5b, we see that MTEG bounds obtained from Eq. (7.24) (solid blue lines) are conservative. In FIG. 7.5, the solid gray curves correspond to the TEG from random initial conditions sampled with $\|\mathbf{x}_0\| = \frac{R}{\sqrt{q}}$, and the red curves correspond to MTEG resulting from the nonlinear optimal perturbation obtained using DAL. For the W parameters and the B&T parameters, the MTEG bounds are reported for $R = 10^{-2}$ and $R = 10^{-4}$, respectively. The initial condition for the Monte Carlo simulations are obtained using the same R value and the corresponding q obtained from solving Eq. (7.24). Even though the QC framework provides a conservative estimate on the MTEG bounds, it can be an effective tool in analyzing transient energy growth in more complex system where DAL and Monte Carlo based estimates are computationally cumbersome, or in situations where exact information about the nonlinear terms may not be precisely known.

7.6 Lagrange Multiplier Analysis: Drawing Physical Insights Into Nonlinear Flow Interactions

In addition to providing a framework to analyze stability and transient energy growth, the quadratic-constraints-based methods can be used to gain insights into the physics and dominating mechanisms underlying these dynamics. These insights are obtained by analyzing the Lagrange multipliers obtained from solving the GEVP in Eq. (7.20) as well as the SDP convex optimization problem in Eq. (7.24). The Lagrange multipliers provide information on the marginal cost of violating the associated constraints, thus indicating the relative importance of the corresponding constraints in the optimization problem. This allows for a quantitative analysis that can be used for identifying dominant nonlinear interactions. Here, we analyze the Lagrange multipliers for the W parameters, since Waleffe discusses these nonlinear interaction terms in [150], providing a basis for comparison. However, the same conclusions are obtained from the Lagrange multiplier analysis of the B&T parameters as well.

The Lagrange multipliers obtained from solving Eq. (7.20) for R_0 with the W parameters over various Re are shown in FIG. 7.6. In FIG. 7.6a we observe that the importance of the nonlinear terms varies as Re is varied. In the initial phase for $Re < 175$, we see the dominating Lagrange multipliers are ξ_{p_1} and ξ_{p_2} corresponding to nonlinear interaction terms $-\gamma w^2 + v\bar{m}$ and δw^2, respectively. As Re increases, we see that the Lagrange multipliers ξ_{p_2} (corresponding to δw^2) and ξ_{p_3} (corresponding to $\gamma wu - \delta wv$) become more dominant with respect to the other multipliers. In FIG. 7.6a, it can be seen that ξ_{p_2} is approximately 100 times more dominant than ξ_{p_3} for $Re > 200$. Further, ξ_{p3} is orders of magnitude larger than the multipliers associated with the other nonlinearities. Over all Re, the most dominant Lagrange multiplier is ξ_{p_2} (i.e., the nonlinear term δw^2), while the least dominating Lagrange multiplier is ξ_{p_4} (i.e., nonlinear interaction $-vu$). Inspecting Lagrange multipliers alone may not provide the complete picture, as the Lagrange multipliers can be influenced by the scaling of the constraint matrix M_i. Hence, we also plot the singular values of $\xi_{p_i} M_i$—denoted by $\sigma_{max}(\xi_{p_i} M_i)$)—in FIG. 7.6b. The singular value analysis captures the overall contribution of each nonlinear interaction term, thereby also verifying these findings.

Similarly in FIG. 7.7a, we show the Lagrange multipliers obtained from MTEG analysis (Eq. (7.24)) of the W parameters for $R = 0.01$. Again it can be observed that the nonlinear terms δw^2 and $\gamma wu - \delta wv$ — from ξ_{p_2} and ξ_{p_3}, respectively —are the dominant flow interactions contributing to MTEG in the WKH system. We obtain similar findings related to dominating

flow interactions when comparing Lagrange multipliers obtained from the R_0 analysis results from Eq. (7.20). Waleffe discusses the importance of the nonlinearities δw^2 and $\gamma wu - \delta wv$ in feeding $\dot{v}$ and $\dot{w}$, thereby serving central roles in sustaining turbulence and conserving energy, respectively. We note that this analysis of Lagrange multipliers allowed the same dominant nonlinear flow physics to be identified without reliance upon any prior knowledge or physical insight. Similar trends are observed for other values of R. The same is true for the B&T parameters.

When we investigate the Lagrange multipliers for the MTEG bound from Eq. (7.24), we observe that the Lagrange multiplier ξ_{p3} (shown in FIG 7.7a) associated with the nonlinear term $\gamma wu - \delta wv$ consistently increases in magnitude with increasing Re, while Lagrange multipliers ξ_{p0}, ξ_{p1} and ξ_{p4} always have magnitude ≤ 1. The multiplier ξ_{p3} has a magnitude of ≈ 110 at $Re = 150$ and it steadily increases by a factor of 6 at $Re = 280$. It should be noted that this increase in magnitude of ξ_{p_3}—while other multipliers are relatively constant—shows the dominance of the associated nonlinear term. The same can be verified by studying the maximum singular values, $\sigma_{max}(\xi_{p_i} M_i)$ as shown in FIG. 7.7b.

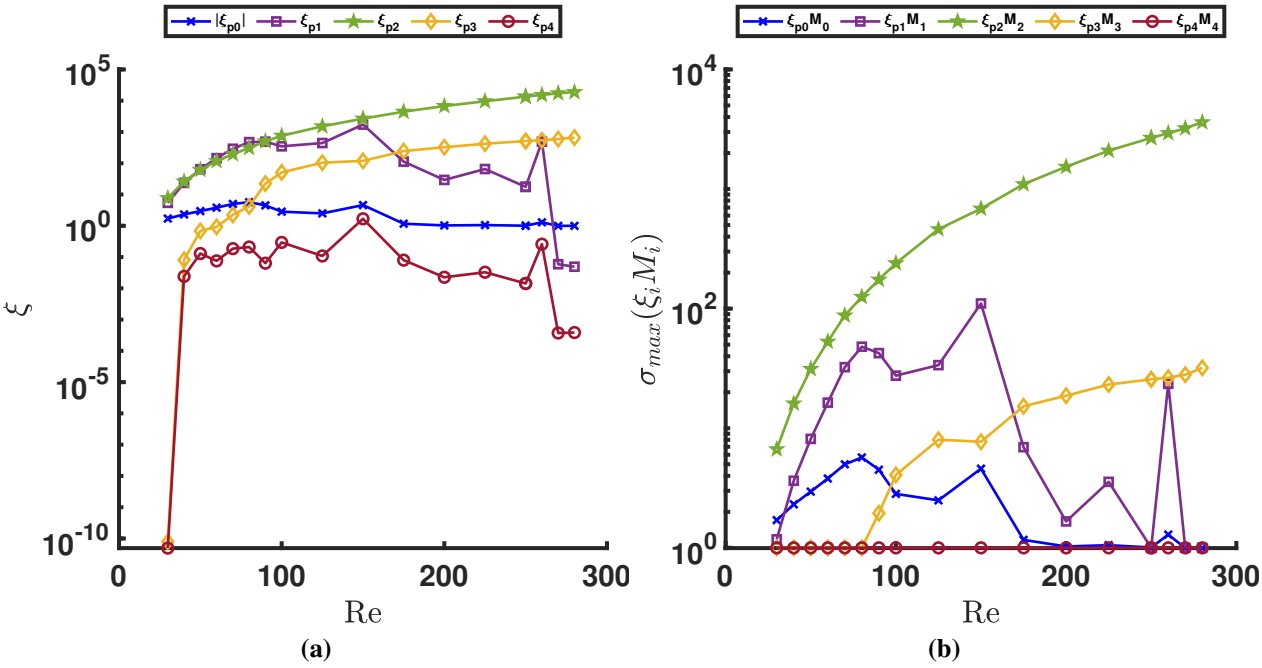


Figure 7.6: *Results obtained from solving R_0 in Eq. (7.20) with W parameters. The dominating nonlinear terms for stability can be identified by analyzing Lagrange multipliers ξ_{p_i} in (a) and its associated singular values $\sigma_{max}(\xi_{p_i} M_i)$ in (b).*

To demonstrate the dominance of these nonlinear interactions, we perform MTEG analysis in Eq. (7.24) while retaining only the local constraints associated with the dominating nonlinear interactions (ξ_{p_2}, ξ_{p_3}) and neglecting the other local interactions (ξ_{p_1}, ξ_{p_4}). We choose $R = 0.01$ as before, but now use only the lossless constraint along with constraints associated with ξ_{p_2} and ξ_{p_3} (see green line in FIG. 7.8) and compare results with the case where all the constraints are retained (see blue line in FIG. 7.8). The MTEG profile based on analysis using two dominating nonlinear interactions (δw^2, $\gamma wu - \delta wv$) and the lossless constraint closely approximates the MTEG response

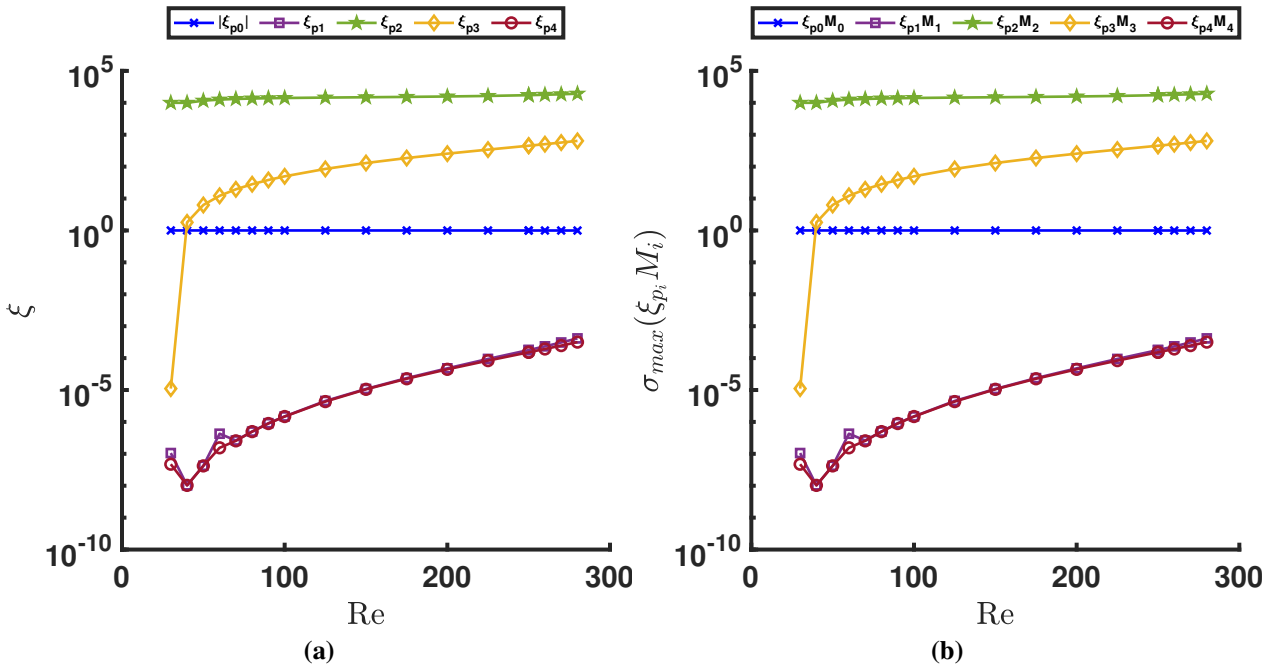


Figure 7.7: *Results obtained from solving for q^* in Eq.* (7.24)*. The dominant nonlinear terms for TEG can be identified by analyzing the dominant Lagrange multipliers ξ_{p_i} in (a) and its associated singular values $\sigma_{max}(\xi_{p_i}M_i)$ in (b).*

of the whole nonlinear system. We observe similar qualitative trends for any other value of R for which the optimization problem is feasible and also for the B&T model parameters.

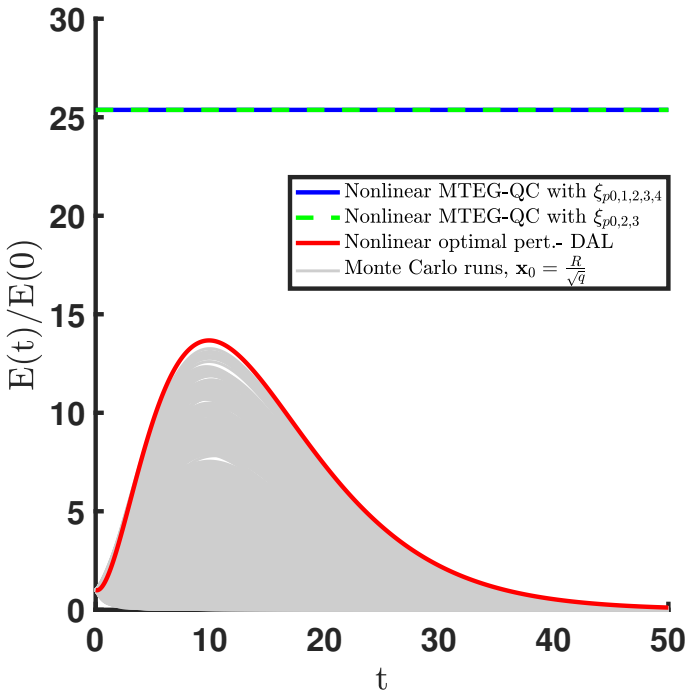


Figure 7.8: *Local MTEG analysis for W parameters with global lossless constraint and the two most dominant local constraints compared against the MTEG of system with global and all local constraints for* $Re = 100$ *and* $R = 0.01$.

7.7 Conclusion

In this chapter, we presented a quadratic constraints framework to perform stability and transient energy growth analysis of nonlinear systems. The proposed framework facilitates stability and transient energy growth analysis in global and local settings around a given equilibrium point. The framework uses exact information from the linear dynamics, while nonlinear interactions are replaced by quadratic constraints that capture input-output properties of the nonlinearity.

We demonstrated the proposed analysis approach on the WKH model of transitional and turbulent flow. We first study the stability of the WKH model, for which the linear part is globally asymptotically stable for all Re. It is found that the nonlinear WKH system with W parameters is globally stable for $Re \leq 20$, consistent with previous results found in the literature. Similarly the global stability of the WKH system for B&T parameters is verified for $Re \leq 2$. It is also observed that the energy conserving nonlinear terms destabilize the system beyond the globally stable regime.

In order to assess stability and maximum transient energy growth performance beyond the globally stable regime, we introduced a new "local" analysis framework to analyze local stability and transient energy growth properties. The local analysis provides an inner approximation for the region of attraction (ROA), which is determined by solving a GEVP. In addition to the ROA analysis, the solution procedure can be used to estimate permissible perturbation amplitudes. These analysis methods were compared with more computationally intensive SOS and DAL methods.

We also introduced a method for estimating maximum transient energy growth bounds when the system is either globally stable or simply locally stable. It was found that the maximum transient energy growth (MTEG) bound was unity below the critical Reynolds number for global stability. In the locally stable regime, we estimated the bounds on the MTEG and compared our results with

those obtained from Monte Carlo simulations and DAL. Lastly, analyzing the Lagrange multipliers associated with each local constraint provided further insights into the physics. By comparing the relative magnitudes of the Lagrange multipliers, we were able to identify the dominating nonlinear interactions without any prior knowledge of the flow physics. The dominant nonlinear terms identified by this analysis were in agreement with the physical mechanisms originally described in [149].

The general QC framework proposed here shows promise in analyzing complex systems with quadratic and lossless nonlinearities, such as the incompressible NSE; however, there are computational challenges involved in generalizing this quadratic-constraint-based analysis for high dimensional fluids systems. The primary hurdle rests in the fact that computational demands of general purpose solvers for the convex optimization methods proposed here scale with $O(n^6)$, where n is the state dimension [181]. Potential avenues forward may rely upon accurate reduced-order models, dedicated solvers, or some combination thereof. Nonetheless, the ideas proposed here establish exciting avenues for fluid flow analysis that— with further development—are expected to provide valuable insights about complex flow physics and their control.

8 | Personnel

The following is a list of individuals who have worked on research supported in whole or in part by the Air Force Office of Scientific Research under Grant FA9550-19-1-0034:

Prof. Maziar S. Hemati, Department of Aerospace Engineering & Mechanics, U. Minnesota
Dr. Yiyang Sun, postdoctoral researcher (now faculty at Syracuse University)
Ms. Huaijin (Grace) Yao, graduate student (PhD completed, now at Seagate Technology)
Mr. Aniketh Kalur, graduate student (PhD completed, now postdoc at UT Austin)
Mr. Talha Mushtaq, graduate student (PhD in progress)
Mr. Nick Conlin, undergraduate student (BS completed, now PhD student at Princeton University)

9 | Publications

The publications listed below represent papers, reports, and theses supported in whole or in part by the Air Force Office of Scientific Research under Grant FA9550-19-1-0034:

Journal Papers:

1. H. Yao, Y. Sun, T. Mushtaq, and M.S. Hemati, "Reducing transient energy growth in a channel flow using static output feedback control," in review, pre-print arXiv:2012.13314.
2. H. Yao, Y. Sun, and M.S. Hemati, "Feedback control of transitional shear flows: Sensor selection for performance recovery," in review, pre-print arXiv:2009.03469
3. A. Kalur, T. Mushtaq, P. Seiler, and M.S. Hemati, "Estimating regions of attraction for transitional flows using quadratic constraints," IEEE Control Systems Letters, vol. 6, pp. 482–487
4. A. Medina and M.S. Hemati, "Lift Disturbance Cancellation with Rapid-Flap Actuation," AIAA Journal, 59(11), 2021.
5. A. Kalur, P. Seiler, and M.S. Hemati, "Nonlinear stability analysis of transitional flows using quadratic constraints," Physical Review Fluids, vol. 6, 044401, 2021.
6. E. Deem, L.N. Cattafesta, M.S. Hemati, H. Zhang, C. Rowley, and R. Mittal, "Adaptive Separation Control of a Laminar Boundary Layer using Online Dynamic Mode Decomposition," Journal of Fluid Mechanics, vol. 903, A21, 2020.
7. S.L. Brunton, M.S. Hemati, and K. Taira, "Special issue on machine learning and data-driven methods in fluid dynamics," Theoretical and Computational Fluid Dynamics, 2020.
8. D. Bhattacharjee, B Klose, G. Jacobs, and M.S. Hemati, "Data-driven selection of actuators for optimal control of airfoil separation," Theoretical and Computational Fluid Dynamics, vol. 34, 2020.
9. A. Medina, M.S. Hemati, M. Rockwood, "Separated flow response to rapid flap deflection," AIAA Journal, 58(4), 2020.
10. A. Kalur and M.S. Hemati, "Control-oriented model reduction for minimizing transient energy growth in shear flows," AIAA Journal, 58(3), 2020.
11. K. Taira, M.S. Hemati, S.L. Brunton, Y. Sun, K., Duraisamy, S. Bagheri, S.T.M. Dawson, C.-A. Yeh, "Modal Analysis of Fluid Flows: Applications and Outlook," AIAA Journal 58(3), 2020.
12. K. Taira, M.S. Hemati, L.S. Ukeiley, "Modal analysis of fluid flows: Introduction to the

virtual collection," AIAA Journal, 58(3), 2020

13. X. An, D.R. Williams, and M.S. Hemati, "A hybrid model for lift response to dynamic actuation on a stalled airfoil," Energies, 13(4), 855, 2020
14. Feedback control for transition suppression in direct numerical simulations of channel flow Y. Sun and M.S. Hemati Energies, 12(21), 4127, 2019

Conference Papers:

1. A. Kalur, T. Mushtaq, P. Seiler, and M.S. Hemati, "Estimating Regions of Attraction for Transitional Flows using Quadratic Constraints," IEEE Conference on Decision and Control, Austin, TX, 13–15 December 2021.
2. T. Mushtaq, P. Seiler, and M.S. Hemati, "Feedback control of transitional flows: A framework for controller verification using quadratic constraints," AIAA Fluid Dynamics Conference, Washington, D.C., 2-6 August 2021 (virtual). AIAA Paper 2021-2825
3. A. Kalur, P. Seiler, and M.S. Hemati, "Stability and performance analysis of nonlinear and non-normal systems using quadratic constraints," AIAA Aerospace Sciences Meeting, Orlando, FL, 6-10 January 2020, AIAA Paper 2020-0833
4. Y. Sun and M.S. Hemati, "Suppressing subcritical transition in plane Poiseuille flow," AIAA Fluid Dynamics Conference, Dallas, TX, 17-21 June 2019, AIAA Paper 2019-3713.
5. H. Yao and M.S. Hemati, "Advances in Output Feedback Control of Transient Energy Growth in a Linearized Channel Flow," AIAA Aerospace Sciences Meeting, San Diego, CA, 7-11 January 2019, AIAA Paper 2019-0882.

Theses:

1. A. Kalur, "Reduced-Complexity Modeling for Control and Nonlinear Analysis of Transitional Flows," Doctoral Dissertation, 2021, University of Minnesota Digital Conservancy, https://hdl.handle.net/11299/225015.
2. H. Yao, "Output Feedback Control for Transient Energy Growth Reduction and Transition Suppression in Shear Flows," Doctoral Thesis, 2020, University of Minnesota Digital Conservancy, https://hdl.handle.net/11299/224621.

10 | Recognitions/Interactions/Transitions

In this section we summarize recognitions, interactions, and plans for transitions associated with research supported by AFOSR Grant FA9550-19-1-0034.

Presentation at Meetings

1. T. Mushtaq, P. Seiler, and M.S. Hemati (2021) "Feedback stabilization of incompressible flows using the quadratic constraint framework," 74th Annual Meeting of the APS Division of Fluid Dynamics, November 21–23, Phoenix, AZ.
2. A. Kalur, T. Mushtaq, P. Seiler, and M.S. Hemati (2021) "Estimating stability margins for transitional flows using quadratic constraints," 74th Annual Meeting of the APS Division of Fluid Dynamics, November 21–23, Phoenix, AZ.
3. N. Conlin, M.S. Hemati, and J. Tithoff (2021) "Data-driven modeling and control of oscillatory instabilities in a Kolmogorov-like flow," 74th Annual Meeting of the APS Division of Fluid Dynamics, November 21–23, Phoenix, AZ.
4. M.S. Hemati, A. Kalur, T. Mushtaq, P. Seiler (2021) "Constrained nonlinear systems analysis and control of transitional and turbulent flows," SIAM CSE (virtual), Fort Worth, TX, March 1–5. **(Invited)**
5. T. Mushtaq, H. Yao, Y. Sun, and M.S. Hemati (2021) "Sensor selection for performance recovery: Controlling transition to turbulence in shear flows," SIAM CSE (virtual), Fort Worth, TX, March 1–5. **(Invited)**
6. H. Yao, Y. Sun, and M.S. Hemati (2020) "Sensor selection for feedback control of transition flows," Remote Colloquium on Vortex Dominated Flows (ReCoVor) (virtual), October 30. **(Invited)**
7. A. Kalur, P. Seiler, and M.S. Hemati (2019) "Nonlinear fluid flow analysis using integral quadratic constraints," 72nd Annual Meeting of the APS Division of Fluid Dynamics, November 23–26, Seattle, WA.
8. Y. Sun, H. Yao, and M.S. Hemati (2019) Nonlinear performance of linear sensor-based output feedback control of transitional channel flow," 72nd Annual Meeting of the APS Division of Fluid Dynamics, November 23–26, Seattle, WA.
9. H. Yao, Y. Sun, and M.S. Hemati, (2019) "Sensor selection for feedback control of transient energy growth in wall-bounded shear flows," 72nd Annual Meeting of the APS Division of Fluid Dynamics, November 23–26, Seattle, WA.
10. Y. Sun, H. Yao, A. Kalur, and M.S. Hemati (2019) "Feedback Control of Transitional Channel

Flow via Reduced-Order Modeling," AIAA Fluid Dynamics Conference, Dallas, TX, June 17–21. **(Invited)**

11. M. Budišić, J.N. Kutz, and M.S. Hemati (2019), "Dynamic Mode Decompositions and Koopman Analysis," SIAM Conference on Applications of Dynamical Systems, Snowbird, UT, May 19–23.
12. M.S. Hemati, D. Bhattacharjee, B. Klose, and G.B. Jacobs (2019) "Optimal actuator selection for airfoil separation control using empirical data," SIAM CSE, February 25–March 1, Spokane, WA. **(Invited)**

Organized Symposia

1. AIAA Fluid Dynamics Conference (2021)
   Reduced-Complexity Modeling for Flow Prediction and Control I & II
   co-organized w/ Karthik Duraisamy
2. AIAA Aerospace Sciences Meeting (2020),
   Joint AIAA-JSASS Session: Martian Aerodynamics,
   co-organized w/ Taku Nonomura and Kunihiko Taira
3. AIAA Aerospace Sciences Meeting (2020),
   Joint AIAA-JSASS Session: Boundary Layer Modification,
   co-organized w/ Taku Nonomura and Kunihiko Taira
4. AIAA Fluid Dynamics Conference (2019),
   Reduced-Complexity Modeling for Flow Control,
   co-organized w/ Karthik Duraisamy
5. SIAM Conference on Applications of Dynamical Systems (2019),
   Dynamic Mode Decompositions and Koopman Analysis,
   co-organized w/ Nathan Kutz and Marko Budišić.

Consultative and Advisory Functions

- A number of interactions with AFRL personnel were maintained, especially with Dr. Albert Medina and Dr. Matthew Rockwood on investigations of fast-flap modeling and control.

A | Stabilizing static output feedback controller

As discussed in section 4.2, an initial stabilizing static output feedback (SOF) gain F_0 is necessary for the calculation of the optimal SOF-LQR controller based on the accelerated Anderson-Moore algorithm (Algorithm 1). Here, we summarize the iterative linear matrix inequality (LMI) algorithm from [100] used for determining such a stabilizing SOF controller in this study.

A stabilizing SOF controller gain can be solved using Lyapunov-based control synthesis methods. This problem can formulated as an LMI feasibility problem, which can be solved using standard methods. A stabilizing SOF gain F_0 must satisfy the following Lyapunov inequality,

$$(A + BF_0C)^\mathsf{T}P + P(A + BF_0C) < 0. \tag{A.1}$$

However, this problem is not linear in the design variables F_0 and P as written. Next, recognize that the following two conditions are sufficient conditions for the inequality above to hold:

Sufficient condition 1

$$\begin{aligned}
&(A + BF_0C)^\mathsf{T}P + P(A + BF_0C) \\
<&(A + BF_0C)^\mathsf{T}P + P(A + BF_0C) + C^\mathsf{T}F_0^\mathsf{T}F_0C \\
=&A^\mathsf{T}P + PA - PBB^\mathsf{T}P + (B^\mathsf{T}P + F_0C)^\mathsf{T}(B^\mathsf{T}P + F_0C) \\
<&0
\end{aligned} \tag{A.2}$$

Sufficient condition 2

$$\begin{aligned}
&A^\mathsf{T}P + PA - PBB^\mathsf{T}P + (B^\mathsf{T}P + F_0C)^\mathsf{T}(B^\mathsf{T}P + F_0C) \\
<&A^\mathsf{T}P + PA \underbrace{+X^\mathsf{T}BB^\mathsf{T}X - P^\mathsf{T}BB^\mathsf{T}X - X^\mathsf{T}BB^\mathsf{T}P}_{\geq -PBB^\mathsf{T}P} \\
&+(B^\mathsf{T}P + F_0C)^\mathsf{T}(B^\mathsf{T}P + F_0C) \\
<&0
\end{aligned} \tag{A.3}$$

where

$$\begin{aligned}
(X - P)^\mathsf{T}BB^\mathsf{T}(X - P) \geq 0 \\
X^\mathsf{T}BB^\mathsf{T}X - P^\mathsf{T}BB^\mathsf{T}X - X^\mathsf{T}BB^\mathsf{T}P \geq -PBB^\mathsf{T}P.
\end{aligned} \tag{A.4}$$

Thus, the original problem (A.1) can be recast as the following LMI feasibility problem for a stabilizing SOF gain F_0:

$$\begin{aligned} &\begin{bmatrix} A^\mathsf{T}P + PA + X^\mathsf{T}BB^\mathsf{T}X - P^\mathsf{T}BB^\mathsf{T}X - X^\mathsf{T}BB^\mathsf{T}P & (B^\mathsf{T}P + F_0C)^\mathsf{T} \\ (B^\mathsf{T}P + F_0C) & -I \end{bmatrix} < 0 \\ &P = P^\mathsf{T} > 0. \end{aligned} \tag{A.5}$$

Further details regarding this formulation can be found in [100].

The SOF gain F_0 can be determined using off-the-shelf interior point solvers; however, the computational cost of solving this problem scales with $O(n^6)$, where n is the state dimension. In this work, we overcome the issue with computational complexity by taking advantage of control-oriented reduced-order models (ROM), similar to those described in [82]. Once we have computed the stabilizing SOF controller gain F_0 using the ROM, this can be used to initialize the Anderson-Moore algorithm (see Algorithm 1) for yielding an SOF-LQR control solution.

We note that the actual synthesis of SOF-LQR controllers based on Algorithm 1 does not require further use of the ROM, as the computational demands scale with $O(n^3)$ (see Appendix B). Although we do not make use of a ROM for the SOF-LQR design in this study, the robustness properties of SOF-LQR control make ROM-based design a potential alternative to designs based on the full-order model. Using a ROM can allow for additional speed-up in the SOF-LQR design, if it is required.

B | Computational complexity of the accelerated Anderson-Moore algorithm

For one iteration, the complexity of the Anderson-Moore algorithm with Armijo-type adaptation is of $O(n^3)$. The computational complexity of the dominant operators are listed in Table B.1, where n and p are the dimensions of state and output vectors, respectively. Recall that $S(F)$ and $H(F)$ are solutions of (4.10) and (4.12).

Table B.1: *Computational complexity of Algorithm 1*

Calculation step	**Dominant operator**	**Complexity**
Solve for $S(F)$ as a function of F	Lyapunov equation (4.10)	n^3
Solve for $H(F)$ as a function of F	Lyapunov equation (4.12)	n^3
Determine descent direction	Matrix inverse	p^3
Objective function evaluation	Trace of matrix multiplication	n^3
Derivative of objective function	Two Lyapunov equations	$2n^3$

C | Grid resolution study

Grid resolution studies have been performed for streamwise- and spanwise-wave disturbances, as shown in figure C.1. The coarse and refined meshes contain $64 \times 101 \times 64$ and $128 \times 101 \times 64$ grid points in the x-, y- and z-direction, respectively. The grids have been tested using different optimal disturbance amplitudes. At the transient energy growth and laminar-to-turbulent transition stages, the results from the coarse and refined meshes overlap before the flows have completely become turbulent. The results in figure C.1 indicate that the grid resolution is sufficient for the flow condition considered in the present work, which does not require fully resolving the turbulent flow. Because we further examine the transition mechanism in the channel flow, the refined mesh is adopted in the direct numerical simulation to better capture relatively small-scale structures present during the transition process. Moreover, because the flow with oblique-wave disturbance has similar characteristics to the one with streamwise-wave disturbance, the grid selected for streamwise-wave disturbance is sufficient to resolve the flow response to the oblique-wave disturbance.

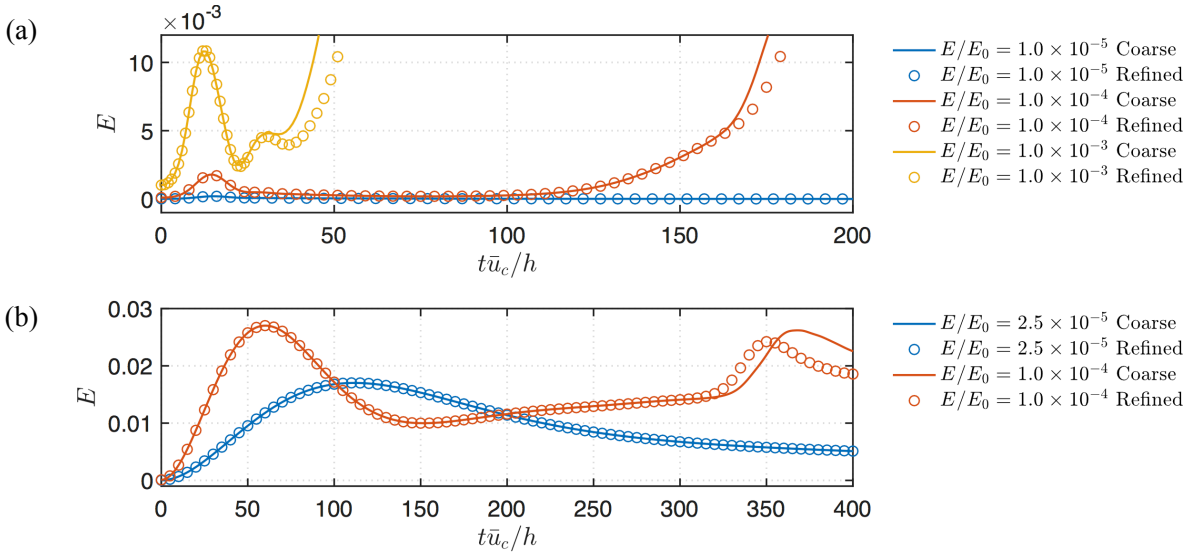


Figure C.1: *Grid resolution study of transient kinetic energy density E for (a) streamwise-wave and (b) spanwise-wave disturbance cases.*

D | Limitations of Modal truncation for MTEG-minimizing control

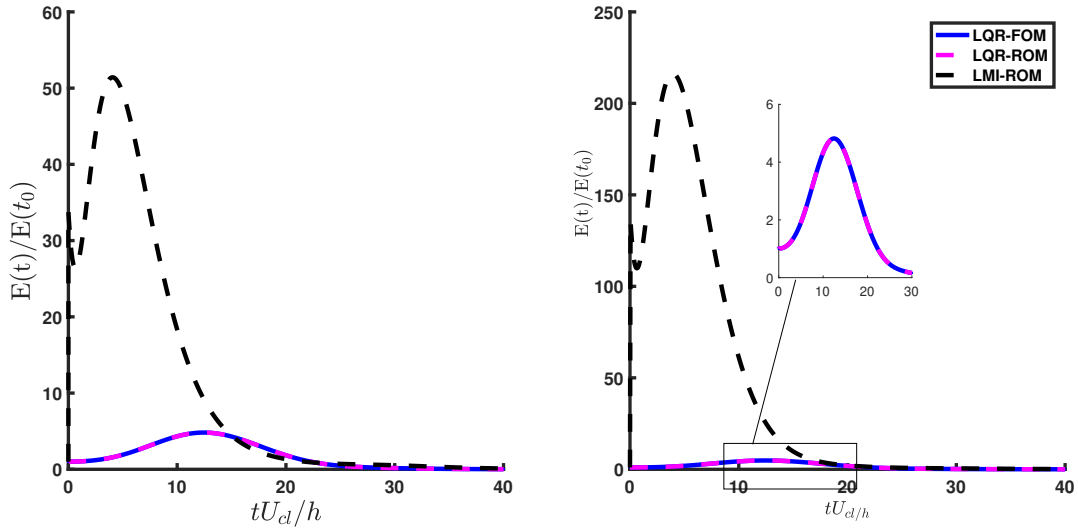
Modal truncation based on the eigendecomposition of the matrix $A = V\Lambda V^{-1}$ in (5.1) is a common approach for reduced-order modeling, primarily owing to its simplicity. Since the eigenvalues λ_i in the diagonal matrix Λ provide information about the relative time-scales of the modal response, a simple strategy for modal truncation is to omit modes using time-scale arguments. For example, when long term behavior is of interest, then modes with fast decay rates and/or high oscillation frequencies can be omitted. ROMs constructed time-scale based modal truncation will not necessarily capture the input-output dynamics needed for controller synthesis. Thus, another common approach considers a measure of modal controllability/observability, given by the ratio [120]

$$\zeta_i = \frac{\|C_i\|\|B_i\|}{|\mathrm{Re}\{\lambda_i\}|}, \tag{D.1}$$

where B_i and C_i correspond to the i^{th} row and column of the modal representations of the matrices B and C from (5.1), respectively. Modes with larger values of ζ_i contribute more to the input-output dynamics and should be be retained, whereas those with lower values of ζ_i can be truncated.

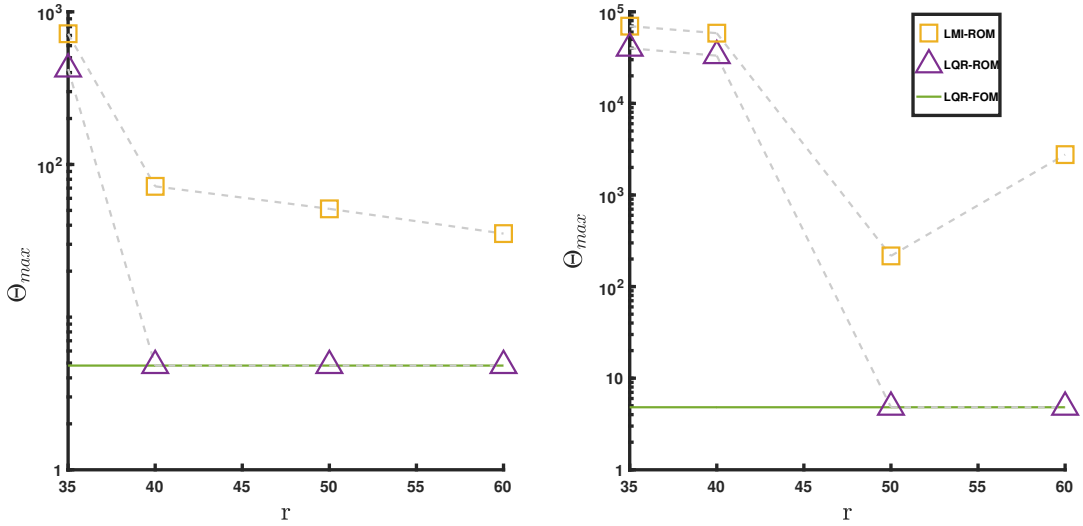
Here, we apply both of these modal truncation approaches to arrive at ROMs with order $r < n$ of the linearized channel flow system with $(\alpha, \beta) = (1, 0)$ and $Re = 3000$. For truncation modal truncation by time-scale arguments, we truncate the "fastest" modes (i.e., stable modes with relatively large $|\mathrm{Re}\{\lambda_i\}|$). For truncation by modal controllability/observability, we truncate the least controllable/observable modes (i.e., stable modes with relatively small ζ_i). Each of these ROMs is then used to design the LMI-ROM and LQR-ROM controllers. The resulting performance of each of these controllers is compared with the LQR-FOM controller in Figure D.1. The model orders here were chosen based on convergence of the ROM open-loop frequency-response relative to the FOM. We note that for the results reported in the Appendix here, the FOM dimension is set to $n = 99$; without doing so, ROMs based on modal truncation converge with $r > 80$, which makes the LMI-based synthesis procedure intractable with the available computational resources. Figure D.2 reports the resulting MTEG $\Theta_{\max}$ as a function of r for ROMs constructed by each of the modal truncation approaches. Interestingly, the truncation of "fast modes" yields improved MTEG performance with the LMI-ROM than truncation based on ζ_i. These results indicate that modal truncation is a poor candidate for designing controllers to reduce TEG. Although in some cases these models can result in effective control laws, the model orders tend to be higher than the tailored approaches considered in this study. The short-comings of modal truncation—and other ROM methods—for TEG reduction further motivates the need for control-oriented model

reduction, like the approach presented in Section 5.2.1.



(a) $|\mathrm{Re}\{\lambda_i\}|$ modal truncation ($r = 50$) **(b)** ζ_i modal truncation ($r = 50$)

Figure D.1: *Worst-case closed-loop TEG response for* $(\alpha, \beta) = (1, 0)$ *and* $Re = 3000$.



(a) $|\mathrm{Re}\{\lambda_i\}|$ modal truncation **(b)** ζ_i modal truncation

Figure D.2: *Closed-loop MTEG* Θ_{max} *as a function of ROM order* r *for* $(\alpha, \beta) = (1, 0)$ *at* $Re = 3000$.

E | Sector-bounded nonlinearities

A comprehensive review of sector bounded systems can be obtained in [155, 182]. Given a nonlinearity $\phi : \mathbb{R} \to \mathbb{R}$, ϕ lies in a sector $[\kappa, \beta]$ if for all $q \in \mathbb{R}$, $p = \phi(q)$ lies between the lines of slope κ and β at each point in time. This property can also written in terms of the input and output of the nonlinearity as a quadratic inequality of the form $(\beta q - \phi(q))(\phi(q) - \kappa q) \geq 0 \; \forall q \in \mathbb{R}$, or equivalently

$$\begin{bmatrix} q \\ p \end{bmatrix}^T \begin{bmatrix} -\kappa\beta & \frac{1}{2}(\kappa+\beta) \\ \frac{1}{2}(\kappa+\beta) & -1 \end{bmatrix} \begin{bmatrix} q \\ p \end{bmatrix} \geq 0 \; \forall q \in \mathbb{R}, \qquad p = \phi(q). \tag{E.1}$$

Graphically this is shown in FIG. E.1, where the shaded region contains the nonlinearity ϕ.

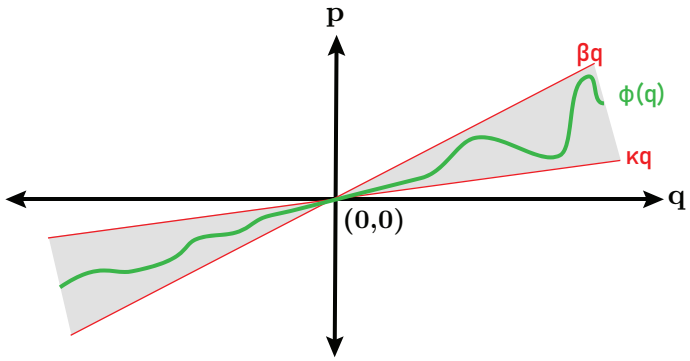


Figure E.1: *Illustration of a generic sector bounded nonlinearity*

F | The set bounded by local region R is invariant

The role of R in this analysis can be made more precise. Assume there is a feasible solution $P > 0$ for the linear matrix inequality in Eq. (7.17). Then the Lyapunov function $V(\mathbf{x}) = \mathbf{x}^T P \mathbf{x}$ satisfies $dV(\mathbf{x}(t))/dt < 0$ as long as $\mathbf{x}(t)^T \mathbf{x}(t) \leq R^2$. This implies that trajectories converge back to $\mathbf{x}_e = 0$ if the initial conditions are sufficiently close to the origin. In particular, the constraint $P > I$ implies that $\mathbf{x}^T \mathbf{x} < V(\mathbf{x})$. A simple proof by contradiction can be used to demonstrate that if $V(\mathbf{x}(0)) < R^2$ then: (i) the trajectory $\mathbf{x}(t)$ remains in the local region $\|\mathbf{x}(t)\|^2 \leq R^2$ and (ii) the trajectory $\mathbf{x}(t)$ decays to the origin. In summary, the set $S_R := \{\mathbf{x} : V(\mathbf{x}) < R^2\}$ is a domain of attraction.

Proof:

Define the set $S_R := \{\mathbf{x} : V(x) < R^2\}$. Assume $\mathbf{x}(0) \in S_R$ and let $\mathbf{x}(t)$ denote the corresponding state trajectory from this initial condition. Assume there exists a time T_1 such that $\mathbf{x}(T_1) \notin S_R$ and let T_0 be the smallest (infimum) of times such that $\mathbf{x}(t) \notin S_R$. The solution $\mathbf{x}(t)$ is a continuous function of time and hence $\mathbf{x}(t) \in S_R$ for all $t \in [0, T_0)$ and, moreover, $\mathbf{x}(t)$ is on the boundary of S_R so that $V(\mathbf{x}(T_0)) = R^2$. As noted above, $P > I$ implies that if $\mathbf{x}(t) \in S_R$ then $\|\mathbf{x}(t)\|^2 < R^2$. Therefore, the local quadratic constraints are valid for all $t \in [0, T_0]$. The constraints in Eq. (7.17) imply that, for a sufficiently small $\epsilon > 0$, the Lyapunov function satisfies $dV(\mathbf{x}(t))/dt \leq -\epsilon \mathbf{x}(t)^T \mathbf{x}(t) \; \forall \; t \in [0, T_0]$. Integrating yields the following bound for any $\mathbf{x}(0) \neq 0$:

$$V(\mathbf{x}(T_0)) \leq V(\mathbf{x}(0)) < R^2 \tag{F.1}$$

This contradicts the assumption that $V(\mathbf{x}(T_0)) = R^2$ and hence trajectories must remain in S_R. Moreover, the Lyapunov condition $dV/dt \leq -\epsilon \mathbf{x}(t)^T \mathbf{x}(t) \; \forall \; t \in [0, T_0]$ implies that the trajectories in this region decay asymptotically back to the origin.

Bibliography

[1] P. J. Schmid and D. S. Henningson, *Stability and transition in shear flows*. Springer, 2001.

[2] L. S. Hultgren, "Algebraic growth of disturbances in a laminar boundary layer," *Physics of Fluids*, vol. 24, 1981.

[3] K. M. Butler and B. F. Farrell, "Three-dimensional optimal perturbations in viscous shear flow," *Physics of Fluids A: Fluid Dynamics*, vol. 4, no. 8, pp. 1637–1650, 1992.

[4] B. F. Farrell and P. J. Ioannou, "Stochastic forcing of the linearized Navier-Stokes equations," *Physics of Fluids*, vol. A5, 1993.

[5] S. C. Reddy and D. S. Henningson, "Energy growth in viscous channel flows," *Journal of Fluid Mechanics*, vol. 252, p. 209, Jul 1993.

[6] L. Trefethen, A. Trefethen, S. Reddy, and T. Driscoll, "Hydrodynamic stability without eigenvalues," *Science*, vol. 261, 1993.

[7] K. M. Butler and B. F. Farrell, "Optimal perturbations and streak spacing in wall-bounded turbulent shear flow," *Physics of Fluids*, vol. A5, 1993.

[8] D. S. Henningson and S. C. Reddy, "On the role of linear mechanisms in transition to turbulence," *Physics of Fluids*, vol. 6, no. 3, pp. 1396–1398, 1994.

[9] P. Luchini, "Reynolds-number-independent instability of the boundary layer over a flat surface," *J. Fluid Mechanics*, vol. 327, 1996.

[10] P. Andersson, M. Berggen, and D. S. Henningson, "Optimal disturbances and bypass transition in boundary layers," *Physics of Fluids*, vol. 11, 1999.

[11] J. Kim, "A linear process in wall-bounded turbulent shear flows," *Physics of Fluids*, vol. 12, 2000.

[12] P. Luchini, "Reynolds-number-independent instability of the boundary layer over a flat surface: Optimal perturbations," *J. Fluid Mechanics*, vol. 404, 2000.

[13] M. R. Jovanovic and B. Bamieh, "Componentwise energy amplification in channel flows," *Journal of Fluid Mechanics*, vol. 534, pp. 145–183, 2005.

[14] D. Tempelmann, A. Hanifi, and D. S. Henningson, "Spatial optimal growth in three-dimensional boundary layers," *J. Fluid Mechanics*, vol. 646, 2010.

[15] J. Jiménez, "How linear is wall-bounded turbulence?," *Physics of Fluids*, vol. 25, 2013.

[16] B. Bamieh and M. Dahleh, "Energy amplification in channel flows with stochastic excitation," *Physics of Fluids*, vol. 13, no. 11, 2001.

[17] S. J. Chapman, "Subcritical transition in channel flows," *J. Fluid Mechanics*, vol. 451, 2002.

[18] P. J. Schmid, "Nonmodal stability theory," *Annual Review of Fluid Mechanics*, vol. 39, 2007.

[19] S. S. Joshi, J. L. Speyer, and J. Kim, "A systems theory approach to feedback stabilization of infinitesimal and finite-amplitude disturbances in plane Poiseuille flow," *J. Fluid Mechanics*, vol. 332, 1997.

[20] T. R. Bewley and S. Liu, "Optimal and robust control and estimation of linear paths to transition," *J. Fluid Mechanics*, vol. 365, 1998.

[21] M. Högberg, T. R. Bewley, and D. S. Henningson, "Relaminarization of $Re_\tau = 100$ turbulence using gain scheduling and linear state-feedback control," *Physics of Fluids*, vol. 15, 2003.

[22] J. Kim and T. R. Bewley, "A linear systems approach to flow control," *Annual Review of Fluid Mechanics*, vol. 39, pp. 383–417, 2007.

[23] J. McKernan, J. F. Whidborne, and G. Papadakis, "Linear quadratic control of plane Poiseuille flow - the transient behavior," *International Journal of Control*, vol. 80, 2007.

[24] J. F. Whidborne and J. McKernan, "On the minimization of maximum transient energy growth," *IEEE Transactions on Automatic Control*, vol. 52, 2007.

[25] F. Martinelli, M. Quadrio, J. McKernan, and J. F. Whidborne, "Linear feedback control of transient energy growth and control performance limitations in subcritical plane poiseuille flow," *Physics of Fluids*, vol. 23, no. 1, p. 014103, 2011.

[26] B. L. Jones, P. H. Heins, E. C. Kerrigan, J. F. Morrison, and A. S. Sharma, "Modelling for robust feedback control of fluid flows," *J. Fluid Mechanics*, vol. 769, 2015.

[27] A. Monokrousos, F. Lundell, and L. Brandt, "Feedback Control of Boundary-Layer Bypass Transition: Comparison of Simulations with Experiments," *AIAA Journal*, vol. 48, no. 8, pp. 1848–1851, 2010.

[28] R. Dadfar, O. Semeraro, A. Hanifi, and D. S. Henningson, "Output Feedback Control of Blasius Flow with Leading Edge Using Plasma Actuator," *AIAA Journal*, vol. 51, no. 9, pp. 2192–2207, 2013.

[29] T. R. Bewley, "Flow control: New challenges for a new renaissance," *Progress in Aerospace Sciences*, vol. 37, no. 1, pp. 21–58, 2001.

[30] J. Kim, "Control of turbulent boundary layers," *Physics of Fluids*, vol. 15, no. 5, 2003.

[31] S. Bagheri, D. S. Henningson, J. Hoepffner, and P. J. Schmid, "Input-output analysis and control design applied to a linear model of spatially developing flows," *Applied Mechanics Review*, vol. 62, no. 2, p. 020803, 2009.

[32] S. Bagheri and D. S. Henningson, "Transition delay using control theory," *Philosophical Transactions of the Royal Society of London A: Mathematical, Physical and Engineering Sciences*, vol. 369, no. 1940, pp. 1365–1381, 2011.

[33] W. L. Brogan, *Modern Control Theory*. Prentice Hall, 1991.

[34] M. Hemati and H. Yao, "Performance limitations of observer-based feedback for transient energy growth suppression," *AIAA Journal*, 2018.

[35] Y. Sun and M. Hemati, "Suppressing subcritical transition in plane poiseuille flow," *AIAA Paper 2019-3713*, 2019.

[36] Y. Sun and M. Hemati, "Feedback control for transition suppression in direct numerical simulations of channel flow," *Energies*, vol. 12, no. 21, 2019.

[37] J. T. Stuart, "On the non-linear mechanics of wave disturbances in stable and unstable parallel flows part 1. the basic behaviour in plane poiseuille flow," *J. Fluid Mech.*, vol. 9, pp. 353–370, November 1960.

[38] J. Watson, "On the non-linear mechanics of wave disturbances in stable and unstable parallel flows part 2. the development of a solution for plane poiseuille flow and for plane couette flow," *J. Fluid Mech.*, vol. 9, pp. 371–389, November 1960.

[39] M. Nishioka, S. I. A, and Y. Ichikawa, "An experimental investigation of the stability of plane poiseuille flow," *J. Fluid Mech.*, vol. 72, pp. 731–751, November 1975.

[40] D. S. Henningson and J. Kim, "On turbulent spots in plane poiseuille flow," *J. Fluid Mech.*, vol. 228, pp. 183–205, 1991.

[41] L. H. Thomas, "The stability of plane poiseuille flow," *Phys. Rev.*, vol. 91, August 1953.

[42] S. A. Orszag, "Accurate solution of the orr-sommerfeld stability equation," *J. Fluid Mech.*, vol. 50, pp. 689–703, 1971.

[43] L. H. Gustavsson, "Energy growth of three-dimensional disturbances in plane poiseuille flow," *J. Fluid Mech.*, vol. 224, pp. 241–260, March 1991.

[44] P. J. Schmid and D. S. Henningson, *Stability and Transition in Shear Flows*. New York: Springer-Verlag, 2001.

[45] S. A. Orszag and L. C. Kells, "Transition to turbulence in plane poiseuille and plane couette flow," *J. Fluid Mech.*, vol. 96, pp. 159–205, 1980.

[46] M. Nishioka and M. Asai, "Some observations of the subcritical transition in plane poiseuille flow," *J. Fluid Mech.*, vol. 150, pp. 441–450, January 1985.

[47] S. J. Chapman, "Subcritical transition in channel flows," *J. Fluid Mech.*, vol. 451, pp. 35–97, 2002.

[48] P. J. Schmid, "Nonmodal stability theory," *Annu. Rev. Fluid Mech.*, vol. 39, pp. 129–162, 2007.

[49] A. Hanifi, P. J. Schmid, and D. S. Henningson, "Transient growth in compressible boundary layer flow," *Phys. Fluids*, vol. 8, no. 826, 1996.

[50] S. S. Joshi, J. L. Speyer, and J. Kim, "A systems theory approach to the feedback stabilization of infinitesimal and finite-amplitude disturbances in plane poiseuille flow," *J. Fluid Mech.*, vol. 332, pp. 157–184, February 1997.

[51] T. R. Bewley and S. Liu, "Optimal and robust control and estimation of linear paths to transition," *J. Fluid Mech.*, vol. 365, pp. 305–349, 1998.

[52] M. Hogberg, T. R. Bewley, and D. Henningson, "Linear feedback control and estimation of transition in plane channel flow," *J. Fluid Mech.*, vol. 481, pp. 149–175, April 2003.

[53] M. Ilak and C. W. Rowley, "Feedback control of transitional channel flow using balanced proper orthogonal decomposition," AIAA Paper 2008-4230, 2008.

[54] F. Martinelli, M. Quadrio, J. McKernan, and J. F. Whidborne, "Linear feedback control of transient energy growth and control performance limitations in subcritical plane poiseuille flow," *Phys. Fluids*, vol. 23, 2011.

[55] J. Kim and T. R. Bewley, "A linear systems approach to flow control," *Annu. Rev. Fluid Mech.*, vol. 39, pp. 383–417, 2007.

[56] M. R. Jovanović and B. Bamieh, "Componentwise energy amplification in channel flows," *J. Fluid Mech.*, vol. 534, pp. 145–183, 2005.

[57] B. L. Jones, P. H. Heins, E. C. Kerrigan, J. F. Morrison, and A. S. Sharma, "Modelling for robust feedback control of fluid flows," *J. Fluid Mech.*, vol. 769, pp. 687–722, 2015.

[58] P. H. Heins, B. L. Jones, and A. S. Sharma, "Passivity-based output-feedback control of turbulent channel flow," *Automatica*, vol. 69, pp. 348–355, 2016.

[59] J. F. Whidborne and N. Amar, "Computing the maximum transient energy growth," *BIT Numerical Mathematics*, vol. 51, pp. 447–457, 2011.

[60] R. R. Kerswell, "Nonlinear nonmodal stability theory," *Annu. Rev. Fluid Mech.*, vol. 50, pp. 319–345, 2018.

[61] M. S. Hemati and H. Yao, "Performance limitation of observer-based feedback for transient energy growth suppression," *AIAA J.*, vol. 56, no. 6, 2018.

[62] H. Yao and M. S. Hemati, "Revisting the separation principle of improved transition control," AIAA Paper 2018-3693, 2018.

[63] A. Kalur and M. S. Hemati, "Control-oriented model reduction for minimizing transient energy growth in shear flows," *AIAA Journal (in-press)*, 2019. arXiv:1907.01664.

[64] H. Yao and M. S. Hemati, "Advances in output feedback control of transient energy growth in a linearized channel flow," AIAA Paper 2019-0882, 2019.

[65] J. F. Gibson, "Channelflow: A spectral Navier-Stokes simulator in C++," tech. rep., U. New Hampshire, 2014. Channelflow.org.

[66] J. F. Gibson, J. Halcrow, and P. Cvitanović, "Visualizing the geometry of state space in plane Couette flow," *J. Fluid Mech.*, vol. 611, pp. 107–130, 2008. arXiv:0705.3957.

[67] S. C. Reddy, P. J. Schmid, J. S. Baggett, and D. S. Henningson, "On stability of streamwise streaks and transition thresholds in plane channel flows," *J. Fluid Mech.*, vol. 365, pp. 269–303, 1998.

[68] J. McKernan, G. Papadakis, and J. F. Whidborne, "A linear state-space representation of plane poiseuille flow for control design - a tutorial," *International J. of Modeling, Identification and Control*, vol. 1, no. 4, pp. 272–280, 2006.

[69] W. L. Brogan, *Modern Control Theory*. Pearson, 1991.

[70] J. C. R. Hunt, A. A. Wray, and P. Moin, "Eddies, streams, and convergence zones in turbulent flows," *Proc. of the Summer Program, Center of Turbulence Research*, pp. 193–208, 1988.

[71] C. Lee, T. Min, and J. Kim, "Stability of a channel flow subject to wall blowing and suction in the form of a traveling wave," *Physics of Fluids*, vol. 20, p. 101513, 2008.

[72] H. Yao and M. S. Hemati, "Advances in output feedback control of transient energy growth in a linearized channel flow," *AIAA Paper 2019-0882*, 2019.

[73] H. Yao, Y. Sun, T. Mushtaq, and M. S. Hemati, "Reducing transient energy growth in a channel flow using static output feedback control," *arXiv pre-print, arXiv:2012.13314*, 2022.

[74] P. J. Schmid, "Nonmodal stability theory," *Annual Review of Fluid Mechanics*, vol. 39, no. 1, pp. 129–162, 2007.

[75] L. N. Trefethen, A. E. Trefethen, S. C. Reddy, and T. A. Driscoll, "Hydrodynamic Stability Without Eigenvalues," *Science*, vol. 261, no. 5121, pp. 578–584, 1993.

[76] S. Reddy and D. Henningson, "Energy growth in viscous channel flows," *J. Fluid Mechanics*, vol. 252, pp. 209–238, 1993.

[77] M. R. Jovanović and B. Bamieh, "Componentwise energy amplification in channel flows," *Journal of Fluid Mechanics*, vol. 534, p. 145–183, 2005.

[78] K. M. Butler and B. Farrell, "Three-dimensional optimal perturbations in viscous shear flow," *Physics of Fluids A: Fluid Dynamics*, vol. 4, pp. 1637–1650, 1992.

[79] S. Bagheri, P. Schlatter, P. J. Schmid, and D. S. Henningson, "Global stability of a jet in crossflow," *J. Fluid Mech.*, vol. 624, pp. 33–44, 2009.

[80] Y. Sun and M. S. Hemati, "Feedback control for transition suppression in direct numerical simulations of channel flow," *Energies*, vol. 12, no. 21, 2019.

[81] M. Ilak and C. W. Rowley, "Feedback control of transitional channel flow using balanced proper orthogonal decomposition," *AIAA paper 2008-4230*, 2008.

[82] A. Kalur and M. S. Hemati, "Control-oriented model reduction for minimizing transient energy growth in shear flows," *AIAA Journal*, 2019.

[83] T. R. Bewley and S. Liu, "Optimal and robust control and estimation of linear paths to transition," *Journal of Fluid Mechanics*, vol. 365, pp. 305–349, 1998.

[84] M. Högberg, T. R. Bewley, and D. S. Henningson, "Linear feedback control and estimation of transition in plane channel flow," *Journal of Fluid Mechanics*, vol. 481, p. 149–175, 2003.

[85] M. S. Hemati and H. Yao, "Performance limitations of observer-based feedback for transient energy growth suppression," *AIAA Journal*, vol. 56, no. 6, pp. 2119–2123, 2018.

[86] H. Yao and M. S. Hemati, "Revisiting the separation principle for improved transition control," AIAA paper 2018-3693, 2018.

[87] J. F. Whidborne, J. McKernan, and A. J. Steer, "Minimization of maximum transient energy growth by output feedback," *IFAC Proceedings*, vol. 38, no. 1, pp. 283–288, 2005.

[88] J. F. Whidborne and J. McKernan, "On the minimization of maximum transient energy growth," *IEEE Transactions on Automatic Control*, vol. 52, no. 9, pp. 1762–1767, 2007.

[89] J. F. Whidborne, J. McKernan, and G. Papadakis, "Minimizing transient energy growth in plane poiseuille flow," *Proceedings of the Institution of Mechanical Engineers, Part I: Journal of Systems and Control Engineering*, vol. 222, no. 5, pp. 323–331, 2008.

[90] P. Apkarian and D. Noll, "Optimizing the kreiss constant," *SIAM Journal on Control and Optimization*, vol. 58, no. 6, pp. 3342–3362, 2020.

[91] J. Hoepffner, M. Chevalier, T. R. Bewley, and D. S. Henningson, "State estimation in wall-bounded flow systems. part 1. perturbed laminar flows," *Journal of Fluid Mechanics*, vol. 534, p. 263–294, 2005.

[92] B. D. Anderson and J. B. Moore, *Linear Optimal Control*. New Jersey: Prentice-Hall, 1971.

[93] M. Ilak and C. W. Rowley, "Modeling of transitional channel flow using balanced propoer orthogonal decomposition," *Phys. Fluids*, vol. 20, p. 034103, 2008.

[94] H. Choi, P. Moin, and J. Kim, "Active turbulence control for drag reduction in wall-bounded flows," *Journal of Fluid Mechanics*, vol. 262, pp. 75–110, 1994.

[95] M. Luhar, A. Sharma, and B. McKeon, "Opposition control within the resolvent analysis framework," *Journal of Fluid Mechanics*, vol. 749, pp. 597–626, 2014.

[96] V. L. Syrmos, C. T. Abdallah, P. Dorato, and K. Grigoriadis, "Static Output Feedback: A Survey," *Automatica*, vol. 33, no. 2, pp. 125–137, 1997.

[97] T. Rautert and E. W. Sachs, "Computational Design of Optimal Output Feedback Controllers," *SIAM J. Optimization*, vol. 7, no. 3, pp. 837–852, 1997.

[98] J. Nocedal and S. J. Wright, *Numerical Optimization*. New York: Springer, 2nd ed. ed., 2006.

[99] H. T. Toivonen and P. M. Mäkilä, "A Descent Anderson-Moore Algorithm for Optimal Decentralized Control," *Automatica*, vol. 21, no. 6, pp. 743–744, 1985.

[100] Y.-Y. Cao, J. Lam, and Y.-X. Sun, "Static Output Feedback Stabilization: An ILMI Approach," *Automatica*, vol. 34, no. 12, pp. 1641–1645, 1998.

[101] J. McKernan, J. Whidborne, and G. Papadakis, "A linear state-space representation of plane poiseuille flow for control design – a tutorial," *International Journal of Modelling Identification and Control*, vol. 1, pp. 272–280, 2006.

[102] S. A. Orszag and L. C. Kells, "Transition to turbulence in plane poiseuille and plane couette flow," *Journal of Fluid Mechanics*, vol. 96, no. 1, p. 159–205, 1980.

[103] S. A. Orszag, "Accurate solution of the orr–sommerfeld stability equation," *Journal of Fluid Mechanics*, vol. 50, no. 4, p. 689–703, 1971.

[104] A. Kalur and M. Hemati, "Control-oriented model reduction for minimizing transient energy growth in shear flows," *AIAA Journal*, 2019.

[105] V. C. Patel and M. R. Head, "Some observations on skin friction and velocity profiles in fully developed pipe and channel flows," *Journal of Fluid Mechanics*, vol. 38, no. 1, pp. 181–201, 1969.

[106] S. C. Reddy and D. S. Henningson, "Energy growth in viscous channel flows," *J. Fluid Mech.*, vol. 252, pp. 209–238, July 1993.

[107] S. J. Chapman, "Subcritical transition in channel flows," *Journal of Fluid Mechanics*, vol. 451, pp. 35–97, 2002.

[108] T. R. Bewley, "Flow control: new challenges for a new Renaissance," *Prog. Aero. Sci.*, vol. 37, pp. 21–58, 2001.

[109] M. Ilak and C. W. Rowley, "Feedback control of transitional channel flow using balanced proper orthogonal decomposition," *AIAA Paper 2008-4230*, 2008.

[110] S. S. Joshi, J. L. Speyer, and J. Kim, "Finite dimensional optimal control of Poiseuille flow," *Journal of Guidance, Control, and Dynamics*, vol. 22, no. 2, p. 340–348, 1999.

[111] H. Yao and M. S. Hemati, "Revisiting the separation principle for improved transition control," *AIAA Paper 2018-3693*, 2018.

[112] H. Yao and M. Hemati, "Advances in output feedback control of transient energy growth in a linearized channel flow," *AIAA Paper 2019-0882*, 2019.

[113] S. Boyd, L. El Ghaoui, E. Feron, and V. Balakrishnan, *Linear matrix inequalities in system and control Theory*. Society for Industrial and Applied Mathematics, Jan 1994.

[114] F. Martinelli, M. Quadrio, J. Mckernan, and J. F. Whidborne, "Linear feedback control of transient energy growth and control performance limitations in subcritical plane Poiseuille flow," *Physics of Fluids*, 2011.

[115] A. Barbagallo, D. Sipp, and P. Schmid, "Why may reduced order models based on global modes not work for closed loop control?," *19 eme Congres Francais de Mecanique*, vol. 1, no. 7, 2011.

[116] K. Taira, S. L. Brunton, S. T. M. Dawson, C. W. Rowley, T. Colonius, B. J. Mckeon, O. T. Schmidt, S. Gordeyev, V. Theofilis, and L. S. Ukeiley, "Modal analysis of fluid flows: an overview," *AIAA Journal*, 2017.

[117] C. W. Rowley and S. T. M. Dawson, "Model reduction for flow analysis and control," *Annual Review of Fluid Mechanics*, vol. 49, pp. 387–417, 2017.

[118] C. W. Rowley, "Model reduction for fluids, using balanced proper orthogonal decomposition," *Int. J. Bif. Chaos*, vol. 15, no. 3, pp. 997–1013, 2005.

[119] B. Moore, "Principal component analysis in linear systems: Controllability, observability, and model reduction," *IEEE Transactions on Automatic Control*, vol. 26, no. 1, pp. 17–32, 1981.

[120] A. C. Antoulas, *Approximation of Large-Scale Dynamical Systems*. Society for Industrial and Applied Mathematics, 2005.

[121] K. Willcox and J. Peraire, "Balanced model reduction via the proper orthogonal decomposition," *AIAA Journal*, vol. 40, no. 11, p. 2323–2330, 2002.

[122] M. Grant and S. Boyd, "CVX: Matlab software for disciplined convex programming, version 2.1." `http://cvxr.com/cvx`, Mar 2014.

[123] M. Ilak and C. W. Rowley, "Modeling of transitional channel flow using balanced proper orthogonal decomposition," *Physics of Fluids*, vol. 20, no. 3, 2008.

[124] A. Laub, M. Heath, C. Paige, and R. Ward, "Computation of system balancing transformations and other applications of simultaneous diagonalization algorithms," *IEEE Transactions on Automatic Control*, vol. 32, no. 2, pp. 115–122, 1987.

[125] J. P. Boyd, *Chebyshev and Fourier Spectral Methods*. New York: Dover Publ., 2000.

[126] J. McKernan, G. Papadakis, and J. F. Whidborne, "A linear state-space representation of plane poiseuille flow for control design: A tutorial," *International Journal of Modelling, Identification and Control*, vol. 1, no. 4, pp. 272–280, 2006.

[127] J. McKernan, "Control of Plane Poiseuille Flow: A Theoretical and Computational Investigation," 2006.

[128] J. F. Whidborne and N. Amar, "Computing the Maximum Transient Energy Growth," *BIT Numerical Mathematics*, vol. 51, no. 2, pp. 447–457, 2011.

[129] H. Yao, Y. Sun, and M. Hemati, "Feedback control of transitional shear flows: Sensor selection for performance recovery," *pre-print arXiv:2009.03469*, 2022.

[130] M. T. Landahl, "A note on an algebraic instability of inviscid parallel shear flows," *Journal of Fluid Mechanics*, vol. 98, no. 2, p. 243–251, 1980.

[131] B. F. Farrell and P. J. Ioannou, "Optimal excitation of three-dimensional perturbations in viscous constant shear flow," *Physics of Fluids A: Fluid Dynamics*, vol. 5, no. 6, pp. 1390–1400, 1993.

[132] B. Bamieh and M. Dahleh, "Energy amplification in channel flows with stochastic excitation," *Physics of Fluids*, vol. 13, no. 11, pp. 3258–3269, 2001.

[133] K. Willcox, "Unsteady flow sensing and estimation via the gappy proper orthogonal decomposition," *Computers & Fluids*, vol. 35, no. 2, pp. 208 – 226, 2006.

[134] K. Manohar, B. W. Brunton, J. N. Kutz, and S. L. Brunton, "Data-driven sparse sensor placement for reconstruction: Demonstrating the benefits of exploiting known patterns," *IEEE Control Systems Magazine*, vol. 38, no. 3, pp. 63–86, 2018.

[135] K. Manohar, J. N. Kutz, and S. L. Brunton, "Optimal sensor and actuator placement using balanced model reduction," *arXiv pre-print, arXiv:1812.01574*, 2018.

[136] E. Clark, T. Askham, S. L. Brunton, and J. N. Kutz, "Greedy sensor placement with cost constraints," *IEEE Sensors Journal*, vol. 19, no. 7, pp. 2642–2656, 2019.

[137] Y. Saito, T. Nonomura, K. Yamada, K. Asai, Y. Sasaki, and D. Tsubakino, "Determinant-based fast greedy sensor selection algorithm," *arXiv pre-print, arXiv:1911.08757*, 2020.

[138] K. Yamada, Y. Saito, K. Nankai, T. Nonomura, K. Asai, and D. Tsubakino, "Fast greedy optimization of sensor selection in measurement with correlated noise," *arXiv pre-print, arXiv:1912.01776*, 2020.

[139] M. Natarajan, J. B. Freund, and D. J. Bodony, "Actuator selection and placement for localized feedback flow control," *Journal of Fluid Mechanics*, vol. 809, p. 775–792, 2016.

[140] K. K. Chen and C. W. Rowley, "H2 optimal actuator and sensor placement in the linearised complex ginzburg–landau system," *Journal of Fluid Mechanics*, vol. 681, p. 241–260, 2011.

[141] S. F. Oehler and S. J. Illingworth, "Sensor and actuator placement trade-offs for a linear model of spatially developing flows," *Journal of Fluid Mechanics*, vol. 854, p. 34–55, 2018.

[142] D. Bhattacharjee, B. Klose, G. Jacobs, and M. Hemati, "Data-driven selection of actuators for optimal control of airfoil separation," *Theor. Comput. Fluid Dyn.*, vol. 34, pp. 557–575, 2020.

[143] F. Lin, M. Fardad, and M. R. Jovanović, "Design of optimal sparse feedback gains via the alternating direction method of multipliers," *IEEE Transactions on Automatic Control*, vol. 58, no. 9, pp. 2426–2431, 2013.

[144] B. Polyak, M. Khlebnikov, and P. Shcherbakov, "Sparse feedback in linear control systems," *Autom Remote Control*, vol. 75, no. 12, p. 2099–2111, 2014.

[145] A. Kalur, P. Seiler, and M. S. Hemati, "Stability and performance analysis of nonlinear and non-normal systems using quadratic constraints," *AIAA Paper 2020-0833*, 2020.

[146] A. Kalur, P. Seiler, and M. S. Hemati, "Nonlinear stability analysis of transitional flows using quadratic constraints," *Physical Review Fluids (in review), pre-print arXiv:2004.05440*.

[147] T. Mushtaq, P. Seiler, and M. Hemati, "Feedback control of transitional flows: A framework for controller verification using quadratic constraints," *AIAA Fluid Dynamics Conference, Washington, D.C., 2-6 August 2021 (virtual). AIAA Paper 2021-2825*, 2021.

[148] A. Kalur, T. Mushtaq, P. Seiler, and M. Hemati, "Estimating regions of attraction for transitional flows using quadratic constraints," *IEEE Control Systems Letters*, vol. 6, pp. 482–487, 2022.

[149] F. Waleffe, "Hydrodynamic stability and turbulence: beyond transients to a self-sustaining process," *Studies in Applied Mathematics*, 1995.

[150] F. Waleffe, "Transition in shear flows. nonlinear normality versus non-normal linearity," *Physics of Fluids*, 1995.

[151] A. Sharma, F. Morrison, J, B. J. McKeon, and W. Limebeer, D.J.N. Koberg, "Relaminarisation of $re_t = 100$ channel flow with globally stabilising linear feedback control," *Physics of Fluids*, 2011.

[152] R. Kerswell, "Nonlinear nonmodal stability theory," *Annual Review of Fluid Mechanics*, 2018.

[153] B. J. McKeon and A. S. Sharma, "A critical-layer framework for turbulent pipe flow," *Journal of Fluid Mechanics*, 2010.

[154] M. R. Jovanovic, "From bypass transition to flow control and data-driven turbulence modeling: An input-output viewpoint," *arXiv:2003.10104v1 [physics.flu-dyn]*, 2020.

[155] H. K. Khalil, *Nonlinear systems*. Prentice Hall, 2002.

[156] K. Taira, M. S. Hemati, S. L. Brunton, Y. Sun, K. Duraisamy, S. Bagheri, S. T. M. Dawson, and C.-A. Yeh, "Modal analysis of fluid flows: applications and outlook," *AIAA Journal*, Mar 2019.

[157] B. J. McKeon, "The engine behind (wall) turbulence: perspectives on scale interactions," *Journal of Fluid Mechanics*, vol. 817, 2017.

[158] A. S. Sharma and B. J. McKeon, "On coherent structure in wall turbulence," *Journal of Fluid Mechanics*, 2013.

[159] Y. Sun, Q. Liu, L. N. Cattafesta, L. S. Ukeiley, and K. Taira, "Resolvent analysis of compressible laminar and turbulent cavity flows," *AIAA Journal*, vol. 58, 2019.

[160] A. Chavarin and M. Luhar, "Resolvent analysis for turbulent channel flow with riblets," *AIAA Journal*, 2019.

[161] P. H. Heins, B. L. Jones, and A. S. Sharma, "Passivity-based output-feedback control of turbulent channel flow," *Automatica*, 2016.

[162] C. J. Damaren, "Laminar-turbulent transition control using passivity analysis of the orr-sommerfeld equation," *Journal of Guidance, Control, and Dynamics*, vol. 39, no. 7, pp. 1602–1613, 2016.

[163] C. J. Damaren, "Transition control of the Blasius boundary layer using passivity," *Aerospace Systems*, vol. 2, no. 1, pp. 21–31, 2018.

[164] M. Ahmadi, G. Valmorbida, D. Gayme, and A. Papachristodoulou, "A framework for input-output analysis of wall-bounded shear flows," *ArXiv ID 1802.04974v1*, 2018.

[165] D. D. Joseph, *Stability of fluid motions I*. New York: Springer-Verlag, 1976.

[166] P. J. Goulart and S. Chernyshenko, "Global stability analysis of fluid flows using sum-of-squares," *Physica D*, vol. 241, pp. 692–704, 2012.

[167] F. Waleffe, J. Kim, and J. Hamilton, "On the origins of streaks in turbulent shear flows," *Turbulent Shear Flows Springer*, 1993.

[168] D. Henningson, "Comment on transition in shear flows. nonlinear normality versus non-normal linearity," *Physics of Fluids*, 1996.

[169] J. S. Baggett and L. N. Trefethen, "Low-dimensional models of subcritical transition to turbulence," *Physics of Fluids*, 1997.

[170] J. E. Prussing, "The principal minor test for semidefinite matrices," *Journal of Guidance, Control, and Dynamics*, vol. 9, no. 1, pp. 121–122, 1986.

[171] R. A. Horn and C. R. Johnson, *Matrix analysis*. Cambridge University Press, 1990.

[172] J. Gallier, "The Schur complement and symmetric positive semidefinite (and Definite) matrices," *Complement*, 2010.

[173] M. Grant and S. Boyd, "Graph implementations for nonsmooth convex programs," in *Recent Advances in Learning and Control* (V. Blondel, S. Boyd, and H. Kimura, eds.), Lecture Notes in Control and Information Sciences, pp. 95–110, Springer-Verlag Limited, 2008.

[174] M. ApS, *The MOSEK optimization toolbox for MATLAB manual. Version 9.0.*, 2019.

[175] S. Boyd and L. E. Ghaoui, "Method of centers for minimizing generalized eigenvalues," *Linear Algebra and Applications, special issue on Linear Algebra in Systems and Control*, 1993.

[176] P. Gahinet and A. Nemirovskii, "General-purpose LMI solvers with benchmarks," in *Proceedings of the IEEE Conference on Decision and Control*, 1993.

[177] R. R. Kerswell, C. C. Pringle, and A. P. Willis, "An optimization approach for analysing nonlinear stability with transition to turbulence in fluids as an exemplar," *arXiv:1408.3539*, 2014.

[178] C. Liu and D. F. Gayme, "An input-output inspired method for permissible perturbation amplitude of transitional wall-bounded shear flows," *arXiv:2006.16484*, Jun 2020.

[179] F. Blanchini, "Set invariance in control," *Automatica*, vol. 35, no. 11, pp. 1747 – 1767, 1999.

[180] C.-T. Chen, *Linear System Theory and Design*. CBS College publishing, 1984.

[181] S. Boyd and L. Vandenberghe, *Convex optimization*. Cambridge University Press, 2004.

[182] J. C. Willems, "Dissipative dynamical systems part i: general theory," *Archive for Rational Mechanics and Analysis*, 1972.